Orientational order parameter in the ordered phase of solid deuterium from neutron-diffraction data

V. V. Danchuk, N. N. Galtsov,* M. A. Strzhemechny, and A. I. Prokhvatilov

B. Verkin Institute for Low Temperature Physics and Engineering, National Academy of Sciences of Ukraine, pr. Lenina 47, Kharkov 61103, Ukraine
(Submitted June 10, 2003; revised August 14, 2003)
Fiz. Nizk. Temp. **30**, 163–168 (February 2004)

The method of direct reconstruction of the orientational order parameter η from diffraction intensities is applied to the case of the orientationally ordered phase of the quantum crystal para-D_2 using the neutron elastic scattering data of Yarnell, Mills, and Schuch. The average value obtained, $\eta=0.368$, is close but somewhat lower than the value 0.4 corresponding to the theoretical value at $T=0$ in the molecular field approximation. The nature of this decrease is assessed theoretically with allowance for three factors that influence the absolute value of η: thermal excitation of librons, rotational anharmonicities, and rotational polarization. It is shown that the total theoretical renormalization (-8.8%) is close to the value obtained in the reconstruction (-8.0%). © *2004 American Institute of Physics.* [DOI: 10.1063/1.1645162]

1. INTRODUCTION

The total nuclear spin I of homonuclear molecules of hydrogen isotopes can assume values of 0 and 1 for H_2 and of 0, 1, and 2 for D_2. In the solid phase at sufficiently low temperatures the species with even I are found in a state with rotational momentum $J=0$, while the species with $I=1$ have a rotational momentum equal to 1. Molecules with $J=1$ have a quadrupole moment, which gives rise to a noncentral intermolecular interaction and the possibility of orientational ordering of the rotational subsystem. Such a transformation occurs at sufficiently low temperatures and sufficiently high concentrations $x\geqslant 0.55$ of the species with $J=1$. This phase transition has been the subject of many theoretical and experimental studies (see, e.g., Refs. 1 and 2), as a result of which it has been established that the transition occurs from the high-temperature orientationally disordered hcp phase to a cubic orientationally ordered phase $Pa3$ with four molecules oriented with their axes along directions of the $\langle 111\rangle$ type in the crystal. The ordering is characterized by the orientational order parameter

$$\eta=\langle P_2(\cos\vartheta)\rangle, \tag{1}$$

where the angle brackets denote thermodynamic and quantum-mechanical averaging over rotational states, ϑ is the angle between the instantaneous orientation of the molecule and the corresponding direction of the $\langle 111\rangle$ type, and $P_2(x)$ is a Legendre polynomial.

Skipping the historical details of the determination of the structure of the ordered phase of solid hydrogens with $J=1$, we refer the reader to review articles.[2] The circumstance that the Pake doublet splitting in the NMR spectrum is proportional to the orientational order parameter[3] was used[4,5] to construct the temperature dependence of the order parameter in a wide region of temperatures and concentrations of para-D_2 ($J=1$). Good agreement was obtained with the results of a calculation by the cluster expansion method[6] and with calculations using experimental data on the energy of libronic excitations.[5] It should be noted that in all the experimental studies mentioned the values reconstructed were those of the reduced quantity $\overline{\eta}$, i.e., the values of η from Eq. (1) relative to its value at $T=0$. The absolute values of η in the low-temperature phases of hydrogen and deuterium, which could in principle be reconstructed from structural data, have long resisted determination. The problem of determining the absolute values of η for ordered phases of crystals formed by symmetric diatomic molecules can be solved relatively easily[7] if one has reliable information about the intensities of both structure and superstructure reflections. The intensity of the latter are directly related to the character and degree of orientational ordering of the molecules in the lattice. In x-ray studies[8–10] of hydrogen and deuterium with high concentrations of the $J=1$ species only the hcp–fcc phase transition has been documented, but it has not been possible to observe the superstructure reflections characteristic of $Pa3$ symmetry in the low-temperature phase. Neutron-diffraction studies[11–14] of the cubic phase of paradeuterium containing over 80% molecules with $J=1$ have been more fruitful. Weak superstructure reflections were observed, and good agreement of the observed and calculated structure amplitudes for the scattering has been obtained; thus the $Pa3$ symmetry of the low-temperature phase of the hydrogens has been confirmed experimentally.[14] The measurements in Refs. 13 and 14 were made on samples with an appreciably higher concentration of the para fraction $J=1$ ($x>90\%$) and with higher precision, making it possible for the investigators to carry out a quantitative comparison of the intensities with the theoretical values calculated with allowance for the quantum nature of the rotation of the molecules. In particular, the experimental values of the scattering amplitudes $F(\mathbf{q})$ were reconstructed for several Bragg reflections (10 in all), and they were compared with the theoretically calculated values of $F(\mathbf{q})$ integrated with the use of the wave functions of the rotational states with $J=1$, $m=1$ in the local frame (along the space diagonal of the cube of the $Pa3$ structure).

These calculations showed satisfactory agreement with the experimental scattering amplitudes, providing strong

proof of the realization of the $Pa3$ structure. At $T=0$ all of the molecules with $J=1$ in $Pa3$ are oriented along the space diagonals of the cube, so that their rotational ground state is described by the function $|J=1, m=0\rangle$, where the projection m of the rotational motion is taken in relation to that diagonal. By definition, the orientational order parameter η for $T=0$ is given by the expression

$$\eta=\langle \mathrm{GS}|P_2(\cos\vartheta)|\mathrm{GS}\rangle, \tag{2}$$

where $|\mathrm{GS}\rangle$ is the ground-state wave function. It is easy to show[15] that if fine effects (see below) are neglected in the framework of the simplest molecular field approximation, $|\mathrm{GS}\rangle$ coincides with $|J=1, m=0\rangle$ and, as a result, we have $\eta_0=2/5$ at $T=0$.

The availability of experimental data on the scattering intensities on ordered sublattices makes it possible to reconstruct the value of the order parameter directly from them. The idea for the correct reconstruction of the characteristics of orientational order from the diffraction intensities by expansion of the scattering amplitudes in spherical harmonics for the particular case of the ordered phases of the hydrogens was apparently first published in the papers by Press.[16] At the time those papers appeared, however, there had not yet been any precision measurements of the intensities of the diffraction lines, and the idea remained without application. To assess the applicability of that approach, the corresponding procedure was used successfully to reconstruct η from x-ray data for the α phase of nitrogen.[7] This same approach has been used[17] for a semi-quantitative estimate of the orientational order parameter of CO_2-Ar mixtures from electron-diffraction data. The application of this method to the case of orientational ordering of triatomic molecules has some peculiarities of its own.[18]

The present study was motivated by the following considerations. First, since the time that Refs. 11 and 14 appeared, our understanding of the nature of quantum crystals has become considerably deeper, making it possible to eliminate a number of inconsistencies in the published treatments. Second, on the basis of the available structural data it has now become possible for the method of direct reconstruction of the absolute values of the orientational order parameter η from the intensities of diffraction lines to be tested on actual quantum crystals.[7,17] Third, the question of numerical estimation of the theoretically predicted fine effects in the rotational dynamics of the solid hydrogens is addressed here for the first time.

2. THEORY

The structure amplitude for neutron scattering can be written in the following form:[19]

$$F(\mathbf{q})=\sum_i b_i e^{-w_i} e^{2\pi i(\mathbf{q}\cdot\mathbf{r}_i)}, \tag{3}$$

where b_i is the amplitude for scattering by the bound nucleus of an atom i (in this particular case, a D atom), $\mathbf{r}_i$ enumerates the vectors of the atomic scatterers within a unit cell, $\mathbf{q}$ is the momentum transfer in the scattering,

$$w_i=8\pi^2\overline{\mathbf{u}_i^2}[\sin\theta/\lambda]^2, \tag{4}$$

θ is the scattering angle, λ is the de Broglie wavelength of the neutrons, and $\overline{\mathbf{u}_i^2}$ is the mean-square thermal displacement of atom i in the isotropic approximation.[19] In neutronography the scattering amplitude on the bound nucleus of an atom i is independent of the interplane distance (the diffraction angle). The dependence on angle enters in the expression for the Debye–Waller temperature factor (4). Proceeding from this, we can write the structure scattering amplitude in the form

$$F(\mathbf{q})=b_D e^{-w(\mathbf{q})}\sum_c \exp(2\pi i\mathbf{q}\cdot\mathbf{R}_c)\cos\xi(\mathbf{q}\cdot\mathbf{m}_c), \tag{5}$$

where the summation is over the four sublattices c of the $Pa3$ structure, $\mathbf{R}_c$ enumerates the centers of the molecules, $\mathbf{m}_c$ is the instantaneous direction of the unit vector along the corresponding molecular axis in sublattice c, $\xi=2\pi d/a$, where $d=0.3707$ Å is one-half the internuclear separation in the D_2 molecule, and $a=5.0760$ Å is the lattice parameter. The values of d and a were taken from Ref. 14. In that paper the experimental structural data are given not in the form of intensities but in the form of values of the structure amplitudes for the corresponding diffraction lines, without allowance for the constant cofactor b_D in Eq. (5). We used those structure amplitudes to reconstruct the orientational order parameter.

For short molecules a good approximation for the structure amplitudes (5) is the sum of the first two terms:[7]

$$F(\mathbf{q})=b_D e^{-w(\mathbf{q})}\left[4j_0(\xi q)-5\eta j_2(\xi q)\sum_c G_c(\mathbf{q})\right], \tag{6}$$

where $j_n(x)$ are the spherical Bessel functions, and $G_c(\mathbf{q})$ has the same meaning as in Ref. 7. The technique proposed in Ref. 7 was used to calculate in an analogous way the error of using the approximate formula (6) for the regular and superstructure lines given in Ref. 14 for almost pure para-D_2. As had been assumed, as a consequence of the short length of the D_2 molecule the error even for the far superstructure lines did not exceed 1% for the case $\eta=1$ in comparison with the results of the exact calculation[20] for rigidly oriented molecules. Such an accuracy gives a high degree of confidence in the procedure of reconstructing the value of η from experimental values of the scattering amplitudes. An important property of formula (6) is that for regular lines only the first term in (6) is nonzero, while for superstructure reflections only the second term is nonzero. This distinction makes it possible to determine the exponent $w(\mathbf{q})$ in Eq. (6) from experiment. Taking this fact into account, we write (6) for the quantity $F(\mathbf{q})/b_D$ in the form

$$F(\mathbf{q})/b_D\equiv f_r^{\mathrm{calc}}+\eta f_s^{\mathrm{calc}}. \tag{7}$$

The problem of taking the Debye–Waller factor $w(\mathbf{q})$ into account consists in the following. The expression for $w(\mathbf{q})$ in (4) is usually written in the form (see, e.g., Ref. 20)

$$w(\mathbf{q})=\frac{6\pi^2\hbar^2H^2}{Mk_B\Theta a^2}\left[\Phi\left(\frac{\Theta}{T}\right)+\frac{1}{4}\right], \tag{8}$$

where Θ is the Debye temperature, $\Phi(x)$ is the well-known Debye–Waller function, M is the mass of a deuterium atom, k_B is Boltzmann's constant, and $H^2\equiv h^2+k^2+l^2$ (h,k,l are the indices of the reflecting planes). Expression (8) was ob-

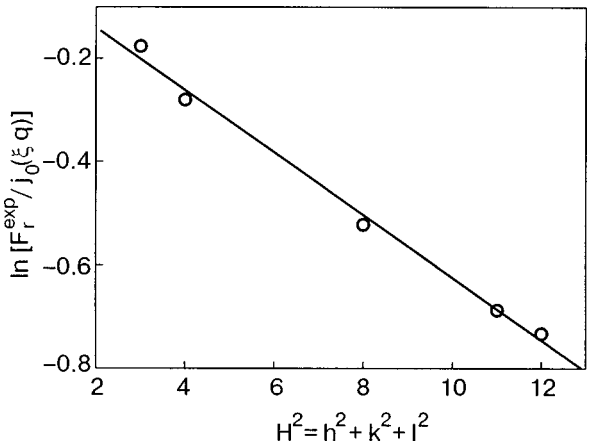

FIG. 1. Plot from which the coefficient B in the Debye–Waller factor is determined.

tained in the approximation that the self-consistent potential well in which the particle moves is quadratic. However, even when all possible factors are taken into account, the potential well in a quantum crystal of any isotope of hydrogen is extremely far from being harmonic.[21] Therefore, the true value of the rms displacement of the particle must be determined from experiment, if possible. Fortunately in the case under discussion such a possibility does exist. In particular, it follows from (4) and (8) that the argument of the exponential function in Ref. (5) is proportional to H^2. This makes it possible to use the scattering amplitudes measured by Yarnell *et al.*[14] for regular reflections, which should be described by the expression $f_r^{\rm calc} \propto j_0(\xi q)\exp[-w(\mathbf{q})]$, where $w(\mathbf{q})$ can be written in the form BH^2. Figure 1 shows a plot of $\ln[F_r^{\rm exp}/j_0(\xi q)]$ versus H^2, where $F_r^{\rm exp}$ is, of course, assumed proportional to $f_r^{\rm calc}$. It is seen that a linear dependence is well obeyed, as a result of which we obtain a value of 0.0605 for B, which after the appropriate adjustments is close to the value determined in Ref. 14 from the formula of the self-consistent harmonic approximation.

In contrast to Ref. 7, where the orientational order parameter was reconstructed directly from the intensities, in Ref. 14 we had the more-convenient structure amplitudes at our disposal. As a result, the values of η were determined from the relation

$$\eta = \frac{F_s^{\rm exp} f_r^{\rm calc}}{F_r^{\rm exp} f_s^{\rm calc}}, \tag{9}$$

where $F_s^{\rm exp}$ and $F_r^{\rm exp}$ are the scattering amplitudes obtained on the basis of the experimental neutron-scattering data for reflections of the corresponding types, and $f_s^{\rm cal}$ and $f_r^{\rm cal}$ are defined in Eq. (7) and are obtained as a result of a numerical calculation.

Performing the calculation of η for the 20 intensity ratios of superstructure to regular reflections at our disposal and averaging the values found for η, we obtained a value $\overline{\eta} = 0.368 \pm 0.006$, or $\eta = 2/5 - \Delta\eta$ with $\Delta\eta = 0.032$. This value agrees remarkably well with the theoretical value in the zeroth approximation, $\eta_0 = 0.4$, but there is a systematic shift to lower values $\Delta\eta/\eta_0 \simeq -8\%$. Thus the present study demonstrates the universality, simplicity, and accuracy of the method proposed in Ref. 7 for reconstruction of the orientational order parameter not only for classical molecular crystals of diatomic molecules but also for quantum crystals. The fact that the values of η were reconstructed from the neutron-diffraction data confirms that the applicability of the method is independent of the experimental techniques. For satisfactory application of the proposed method it is only necessary to know the integrated intensities (or structure amplitudes) to sufficient accuracy.

Besides the calculation of η from the results of neutron-diffraction studies of D_2 with a para concentration $x > 90\%$,[14] we have attempted to reconstruct the orientational order parameter from the results of Ref. 11, where to the p-D_2 concentration was barely over 80%. However, our calculations of the corresponding structure amplitudes showed (and this agrees with the conclusions of the analysis by Yarnell *et al.*[14]) that for the superstructure lines the values of the structure amplitudes in Ref. 11 are highly overstated. The authors of Ref. 14 estimated the change in the concentration of the para species during the course of the experiment. It follows from the data given that even for the highest p-D_2 concentration $x \simeq 96\%$, its change during the experiment did not exceed 2%. For samples with a lower concentration the changes would be proportionately smaller.

3. DISCUSSION OF THE RESULTS

Thus we have obtained absolute values of η in good agreement with the theoretical value in the molecular field approximation, 0.4, but systematically lower by $\Delta\eta \cong 0.032$. Let us consider and estimate the three most ponderable causes of this decrease.

Thermal librons. The most obvious cause is the influence of thermal librations, the excitation of which is a disordering factor. An estimate of this effect can be obtained in the framework of the simplest single-particle approximation, in which the wave functions of local excited states are $|\mathrm{Ex}(\pm 1)\rangle = |J=1, m=\pm 1\rangle$. We assume that the population of these states is proportional to $p = \mathrm{e}^{-E/kT}$, where E is the weighted mean energy of the libronic excitations relative to the ground state. The quantum-mechanical average over the excited state,

$$\eta_m \equiv \langle \mathrm{Ex}(m)|P_2(\cos\vartheta)|\mathrm{Ex}(m)\rangle = 1/5$$

is independent of the sign of m. The value of η as the thermodynamic mean has the form ($\eta_0 = 2/5$)

$$\eta = \frac{\sum_m \eta_m \mathrm{e}^{-E_m/kT}}{\sum_m \mathrm{e}^{-E_m/kT}}, \tag{10}$$

where the summation is over the three values of the projection of the rotational momentum in the state $J=1$. In sum, we have (the subscript 1 denotes the deviation due to thermal librons)

$$\eta \equiv 2/5 - \Delta\eta_1 = \frac{2/5(1-p)}{1+2p}, \tag{11}$$

which gives $\Delta\eta_1 = 2/[5p/(1+2p)]$, or $\Delta\eta_1/\eta_0 = p/(1+2p)$. When the temperature of the neutron-diffraction experiment[14] $T = 1.5$ K and the experimentally determined[22] thermodynamically weighted mean value $E = 19.2$ K are taken into account, we obtain the estimate $\Delta\eta_1/\eta_0 = 2.3 \times 10^{-4}$. Thus the influence of librons is negligible.

Rotational polarization. Each molecule in the $Pa3$ structure is found in a molecular field which in the proper frame of this molecule has the form[15,23]

$$V = V_c C_{20}(\mathbf{w}), \tag{12}$$

where $\mathbf{w}$ is the orientation vector of the molecule, and

$$V_c = -(5/3)19\Gamma, \tag{13}$$

where the experimentally determined[1] value of the quadrupole–quadrupole coupling constant Γ for deuterium is 1.026 K. The field (12) polarizes the ground eigenstate $|10\rangle$ of the molecule, mixing in higher rotational states, primarily the state with $J=3$. Using a standard perturbation theory, one can easily show that to a first approximation the single-particle wave function Ψ has the form

$$\Psi = |10\rangle + \frac{3\sqrt{3}V_c}{50\sqrt{7}B}|30\rangle, \tag{14}$$

where $B=42.97$ K is the rotational constant of the deuterium molecule (the correction to the normalization is neglected because it is of second order in the small parameter of the expansion, $V_c/(10B)\cong 0.076$). Starting from Eq. (14), one can estimate the correction $\Delta\eta_2/\eta_0$ due to the rotational polarization of the rotational ground state:

$$\Delta\eta_2/\eta_0 = \frac{27}{350}\frac{V_c}{B}, \tag{15}$$

which gives $\Delta\eta_2/\eta_0 \cong -5.8\%$. It is interesting that at small negative V_c the molecular field has a disordering effect on the antisymmetric state $J=1$. At large ratios V_c/B the ordering is, of course, enhanced. A similar situation occurs for a rotator in a field of cubic symmetry.[24]

Rotational anharmonicity. It is well known[23,25] that the rotational dynamics of $J=1$ states interacting by quadrupole–quadrupole forces is characterized (especially in the orientationally ordered phase) by distinctly large anharmonicities. The influence of this factor on the orientational order parameter η leads to a decrease of the latter by an amount $\Delta\eta_3/\eta_0 \simeq -2.5\%$.[23] A more careful treatment of this problem gave the value -3.0%.[26]

Thus the combined effect of taking these three factors into account is a theoretical value $\Delta\eta_{\text{calc}}/\eta_0 \simeq -8.8\%$, which turns out very close to the value -8.0% which we obtained experimentally (although with a large total error). We can give only the statistical error (see above); the systematic error of the method and the error of reconstruction of the constants in the Debye–Waller factor are insignificant. Unfortunately, Yarnell *et al.*[14] do not give the error of determination of the scattering amplitudes, but, judging from the published neutron diffraction patterns (see Fig. 5 of Ref. 14), the error cannot be small.

4. CONCLUSIONS

1. The method of reconstruction of the absolute values of the orientational order parameter in the ordered phases of diatomic molecular crystals from the diffraction (in this case, neutron diffraction) data was found to be effective also in application to the quantum deuterium crystal.

2. The value of the rotational order parameter $\eta = 0.368$ obtained from the neutron diffraction data of Yarnell *et al.*[14] is close to the value $\eta_0 = 0.4$ obtained in molecular field theory at $T=0$. The relative deviation from η_0 is -8%.

3. We have carried out a theoretical analysis of the factors capable of renormalizing η. We showed that the strongest influence is due to two causes: rotational polarization of the rotational ground state, and rotational anharmonicity. The total renormalization due to these two factors is -8.8%, surprisingly close to the value obtained in the reconstruction of η from the neutron diffraction data. Thermal librons have a negligible effect on the value of η (at least at the temperature 1.8 K of the neutron experiment). Since the first two factors depend weakly on temperature, the value of η divided by its value at $T=0$ should depend weakly on temperature, as in fact follows from various experiments.[4,5]

The authors are sincerely grateful to the referee for constructive comments that helped improve this paper significantly. This study was supported by the CRDF (Grant UP2-2445-KH-02).

*E-mail: galtsov@ilt.kharkov.ua

[1] I. F. Silvera, Rev. Mod. Phys. **52**, 393 (1980).
[2] V. G. Manzhelii and Yu. A. Freiman (eds.), *Physics of Cryocrystals*, AIP Publ., New York (1996).
[3] A. B. Harris, Phys. Rev. B **1**, 1881 (1970); *ibid.* **2**, 3495 (1970); J. Appl. Phys. **42**, 1574 (1971).
[4] H. Meyer, F. Weinhaus, B. Maraviglia, and R. L. Mills, Phys. Rev. B **6**, 1112 (1972).
[5] W. N. Hardy, I. F. Silvera, and J. P. McTague, Phys. Rev. B **12**, 753 (1975).
[6] J. Lee and J. C. Raich, Phys. Rev. Lett. **27**, 1137 (1971).
[7] N. N. Galtsov, O. A. Klenova, and M. A. Strzhemechny, Fiz. Nizk. Temp. **28**, 517 (2002) [Low Temp. Phys. **28**, 365 (2002)].
[8] A. F. Schuch and R. L. Mills, Phys. Rev. Lett. **16**, 616 (1966).
[9] A. F. Schuch, R. L. Mills, and D. A. Depatie, Phys. Rev. **165**, 1032 (1968).
[10] C. S. Barrett, L. Meyer, and D. A. Depatie, J. Chem. Phys. **45**, 834 (1966).
[11] K. F. Mucker, S. Talhouk, P. S. Harris, and D. White, Phys. Rev. Lett. **16**, 799 (1966).
[12] K. F. Mucker, P. M. Harris, D. White, and R. A. Erikson, J. Chem. Phys. **49**, 1922 (1968).
[13] R. L. Mills, J. L. Yarnell, and A. F. Schuch, *Proceedings LT-19*, Part 2, Plenum Press, New York (1974), p. 203.
[14] J. L. Yarnell, R. L. Mills, and A. F. Schuch, Fiz. Nizk. Temp. **1**, 366 (1975) [Sov. J. Low Temp. Phys. **1**, 366 (1975)].
[15] J. Van Kranendonk, *Solid Hydrogen*, Plenum Press, New York–London (1983).
[16] W. Press, Acta Crystallogr., Sect. A: Cryst. Phys., Diffr., Theor. Gen. Crystallogr. **29**, 252, 257 (1973).
[17] M. A. Strzhemechny, A. A. Solodovnik, and S. I. Kovalenko, Fiz. Nizk. Temp. **24**, 889 (1998) [Low Temp. Phys. **24**, 669 (1998)].
[18] V. V. Danchuk, A. A. Solodovnik, and M. A. Strzhemechny (for publication).
[19] Yu. Z. Nozik, R. P. Ozerov, and K. Khennig, *Structural Neutronography* [in Russian], Vol. 1, Atomizdat, Moscow (1979).
[20] L. I. Mirkin, *Handbook of X-Ray Structural Analysis of Polycrystals* [in Russian], GIFML, Moscow (1961).
[21] W. B. J. M. Janssen and A. van der Avoird, Phys. Rev. B **42**, 838 (1990).
[22] D. Ramm, H. Meyer, and R. L. Mills, Phys. Rev. B **1**, 2763 (1970).
[23] C. F. Coll III and A. B. Harris, Phys. Rev. **2**, 1176 (1970); **4**, 2781 (1971).
[24] A. F. Devonshire, Proc. R. Soc. London, Ser. A **153**, 601 (1936).
[25] J. C. Raich and R. D. Etters, Phys. Rev. **168**, 425 (1968).
[26] F. P. Onufrieva, Fiz. Nizk. Temp. **3**, 1050 (1977) [Sov. J. Low Temp. Phys. **3**, 512 (1977)].

Translated by Steve Torstveit

Relaxation of temperature and concentration in superfluid ^{3}He–^{4}He mixtures. Effective thermal conductivity

A. A. Zadorozhko,* T. V. Kalko, É. Ya. Rudavskii, V. K. Chagovets, and G. A. Sheshin

B. Verkin Institute for Low Temperature Physics and Engineering, National Academy of Sciences of Ukraine, pr. Lenina 47, Kharkov 61103, Ukraine

K. É. Nemchenko

V. N. Karazin Kharkov National University, pl. Svobody 4, Kharkov 61022, Ukraine

(Submitted June 13, 2003; revised August 21, 2003)
Fiz. Nizk. Temp. **30**, 169–176 (February 2004)

The relaxation of temperature and concentration of a superfluid ^{3}He–^{4}He mixture with an initial molar concentration of 9.8% ^{3}He is investigated in the temperature interval 100–500 mK for different values of the heat flux. It is shown that the kinetics of the change in temperature of the liquid can be approximated by an exponential function, and the time constants obtained depend weakly on temperature. The concentration relaxation processes are analogous to the temperature relaxation processes only in the region of the single-phase mixture, while below the phase separation temperature the change in concentration with time is of a nonmonotonic character and can be described by a superposition of two exponential functions. This kind of kinetic behavior of the mixture is explained in the framework of a simple model which illustrates the distribution of the concentration over the height of the cell at various times after a heat flux is turned on. In this case the concentration relaxation of the dilute phase consists of two processes—growth of the concentration due to the participation of ^{3}He in the normal motion, and decline of the concentration due to the formation and growth of the concentrated phase. The data on the relaxation times are used for determining the effective thermal conductivity of the mixture; the value obtained is in agreement with a calculation done in the framework of a kinetic theory of the phonon–impurity system of superfluid mixtures. [DOI: 10.1063/1.1645163]

1. INTRODUCTION

The principles of description of the kinetic properties of superfluid ^{3}He–^{4}He mixtures were set forth by Khalatnikov and Zharkov,[1] who showed that the mechanism of heat transfer in such mixtures is much richer and more complex than in pure He II. Whereas in He II, according to Landau theory, the heat carriers are thermal excitations—phonons and rotons—in superfluid mixtures a substantial role can also be played by impurity excitations (^{3}He quasiparticles), which collide and interact with phonons and rotons and are entrained by their motion.

In the general case, temperature and concentration gradients will arise in a mixture in the presence of a heat flux, and those gradients determine the flow of impurity excitations. In such a situation the processes of heat conduction, mass diffusion, and thermodiffusion are interrelated. Further theoretical studies of the kinetic and relaxation processes in superfluid mixtures were done in Refs. 2–9, where it was noted that relaxation of the temperature and concentration can come about through two mechanisms: second sound, and a mechanism involving dissipation processes.

The experimental study of processes of temperature and concentration relaxation in superfluid ^{3}He–^{4}He mixtures has so far been carried out only at rather high temperatures (above $\sim$0.8 K), close to the temperature of the superfluid transition.[4,5,10,11] The authors have made measurements at a low input of thermal power and found that the characteristic times describing the relaxation of temperature and concentration are practically equal. The time constants corresponding to the switching on and switching off of the power input are also the same. These experimental results are in agreement with the theoretical analysis done by the authors of Refs. 4 and 5.

In the present paper we report an experimental study of the processes of temperature and concentration relaxation in a lower temperature region over a wide range of heat flux powers. An important factor is the presence of phase separation of the superfluid mixtures, the features of which in the presence of a heat flux have been studied in Ref. 12.

2. EXPERIMENTAL TECHNIQUE

We investigated a ^{3}He–^{4}He mixture with an initial molar concentration of 9.8% ^{3}He in the temperature interval 100–500 mK at the saturated vapor pressure. We used a cylindrical cell 24 mm in diameter and 47 mm in height, the construction of which is described in Ref. 12. To prevent the walls of the cell from introducing a noticeable contribution to the heat transfer, they were made of stainless steel, 0.1 mm thick. The upper flange of the cell was in thermal contact with the mixing chamber, and a special heat exchanger of

ultradisperse silver powder, with a surface area of ~ 1.5 m^2, was used to decrease the thermal boundary resistance between the liquid and flange.

The heat flux was produced by a flat heater placed directly in the liquid in the lower part of the cell. The temperature was registered by means of two miniature RuO_2 resistance thermometers placed at distances of 15 and 25 mm from the lower edge of the cell. The maximum absolute error in the temperature determination was 0.2 mK.

The change in the concentration of the mixture was determined from the change in the dielectric constant of two special capacitive sensors with the use of the Clausius–Mossotti equation. The sensors were cylindrical capacitors 5 mm in height, the electrodes of which were wound in a helix with a gap between windings. Both capacitive sensors were placed near the resistance thermometers a distance 10 mm apart. The accuracy of determination of the ^{3}He concentration was $\pm 0.1\%$. Owing to the mutual influence via the electric coupling the sensors operated alternately, and therefore the time dependence of the change in concentration was determined according to the upper sensor, while the lower sensor was used only for determination of the steady-state concentration gradients.

The thermometers and concentration sensors were calibrated in the absence of heat flux, when the temperature and concentration were the same throughout the entire cell. Data on the variation of the temperature, concentration, and pressure were automatically registered with the aid of a computer program.

Several types of experiments were done.

Experiment A. The temperature of the upper flange of the cell was fixed at values of 150 and 270 mK, and a specific power of from 1 to 20 μW/cm^2 was delivered to the heater. The relaxation of the temperature and concentration was measured both with the heat flux turned on and turned off.

Experiment B. The relaxation of the temperature and concentration in the mixture was measured upon the switching on and off of the same heat flux $\dot{Q}=4.5$ μW/cm^2 but for different mean temperatures of the liquid, which were set by varying the temperature of the mixing chamber.

Experiment C. The variations of the temperature and concentration were registered upon a stepwise increase of the heat flux $\dot{Q}$ from 0.2 to 15 μW/cm^2. Here the starting equilibrium temperatures of the liquid were 150 and 270 mK.

3. TEMPERATURE RELAXATION

Figure 1 shows the typical time dependence of the temperature change $\Delta T(t)$ upon the switching on and off of the heat flux. Both of these time dependences can be well approximated by a single exponential function:

$$\Delta T(t)=be^{-t/\tau_T}, \tag{1}$$

where b is a function that depends on the distance along the height of the cell, while the time constant τ_T is a quantitative characteristic describing the relaxation of the temperature. Here it was found that the values of τ_T for the switching on and off of the heat flux are practically the same.

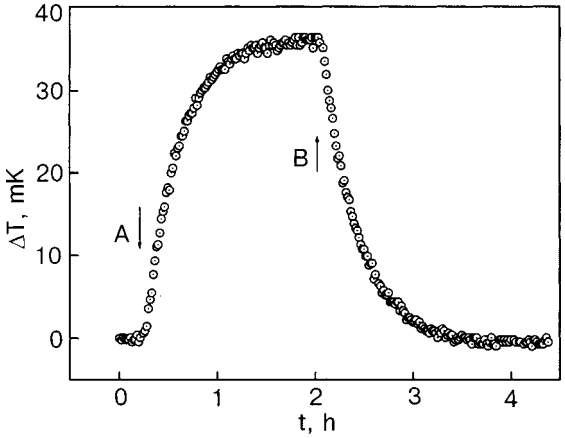

FIG. 1. Typical time dependence of the change in temperature in experiment A ($\dot{Q}=4.4$ μW/cm^2). The arrows indicate the times at which the heat flux was turned on (A) and off (B).

We note that the function (1) gives a good approximation of the time dependence of the temperature registered by the two thermometers used in the experiment, and practically the same values of τ_T were obtained. The same values of the time constant τ_T were also obtained in an analysis of the time dependence of the difference of the readings of the two thermometers, T_1-T_2.

The exponential character of the change in temperature upon switching on of the heat flux is most clearly revealed in a semilog plot (see Fig. 2), where a linear dependence indicates the presence of a single exponential. The influence of the heat flux power $\dot{Q}$ on the character of the temperature relaxation is illustrated in Fig. 3, which shows the data obtained in experiment A at a constant temperature of the upper flange of the cell.

The kinetics of the change in temperature of the mixture upon a stepwise increase in the heat flux power $\dot{Q}$ (experiment C) is shown in Fig. 4. In this case the values of $\dot{Q}$ were chosen the same as in experiment A (Fig. 3), and at each step the dependence $T(t)$ is also well described by the function (1). The values obtained for the temperature relaxation time constant τ_T in all three types of experiments are summarized in Fig. 5 as a function of the mean temperature of the mix-

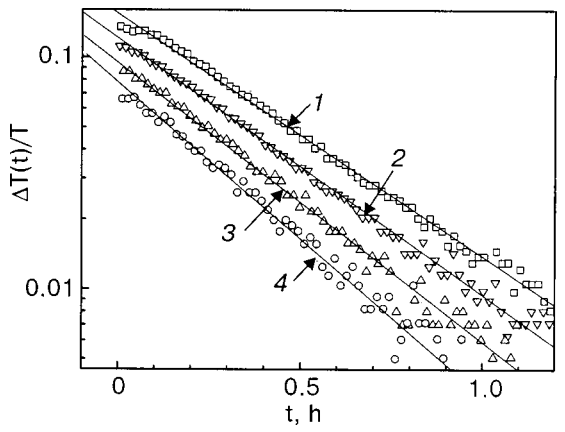

FIG. 2. Semilogarithmic plot of the change in temperature versus time upon the turning on a heat flux $\dot{Q}=4.4$ μW/cm^2 in experiment B at various mean temperatures T of the liquid [mK]: 253 (*1*), 290 (*2*), 328 (*3*), 371 (*4*).

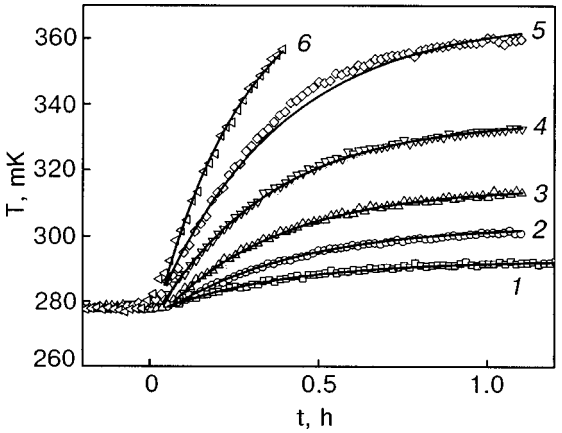

FIG. 3. Change in the temperature of the liquid upon the turning on ($t=0$) of various heat fluxes in experiment *A*, $\dot{Q}$ [μW/cm^2]: 2.2 (*1*), 3.8 (*2*), 5.5 (*3*), 8.9 (*4*), 13.3 (*5*), 17.8 (*6*). The temperature of the upper flange of the cell was constant and equal to 270 mK. The solid curves show the calculation according to formula (1).

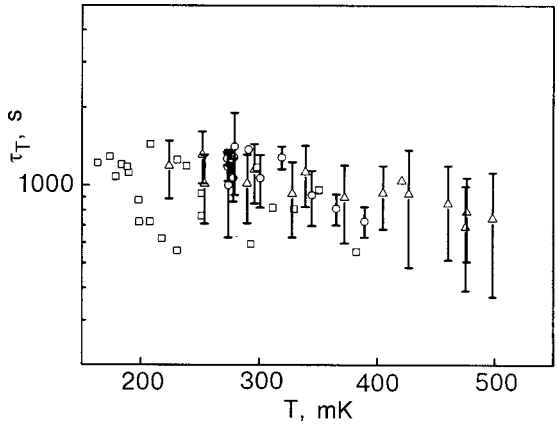

FIG. 5. Dependence of the temperature relaxation time of the mixture on the mean temperature: ○—experiment *A*, Δ—experiment *B*; □—experiment *C*.

ture. As can be seen from this figure, all of the data are in agreement with each other within the experimental error limits and do not show any noticeable temperature dependence.

4. RELAXATION OF THE CONCENTRATION OF THE MIXTURE

When a heat flux is turned on in superfluid ^{3}He–^{4}He mixtures the local increase in the density of thermal excitations near the heater relaxes very rapidly (at the velocity of second sound). This is accompanied by the establishment in the mixture of a nonequilibrium state which is characterized by the simultaneous creation of a temperature gradient ∇T and concentration gradient ∇x in the absence of gradients of both the total pressure and the sum of the osmotic pressures of the thermal and impurity excitations; this is a consequence of the constancy of the chemical potential of ^{4}He in the mixture. Such processes represent the first rapid step of the temperature and concentration relaxation, governed by a sonic mechanism.

In the second step of the relaxation process, as a consequence of the presence of temperature and concentration gradients in the liquid, dissipative flows of thermal and impurity excitations arise in it, governed by the effective thermal conductivity of the mixture. Here at each point in time the variations arising in the gradients of the osmotic pressure of the thermal and impurity excitations also relax at the velocity of second sound.[8] The relaxation time in the second step, which is governed by a dissipative mechanism, is much longer than the time constant for relaxation of the concentration and temperature due to the sonic mechanism. In an experiment one actually registers the time of the second step of the relaxation, in comparison with which the characteristic time of the first step is negligibly short.

According to this model, the characteristic relaxation times τ_T and τ_x for the temperature and concentration should be close to each other. The experiments showed that this holds under the condition that phase separation does not occur in the mixture under the influence of the heat flux. The corresponding dependence of the concentration of the mixture on the time after the turning on of the heat flux (experiment B) is shown in Fig. 6 (curves *1–3*). These curves can be approximated by the function

$$\Delta x(t)=x_0+B\exp\left(-\frac{t-t_0}{\tau_x}\right), \tag{2}$$

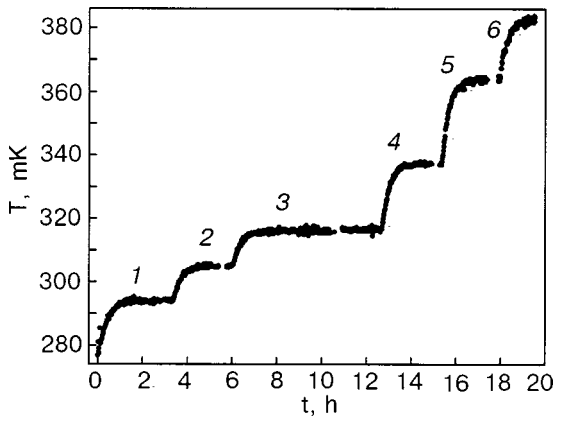

FIG. 4. Typical time dependence of the liquid temperature registered by one of the thermometers upon a stepwise change in the heat flux $\dot{Q}$ (experiment *C*) [μW/cm^2]: 2.2 (*1*), 3.8 (*2*), 5.5 (*3*), 8.9 (*4*), 13.3 (*5*), 17.8 (*6*).

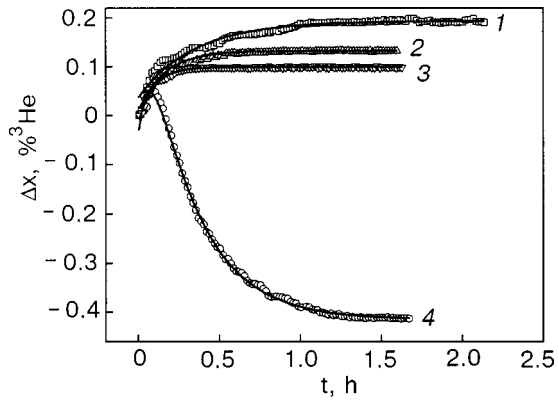

FIG. 6. Time dependence of the change in concentration of the mixture after the turning on of a heat flux $\dot{Q}=4.4$ μW/cm^2 (experiment *B*) for different final temperatures *T* near the concentration sensor [mK]: 290 (*1*), 330 (*2*), 370 (*3*), 255 (*4*). The solid curves show a calculation according to formulas (2) and (3).

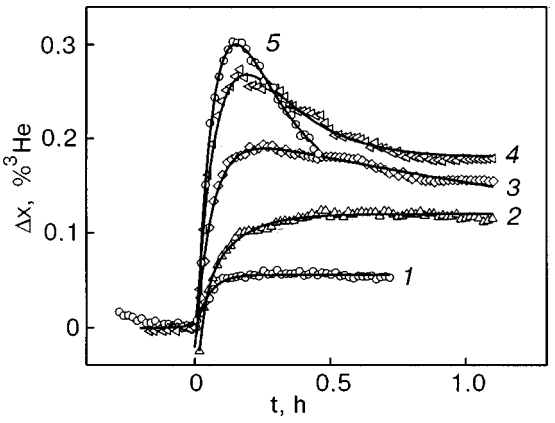

FIG. 7. Change in the concentration with time in experiment *A* at a fixed temperature of the upper flange of the cell, $T_0 = 270$ mK, and various values of the heat flux power $\dot{Q}$ [μW/cm^2]: 2.2 (*1*), 3.8 (*2*), 8.9 (*3*), 13.3 (*4*), 17.8 (*5*). The solid curves show a calculation according to formulas (2) and (3).

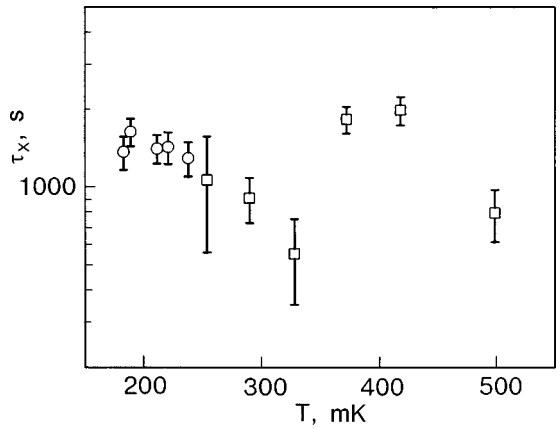

FIG. 8. Temperature dependence of the time constant for relaxation of the concentration: □—experiment B, ○—experiment *C*.

where x_0 is the concentration of the mixture at the initial time t_0, when $\dot{Q}=0$, and the parameter B is determined by the initial and boundary conditions.

Curve *4* in Fig. 6 corresponds to a lower temperature of the liquid, when phase separation occurs in the mixture under the influence of a heat flux.[12] For this case the dependence obtained for $\Delta x(t)$ can be described by a superposition of two exponential functions with weight factors B_1 and B_2:

$$\Delta x(t) = x_0 + B_1 \exp\left(-\frac{t-t_0}{\tau_{x1}}\right) + B_2 \exp\left(-\frac{t-t_0}{\tau_{x2}}\right), \qquad (3)$$

with two characteristic relaxation times for the concentration, τ_{x1} and τ_{x2}.

This kind of behavior is manifested more clearly in experiment *A* (Fig. 7). The data shown pertain to a fixed temperature of the upper flange of the cell $T_0 = 270$ mK under the influence of various heat fluxes. Curves *1* and *2* in Fig. 7 correspond to conditions for which phase separation does not occur in the mixture, and, as for experiment *B* (curves *1–3* in Fig. 6) the experimental data are well described by expression (2) with a single exponential. The evolution of the $\Delta x(T)$ curves with increasing heat flux power $\dot{Q}$ can be seen by examining curves *3–5* in Fig. 7. The time dependence of the change in concentration becomes nonmonotonic, the value of the maximum increasing with increasing $\dot{Q}$. An analogous nonmonotonicity was also observed in experiment C in those cases when phase separation occurs in the mixture under the influence of the heat flux.

The measured values of the concentration relaxation time constant τ_x as a function of the mean temperature in the absence of phase separation are shown in Fig. 8 for two types of experiments. The values of τ_x are practically independent of temperature, within the experimental error, and, as it turned out, the characteristic relaxation times of the concentration and temperature are practically the same.

The nonmonotonic character of the kinetics of the change in concentration of the mixture in the presence of phase separation can be explained by starting from a simple model illustrating the distribution of the concentration over the height of the cell at different times after the heat flux was turned on (Fig. 9). Figure 9a corresponds to the initial time prior to the turning on of the heat flux, when the concentration x_0 of the mixture is the same along the entire height. After the heat flux is turned on, when the ^{3}He atoms together with the normal component of the mixture tend to move toward the colder part of the cell, the ^{3}He concentration will increase in the upper part of the cell. On the assumption of a linear distribution of the ^{3}He concentration along the height of the cell (Fig. 9b), the concentration at the center of the cell will remain equal to x_0. This corresponds to the point in time when the concentration near the upper flange of the cell is lower than the concentration x_s at which phase separation occurs.

Figure 9c corresponds to the time when the concentration at the top of the cell becomes equal to x_s, and phase separation of the mixture begins. The lighter concentrated phase is located in the upper part, and the concentration sensor lies in the dilute phase. From that time on, the further relaxation of the solution toward an equilibrium relation between the amounts of the concentrated and dilute phases occurs on account of depletion of the lower dilute phase. This means that the ^{3}He concentration at the place where the sensor is located will decrease until a steady state is reached, and the concentration at the center of the cell becomes less than x_0.

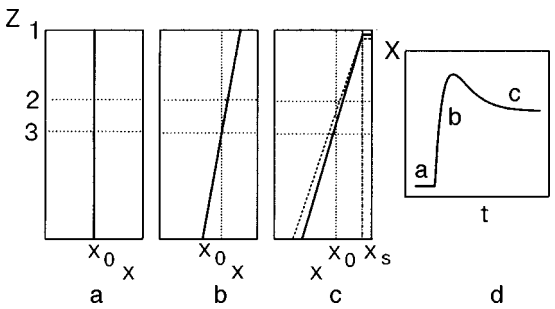

FIG. 9. Diagram illustrating the concentration distribution over height in the cell at different times: a—before the heat flux was turned on; b—after the heat flux was turned on but before the onset of phase separation; c—after phase separation (the dotted line corresponds to a time when the volume of the upper phase had grown), d—distribution of the concentration with time at the site of the sensor. *1*—Position of the cell's upper flange, which was cooled by the dilution refrigerator; *2*—position of the capacitive concentration sensor; *3*—center of the cell.

Thus, if phase separation occurs in a mixture under the influence of a heat flux, then the relaxation of the concentration of the dilute phase consists of two processes: growth of the concentration under the influence of the heat flux, and (after phase separation) a decrease in the concentration of the dilute phase necessary for the formation of the normal phase, which at sufficiently low temperatures is almost pure ^{3}He. Hence a maximum arises in the time dependence of x, and there are two characteristic concentration relaxation times (Fig. 9d).

5. RELAXATION PROCESSES AND THE EFFECTIVE THERMAL CONDUCTIVITY

In superfluid ^{3}He–^{4}He mixtures the relaxation time constants are determined by the effective thermal conductivity κ_{eff} introduced by Khalatnikov,[1] which is a combination of the diffusion coefficient, thermal conductivity, and thermodiffusion coefficient:

$$\kappa_{\text{eff}}=\tilde{\kappa}+\kappa_3, \tag{4}$$

where the so-called phonon–impurity thermal conductivity $\tilde{\kappa}$ is due to the macroscopic motion of the normal component of the mixture, diffusion, and thermodiffusion of impuritons, while κ_3 is due to the thermal conductivity of the gas of impuritons. We note that formula (4) was obtained in neglect of the roton contribution.

A relation between the temperature (or concentration) relaxation time τ_T (or τ_x) and the effective thermal conductivity for superfluid mixtures was obtained in Ref. 5 on the basis of an analysis of the dispersion relation for the diffusion mode, obtained by solving a system of hydrodynamic equations for $P=\text{const}$. When the corresponding boundary conditions are taken into account, this relation is expressed as follows:

$$\tau_T=\frac{d^2\rho C_{P,x}}{\kappa_{\text{eff}}}f(T,x), \tag{5}$$

where d is the height of the experimental cell, ρ is the density of the liquid, $C_{p,x}$ is the heat capacity per unit volume of the mixture, and the function $f(T,x)$ is determined by the properties of the mixture and the boundary conditions. In Ref. 5 the function $f(T,x)$ was calculated only for the temperature region near the λ point under the condition that the impurity flux equals zero on both ends of the cell. Then a steady heat flux is applied to one of the flanges, while the temperature of the other flange is held constant. In a similar situation for the conditions of the given experiment at $T<0.5$ K, estimates show that the value of $f(T,x)$ is close to unity.

In this approximation the values of κ_{eff} calculated according to formula (5) with the use of the relaxation times τ_T measured in the present paper are plotted in Fig. 10. Also shown for comparison are the corresponding values of κ_{eff} obtained for the same mixture from measurements of the steady-state temperature gradients[12] under conditions such that thermal convection has not yet arisen in the mixture. Figure 10 also shows the results of high-temperature measurements of the effective thermal conductivity obtained in Ref. 13 for a mixture with the same 9.8% ^{3}He concentration. It is seen that the experimental results are all in satisfactory

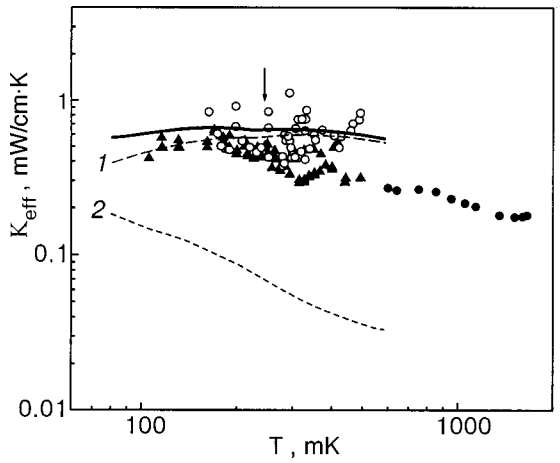

FIG. 10. Temperature dependence of the effective thermal conductivity in a mixture with a 9.8% ^{3}He concentration: ▲—steady-state measurements; ○—relaxation measurements; ●—the results of Ref. 13; the solid curve is the total effective thermal conductivity calculated according to Eq. (4); *1*—the phonon–impurity thermal conductivity calculated according to Eq. (6); *2*—the impurity thermal conductivity calculated according to Eq. (12). The arrow indicates the phase separation temperature.

agreement with one another. The agreement between the results of the relaxation and steady-state measurements of the effective thermal conductivity means physically that the assumption that $f(T,x)$ is equal to unity adequately reflects the experimental conditions.

The values of κ_{eff} obtained can be compared with the result of a calculation in the framework of the kinetic theory of superfluid ^{3}He–^{4}He mixtures (see, e.g., Ref. 14). The term $\tilde{\kappa}$ was calculated in neglect of rotons in Ref. 6:

$$\tilde{\kappa}=\frac{1}{3}C_{\text{ph}}u_1^2\tau_{\text{phi}}, \tag{6}$$

where C_{ph} is the phonon heat capacity of the mixture, u_1 is the velocity of first sound in the mixture, and τ_{phi} is the effective phonon–impurity relaxation time. The calculation of τ_{phi} in Ref. 6 was done with allowance for extremely complex and diverse mechanisms for establishing equilibrium in the phonon subsystem in the presence of ^{3}He impurities. Because of the decomposing character of the phonon spectrum in mixtures at low pressures,[14] three-particle phonon processes are allowed, ensuring a rapid establishment of equilibrium along a specified direction (longitudinal relaxation) with a characteristic time

$$\tau_{\parallel}=2.6\cdot 10^{-10}T^{-5}\ \ [\text{s}]. \tag{7}$$

Besides the time $\tau_{\parallel}$, the value of τ_{phi} is also determined by processes of interaction between phonons and impurity excitations. As was shown in Ref. 15, these processes are described by two relaxation times—the time t_{sc}, which takes into account Rayleigh scattering of long-wavelength ''light'' phonon on a ''heavy'' impurity, and the time t_a, which takes into account processes of absorption and emission of phonons by impurity excitations, which limit the free path of the phonons at low momenta. In sum, we have

$$\tau_{\mathrm{phi}}=\frac{\int_0^\infty \tilde{t}_{\mathrm{phi}}(\tau_\parallel+\tilde{t}_{\mathrm{phi}})^{-1}p^4n'dp}{\int_0^\infty(\tau_\parallel+\tilde{t}_{\mathrm{phi}})^{-1}p^4n'dp}, \tag{8}$$

where

$$\tilde{t}_{\mathrm{phi}}^{-1}=t_{\mathrm{sc}}^{-1}+t_a^{-1}, \tag{9}$$

and p and n' are, respectively, the momentum and the derivative of the phonon distribution function with respect to momentum.[14] The relaxation time corresponding to Rayleigh scattering of phonons on impurities can be written in the form

$$t_{\mathrm{sc}}(p)=\frac{7.7N_4\hbar^4}{u_1 x p^4}, \tag{10}$$

where N_4 is the number of ^{4}He atoms per unit volume.

The relaxation rate characterizing the absorption of phonons by impurities is given, according to Ref. 16, by

$$t_a^{-1}(p)=\frac{4}{3}\frac{P_F\lambda_i^2p^2\tau_{ii}\left[1+\left(\frac{\varepsilon}{2\pi T}\right)^2\right]}{\rho_4\hbar^2\left\{\left[1+\left(\frac{\varepsilon}{2\pi T}\right)^2\right]^2+\varepsilon^2\tau_{ii}^2\right\}}, \tag{11}$$

where P_F is the pressure of the Fermi gas, ε is the phonon energy, τ_{ii} is the impurity–impurity relaxation time, which can usually be found from experiments on the viscosity and absorption of first sound, and λ_i is a parameter of the mixture which is determined by the energy and effective mass of the impurity excitations.[14]

Since the main role in the integration of expressions (10) and (11) over momenta is played by phonons with a mean thermal energy $3kT$, in calculating the times t_{sc} and t_a we used the values $\varepsilon=3kT$ and $p=3kT/u_1$. In accordance with Ref. 6, here the role of the longitudinal phonon relaxation was not taken into account for concentrated mixtures. The calculated phonon–impurity part $\tilde{\kappa}$ of the effective thermal conductivity is shown by the dashed curve *1* in Fig. 10.

The impuriton part κ_3 of the effective thermal conductivity can be calculated in the usual gas-kinetic approximation, and for the degenerate case it is given by

$$\kappa_3=\frac{1}{3}C_3v_F^2\tau_{ii}, \tag{12}$$

where C_3 is the impurity part of the heat capacity and v_F is the Fermi velocity of the impurity excitations. The calculation of κ_3 according to Eq. (12) is shown by the dotted curve *2* in Fig. 10, and the total effective thermal conductivity is shown by the solid curve. The arrow denotes the phase separation temperature, below which the calculation was done with allowance for the change of the concentration of the dilute phase with decreasing temperature. As is seen in Fig. 10, the experimental data obtained for κ_{eff} agree with the calculation in the framework of the kinetic theory of the phonon–impuriton system of superfluid ^{3}He–^{4}He mixtures. Here the dominant contribution to κ_{eff} is from the phonon–impurity thermal conductivity.

6. CONCLUSION

The experiments done here comprise the first systematic study of temperature and concentration relaxation processes in superfluid ^{3}He–^{4}He mixtures at low temperatures, when the initial mixture separates into a concentrated and a dilute phase. They showed that only in the homogeneous region do the temperature and concentration of the mixture relax according to the same law with close values of the relaxation times. In the phase-separation region the relaxation of the concentration is more complicated because of the formation and growth of the concentrated phase in the upper part of the cell.

Another specific feature of superfluid ^{3}He–^{4}He mixtures is due to the presence of two modes—sonic and dissipative, which leads to a peculiar two-step relaxation. In the presence of a heat flux the variations that arise in the osmotic pressure of the thermal and impurity excitations relax at the velocity of second sound, and then, on account of the appearance of temperature and concentration gradients, there arise dissipative flows of excitations, which are characterized by an effective thermal conductivity. The values of the effective thermal conductivity obtained from relaxation measurements are in good agreement with the corresponding data obtained upon a change in steady-state temperature gradients.

This study was supported in part by the NATO Science Program, Grant PST.CLG.978495.

*E-mail: zadorozhko@ilt.kharkov.ua

[1] I. M. Khalatnikov and V. A. Zharkov, Zh. Éksp. Teor. Fiz. **32**, 1108 (1957) [Sov. Phys. JETP **5**, 905 (1957)]; I. M. Khalatnikov, *An Introduction to the Theory of Superfluidity*, Benjamin, New York (1965), Nauka, Moscow (1971).
[2] L. P. Gor'kov and L. P. Pitaevskiĭ, Zh. Éksp. Teor. Fiz. **33**, 634 (1957) [Sov. Phys. JETP **6**, 486 (1958)].
[3] A. Griffin, Can. J. Phys. **47**, 429 (1969).
[4] R. P. Behringer and H. Meyer, J. Low Temp. Phys. **46**, 407 (1982).
[5] R. P. Behringer and H. Meyer, J. Low Temp. Phys. **46**, 435 (1982).
[6] I. N. Adamenko and V. I. Tsyganok, Zh. Éksp. Teor. Fiz. **88**, 1641 (1985) [Sov. Phys. JETP **61**, 978 (1985)].
[7] I. N. Adamenko, K. É. Nemchenko, V. I. Tsyganok, and A. I. Chervanev, Fiz. Nizk. Temp. **20**, 636 (1994) [Low Temp. Phys. **20**, 498 (1994)].
[8] K. É. Nemchenko, Fiz. Nizk. Temp. **23**, 799 (1997) [Low Temp. Phys. **23**, 599 (1997)].
[9] K. É. Nemchenko, Fiz. Nizk. Temp. **24**, 941 (1998) [Low Temp. Phys. **24**, 708 (1998)].
[10] J. Tuttle, F. Zhong, and H. Meyer, J. Low Temp. Phys. **82**, 15 (1991).
[11] D. Murphy and H. Meyer, J. Low Temp. Phys. **107**, 175 (1997).
[12] A. A. Zadorozhko, T. V. Kalko, É. Ya. Rudavskii, V. K. Chagovets, and G. A. Sheshin, Fiz. Nizk. Temp. **29**, 367 (2003) [Low Temp. Phys. **29**, 275 (2003)].
[13] T. S. Sullivan, V. Steinberg, and R. E. Ecke, J. Low Temp. Phys. **90**, 343 (1993).
[14] I. N. Adamenko and É. Ya. Rudavskii, Fiz. Nizk. Temp. **13**, 3 (1987) [Sov. J. Low Temp. Phys. **13**, 1 (1987)].
[15] G. Baym and W. F. Saam, Phys. Rev. **171**, 172 (1968).
[16] G. Baym and C. Ebner, Phys. Rev. **164**, 235 (1967).

Translated by Steve Torstveit

Kinetics of the phase transition in solid solutions of ^{4}He in ^{3}He at different degrees of supersaturation

V. N. Grigor'ev, V. A. Maidanov, A. A. Penzev, É. Ya. Rudavskii, A. S. Rybalko, and Ye. V. Syrnikov*

B. Verkin Institute for Low Temperature Physics and Engineering, National Academy of Sciences of Ukraine, pr. Lenina 47, Kharkov 61103, Ukraine

V. V. Slezov

National Research Center "Kharkov Physicotechnical Institute," ul. Akademicheskaya 1, Kharkov 61108, Ukraine

(Submitted July 8, 2003)
Fiz. Nizk. Temp. **30**, 177–183 (February 2004)

Precision measurements of the pressure during phase separation in samples of solid solutions of ^{4}He in ^{3}He have been used to obtain data on the characteristic times of the phase transition. A processing of the results gives additional evidence supporting the view that homogeneous nucleation is realized in ^{3}He–^{4}He solid solutions at significant supercoolings and heterogeneous nucleation at the smallest supercoolings. Two different ways are proposed for comparing the results with a theoretical calculation taking into account the processes at the boundary of a nucleus of the new phase. Both give roughly similar values of the coefficient of surface tension at the nucleus–matrix boundary, and those values agree with those obtained in other studies. It is conjectured that the bcc–hcp transition has a substantial influence on the kinetics of separation at the lowest supersaturations. © *2004 American Institute of Physics.* [DOI: 10.1063/1.1645164]

1. INTRODUCTION

Solid helium has been of interest as an object of physics research primarily as a typical representative of the quantum crystals. Indeed, it is helium that is typified by such unusual properties as melting at arbitrarily low temperatures, quantum diffusion of impurities, and phase separation of mixtures at low temperatures. On the other hand, a number of effects first observed and studied in solid helium have been subsequently found in other substances: the hydrodynamic flow of phonons, second sound in crystals, and faceting phase transitions. It has turned out that the study of these and other phenomena can be done more efficiently in helium thanks to the possibility of obtaining pure and perfect crystals and the presence of diverse well-developed low-temperature experimental techniques.

A number of papers[1–3] have expressed the idea that helium would be a good object on which to study the kinetics of phase transformations. Research on this topic has now been done for several decades, and yet many important aspects of this fundamental problem remain unclear. It can be hoped that the advantages of helium will permit a detailed investigation of the physical mechanisms of the phase separation of isotopic mixtures and to obtain experimental data suitable for quantitative comparison with the calculations done in the theory of homogeneous nucleation.

Our recent experimental research on phase separation in solid mixtures of helium isotopes has already led to the discovery of a number of interesting, often unexpected effects (see Refs. 4–7). The present paper reports a continuation of this research and is devoted to a study of the influence of the degree of supersaturation on the rate of the phase transition and a comparison with theoretical results.

2. BASIC RELATIONS OF THE THEORY OF HOMOGENEOUS NUCLEATION

A phase transition under conditions of homogeneous nucleation occurs in a supersaturated solution by the fluctuational formation of new-phase nuclei randomly distributed in the volume. Nuclei in which the number of particles n is less than a certain critical value n_c, specified by the condition of equality of the bulk and surface contributions to the thermodynamic potential, are unstable and rapidly dissolve. For $n>n_c$ the nuclei are stable, and their size increases with time, bringing about the development of the phase transition. The number of particles in a roughly spherical critical nucleus formed in an initially homogeneous solution with a concentration c_0 and supercooled from the phase separation temperature T_{s0} to a temperature T_f corresponding to an equilibrium concentration c_f is determined by the relations (see, e.g., Ref. 8)

$$n_c=\left(\frac{\beta}{\ln(c_0/c_f)}\right)^3, \tag{1}$$

where

$$\beta=\frac{8\pi}{3}\frac{\sigma a^2}{T_f}, \tag{2}$$

σ is the surface tension at the nucleus–matrix boundary, a is the interatomic separation, determined by the relation $4\pi a^3/3=V_\mu/N_A$ (V_μ is the molar volume, and N_A is Avogadro's number).

A governing role in the kinetics of the phase transition is played by a function $I(n)$ which characterizes the rate of growth of the nuclei and can be regarded as the flux in the space of nucleus sizes (numbers of particles in the nucleus). $I(n)$ is a very sharp (exponential) function of the nucleus size, and the development of practically all the processes occurring at the phase transition is specified by the value $I_0 \equiv I(n_c)$, which is the flux of particles through the critical point in the size space. I_0 can be written in the form[8,9]

$$I_0 = \sqrt{\frac{3\beta}{2\pi}} c_0^2 \exp\left[-\frac{\Delta\Phi(n_c)}{T} \right], \tag{3}$$

where $\Delta\Phi(n)$ is the change of the thermodynamic potential upon the transition of n particles from the initial solution into the nucleus. If the nucleus is assumed spherical, then one can write

$$\Delta\Phi(n) = n\Delta\mu + 4\pi a^2 \sigma n^{2/3}. \tag{4}$$

For an ideal solution the difference of the chemical potentials of an impurity in the initial solution and in the nucleus is

$$\Delta\mu = T \ln \frac{c_f}{c_0}. \tag{5}$$

Taking Eqs. (1), (2), and (5) into account, one can get

$$\frac{\Delta\Phi(n_c)}{T_f} = \frac{\beta^3}{2\ln^2 \dfrac{c_0}{c_f}},$$

$$I_0 = \sqrt{\frac{3\beta}{2\pi}} c_0^2 \exp\left(-\frac{\beta^3}{2\ln^2(c_0/c_f)} \right). \tag{6}$$

An expression for the nucleation time in the approach considered here was found in Ref. 8:

$$\tau_N = \left(\frac{4c_0}{\beta^3 I_0} \right)^{1/4} \frac{a^2 c_0}{D}, \tag{7}$$

where D is the diffusion coefficient of the impurities. Estimates show that τ_N is an extremely small quantity, at least in comparison with the time of the next stage of diffusional growth of the nucleus. Indeed, this circumstance provides grounds for assuming that the nucleation process takes place at a practically constant concentration, since it is essentially completed at a concentration c_c determined by the condition $(c_0 - c_c)/c_0 \approx n_c^{-1} \ll 1$. This, in turn, allows one to introduce the concept of a maximum concentration of new-phase nuclei,[8] equal to the ratio of the number of nuclei to the number of lattice sites:

$$N_m = I_0 \tau_N \frac{D}{c_0 a^2} = (4c_0)^{1/4} \left(\frac{I_0}{\beta} \right)^{3/4}. \tag{8}$$

If it is assumed that the diffusional growth of the nuclei takes place under conditions such that each nucleus of radius r is found in a sphere of mean radius $R = a/N_m^{1/3}$, then the characteristic time for the diffusional growth will be equal to (see, e.g., Ref. 5)

$$\tau_D = \frac{1}{\lambda^2 D}, \tag{9}$$

where λ is a solution of the transcendental equation

$$\tan\lambda(R-r) = \lambda R. \tag{10}$$

For

$$\lambda(R-r) < 1 \tag{10a}$$

$\tan\lambda(R-r)$ can be expanded in a series; keeping only the cubic terms of this expansion, we get

$$\lambda^2 = \frac{3z}{R^2(1-z)^3}, \tag{11}$$

where

$$z = \frac{r}{R} = \left(\frac{c_0 - \overline{c}}{1 - 2\overline{c}} \right)^{1/3}, \tag{12}$$

and $\overline{c}$ is the mean concentration of the impurity in the matrix. Equation (12) was obtained with the use of the conservation law for impurities in the volume of a sphere of radius R.

Taking Eq. (11) into account, we can write an expression for τ_D:

$$\tau_D = \frac{R^2}{3D} \frac{(1-z)^3}{z} = \frac{a^2}{3DN_m^{2/3}} \frac{(1-z)^3}{z}$$

$$= \frac{a^2 \beta^{1/2}}{3D(4c_0)^{1/6} I_0^{1/2}} \frac{(1-z)^3}{z} \tag{13}$$

and, substituting I_0 from Eq. (6), we find

$$\tau_D = \frac{\alpha \beta^{1/4} a^2}{D c_0^{7/6}} \frac{(1-z)^3}{z} \exp\left(\frac{\beta^3}{4\ln^2(c_0/c_f)} \right), \tag{14}$$

where $\alpha = \dfrac{\pi^{1/4}}{3^{5/4} 2^{1/12}} \approx 0.32$.

Thus for a known D, Eq. (14) can be used with values obtained for τ_D to determine β and hence the surface tension σ which enters into it.

3. EXPERIMENTAL RESULTS AND DISCUSSION

In the experiment the time dependence of the pressure in samples of solid solutions of ^{4}He in ^{3}He was measured after cooling from the region of the homogeneous state to various temperatures T_f below the phase separation temperature T_{s0} of the initial solution. The measurement techniques and the experimental setup are described in detail in Ref. 5. An important element of the previous experiments was the development of a technique for obtaining homogeneous samples, making it possible to obtain practically equilibrium solutions. Samples of solid helium in the form a disk 9 mm in diameter and 1.5 mm in height were located inside a metal chamber cooled by a dilution refrigerator; the samples were grown by the capillary blocking method from a gaseous mixture containing approximately 2% ^{4}He. The bottom of the chamber, which was ≈ 1 mm thick, served as the movable plate of a precision capacitive pressure gauge of the Straty–Adams type. The ^{4}He concentration in the sample was refined according to the value of the change in pressure upon complete separation, ΔP_0, by the Mullin formula:[10]

$$\Delta P_0 = 0.4 \frac{V_\mu}{\gamma} c_0 (1 - c_0), \tag{15}$$

TABLE I. Some characteristics of the samples studied.

Sample No.	c_0, % ^{4}He	P_0, bar	V_μ, cm^3/mole	T_{s0},K	T^*,K	$\sigma^*\cdot10^2$, erg/cm^2	$\bar{\sigma}\cdot10^2$, erg/cm^2
1	2.25	34.82	23.99	0.199	0.170	2.20	1.4
2	2.43	38.616	23.55	0.201	0.191	1.11	–
3	2.8	31.435	24.42	0.212	0.182	2.21	1.4
4	2.93	35.465	23.89	0.212	0.189	1.84	1.1
5	3.34	32.85	24.20	0.220	–	–	1.2

Note: c_0 is the ^{4}He concentration, P_0 is the pressure, V_μ is the molar volume, T_{s0} is the phase separation temperature of the intial solution, T^* is the temperature of intense nucleation, and σ^* and $\bar{\sigma}$ are the coefficients of interfacial surface tension found by different means.

where γ is the compressibility.

We studied five samples with concentrations from 2.2 to 3.35% ^{4}He. We note that for all the samples the experimental values of the separation temperature corresponded within the error limits with those calculated according to the formulas of Edwards and Balibar.[11] Some of the characteristics of the samples studied are presented in Table I.

As in the majority of previously studied situations, the time dependence of the pressure in the sample upon a stepwise lowering of the temperature in the phase separation region is described well by an exponential function of the form

$$P_f - P(t) = \Delta P_m \exp(-t/\tau), \tag{16}$$

where $\Delta P_m = P_f - P_i$ is the difference of the equilibrium values of the final pressure P_f and initial pressure P_i; τ is the characteristic time for establishment of equilibrium at the step under consideration. In the present study we measured the values of τ corresponding to lowering of the temperature from the region of the homogeneous solution into the phase separation region. The primary data for one of the samples are presented in Fig. 1, which shows the time dependence $\Delta P = P(t) - P_0$ for different values of T_f. All of the curves are described satisfactorily by relation (16), and the time τ decreases noticeably at large T_f and becomes practically independent of T_f for $T_f \leqslant 160$ mK. This is more clearly seen in Fig. 2, where the values of τ for all the samples are plotted as a function of the relative supercooling $\Delta T/T_s$ ($\Delta T = T_s - T_f$).

At small supercoolings ($\Delta T < 20$ mK) the characteristic times turn out to be extremely long (up to 10^4 s), and they decrease rapidly with increasing ΔT to values of the order of 500–700 s, and at $\Delta T \geqslant 50$ mK they become practically independent of the degree of supercooling. This behavior agrees qualitatively with what is expected under conditions of homogeneous nucleation. According to Eq. (15), the change in pressure is uniquely related to the change in concentration, and the times τ found characterize the progress of the diffusion process in the presence of separation, which is governed by a time $\tau_D \approx R^2/D \approx N_m^{-2/3} D^{-1}$ (see Sec. 2). The concentration of nuclei N_m in the presence of separation grows sharply with increasing degree of supersaturation (supercooling) [see Eq. (8)], and that brings about a corresponding decrease of τ. The ultimate plateauing of τ can be come about for several reasons.

1. At short diffusion times, as we have mentioned previously,[12,13] the impurity atoms at the nucleus–matrix boundary have a resistance to transition characterized by a time τ_s that is practically independent of T at low temperatures.[13]

2. As was shown in Refs. 3 and 14, at a finite rate of cooling, when it is necessary to take into account the change of the concentration c_f with time, one can introduce the concept of the temperature of maximum nucleation rate, T^*, at

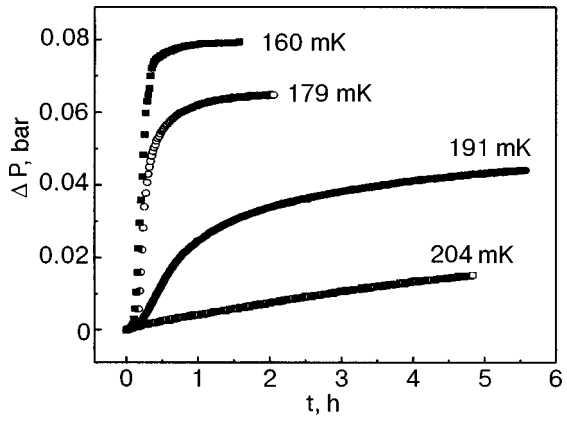

FIG. 1. Time dependence of the change in pressure in sample No. 4 upon cooling from the region of the homogeneous solution to different temperatures T_f, indicated in the figure.

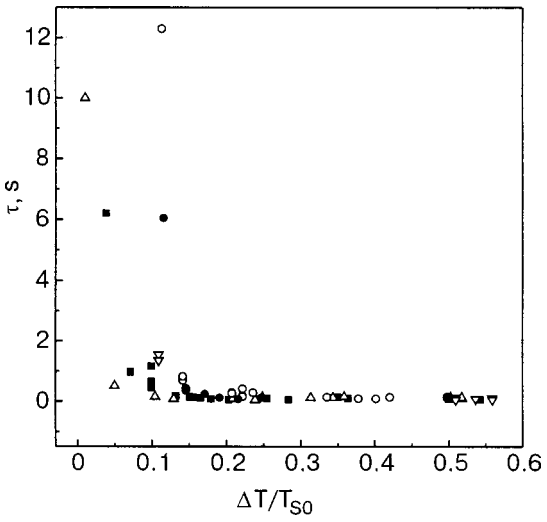

FIG. 2. Characteristic times τ versus the relative supercooling for all the samples studied: samples No. 1 (●), No. 2 (△), No. 3 (○), No. 4 (■), No. 5 (▽).

which the decrease of the degree of supersaturation $\varepsilon = c(t) - c_f(t)$ due to the decrease of the matrix concentration $c(t)$ with time owing to the escape of impurities into the new-phase nuclei is comparable to the increase in ε due to the decrease of $c_f(t)$. The value of T^* becomes the determining factor specifying the concentration of nuclei, and decreasing T_f further does not alter the value of N_m, and, hence, of τ for a sufficiently weak temperature dependence of $D(T)$.

3. The minimum times τ found are close to the characteristic times for establishment of a temperature.

4. With decreasing T^* a fundamental circumstance can be come into play: at sufficiently high supersaturations the number of atoms in a nucleus becomes of the order of 1. This will mean that the macroscopic approach described in Sec. 2 will not be applicable under these conditions, and there is probably a change of nucleation mechanism.

Apparently the most probable cause of the plateauing of τ with increasing supersaturation is a combination of the first two factors. The time for establishment of an equilibrium temperature was practically always less than the experimental values of τ. It was shown in Ref. 13 that under condition (10a) the measured characteristic time for the influence of the boundary resistance to be noticeable can be written in the form

$$\tau = \tau_D + \tau_s, \tag{17}$$

where τ_D as before is described by formula (13), and

$$\tau_s = \frac{R}{3K}\,\frac{1-z^3}{z^2}, \tag{18}$$

where K is a constant characterizing the probability of penetration of an impurity through the boundary of a nucleus. If $T_f \leqslant T^*$, then R ceases to depend on T_f, and then the expression

$$\tau \equiv \tau\,\frac{z^2}{1-z^3} - \frac{R^2}{3D}\,\frac{(1-z)^3 z}{1-z^3} = \frac{R}{3K}, \tag{19}$$

obtained by substituting formulas (11) and (18) into (17) will be a constant. Relation (19) can be used to estimate T^* as the temperature starting with which the left-hand side of this formula becomes independent of T_f, and the value of R here is figured as the minimum value of R_m corresponding to the temperature T^*. For determination of the values of T^* and R_m we constructed a plot of τ versus T_f according to Eq. (19) (see Fig. 3). In constructing the plot we used the value $K = 2.7\times10^{-5}$ cm/s from Ref. 13, while the values of the diffusion coefficient D obtained in Ref. 13 were adjusted to the molar volumes of the samples studied. From the values of $\tilde{\tau}$ in the plateau region one can use Eq. (18) to estimate the experimental value of R_m corresponding to the concentration of nuclei formed at the temperature T^* (see Table I) and compare it with the calculated value

$$R_m = \frac{a}{N^{1/3}} \approx a c_0^{-7/12} \exp\left[\frac{\beta^{*3}}{8\ln^2(c_0/c_f^*)}\right], \tag{20}$$

where the asterisk $*$ denotes values corresponding to the temperature T^*. Such a comparison makes it possible to determine β and the quantity σ which enters into β. The values thus found are listed in the table under σ^*. The noticeable

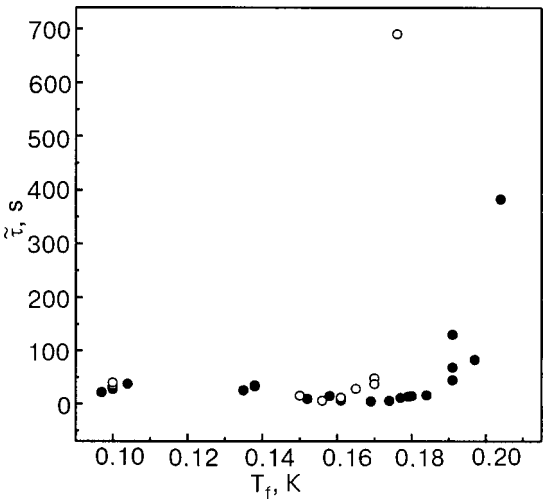

FIG. 3. Dependence of the reduced time $\tilde{\tau}$ (see text) on the final temperature for samples No. 4 (●) and No. 1 (○).

scatter of the values of σ^* for different samples is most likely due to inaccuracy of the purely visual estimate of T^* from the plot in Fig. 3.

The data obtained at medium supersaturations, i.e., for $T_f > T^*$, can also be used for an estimate of σ. Formula (17), written in the form

$$\tau = \frac{R^2}{3D}\,\frac{(1-z)^3}{z} + \frac{R}{3K}\,\frac{1-z^3}{z^2}, \tag{21}$$

can be considered to be an equation for finding R and can thus be used with the measured values of $\tau(T_f)$ to determine $R(T_f)$ and, with the use of (20), σ. The values of σ thus obtained, averaged for the different T_f, are listed in the table under $\overline{\sigma}$. The difference of the mean values of the surface of surface tension ($\sigma^* = 1.8\times10^{-2}$ erg/cm^2 and $\overline{\sigma} = 1.3\times10^{-2}$ erg/cm^2) estimated by the two methods is ~20%. An averaging of all the data gives a value $\sigma = 1.5\times10^{-2}$ erg/cm^2, practically the same as the results of previous estimates.[12,13]

Curious features of the time dependence are observed at the lowest supersaturations (Fig. 4): the total time for establishment of equilibrium turns out to be very long there, and the $\Delta P(t)$ curves display noticeable irregularities. Since the probability of homogeneous nucleation at such low super-

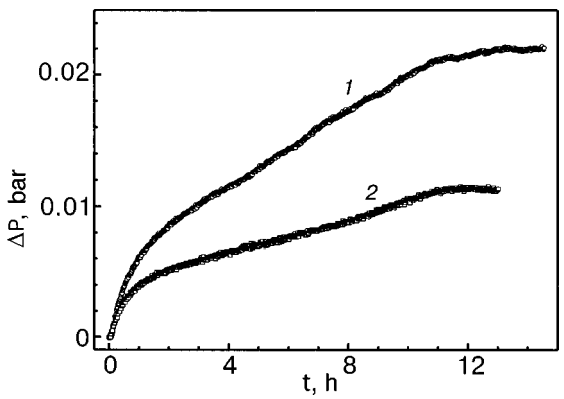

FIG. 4. Time dependence of the change in pressure at very low degrees of supersaturation for samples No. 1 (□; curve *2*) and No. 3 (○; curve *1*).

saturations is very small, it can be assumed that heterogeneous nucleation becomes the governing process. If heterogeneous nucleation occurs on the wall of the cell, then the change in the mean concentration (and, hence, the pressure) should correspond to the solution of the diffusion problem for a sample situated between two planes and is described by the expression (see, e.g., Ref. 15)

$$\Delta P=\Delta P_m\left[1-a_N^{-1}\sum_{n=0}^{N}\frac{1}{(2n+1)^2}\exp\left(-\frac{\pi^2 Dt}{d^2}(2n+1)^2\right)\right], \tag{22}$$

where $a_N=\Sigma_{n=0}^{N}1/(2n+1)^2$, d is the distance between planes, and N is the number of terms in the sum.

A processing of the curves in Fig. 4 with the aid of (22) shows that the use of 3–4 terms of the sum decreases the rms deviation δ by more than a factor of 3 compared to processing with the use of a single exponential, and increasing N further has little effect on the value of δ. We note that formula (22) differs from the analogous formula for a spherical geometry (see, e.g., Ref. 5) by a significantly slower decrease of the successive terms of the sum. The relaxation time $\tau=d^2/\pi^2 D$ obtained here is of the order of 4×10^4 s, and when the height of the cell is substituted in for d one obtains a value $D\sim5\times10^{-8}$ cm^2/s for the diffusion coefficient, which agrees with the data obtained in Ref. 13. This fact argues strongly in favor of heterogeneous nucleation under these conditions.

The irregularity of the curves in Fig. 4 may be due to the formation, at low supersaturations, of new-phase nuclei with the bcc structure, which later transforms to the hcp structure. A similar phenomenon has been observed[16] in the crystallization of ^{4}He in the region of the triple points. This possibility is also supported by the fact, registered in x-ray studies of the decomposition of the solutions, that a nonequilibrium bcc structure of the new phase persists to temperatures of $\sim$100 mK.[17]

4. CONCLUSION

In this paper we have reported measurements of the characteristic times for the diffusional decomposition of solid solutions of ^{4}He in ^{3}He. The results of the experiments were compared with theoretical calculations of the parameters of homogeneous nucleation under conditions of a finite resistance at the nucleus–matrix boundary, and on the basis of that comparison the value of the coefficient of interphase surface tension was estimated by two methods.

The closeness of the surface-tension results obtained by the different methods and their good agreement with values of σ found previously[13] (see also Ref. 18) furnish additional evidence for the realization of conditions for homogeneous nucleation in perfect samples of ^{3}He–^{4}He solid solutions. However, for a final answer to this question it will be necessary to do more careful and systematic studies to minimize if not eliminate the errors existing in the present treatment, viz:

a) the approximate character of formulas (17) and (19), which are based on an expansion of Eq. (10), because of the proximity of $\lambda(R-r)$ to 1;

b) insufficient accuracy of the estimate of T^*, owing to the small number of experimental points;

c) possible errors in bringing in the parameters D and K from Ref. 13 (it would be desirable to measure them in the same experiment);

d) possible influence of heterogeneous nucleation and a bcc–hcp transition, especially at low supersaturations.

Experiments done with these circumstances taken into account will make it possible to perform a more quantitative comparison with the results of the theory of homogeneous nucleation, extended to the situation with a finite rate of supercooling,[14] and to trace the transition from heterogeneous to homogeneous nucleation in ^{3}He–^{4}He solutions.

This study was supported in part by the Ukrainian Government Foundation for Basic Research (Project 02.07/00391, contract F7/286-2001).

*E-mail: syrnikov@ilt.kharkov.ua

[1] I. M. Lifshitz, V. I. Poleskiĭ, and V. A. Khokhlov, Zh. Éksp. Teor. Fiz. **74**, 268 (1978) [Sov. Phys. JETP **47**, 137 (1978)].
[2] S. Balibar, T. Misusaki, and V. Sasaki, J. Low Temp. Phys. **120**, 293 (2000).
[3] A. Ganshin, V. Grigor'ev, V. Maidanov, E. Rudavskii, A. Rybalko, V. Slezov, and Ye. Syrnikov, J. Low Temp. Phys. **126**, 151 (2002).
[4] A. Ganshin, V. Grigor'ev, V. Maidanov, N. Omelaenko, A. Penzev, E. Rudavskii, and A. Rybalko, J. Low Temp. Phys. **116**, 349 (1999).
[5] A. N. Gan'shin, V. N. Grigor'ev, V. A. Maĭdanov, N. F. Omelaenko, A. A. Penzev, E. Ya. Rudavskiĭ, A. S. Rybalko, and Yu. A. Tokar, Fiz. Nizk. Temp. **25**, 796 (1999) [Low Temp. Phys. **25**, 592, Erratum 928 (1999)].
[6] A. N. Ganshin, V. N. Grigor'ev, V. A. Maĭdanov, A. A. Penzev, É. Ya. Rudavskiĭ, A. S. Rybalko, and E. V. Syrnikov, JETP Lett. **73**, 289 (2001).
[7] A. N. Gan'shin, V. N. Grigor'ev, V. A. Maĭdanov, N. F. Omelaenko, A. A. Penzev, É. Ya. Rudavskiĭ, and A. S. Rybalko, Fiz. Nizk. Temp. **26**, 550 (2000) [Low Temp. Phys. **26**, 401 (2000)].
[8] V. V. Slezov and J. Shmelzer, Fiz. Tverd. Tela (St. Petersburg) **39**, 2210 (1997) [Phys. Solid State **39**, 1971 (1997)].
[9] V. Volmer, *Kinetik der Phasenbildung*, Steinkopff, Dresden (1939).
[10] W. J. Mullin, Phys. Rev. Lett. **20**, 254 (1968).
[11] E. D. Edwards and S. Balibar, Phys. Rev. B **39**, 4083 (1989).
[12] A. N. Gan'shin, V. N. Grigor'ev, V. A. Maĭdanov, A. A. Penzev, É. Ya. Rudavskiĭ, A. S. Rybalko, and E. V. Syrnikov, Fiz. Nizk. Temp. **29**, 487 (2003) [Low Temp. Phys. **29**, 362 (2003)].
[13] V. N. Grigor'ev, V. A. Maĭdanov, A. A. Penzev, É. Ya. Rudavskiĭ, A. S. Rybalko, and E. V. Syrnikov, Fiz. Nizk. Temp. **29**, 1165 (2003) [Low Temp. Phys. **29**, 883 (2003)].
[14] V. V. Slezov, Fiz. Tverd. Tela (St. Petersburg) **45**, 317 (2003) [Phys. Solid State **45**, 335 (2003)].
[15] P. G. Shewmon, *Diffusion in Solids*, McGraw-Hill, New York (1963), Metallurgiya, Moscow (1966).
[16] M. Mackawa, Y. Okumura, and Y. Okuda, Phys. Rev. B **65**, 144525 (2002).
[17] S. N. Ehrlich and R. D. Simmons, J. Low Temp. Phys. **68**, 125 (1987).
[18] A. Smith, V. A. Maidanov, E. Ya. Rudavskii, V. N. Grigor'ev, V. V. Slezov, M. Poole, J. Saunders, and B. Cowan, Phys. Rev. B (to be published).

Translated by Steve Torstveit

LOW-TEMPERATURE MAGNETISM

Neutron scattering study of the layered Ising magnet $CsDy(MoO_4)_2$

E. N. Khatsko*

B. Verkin Institute for Low Temperatures Physics and Engineering of the National Academy of Sciences of Ukraine, 47 Lenin Ave., Kharkov 61103, Ukraine

A. Zheludev[a] and J. M. Tranquada

Physics Department, Brookhaven National Laboratory, Upton, NY 11973-5000, USA

W. T. Klooster[b]

Chemistry Department, Brookhaven National Laboratory, Upton, NY 11973-5000, USA

A. M. Knigavko

Department of Physics, University of Alberta, Edmonton, Alberta, T6G 2J1 Canada

R. C. Srivastava

Department of Physics, Indian Institute of Technology, Kanpur 208016, India
(Received June 18, 2003; revised August 13, 2003)
Fiz. Nizk. Temp. **30**, 184–192 (February 2004)

The quasi-two-dimensional antiferromagnet $CsDy(MoO_4)_2$ is studied by neutron diffraction and quasielastic neutron scattering. The crystal structure of two low-temperature phases (below 120 K and below 40 K) is determined. An approximate structure of the magnetically ordered phase ($T_N = 1.36$ K) is proposed. In the ordered state the order-parameter critical exponent $\beta = 0.17(0.01)$, the in-plane correlation length exponent $\nu = 0.94(0.07)$, and the staggered susceptibility critical index $\gamma = 1.01(0.04)$ were determined. Comparing these results to the exact solution for a 2D Ising magnet, we conclude that, although 2D behavior is apparent in $CsDy(MoO_4)_2$, there are deviations from the simple 2D Ising model. © *2004 American Institute of Physics.* [DOI: 10.1063/1.1645155]

1. INTRODUCTION

For many years low-dimensional (low-D) magnetism has remained at the forefront of solid-state research. Experimental studies of magnetic phase transitions in quasi-low-D compounds are very important for the general understanding of critical phenomena. The study of 2D Ising compounds is of special interest, since for certain low-dimensional Ising theoretical models there is an exact solution and the results can be directly compared to experiment. A relatively few materials simultaneously have strong single-ion anisotropy and adequate two-dimensional magnetic interactions to qualify as model 2D Ising magnets.

Double rare-earth molybdates (DRMs) with the general formula $MR(MoO_4)_2$ (R = rare earth, M = alkali metal) crystallize in a variety of layered structures (see for example Refs. 1–4) and are a large family of 2D compounds with some very interesting species. The magnetism of molybdates is entirely due to the presence of trivalent rare-earth ions. For the latter, magnetic anisotropy effects are crucial, and components of the g tensor may vary from almost 0 to as much as 20. In many DRMs the rare-earth sites behave as nearly ideal Ising centers. Typically large rare-earth magnetic moments in many cases result in appreciable dipolar magnetic interactions.[5,6] Long-range magnetic order has been detected in several species[7–9] and typically occurs only at sub-kelvin temperatures. The rather unusual magnetic properties of DRMs have been investigated using dc and ac magnetic measurements,[7–9] optical experiments[10,11] and ESR.[12,13]

Although neutron diffraction has been widely used in the study of crystal structures,[1,3,14] we were surprised not to find any reports in the literature on magnetic neutron scattering experiments on DRMs. Although magnetic neutron diffraction often is the ''ultimate'' technique for studying magnetic phase transitions and critical behavior, actual experiments may be, from a purely technical point of view, nontrivial to carry out. Low magnetic ordering temperatures require the use of bulky cryogenic equipment that limits the region of Q space accessible in a diffraction experiment. In addition, most DRMs go through a whole series of structural transformations when cooled down from room temperature, and the formation of crystallographic domains may complicate the interpretation of the diffraction pattern. These problems indeed have to be dealt with, but, as we show below, do not present an insurmountable obstacle.

In the present paper we report the results of neutron scattering experiments on one particular compound, namely $CsDy(MoO_4)_2$. Data pertaining to the crystallographic and magnetic structures, as well as measurements of the mag-

netic critical behavior, confirm the 2D Ising nature of this system. At the same time, certain new features hint at the important role played by dipolar interactions.

2. EXPERIMENTAL

Our choice of $CsDy(MoO_4)_2$ over other DRM species was largely governed by the availability of large single-crystal samples. Among the rare-earth ions, Dy^{3+} in the molybdates has the advantage of having one of the largest magnetic moments. The tradeoff is its appreciable neutron absorption cross section. $CsDy(MoO_4)_2$ would not be an ideal candidate for inelastic experiments, but it is well suited for measurements of elastic magnetic scattering. Mica-like transparent rectangular single-crystal samples for our experiments were prepared by spontaneous crystallization from melt solution.[15] $4\times4\times0.15$ mm and $8\times12\times0.15$ mm samples were used for conventional and magnetic neutron scattering experiments, respectively.

4-circle diffraction data were collected at the H6M 4-circle diffractometer at the High Flux Beam Reactor (HFBR) at Brookhaven National Laboratory. In this experiment the sample environment was a standard Displex refrigerator. Two separate sets of (hkl) data were collected at 50 K and 15 K, respectively.

Low-temperature (0.35–5 K) neutron scattering experiments were performed at the H8, H7, and H4M 3-axis spectrometers at the HFBR with the use of a pumped-^{3}He Dewar. The temperature was controlled with an automated resistance bridge to a precision of ≈0.01 K. The sample was wrapped in thin aluminum foil and mounted as strain-free as possible. A neutron beam of fixed final energy $E_f=14.7$ MeV was used with a pyrolitic graphite (PG) filter positioned after the sample. Pyrolitic graphite (002) reflections were used for the monochromator and analyzer. The collimation setup was $40'-40'-40'-80'$. The sample mosaic was found to be of the order of 2.5° full width at half maximum (FWHM). Special care was taken to precisely measure the dimensions and orientations of the crystallographic faces. This information was later used to analytically calculate absorption corrections to the measured intensities.

3. RESULTS

3.1. Crystal structure

At room temperature $CsDy(MoO_4)_2$ was believed to be orthorhombic, space group $Pccm$, with cell constants $a=9.51$ Å, $b=5.05$ Å, and $c=7.97$ Å.[3] This structure is essentially the same as for $CsPr(MoO_4)_2$ (Ref. 16). The most prominent feature is a stacking of alternating layers along the crystallographic a axis: $-Dy-(MoO_4)-Cs-(MoO_4)-$ (Fig. 1a). Each layer is parallel to the (100) perfect cleavage plane. The arrangement of magnetic ions is quasi-two-dimensional. The interlayer Dy–Dy distance is large, ≈9.5 Å$=a$ (Fig. 1b). Within each layer the magnetic sites form a rectangular lattice with nearest-neighbor distances ≈5 Å$=b$ and ≈4 Å $=c/2$. Although the $Pccm$ structure has not been seen in any of our $CsDy(MoO_4)_2$ samples at any temperature, all the crystallographic phases that were observed (see below) can be described as distortions of this ''parent'' structure.

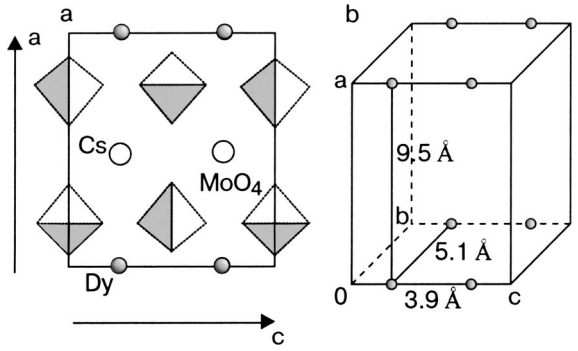

FIG. 1. ''Parent'' model of the $Pccm$ structure of $CsDy(MoO_4)_2$. (a) A projection onto the ac crystallographic plane showing the Dy and Cs sites as well as the MoO_4 tetrahedra. (b) Structural relation between nearest-neighbor magnetic Dy^{3+} ions in the unit cell.

For our samples the room-temperature structure was found to be *monoclinic*, with the measured cell parameters $a=9.49$ Å, $b=5.05$ Å, $c=7.97$ Å, and $\beta=88.4°$. The two monoclinic domains share common a^* and b^* axes. A typical rocking curve of the (0,0,4) Bragg reflection, rotating around the [0,1,0] axis, is shown in Fig. 2 and illustrates the domain structure. It should be noted that monoclinic structure at room temperature correlates with recent x-ray analysis.[17] No further crystallographic information was obtained at room temperature, since our main interest was with the low-temperature behavior.

Below $T_1\approx120$ K, a structural phase transition takes place and $CsDy(MoO_4)_2$ becomes orthorhombic (Fig. 2, curve *2*). An analysis of the 4-circle diffraction data suggests the space group in this low-temperature (LT-1) phase is $Pcca$, with the 50 K cell parameters $a=18.760(7)$ Å

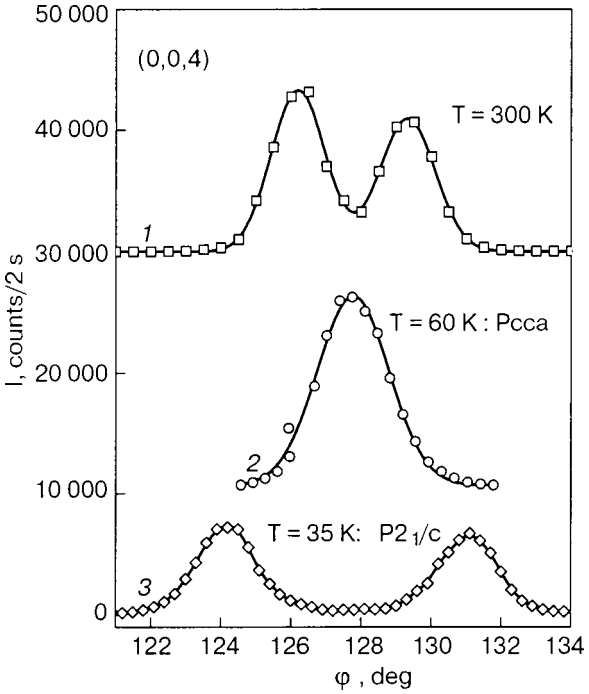

FIG. 2. Rocking curves of the (0,0,4) Bragg peak (rotation around (0,1,0)) measured at different temperatures in a $CsDy(MoO_4)_2$ single crystal. The crystal structure is monoclinic at room temperature (*1*), becomes orthorhombic ($Pcca$) below $T_1\approx120$ K (*2*), and finally turns monoclinic again ($P2_1/c$) on cooling through $T_2\approx40$ K (*3*).

$=2a_{Pccm}$, $b=5.013(4)$ Å, and $c=7.920(6)$ Å. Compared to the "parent" $Pccm$ structure the a axis is doubled and the Dy ions are displaced along the c axis in a direction that alternates from site to site along the a axis.[18] The Dy point group is C_2, as compared to D_2 in the $Pccm$ cell.

On cooling through $T_2 \approx 40$ K a structural phase transition to yet another monoclinic structure occurs (Fig. 2, curve *3*). It is interesting to note that both crystallographic transitions at T_1 and T_2 are totally reversible. The low-temperature monoclinic (LT-2) phase is of $P2_1/c$ symmetry, with $a=18.86(5)$ Å $=2a_{Pccm}$, $b=10.05(3)$ Å $=2b_{Pccm}$, $c=7.78(2)$ Å, and $\beta=86.6(2)°$ at $T=15$ K. As in the high-temperature monoclinic phase, the two types of monoclinic domains share common a^* and b^* axes. Atom positions above (50 K) and below (15 K) the phase transition at T_2 are summarized in Table I. The phase transition at T_2 has been previously observed by Zvyagin *et al.*,[10] but the low-temperature phase structure could not be determined from their experiments. It is accompanied by an abrupt change in the energy spectrum of the Dy^{3+} ions which is due to a lowering of the Dy site symmetry (point group 1 in the LT-2 phase).[19] In the low-temperature phase there are two crystallographically inequivalent Dy sites.[20]

TABLE I. Positions of atoms in the $CsDy(MoO_4)_2$ lattice.

Atom	x/a	y/b	z/c	occ.	scat. l.
T = 50 K					
Pcca (54) a = 18.760(7) Å, b = 5.013(4) Å, c = 7.920(6) Å, α = 90°, β = 90°, γ = 90°					
Cs	0.500000	0.030423	0.250000	0.5	0.542000
Dy	0.250000	0.000000	0.265612	0.5	1.690000
Mo	0.347931	0.476683	0.015128	1.0	0.695000
O(1)	0.346349	0.260980	−0.160873	1.0	0.580300
O(2)	0.281962	0.747241	0.014366	1.0	0.580300
O(3)	0.430135	0.616141	0.018499	1.0	0.580300
O(4)	0.343858	0.259971	0.193318	1.0	0.580300
T = 15 K					
$P2_1/c$ (14) a = 18.860(5) Å, b = 10.05(3) Å, c = 7.78(2) Å, α = 90°, β = 86°, γ = 90°					
Dy(1)	0.748648	0.250331	0.305721	1.0	1.690000
Dy(2)	0.748415	−0.249622	0.259788	1.0	1.690000
Cs(1)	0.505550	0.217766	0.252675	1.0	0.542000
Cs(2)	0.005550	−0.217766	0.252675	1.0	0.542000
Mo(1)	0.840773	−0.504712	0.040900	1.0	0.695000
O(11)	0.781186	−0.377342	0.004581	1.0	0.580300
O(12)	0.923480	−0.448149	0.036071	1.0	0.580300
O(13)	0.842379	−0.625712	0.229138	1.0	0.580300
O(14)	0.844800	−0.617309	−0.105179	1.0	0.580300
Mo(2)	0.647130	0.008269	0.081290	1.0	0.695000
O(21)	0.654182	0.127886	0.245055	1.0	0.580300
O(22)	0.654667	0.117729	−0.084289	1.0	0.580300
O(23)	0.717159	−0.122156	0.015003	1.0	0.580300
O(24)	0.571327	−0.049736	0.086437	1.0	0.580300
Mo(3)	0.649459	−0.008883	0.520559	1.0	0.695000
O(31)	0.649830	−0.117424	0.708992	1.0	0.580300
O(32)	0.653336	−0.119275	0.347094	1.0	0.580300
O(33)	0.566060	0.068861	0.544750	1.0	0.580300
O(34)	0.715736	0.121061	0.538746	1.0	0.580300
Mo(4)	0.841970	0.509006	0.494863	1.0	0.695000
O(41)	0.846766	0.624122	0.296780	1.0	0.580300
O(42)	0.783495	0.379413	0.524604	1.0	0.580300
O(43)	0.841672	0.620472	0.663917	1.0	0.580300
O(44)	0.923446	0.438145	0.486899	1.0	0.580300

3.2. Magnetic long-range order

Below $T_N=1.36$ K new magnetic Bragg reflections with Miller indices ($P2_1/c$ notation) $(h,0,l)$ (h-odd, l-even) and $(h,k,0)$ (h,k-integer, h-odd, k-even) were observed in the (0,1,0) and (0,0,1) reciprocal-space planes, respectively. Much weaker magnetic peaks were seen at $(h,l,0)$ (h,l-odd) positions. Constraints imposed by the experimental geometry prevented us from measuring magnetic scattering in other planes. Most of the diffraction data were collected at $T=0.35$ K in the $(h,0,l)$ zone. In general, magnetic reflections from different structural domains could always be separated, although partial overlap occurs in some cases. A typical h-scan along $(h,0,2)$ measured at $T=0.35$ K is presented in Fig. 3. It shows both the nuclear and magnetic peaks originating from the two monoclinic domains.

Peak shapes. As can be seen in Fig. 3 (for example, by comparing the (3,0,2) magnetic and (4,0,2) nuclear peaks) the magnetic Bragg reflections are visibly broader than the nuclear ones. This anomalously large width of magnetic reflections, more clearly seen in Fig. 4, was only observed along the a^* direction. The Q-width of all the magnetic peaks investigated is resolution-limited in the b^* and c^* directions. The anomalous h-width was found to be dependent on the rate at which the sample is brought down to low temperature. Fast cooling (10 min) from $T=1.5$ K down to $T=0.35$ K produces the broadest peaks (Fig. 4, open circles), whereas slow (2 hours) cooling through T_N results in sharper peaks (Fig. 4, solid circles). The Q-integrated magnetic Bragg intensity was slightly higher in slow-cooling experiments. Moreover, some annealing (sharpening and intensifying of the magnetic peaks) over a time scale of 24 hours was observed even at $T=0.35$ K.

Order parameter. The large time constants associated with the establishing of long-range magnetic order make temperature-dependent measurements of the order parameter extremely difficult. $T_N \approx 1.3$ K happens to be close to the condensation temperature of ^{3}He, and long measurements above $T=1$ K are hard to perform due to a high consumption of liquid ^{3}He. The best we could do was to collect data on slow cooling (1 hour per fixed temperature with a 0.05 K step). The resulting order parameter deduced from the measured (3,0,0) magnetic Bragg intensity is plotted against temperature in Fig. 5. The critical exponent β and the Néel tem-

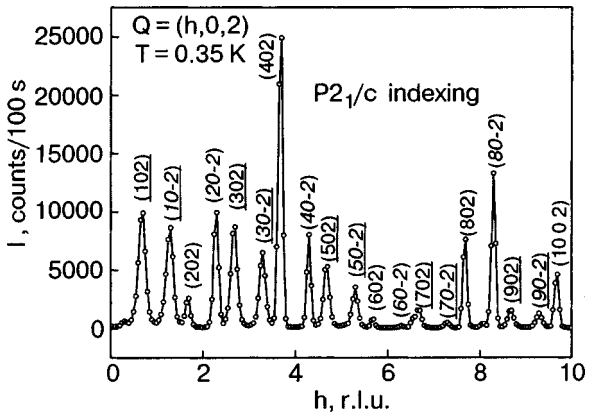

FIG. 3. Elastic scan along $(h,0,2)_{P2_1/c}$ measured in a $CsDy(MoO_4)_2$ single crystal. Bragg reflections originating from the two monoclinic domains are labeled in italic and normal characters, respectively. The indices of magnetic reflections are underlined.

perature were obtained in log–log plots. The analysis yielded $T_N = 1.36(0.01)$ K and $\beta = 0.17(0.01)$. The normalization of the data in Fig. 5 is as discussed below.

Approximate spin structure. Detailed magnetic diffraction data could only be collected in the $(h,0,l)$ reciprocal-space plane. Accurately determining the magnetic structure is further hindered by the necessity of making strong absorption corrections to the measured Bragg intensities. The latter introduces systematic errors, which become very important at large reflection (transmission) angles. The quantity and quality of the data do not allow us to base the analysis of magnetic intensities on the complicated low-temperature crystal structure determined in the experiments with the 4-circle diffractometer. Instead, we have utilized an oversimplified *a priori* model for the arrangement of magnetic ions in the crystal to obtain information on the spin structure.

For each monoclinic domain the observed resolution- and absorption-corrected intensities of $P2_1/c$-inequivalent $(h,0,l)$ and $(h,0,-l)$ Bragg peaks were found to be the same within experimental error. In addition, in our treatment we

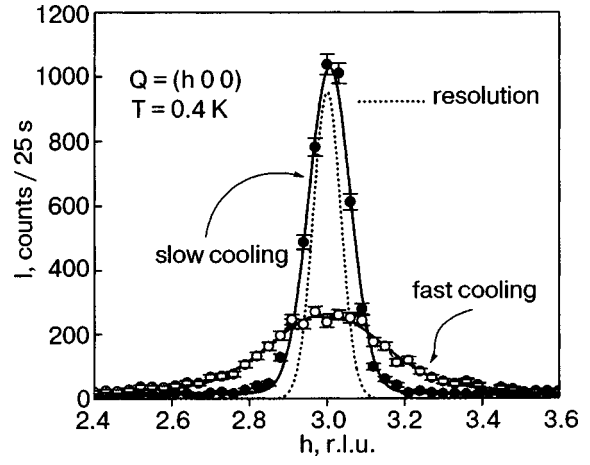

FIG. 4. Longitudinal h-scans through the (3,0,0) magnetic Bragg peak in $CsDy(MoO_4)_2$ measured at $T = 0.4$ K. Fast cooling through T_N produces very broad peaks (open circles), as compared to the experimental resolution (dotted line). Slow cooling results in much sharper Bragg reflections (solid circles). The k- and l-width of all magnetic reflections is resolution-limited independently of the cooling rate.

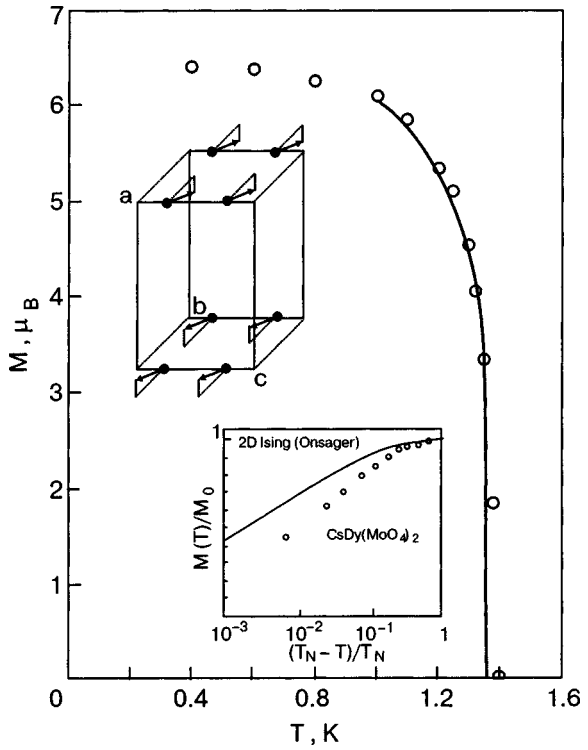

FIG. 5. Magnetic order parameter in $CsDy(MoO_4)_2$ plotted against temperature (circles), as deduced from the temperature dependence of the (3,0,0) magnetic Bragg intensity. The solid line represents a power law with the critical exponent $\beta = 0.17$ and $T_N = 1.36$ K. The top inset shows the approximate spin structure determined at $T = 0.4$ K. In the bottom inset the measured temperature dependence of the magnetization (open circles) is compared to the exact result of Onsager for a 2D Ising system (solid line).

have totally neglected the $(h,0,l)$ $(h,l$-odd) magnetic peaks, since they are significantly weaker than those at $(h,0,l)$ $(h$-odd, l-even) and only a few could be measured. The simplified monoclinic arrangement for the Dy^{3+} ions that we employed in the analysis of the magnetic structure was therefore based on a reduced cell with $\tilde{a} \equiv \frac{1}{2}a_{P21/c} \approx 9.43$ Å, $\tilde{b} \equiv \frac{1}{2}b_{P21/c} \approx 5.03$ Å, $\tilde{c} \equiv c_{P21/c} \approx 7.82$ Å, and $\beta = 86.6(2)°$. We have also assumed all the Dy sites to be crystallographically equivalent and positioned at (0,0,1/4) and (0,0,3/4). The above construct is oversimplified, but a model for the magnetic structure based on these positional coordinates accounts reasonably well for the experimental data.

A good consistency test for our experiments is an analysis of Bragg intensities measured in h-scans along $(h,0,0)$. These were corrected for absorption and resolution effects and are plotted against momentum transfer in Fig. 6 (open circles). The experimental Q dependence is in good agreement with a theoretical prediction for the square of the form factor of a free Dy^{3+} ion,[21] shown as solid line in Fig. 6.

The models used for the analysis of the magnetic structure assumed a parallel alignment of nearest-neighbor spins along the b and c axes. The nearest neighbors along a were assumed to have antiparallel spins. Three models were considered, with spins lying in the ac, bc, and ab planes. Only the last model was found to be consistent with the data. The tilt of the spins in the ab plane with respect to the b axis and an overall scaling factor were the only two adjustable parameters. These were refined to best fit the experimental intensities of 17 magnetic Bragg peaks of the type $(h,0,l)$ (h-odd,

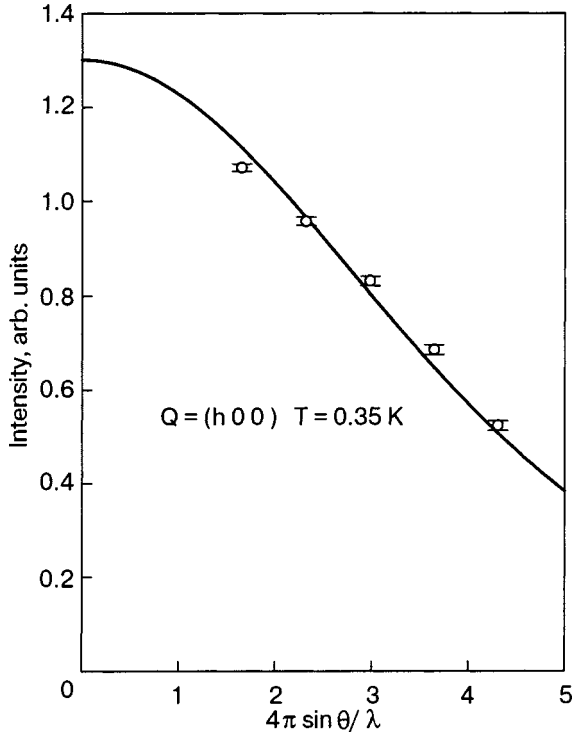

FIG. 6. Intensity of $(h,0,0)$ magnetic Bragg reflections measured in $CsDy(MoO_4)_2$ as a function of momentum transfer (open circles). The data were corrected for absorption and resolution effects. The solid line represents the square of the magnetic form factor for a free Dy^{3+} ion.

TABLE II. List of calculated I_{calc} and experimentally observed I_{obs} intensities for the 17 independent magnetic reflections in $CsDy(MoO_4)_2$ at $T=0.35$ K.

$(h0l)P2_1/c$	I_{obs}	σ_{obs}	I_{calc}
3 0 −2	3379	34	3681
5 0 −2	3092	49	3140
9 0 −2	2228	121	2135
11 0 −2	1720	110	1704
3 0 4	3511	219	2656
5 0 4	2403	267	2362
7 0 4	2384	1328	2014
1 0 2	4568	50	4110
3 0 2	3726	56	3681
5 0 2	3020	84	3140
9 0 2	1937	164	2135
11 0 2	1461	71	1707
5 0 0	3040	23	3114
7 0 0	2716	25	2701
9 0 0	2359	29	2254
11 0 0	1947	28	1819
13 0 0	1486	30	1427

l-even) that were measured in h-scans to compensate for the anomalous broadening of magnetic peaks in the a^* direction. Measurements were done separately for each monoclinic domain and corrected for resolution and absorption effects. The results of the refinement are summarized in Table II. Considering the limiting systematic errors arising from severe resolution and absorption effects, a reasonably good fit to the experimental data was obtained.

The refined value for the angle between the spin direction and the b axis is $17.7(0.5)°$. The resulting spin structure is visualized in the top inset in Fig. 5. The absolute value of the magnetic moment residing on the Dy sites was obtained through normalizing the magnetic Bragg intensities by those of several $(h,0,0)$ nuclear peaks. The structure factors for the latter were calculated from the known atomic fractional coordinates. At $T=0.35$ K the Dy^{3+} moment was estimated to be $M_{Dy}\approx 6.8\mu_B$. This is to be compared to $M_{Dy}=g_L J\mu_B \approx 10\mu_B$ for a free ion.

3.3. Magnetic critical scattering

Generous magnetic neutron scattering intensities allowed us to study the magnetic critical scattering, which could be plainly seen at temperatures up to $T=1.8$ K. All of the measurements were performed on the $(2.5,0,0)_{Pccm}$ magnetic Bragg reflection in a two-axis mode. Scans along $(h,0,0)$ and $(2.5,0,l)$ were analyzed by first subtracting (point by point) the background measured at $T=4$ K and then fitting the data to Voigt profiles. Some typical scans are shown in Fig. 7a. The width of the Gaussian component of the Voigt function was fixed to the experimental Q resolution determined from measurements on nearby nuclear Bragg reflections. The Lorentzian component represents the classical Ornstein—Zernike form for the energy-integrated neutron cross section:[22,23]

$$\frac{d\sigma}{d\Omega}=\frac{AT}{\kappa^2+q^2}, \quad \chi=A/\kappa^2. \tag{1}$$

The Lorentzian widths κ (reciprocal correlation lengths) and temperature-adjusted amplitudes A were refined to best fit the data. The solid lines in Fig. 7a show the results of such fits. The reciprocal correlation lengths along a^* and c^*, κ_a and κ_c, respectively, are plotted against $(T-T_N)/T_N$ in Fig. 7b using $T_N=1.36$ K. The same figure shows the temperature evolution of the staggered susceptibility χ. As shown by solid lines in Fig. 7b, the experimental temperature dependences were analyzed using power-law fits to the data. We have obtained the following values for the critical exponents: $\gamma=1.01\pm0.04$, $\nu_a=0.35\pm0.04$, and $\nu_c=0.94\pm0.07$.

4. DISCUSSION

The distinguishing features of rare-earth double molybdates in general, and $CsDy(MoO_4)_2$ in particular, are the relatively low crystallographic symmetry and rather high magnetic moments associated with the rare-earth ions. These peculiarities make single-ion crystal-field effects extremely important and result in a huge anisotropy of magnetic susceptibility.[7,8] The site symmetry of the Dy^{3+} ions (the ground term $^6H_{15/2}$) in the low-temperature phase is low enough for the ground state to be a single Kramers doublet with $J=\pm 15/2$ (Ref. 8). In other words, the Dy^{3+} are expected to be Ising magnetic centers. Indeed, according to EPR studies,[24] there are two magnetically inequivalent sites

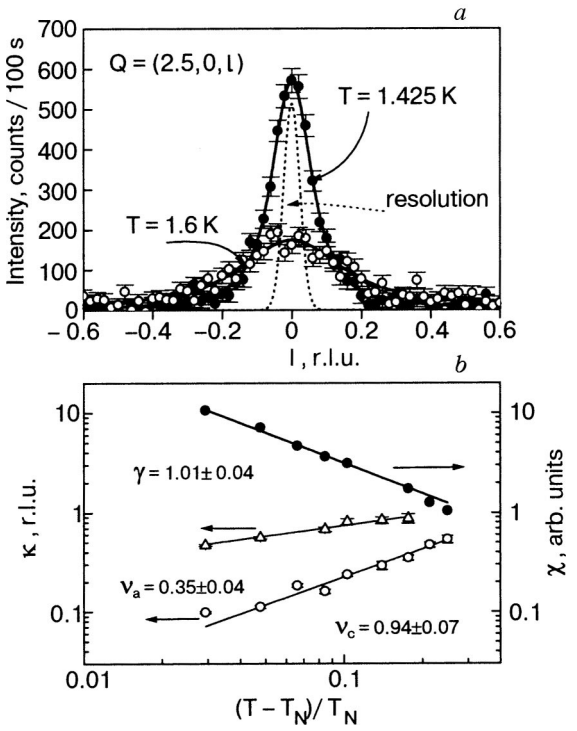

FIG. 7. Magnetic critical scattering measured in $CsDy(MoO_4)_2$ above $T_N = 1.36$ K. (a) Example two-axis scans across the magnetic zone center. The background has been subtracted, as described in the text. The solid lines represent fits with Lorentzian profiles, convolved with the Gaussian experimental resolution (dotted line). (b) Measured temperature dependence of the staggered susceptibility χ (solid circles) and reciprocal magnetic correlation length κ along the a (triangles) and c (open circles) crystallographic axes. The solid lines are power-law fits to the data.

with similar principal values of the effective g-factor tensor ($g_{a'} = 3.7 \pm 0.2$, $g_{b'} = 13.4 \pm 0.5$, $g_{c'} = 1 \pm 0.5$). The g-tensor principal axis a' is reportedly tilted by $\approx \pm 10°$ with respect to the a direction in the ab plane, and b' forms an angle of no more than $\approx \pm 5°$ with the b axis in the bc plane. These two g-tensor orientations presumably correspond to the two crystallographically inequivalent Dy^{3+} sites that are identified in this work.

The crystal-field separation of Dy^{3+} Kramers doublets in $CsDy(MoO_4)_2$ is expected to be much larger than the ordering temperature, i.e., than the characteristic energy of magnetic interactions. The direction of magnetic moments in the ordered phase is therefore dictated by the orientations of single-ion easy axes. From our analysis of the magnetic diffraction data we conclude that the moments lie in the ab crystallographic plane and are tilted by 17° with respect to the b axis. It is important to emphasize, though, that since two inequivalent magnetic sites are present, the actual structure should be noncollinear, and that the collinear model is no more than an approximation.

The 2D Ising character of the material becomes apparent in its critical behavior. The technique used to measure the indices ν and γ relies on the so-called static approximation,[22] i.e., on the assumption that the incident neutron energy in two-axis experiments is much larger than the characteristic energy width of critical scattering. Fortunately, for Ising systems the approximation is excellent, since the time scale of critical fluctuations is infinitely long. The in-plane correlation length exponent $\nu_c = 0.94$ and the order-parameter exponent $\beta = 0.17$ measured in $CsDy(MoO_4)_2$ are reasonably close to the exact characteristics of a 2D Ising magnet, where $\beta = 0.125$ and $\nu = 1$. Such behavior is consistent with the layered structure of $CsDy(MoO_4)_2$.

Other data obtained in the present study indicate that the temperature dependences of magnetic characteristics of $CsDy(MoO_4)_2$ are more complicated than simple 2D Ising behavior. In particular, the measured temperature dependence of the order parameter deviates from the exact results of Onsager in a wide temperature range (Fig. 5, bottom inset). An even more obvious discrepancy is revealed in the behavior of the critical index γ. The experimental value $\gamma = 1$ is the same as in Ginsburg–Landau theory and quite different from that for a 2D Ising magnet, where $\gamma = 1.75$ is expected. Note that in well-established 2D Ising materials, such as K_2CoF_4 (Refs. 25 and 26) and Rb_2CoF_4 (Refs. 27–29), all three critical indices β, γ, and ν are in good agreement with theory.

We tentatively propose that the main reason for any deviations from 2D Ising behavior in $CsDy(MoO_4)_2$ are due to dipolar interactions. As indicated in experiments and calculations on related molybdates, dipolar coupling of Ising chains or planes may be responsible for experimentally observable short-range effects[6,30] and may even drive the magnetic phase transition, as, for example, in $KEr(MoO_4)_2$ (Ref. 5). For $CsDy(MoO_4)_2$ the in-plane interactions are relatively strong and are, most likely, of exchange origin. On the other hand, interplane coupling is much weaker and yields only short-range order between the planes. At $(T - T_N)/T_N = 0.03$, for instance, the interplane magnetic correlation length amounts to only a few lattice repeats [Fig. 7b]. All relevant interactions, but the weak interplane coupling most of all, should have a significant contribution from dipolar effects. The latter must be enhanced by i) large magnetic moments of the Dy^{3+} ions, and ii) *ferromagnetic* correlations in the planes. Indeed, the ordered moments are nearly parallel to the planes and generate a large magnetic field that favors antiparallel spin alignment in adjacent planes. If the correlations within the planes were antiferromagnetic, the dipolar field would decay much more rapidly with distance. As has been experimentally confirmed[31] for $LiTbF_4$, dipolar magnets fall into a universality class different from that of exchange systems, and this may be responsible for the observed values of critical indices in $CsDy(MoO_4)_2$.

Finally, let us comment on the observed anomalous a^*-width of the magnetic Bragg reflections. The effect can be easily explained. Critical slowing down of spin fluctuations is enhanced in Ising systems. On relatively fast cooling through T_N the short-range magnetic correlations present in the critical regime are ''frozen'' in the ordered phase. Since in-plane spin correlations are much stronger that interplane ones, the broadening of magnetic Bragg peaks is most pronounced in the direction normal to the planes.

CONCLUSION

In summary, the present investigations enabled us to determine the crystal structure of two low-temperature structural phases (below 120 K and below 40 K), and suggest an approximate magnetic structure of the $CsDy(MoO_4)_2$. A more precise model of the magnetic structure calls for further

investigations. In the ordered state the order-parameter critical exponent $\beta = 0.17(0.01)$, the in-plane correlation length exponent $\nu = 0.94(0.07)$, and the staggered susceptibility critical index $\gamma = 1.01(0.04)$ were determined. Comparing these results to the exact solution for a 2D Ising magnet, we conclude that, although 2D behavior is apparent in $CsDy(MoO_4)_2$, there are deviations from the simple 2D Ising model. One of the possible reasons is the influence of the dipole–dipole interplane interaction.

Work at ORNL and BNL was carried out under DOE Contracts No. DE-AC05-00OR22725 and DE-AC02-98CH10886, respectively.

*E-mail: khatsko@ilt.kharkov.ua
[a)]Present address: Solid State Division, Oak Ridge National Laboratory, Oak Ridge, TN 37830, USA
[b)]Present address: Bragg Institute, Building 58, Australian Nuclear Science and Technology Organization, PMB 1, Menai NSW 2234, Australia

[1] P. V. Klevtsov and R. F. Klevtsova, Sov. Phys. Crystallogr. **15**, 395 (1970).
[2] P. V. Klevtsov, R. F. Klevtsova, and A. V. Demenev, Sov. Phys. Crystallogr. **17**, 474 (1972).
[3] V. A. Vinokurov and P. V. Klevtsov, Sov. Phys. Crystallogr. **17**, 127 (1972).
[4] B. M. Wanklyan and F. R. Wonder, J. Cryst. Growth **43**, 93 (1978).
[5] A. G. Anders, S. V. Volotskii, and O. E. Zubkov, Fiz. Nizk. Temp. **20**, 137 (1994) [Low Temp. Phys. **20**, 110 (1994)].
[6] A. G. Anders, S. V. Volotskii, and O. E. Zubkov, Fiz. Nizk. Temp. **20**, 131 (1994) [Low Temp. Phys. **20**, 105 (1994)].
[7] E. N. Khatsko and A. S. Cherny, Fiz. Nizk. Temp. **11**, 540 (1985) [Sov. J. Low Temp. Phys. **11**, 296 (1985)].
[8] E. N. Khatsko and A. S. Cherny, Ferroelectrics **130**, 321 (1992).
[9] E. N. Khatsko, A. S. Cherny, and A. I. Kaplienko, Fiz. Nizk. Temp. **19**, 1217 (1993) [Low Temp. Phys. **19**, 864 (1993)].
[10] A. I. Zvyagin, S. D. El'chaninova, T. S. Stetsenko, L. N. Pelikh, E. N. Khatsko, V. I. Startsev, V. P. Soldatov, and A. I. Osetskii, Fiz. Nizk. Temp. **1**, 79 (1975) [Sov. J. Low Temp. Phys. **1**, 39 (1975).
[11] V. I. Kut'ko, Y. N. Kharchenko, A. A. Stepanov, and N. M. Nesterenko, Fiz. Nizk. Temp. **20**, 361 (1994) [Low Temp. Phys. **20**, 288 (1994)].
[12] A. M. Pshisukha, A. S. Cherny, and A. I. Zvyagin, Fiz. Nizk. Temp. **1**, 473 (1975) [Sov. J. Low Temp. Phys. **1**, 233 (1975)].
[13] A. M. Pshisukha, A. I. Zvyagin, and A. S. Cherny, Fiz. Nizk. Temp. **2**, 339 (1976) [Sov. J. Low Temp. Phys. **2**, 170 (1976)].
[14] R. F. Klevtsov and S. V. Borisov, Sov. Phys. Dokl. **12**, 1095 (1968).
[15] P. V. Klevtsov and L. P. Kozeeva, Dokl. Akad. Nauk SSSR **185**, 571 (1969).
[16] R. F. Klevtsova, V. A. Vinokurov, and P. V. Klevtsov, Sov. Phys. Crystallogr. **17**, 240 (1972).
[17] S. D. Elchaninova, V. P. Kuznetsov, *et al.*, Ferroelectrics **175**, 85 (1996).
[18] Preliminary structural refinement gives the following fractional cell coordinates for Dy in the LT-1 phase ($T = 50$ K): (0.25,0,0.26561). In the "parent" *Pccm* structure the symmetry of the Dy site is higher: (0.25,0,0.25).
[19] E. N. Khatsko and A. S. Cherny, Fiz. Nizk. Temp. **7**, 1048 (1981) [Sov. J. Low Temp. Phys. **7**, 509 (1981)].
[20] There are two inequivalent Dy sites in the LT-2 phase ($T = 15$ K): Dy1 (0.7486,0.2503,0.3057) and Dy2 (0.7484,−0.2496,0.2597).
[21] P. J. Brown, in *International Tables for Crystallography*, A. J. C. Wilson (ed.), Kluwer Academic Publishers, London (1995), Vol. C, Chap. 4.4.5.
[22] M. F. Collins, in *Magnetic Critical Scattering*, Oxford University Press, Oxford (1989).
[23] R. J. Birgeneau, J. J. Skalyo, and G. Shirane, Phys. Rev. B **3**, 1736 (1971).
[24] A. G. Anders, V. S. Bondarenko, A. Feher, and A. Orendacheva, Fiz. Nizk. Temp. **22**, 1042 (1996) [Low Temp. Phys. **22**, 794 (1996)].
[25] H. Ikeda and K. Hirakawa, Solid State Commun. **14**, 529 (1974).
[26] H. R. A. Cowley, M. Hagen, and D. P. Belanger, J. Phys. C **17**, 3763 (1984).
[27] E. Samuelsen, Phys. Rev. Lett. **31**, 936 (1973).
[28] H. Ikeda, M. Suzuki, and M. T. Hutchings, J. Phys. Soc. Jpn. **46**, 1153 (1979).
[29] M. Hagen and D. M. Paul, J. Phys. C **17**, 5605 (1984).
[30] E. N. Khatsko, A. S. Cherny, M. I. Kobets, V. A. Pashchenko, A. I. Kaplienko, A. A. Curskas, V. V. Mitkevich, and S. M. Tret'yak, Fiz. Nizk. Temp. **20**, 1022 (1994) [Low Temp. Phys. **20**, 805 (1994)].
[31] J. Als-Nielsen, Phys. Rev. Lett. **37**, 1161 (1976).

This article was published in English in the original Russian journal. Reproduced here with stylistic changes by AIP.

Coercive properties of a Gd/Si/Co multilayer film with a compensation point

D. N. Merenkov,* S. L. Gnatchenko, A. B. Chizhik, and Yu. A. Shakhaeva

B. Verkin Institute for Low Temperature Physics and Engineering, National Academy of Sciences of Ukraine, pr. Lenina 47, Kharkov 61103, Ukraine

M. Baran and R. Szymczak

Institute of Physics, Polish Academy of Sciences, Al. Lotnikow 32/46, 02-688 Warsaw, Poland

V. O. Vas'kovskiy and A. V. Svalov

Urals State University, pr. Lenina 51, Ekaterinburg 620083, Russia
(Submitted July 2, 2003; revised August 29, 2003)
Fiz. Nizk. Temp. **30**, 193–197 (February 2004)

The temperature dependence of the coercive field H_c is determined for a multilayer $[\text{Gd75 Å/Si5 Å/Co30 Å/Si5 Å}]_{20}$ film with ferrimagnetic ordering of the magnetic moments of the cobalt and gadolinium layers. The maximum value of H_c is observed at a temperature of around 118 K, which corresponds to the compensation point of the film. It is established that in the entire interval of temperatures studied, the variation of the coercive field is due to the variation of the spontaneous magnetization. © *2004 American Institute of Physics.* [DOI: 10.1063/1.1645165]

Multilayer films grown on the basis of alternating nanoscopic layers of a rare-earth metal (REM) and a $3d$ transition metal (TM) are attracting attention primarily as model objects for studying fundamental physical phenomena. By studying them, one can obtain information about the nature of the exchange coupling between magnetic metals of different types. It has been established that an external field can induce the formation of noncollinear surface phases in multilayer films.[1,2] On the other hand, these films may find application in magnetooptical recording devices and also as ''pinning'' layers in so-called spin-valve structures with giant magnetoresistance (GMR).[3] It is known that a necessary condition for the appearance of the GMR effect in such structures is a layer-by-layer magnetization reversal, which occurs on account of the different coercive force of the different components of the structure. Devices working on the basis of the GMR effect are used, for example, as sensitive probes or heads for magnetic recording systems.

In multilayer REM/TM films the magnetic moments of adjacent layers lie in the plane of the film and are ordered antiparallel owing to the antiferromagnetic exchange coupling on the interface between layers. Therefore, in such films one can observe effects which are characteristic for ferromagnets—in particular, compensation of the magnetization. However, the properties of artificial magnetic superlattices obtained on the basis of nanoscopic layers of an REM and a TM can differ appreciably from the properties of conventional ferrimagnets. The superlattice period is usually much greater than the unit cell parameter of any known ferrimagnet. At the same time, the antiferromagnetic exchange in multilayer films is localized in narrow regions adjacent to the interfaces between layers, and the magnetic order in the rest of the film is maintained by the ferromagnetic intralayer exchange interaction. Therefore, a decrease in the antiferromagnetic exchange, an increase in the superlattice period, and also differences in the structural properties of the layers of the film can promote the magnetization reversal of individual layers of its rare-earth and transition-metal subsystems. In this case the coercive properties of the film will differ significantly from those of ordinary ferrimagnets.

It is known[4,5] that near the compensation point of typical ferrimagnets, in particular, of REM–TM alloys, there is a sharp increase in the coercive field H_c, which is one of the most important characteristics of magnetic materials. Nevertheless, the temperature dependence of H_c observed in multilayer films is of a different character. For example, in Gd/Co films[6] the value of H_c does not vary with temperature; in Dy/Co films[7] heating causes a weak growth of H_c for $T > T_{\text{comp}}$ (where T_{comp} is the compensation temperature of the particular film), while for $T < T_{\text{comp}}$ the coercive field is

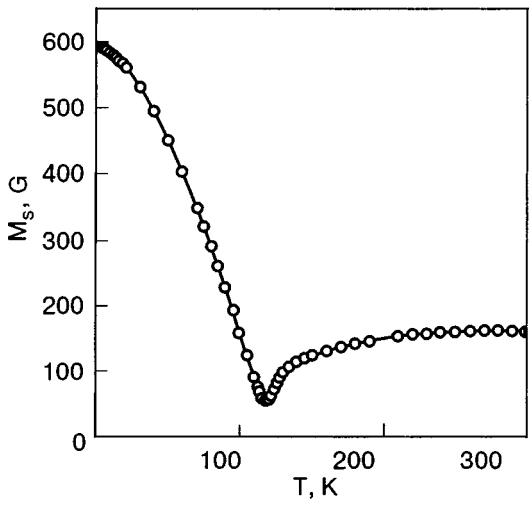

FIG. 1. Temperature dependence of the spontaneous magnetization of a $[\text{Gd75 Å/Si5 Å/Co30 Å/Si5 Å}]_{20}$ film, measured in an external field $H = 500$ Oe. This film had a compensation temperature $T_{\text{comp}} \simeq 118$ K.

practical independent of temperature. In Gd/Co films having different ratios of the layer thicknesses and lacking a compensation point at temperatures of 5–300 K (Ref. 8) it is observed that the values of the coercive field and spontaneous magnetization M_s are related. In view of this it is undoubtedly of interest to investigate further the coercive properties and the possibilities for their control in multilayer REM/TM films. It should also be noted that the properties of REM/TM films with nonmagnetic spacer layers deposited between the magnetic layers have been little studied, although it is known that variation of the thickness of the spacers leads to a shift of the compensation temperature.[9] A nonmagnetic spacer of silicon weakens the antiferromagnetic interlayer exchange in the film under study by more than an order of magnitude.[10]

In the this paper we report the results of investigations of the temperature dependence of the coercive field of a $[\mathrm{Gd75\ \AA/Si5\ \AA/Co30\ \AA/Si5\ \AA}]_{20}$ multilayer film. The film was grown by rf ion sputtering on a glass substrate at a base pressure of 10^{-6} torr and a working-gas (Ar) pressure of 10^{-4} torr. The deposition took place at a temperature not above 100 °C. The rate of deposition of Gd, Co, and Si, according to the results of a preliminary calibration, were 1, 0.4, and 0.3 Å/s, respectively.

In this study we used a magnetooptic method based on the use of the longitudinal Kerr effect. The magnetic field was oriented parallel to the film in the plane of incidence of a He–Ne laser beam (wavelength 633 nm). The angle of rotation Φ of the plane of polarization of the reflected light was measured as a function of external field. In this geometry the Kerr rotation of the plane of polarization is proportional to the magnetization component lying in the plane of the film parallel to the plane of incidence of the light. A helium cryostat was used in the experiments. The sample was placed on a cold finger in vacuum inside a superconducting solenoid. Measurements of the magnetization of the

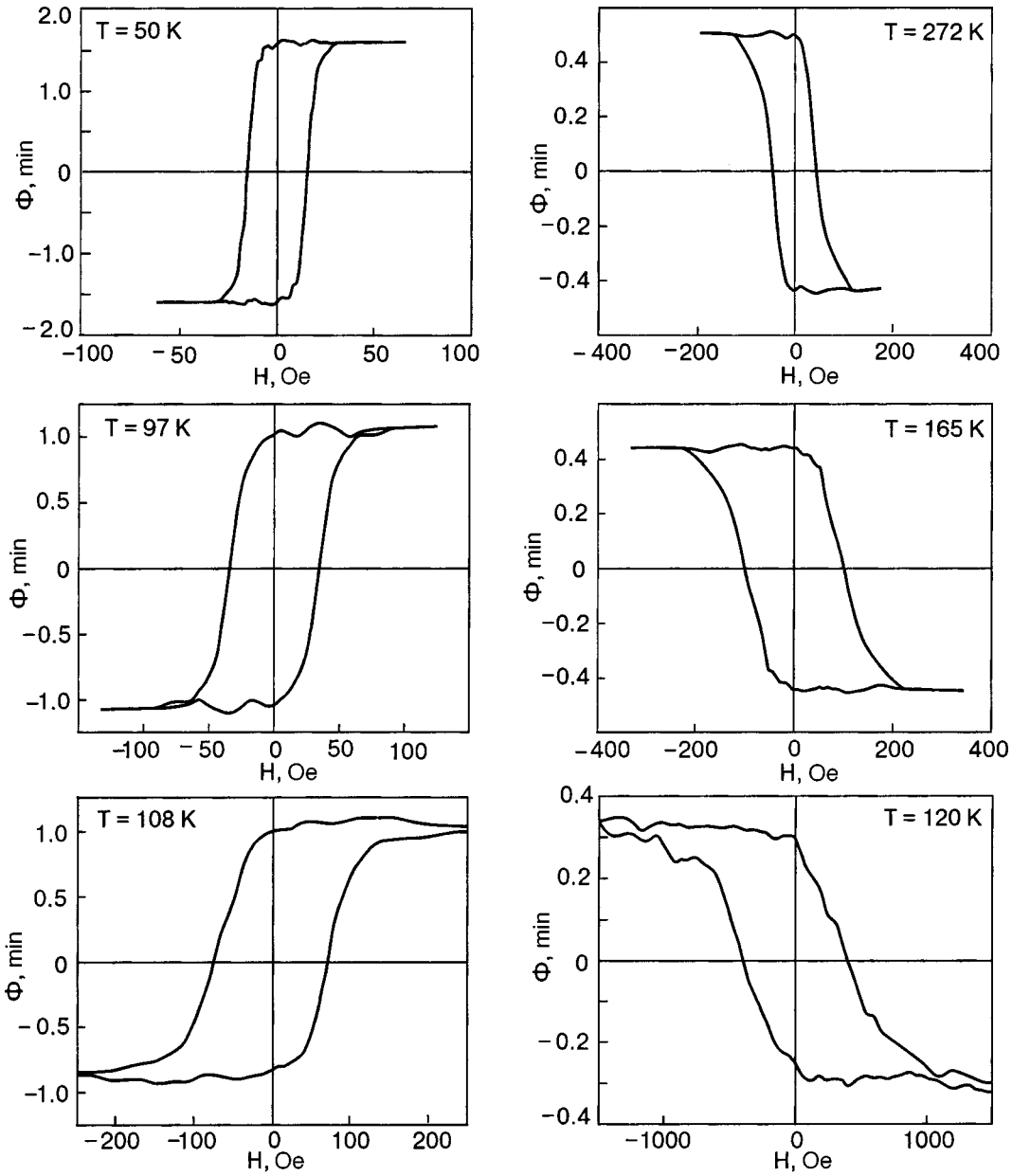

FIG. 2. Hysteresis loops measured by a magnetooptic method in a $[\mathrm{Gd75\ \AA/Si5\ \AA/Co30\ \AA/Si5\ \AA}]_{20}$ film at various temperatures.

film were also made on an MPMS-5 Quantum Design SQUID magnetometer.

Figure 1 shows the temperature dependence of the spontaneous magnetization M_s measured on the SQUID magnetometer; it has a pronounced minimum at $T \simeq 118$ K associated with the compensation of the magnetic moments of the Gd and Co layers. The observed nonzero minimum value of the magnetization may be due to some nonuniformity of the film and also to the onset of a noncollinear phase near T_{comp} in the field $H = 500$ Oe in which the magnetization measurements were made.[10] The spontaneous magnetization falls off as the film is heated from 5 K to the compensation temperature and then increases for $T > T_{\text{comp}}$. The sharpest change in M_s occurs near T_{comp}.

Figure 2 shows the field dependence of the Kerr rotation $\Phi(H)$ obtained at different temperatures for the film under study. The magnetooptic curves shown carry information about the magnetization reversal in a few layers near the surface. However, those curves are practically no different from the $M(H)$ curves measured on the SQUID magnetometer, which reflect the magnetization reversal process in the entire sample. The rather simple form of the $M(H)$ and $\Phi(H)$ loops is evidence that the cobalt and gadolinium layers forming the magnetic structure of the film are not independent during magnetization reversal. At a fixed temperature these loops are close in shape and practically identical in width within the measurement error. It should be concluded that magnetization reversal occurs uniformly over the entire thickness of the film, including its surface layers. Thus the value of the coercive field of a film is quite correctly determined from the half-width of the magnetooptic hysteresis loop at $\Phi = 0$.

It should be noted that the sign of the Kerr rotation is different at temperatures below and above 118 K. This is due to the dominance of the contribution of the transition metal to the Kerr effect. Below the compensation temperature the magnetic moment of the cobalt layer, m_{Co}, is smaller than that of the gadolinium layer, m_{Gd}. Because of this, it is directed counter to the external field. At $T > T_{\text{comp}}$ the situation is reversed: m_{Co} is greater than m_{Gd} and is codirectional with the external field. Accordingly, a change in the sign of the magnetooptic rotation occurs at the transition through the compensation point. Such a change in the sign of rotation has been observed[1] for multilayer Gd/Fe films.

Figure 3 shows the temperature dependence of the coercive field of a film from the magnetooptic measurements. The value of H_c increases as the compensation point is approached from both the low- and high-temperature sides. The $H_c(T)$ curve has a pronounced maximum near 118 K.

As we know, magnetization reversal occurs by nucleation of domains of an energetically favorable phase and the spreading of these domains to the whole volume of the sample. The coercivity, accordingly, is related to the nucleation process and to the pinning of the domain walls at defects. The expression for the coercive field can be written as[11,12]

$$H_c = \frac{\alpha}{M_s} - NM_s, \tag{1}$$

where the first term is due to energy losses in the formation of a nucleus and motion of the domain wall, and the second is due to demagnetizing fields of the nucleus (N is the demagnetizing factor). If nucleation is the dominant process, then one can assume that, to within a numerical coefficient, $\alpha = \sigma / v^{1/3}$, where σ is the domain-wall energy and v is the critical volume of a nucleus. If, on the contrary, the main contribution to the coercivity comes from the pinning of domain walls on structural defects, then the coercive field is also described by formula (1) but with α being the energy barrier surmounted by the domain wall in its motion.

It has been shown previously[8] that the temperature dependence of the coercive field of two thin multilayer films, $[\text{Gd30 Å/Co30 Å}]_{20}$ and $[\text{Gd30 Å/Co38 Å}]_{10}$, which do not have compensation points, is determined by the variation of their spontaneous magnetization. The curves of H_c/M_s versus $1/M_s^2$ constructed with the use of the experimental data are straight lines with slopes determined by the coefficients α_1 (for the first film) and α_2 (for the second). The values of α_1 and α_2 remained constant over the entire tem-

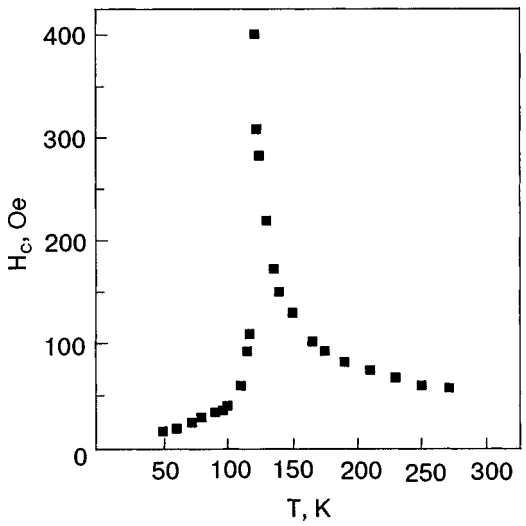

FIG. 3. Temperature dependence of the coercive field of a $[\text{Gd75 Å/Si5 Å/Co30 Å/Si5 Å}]_{20}$ film.

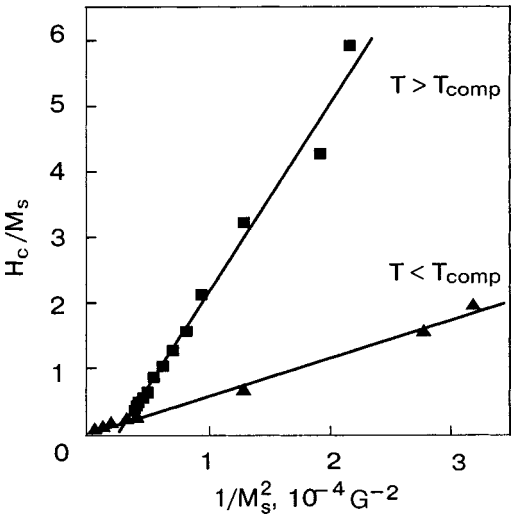

FIG. 4. The dependence of H_c/M_s on $1/M_s^2$ for a $[\text{Gd75 Å/Si5 Å/Co30 Å/Si5 Å}]_{20}$ film, from experimental measurements at $T < T_{\text{comp}}$ and $T > T_{\text{comp}}$.

perature interval investigated, from 25 to 300 K, and had the values: $\alpha_1 \approx 0.7 \times 10^4$ erg/cm^3 and $\alpha_2 \approx 8.2 \times 10^4$ erg/cm^3.

Figure 4 shows the dependence of H_c/M_s on $1/M_s^2$ for a Gd/Si/Co film. As can be seen in the figure, all of the points plotted are well approximated by straight lines. Thus a linear dependence of H_c/M_s on $1/M_s^2$ is observed on both sides of the compensation temperature. This allows us to conclude: 1) the variation of the coercive field of this film, which has a compensation point, is determined mainly by the variation of the spontaneous magnetization; 2) the value of α changes only at the transition through the compensation point and remains constant on either side of that point: $\alpha_{T<118\ \mathrm{K}} \approx 0.6 \times 10^4$ erg/cm^3, $\alpha_{T>118\ \mathrm{K}} \approx 3.5 \times 10^4$ erg/cm^3. We note the coincidence in order of magnitude of the values of α_1 and $\alpha_{T<118\ \mathrm{K}}$, on the one side, and the values of α_2 and $\alpha_{T>118\ \mathrm{K}}$, on the other. In the former case the magnetic moment of the gadolinium layer, m_{Gd}, exceeds the magnetic moment m_{Co} of the cobalt layer in both films, while in the latter case $m_{\mathrm{Gd}} < m_{\mathrm{Co}}$.

The Gd/Si/Co film has a nonmagnetic silicon spacer, appreciably lowering the antiferromagnetic exchange, which is localized at the boundaries of the layers. However, we did not establish any experimental facts indicating a layer-by-layer magnetization reversal of the film. The temperature dependence of the coercive field of the investigated multilayer film with a compensation point is due to the variation of the spontaneous magnetization of the film. The coercive field reaches a maximum value in the region of the compensation point. In this regard the film that we investigated is fundamentally no different from ordinary ferrimagnets. Therefore, one way to effectively influence the coercive properties of thin REM/TM multilayer films is to deposit nonmagnetic spacers between magnetic layers and also, within certain limits, to vary the thickness of these spacers, which leads to changes in the temperature dependence of the spontaneous magnetization of the film and in the compensation temperature.

V. O. Vas'kovskiy and A. V. Svalov thank the Ministry of Education of the Russian Federation for partial support of this study under Grant T02-05.1-3153.

*E-mail: merenkov@ilt.kharkov.ua

[1] W. Hahn, M. Loewenhaupt, Y. Y. Huang, G. P. Felcher, and S. S. P. Parkin, Phys. Rev. B **52**, 16041 (1995).
[2] S. L. Gnatchenko, A. B. Chizhik, D. N. Merenkov, V. V. Eremenko, H. Szymczak, R. Szymczak, K. Fronc, and R. Zuberek, J. Magn. Magn. Mater. **186**, 139 (1998).
[3] A. V. Svalov, P. A. Savin, G. V. Kurlyandskaya, I. Gutiérrez, and V. O. Vas'kovskiy, Zh. Tekh. Fiz. **72**(8), 54 (2002) [Tech. Phys. **47**, 987 (2002)].
[4] P. Chaudhari, J. J. Cuomo, and R. J. Gambino, Appl. Phys. Lett. **22**, 337 (1973).
[5] R. C. Taylor, J. Appl. Phys. **47**, 1164 (1976).
[6] D. J. Webb, R. G. Wamsley, K. Parvin, P. H. Dickinson, T. H. Geballe, and R. M. White, Phys. Rev. B **32**, 4667 (1985).
[7] Z. S. Shahn and P. Sellmyer, Phys. Rev. B **42**, 10433 (1990).
[8] S. L. Gnatchenko, A. B. Chizhik, D. N. Merenkov, H. Szymczak, L. T. Baczewski, A. Wawro, and H. Gamari-Seale, J. Appl. Phys. **84**, 5105 (1998).
[9] K. Takanashi, H. Fujimori, and H. Kurokawa, J. Magn. Magn. Mater. **126**, 242 (1993).
[10] D. N. Merenkov, A. B. Chizhik, S. L. Gnatchenko, M. Baran, R. Szymczak, V. O. Vas'kovskiy, and A. V. Svalov, Fiz. Nizk. Temp. **27**, 188 (2001) [Low Temp. Phys. **27**, 137 (2001)].
[11] D. Givord, P. Teneaud, and T. Viadeu, IEEE Trans. Magn. **MAG-24**, 1921 (1988).
[12] D. W. Taylor, V. Villas-Boas, Q. Lu, M. F. Rossignol, F. P. Missell, D. Givord, and S. Hirosawa, J. Magn. Magn. Mater. **130**, 225 (1994).

Translated by Steve Torstveit

Electron paramagnetic resonance in powder samples of metalorganic copper compounds

O. V. Kravchyna, A. I. Kaplienko, and A. G. Anders*

B. Verkin Institute for Low Temperature Physics and Engineering, National Academy of Sciences of Ukraine, pr. Lenina 47, kharkov 61103, Ukraine

M. Orendáč, A. Orendáčova, M. Kajňaková, and A. Feher**

Centre of Low Temperature Physics, Faculty of Sciences, P. J. Šafárik University and Institute of Experimental Physics, Slovak Academy of Sciences, Park Angelinum 9, 04154 Košice, Slovakia

(Submitted July 4, 2003)
Fiz. Nizk. Temp. **30**, 198–204 (February 2004)

The EPR spectra of powder samples of a number of metalorganic compounds containing Cu^{2+} ions are investigated. These compounds are characterized by the presence of identical chains of octahedra forming the local environment of Cu^{2+}, but they differ strongly in their interchain ligand structure. The resonance absorption bands permit determination of the components of the effective g factor and linewidth of individual powder particles and also their temperature dependence. It is found that the orbital singlet $|x^2-y^2\rangle$ is the ground state of the copper ion in all the compounds, and the exchange interaction parameters in them are estimated. The maximum exchange is observed in the system with the simplest geometry of the interchain structure in the series of compounds studied. © *2004 American Institute of Physics.* [DOI: 10.1063/1.1645166]

INTRODUCTION

Crystals of metalorganic compounds often have pronounced chains or planes of metallic ions with a comparatively simple local environment while at the same time the interchain or interplane space is filled with large fragments of organic complexes. If the metal ions belong to an element of a transition group, this can lead to the formation of a quasi-one-dimensional or quasi-two-dimensional magnetic system with a high degree of low-dimensionality. Such metalorganic complexes are of interest for magnetic, coordination-chemical, biological, biochemical, etc. studies, but the use of the informative magnetic resonance methods for this has a certain peculiarity because such compounds are generally synthesized in the form of finely disperse powders.

In this paper we report an EPR study of a number of metalorganic complexes of copper. The members of this series of compounds are of the general structure formula $[Cu(SO_4)L(H_2O)_2]$, among which are $[Cu(SO_4)(C_2H_8N_2)\times(H_2O)_2]$—henceforth referred to as Cu(en), $[Cu(SO_4)\times(C_6H_6N_2O)_2(H_2O)_2]$—Cu(nad), and $[Cu(SO_4)\times(C_{12}H_8N_2)(H_2O)_2]$—Cu(phen). These compounds have a very similar local environment of the paramagnetic ion and differ markedly in the structure of the organic ligands. Analysis of the magnetoresistive properties of such a series of compounds can reveal the common traits of the EPR spectra formed by the local environment and to find correlations in the differences of their structures and magnetic characteristics.

The goal of this study was to compare the properties of the paramagnetic centers in powder samples of the given compounds in order to clarify both the influence of deformations of the local environment on the parameters of the resonance spectrum and the role of the ligand structures in the forming of the interactions between magnetic centers.

STRUCTURAL CHARACTERISTICS OF THE SYSTEMS AND THE MEASUREMENT TECHNIQUES

Despite the substantial differences of the chemical composition, all of the compounds investigated here have a unified structural motif: the presence of chains of octahedra forming the local environment of divalent copper ions and lying along the direction of the smallest parameter of the cell. Octahedra in a chain are linked by apical oxygen ions O2, which also belong to tetrahedral sulfate groups SO_4^{-2}. The basal plane of the octahedra is formed by two oxygen

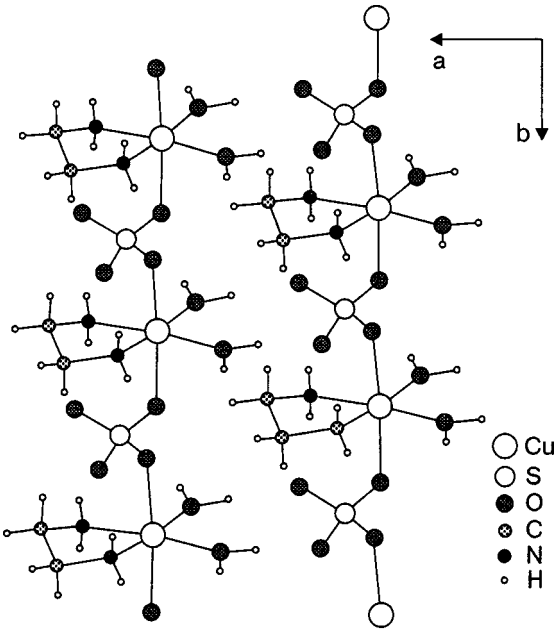

FIG. 1. Projection of the crystallographic structure of the compound Cu(en) on the *ab* plane.

atoms O1 belonging to two water molecules and two nitrogen atoms belonging to ligand groups. The position of the ions in the cell of the compound Cu(en), with the simplest ligand group, is shown schematically in Fig. 1, and the basic structural parameters of the compounds studied are presented in Table I.

The basal plane of the octahedra in all these compounds has a configuration close to square, with a distance from the central ion of ≈ 2 Å, while at the same time the distance to the vertex ions O2 is around 2.4–2.5 Å. The noticeable elongation of the octahedra along the direction of the chains should give rise to a substantial axial component of the intracrystalline field, increasing with the change in bond length $r_{\text{Cu-O2}}$. Consequently, the EPR spectra of the copper ion in these compounds, which are largely determined by the local environment, should have axial anisotropy, at least.

In contrast to the simple geometry of the octahedral chains, the interchain space in the compounds of this series is of rather complex construction. It is filled with fragments of molecules of the different compounds, which are five- and six-member rings of organic ligand groups. Under these conditions the interchain interaction can most likely be realized via a complex path of hydrogen bonds involving hydrogen atoms in water molecules or in the ligand groups. The value of this interchain coupling is not very amenable to prediction and must be determined experimentally.

The compounds Cu(nad) and Cu(phen) investigated in this study were synthesized in the form of fine-crystalline powders. For Cu(en) we first obtained small needle-shaped single crystals, for which we had previously studied the features of the low-temperature resonance spectra.[4] Powder samples were then prepared from them. A comparison of the data obtained on the two types of samples confirmed the correctness of our measurement technique and the method of processing of the results in working with powder samples.

The EPR spectra were studied in the wavelength range $\lambda \approx 4$ mm to increase the resolving power with respect to magnetic field. The appreciable intensity of the signal made it possible to record the integrated shape of the resonance absorption band. To avoid the influence of spin–lattice relaxation processes, which broaden the resonance line, the temperature range of the measurements was $\sim 2-30$ K. This made it possible to track the most interesting features due to interionic interaction processes in the low-temperature behavior of the resonance spectra. The precision of the temperature stabilization and measurement was 0.1 K on the interval 2.3–15 K and ~ 0.5 K for $T > 15$ K.

GENERAL CHARACTERISTICS OF THE RESONANCE SPECTRA OF POWDER SAMPLES

The EPR spectrum of a powder is a superposition of the spectra of small single-crystal particles with a random and equiprobable orientation with respect to the direction of the external magnetic field **H**. The intensity of the total envelope of a line at each point will be determined by both the number of particles having a given orientation and the transition probability for the given orientation.

In the case of axial symmetry of the intracrystalline field and, hence, of the resonance spectra of the individual particles, the angular dependence of the effective g factor has the form

$$g^2 = g_{\parallel}^2 \cos^2\theta + g_{\perp}^2 \sin^2\theta, \tag{1}$$

where $g_{\parallel} = g_z$, $g_{\perp} = g_x = g_y$, and θ is the angle between the direction of the external field and the axis of anisotropy. The transition probability in the case of a linearly polarized rf field is proportional to the quantity

$$K \sim g_{\perp}^2 [(g_{\parallel}/g)^2 + 1] \tag{2}$$

at small anisotropy of the g factor. The number of particles with axes of crystallographic anisotropy lying at an angle θ to the field direction is given by

$$dN = 2\pi N_0 \sin\theta d\theta, \tag{3}$$

where N_0 is the total number of particles in the sample.

For spectra with spin $S = 1/2$ one can use the basic resonance relation $h\nu = g\mu_B H'$, where H' is the resonance field, to introduce the fields

$$H_{\parallel} = h\nu/g_{\parallel}\mu_B \quad \text{and} \quad H_{\perp} = h\nu/g_{\perp}\mu_B, \tag{4}$$

which determine the boundaries of the powder spectrum with respect to field for the extreme orientations $\theta = 0$ and $\theta = \pi/2$, respectively. Here h is Planck's constant, ν is the working frequency, and μ_B is the Bohr magneton.

Then taking relations (2) and (3) into account, an expression for the field dependence of the intensity of the signal in an absorption band in which all the orientations are realized takes the form

$$I(H) \sim \int_0^{\pi/2} K f(H) \sin\theta d\theta, \tag{5}$$

where the resonance line shape of the individual particles $f(H)$ is assumed Lorentzian and independent of orientation:

$$f(H) \sim [(H - H')^2 + (\Delta H/2)^2]^{-1}. \tag{6}$$

TABLE I. Some structural characteristics of the copper–organic complexes investigated in this study.

Complex	Structural characteristics									
	a, Å	b, Å	c, Å	β, deg	Space group	$r_{\text{Cu-N}}$, Å	$r_{\text{Cu-O1}}$, Å	$r_{\text{Cu-O2}}$, Å	Number of molecules in cell	Ref.
Cu(nad)	11.019	6.844	21.424	93.80	$P2_1/c$	2.016 2.018	1.986 1.989	2.418 2.421	4	[1]
Cu(phen)	14.889	13.843	7.019	108.60	$C2/c$	2.009	1.970	2.486	4	[2]
Cu(en)	7.232	11.725	9.768	105.50	$C2/c$	1.984	1.976	2.498	4	[3]

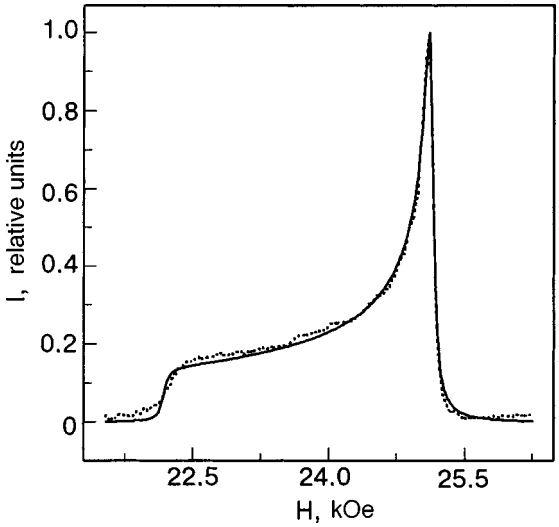

FIG. 2. Low-temperature EPR spectrum of a powder sample of Cu(phen) at a frequency $\nu = 72.81$ GHz. The solid curve was calculated according to expression (7) for the parameter values $g_\perp = 2.067$, $g_\parallel = 2.342$, and $\Delta H = 38.35$ Oe.

Here $\Delta H/2$ is the half width of the line at half maximum. Making a change of integration variable in (5) and taking (1) and (2) into account, we obtain[5]

$$I(H) \sim \int_{H_\parallel}^{H_\perp} \frac{(1+H_\parallel^2 H'^2)dH'}{[(H-H')^2+(\Delta H/2)^2]H'^2(H_\perp^2-H'^2)^{1/2}} \tag{7}$$

for $H_\parallel < H_\perp$.

The contour of the absorption band determined by this expression has a specific shape. Since according to expression (3) the main mass of particles is oriented perpendicular to the field, at small ΔH a rather narrow peak is formed at the band edge near $H_\perp$ while the intensity of the band near $H_\parallel$ should be minimum though finite, forming a narrow shelf. With increasing ΔH these features are smeared out to such a degree that the inflection at $H_\parallel$ vanishes completely. Therefore, it is desirable to use the highest possible working frequency ν in an experiment, since the distance $H_\parallel - H_\perp$ increases linearly with it.

For all of the systems studied, the shape of the resonance absorption band corresponds to that described above. As an example, Fig. 2 shows the absorption band for Cu(phen) taken at $T = 6$ K at a frequency of 72.81 GHz. Also shown there is its dependence calculated according to expression (7).

EXPERIMENTAL RESULTS

For all the systems studied here the shape of the band was calculated according to (7) by the least-squares method with $g_\parallel$, $g_\perp$, and ΔH used as adjustable parameters. The computer program terminated the iteration procedure applied to fit the parameters when the change in the sum of the squares of the deviations calculated from 100 points became less than 0.1%. From observation of the band shape over a wide range of temperatures we could determine the temperature dependence of these parameters. The results of the experiment are presented in Fig. 3.

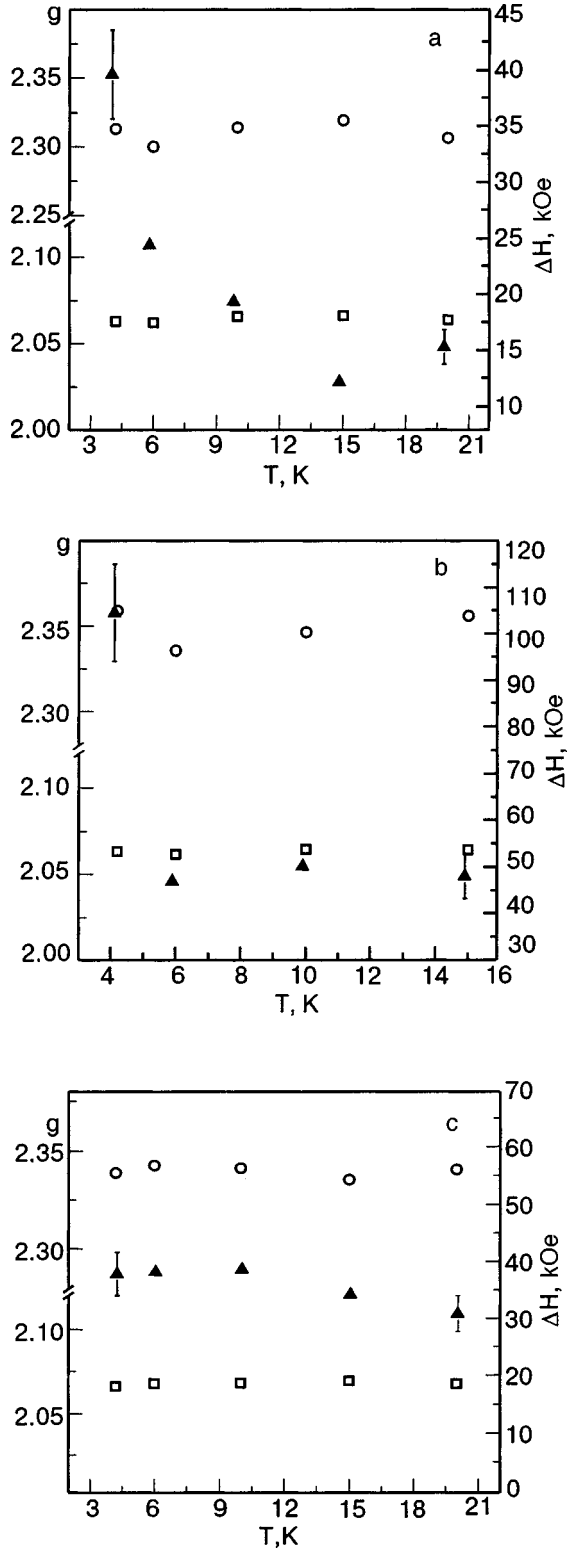

FIG. 3. Temperature dependence of the components of the effective g factor $g_\parallel$ (○) and $g_\perp$ (□) and the resonance linewidth ΔH (▲) for the compounds Cu(en) (a), Cu(nad) (b), and Cu(phen) (c).

1) Cu(en), Fig. 3a. The components of the effective g factor have the values $g_\parallel = 2.31$ and $g_\perp = 2.06$ and are independent of temperature, whereas the resonance linewidth increases sharply with decreasing temperature at $T < 15$ K. This behavior of the parameters of the resonance absorption of the powder agrees completely with results obtained[4] for a single crystal of this compound, where in the same tempera-

TABLE II. Parameters of the resonance spectra and energy interactions of the systems studied.

Complex	Parameters						
	$g_\parallel$	$g_\perp$	ΔH, Oe	M_2, Oe^2	H_{dip}, Oe	H_e, Oe	T_c, K
Cu(en)	2.31	2.06	12.13	$3.2\cdot10^4$	180	$5.35\cdot10^3$	0.359
Cu(nad)	2.35	2.06	50.2	$3.64\cdot10^4$	191	$1.45\cdot10^3$	0.098
Cu(phen)	2.34	2.07	34.4	$8.63\cdot10^3$	93	$5.02\cdot10^2$	0.034

ture interval a weak ($\sim$1%) change of $g_\perp$ and an even weaker ($\sim$0.5%) change of $g_\perp$ were observed, which were attributed to the Jahn–Teller effect. The values of the g factors are determined with a considerably larger error on a powder, of course, because these weak variations are obscured by the process of computer calculation.

At the same time, the low-temperature line-broadening process at $T<15$ K, which in the single crystal was attributed to the establishment of short-range magnetic order as the Néel point is approached, was reproduced completely in the case of the powder. It should be noted that the high-temperature ($T>15$ K) value of the linewidth in the powder turned out the be about a factor of two lower than in the single crystal. Apparently this can be explained by significant inhomogeneous broadening of the line in the single crystal due to internal stresses. In the powder, which was obtained by grinding those single crystals, the stresses are relieved by mechanical strains and, despite the increase in the number of defect centers on the developed surface of the powder particles, on the whole the linewidth turned out to be narrower.

2) Cu(nad), Fig. 3b. For this compound the values of the g-factor components have the values $g_\parallel=2.35$ and $g_\perp=2.065$ and are independent of temperature. One observes appreciable low-temperature broadening of the line at $T<6$ K, which can also be attributed to the establishment of short-range magnetic order in the region near the surface.

3) Cu(phen), Fig. 3c. The values of the g-factor components are close to those obtained for the previous compounds, $g_\parallel=2.34$ and $g_\perp=2.07$, and no temperature dependence of them is observed. The resonance has a markedly weaker temperature dependence than in the previous cases.

The values obtained for the effective g factor and resonance linewidth in the high-temperature part of the investigated range are presented in Table II.

DISCUSSION OF THE RESULTS

It is known that[6] the main orbital D term of the Cu^{2+} ion is split in an octahedral crystalline field into a doublet and a triplet, the doublet lying lower. Under the combined influence of the axial component of the crystalline field and the spin–orbit coupling the degeneracy of the doublet is lifted, and the sign of the axial component determines which of the states $|z^2\rangle$ or $|x^2-y^2\rangle$ (which are still Kramers doublets) is the ground state. For the spin doublet $|z^2\rangle$ the components of the effective g factor obtained in first-order perturbation theory are

$$g_\parallel=2; \quad g_\perp=2-6\lambda/\Delta,$$

where λ is the spin–orbit coupling parameter (for a free ion $\lambda=-830$ cm^{-1}), and Δ is the energy splitting of the term by a cubic field. For a typical value of the ratio $\lambda/\Delta=-0.05$ in this case one should expect the relation $g_\parallel<g_\perp$ to hold, with a value $g_\perp\cong2.3$.

For the Kramers doublet $|x^2-y^2\rangle$ the components of the g factor look like

$$g_\parallel=2-8\lambda/\Delta; \quad g_\perp=2-2\lambda/\Delta,$$

i.e., the opposite inequality, $g_\parallel>g_\perp$, should hold, with $(g_\parallel-2)/(g_\perp-2)\approx4$.

As may be seen from the results of our experiments, for all of the systems studied this last relation holds fairly well. This means that the orbital singlet $|x^2-y^2\rangle$ is in all cases the ground state.

For that orbital state the angular distribution of the electron density lies in the basal plane of the octahedron, with the maxima in the directions of the ligand atoms. Such a distribution should promote realization of indirect exchange interactions between copper ions predominantly in the directions perpendicular to the chains of octahedra. As we have said, because of the complexity of the structure of the ligand configurations the exchange in the interchain directions is hard to calculate. Nevertheless, a general estimate of the exchange interactions can be obtained starting from the expression relating the exchange field H_e with the second moment M_2 and the resonance linewidth ΔH observed in the experiment of Ref. 7:

$$H_e=2M_2/\Delta H.$$

The second moment of the line for a powder can be calculated numerically[8] by starting from the inter-ion distances in the lattice:

$$M_2=\frac{3}{5}g^4\mu_B^4h^{-2}S(S+1)\sum_k\frac{1}{r_{ik}^6}.$$

The results of a calculation of the second moment of the line for the systems analyzed, obtained by summing over 10^6 cells of the lattice, are presented in Table II. Also shown there are the calculated values of the Lorentzian linewidth (6) corresponding to this value of the second moment in the absence of exchange, i.e., in the presence of only the magnetic dipole–dipole interaction:

$$\Delta H_{dip}\approx(M_2)^{1/2},$$

and also the values of the linewidths observed in the experiment and the corresponding values of the exchange field.

Analysis of Table II shows that Cu(en) has the highest value of the exchange interactions in the series of compounds studied, while the exchange field for Cu(phen) is an order of magnitude lower; for Cu(nad) it occupies an intermediate position. This agrees qualitatively with the experi-

mental dependence of the resonance linewidths of these compounds. For them, as we have said, the region of low-temperature line broadening in them corresponds to the critical region of the short-range magnetic order, which precedes the magnetic ordering point. The values of the critical temperature T_c corresponding to the calculated exchange fields $g\mu_B H_e = kT_c$ are also indicated in Table II. The compound Cu(en), which has the highest value of T_c, accordingly demonstrates the widest range of critical broadening.

It should be noted that the results of studies of the low-temperature heat capacity and magnetic susceptibility of these compounds[9,10] have shown that the magnetic ordering temperature of Cu(nad) and Cu(phen) lie below 0.1 K, while for Cu(en) it is $T_N = 0.9$ K, and it is preceded by a region (≈ 10 K wide) of short-range magnetic order. In order of magnitude these values correlate well the values obtained in the present study.

As was pointed out above, the crystal structure of all three compounds investigated is characterized by the presence of practically identical chains of octahedra forming the local environment of the copper, and that should make for identical intrachain interactions. Therefore the marked differences observed in the exchange interactions of the systems must be generated by features of not the intrachain but the interchain interactions, which most likely involve interchain hydrogen bonds. This picture is in qualitative agreement both with the symmetry of the ground state of the copper ion, which promotes interchain exchange, and with the correlation between the simplified geometry of the interchain structure and the ascending values of the exchange interactions in the series of compounds studied.

CONCLUSIONS

1. The EPR spectra of samples in the form of finely disperse powders in which the paramagnetic ion has spin $S = 1/2$ are quite informative if sufficiently high working frequencies are used. These spectra yield numerical values of the main spectroscopic parameters of the system and their anisotropy parameters and make it possible to study the dependence of those parameters on external influences—temperature, in particular.

2. For the compounds Cu(en) and Cu(nad) on the low-temperature part of the investigated range a region of short-range magnetic order is realized before the magnetic ordering point is reached. In that region the components of the effective g factor are independent of temperature, while the resonance linewidth increases noticeably with decreasing temperature.

3. The ground state of the copper ion in the investigated series of metalorganic compounds, which are characterized by the presence of chains of octahedra forming the local environment, is an orbital singlet $|x^2 - y^2\rangle$. The angular distribution of the electron density for this state promotes the formation of interchain exchange interactions.

4. The largest value of the exchange interactions in the investigated series is found in Cu(en), which has the simplest geometry of the interchain couplings in the series. This may also attest to the dominance of the interchain exchange in these compounds.

This investigation has been supported in part by the Grant Agency VEGA Grant No. 1/0430/03 and APVT 20-009902.

*E-mail: aanders@ilt.kharkov.ua
**E-mail: feher@kosice.upjs.sk

[1] B. Kozlevcar, I. Levan, J. Sieler, and P. Segedin, Acta Crystallogr., Sect. C: Cryst. Struct. Commun. **54**, 39 (1998).
[2] P. C. Healy, J. M. Patrick, and A. H. White, Aust. J. Chem. **37**, 1111 (1984).
[3] V. Manriquez, M. Campos-Vallette, N. Lara, N. Gonzalez-Tejeda, O. Wittke, G. Diaz, S. Diez, R. Muñoz, and L. Kriskovic, J. Chem. Crystallogr. **26**, 15 (1996).
[4] A. G. Anders, A. I. Kaplienko, O. V. Kravchina, V. S. Bondarenko, A. Feher, M. Orendáč, A. Orendáčova, and M. Kajňaková, and J. Černák, Fiz. Nizk. Temp. **28**, 642 (2002) [Low Temp. Phys. **28**, 642 (2002)].
[5] J. A. Ibers and J. D. Swalen, Phys. Rev. **127**, 1914 (1962); T. S. Al'tshuler, Zh. Éksp. Teor. Fiz. **55**, 1821 (1968) [Sov. Phys. JETP **28**, 962 (1969)].
[6] A. Abragam and B. Bleany, *Electron Paramagnetic Resonance of Transition Ions*, Clarendon Press, Oxford (1970), Mir, Moscow (1973).
[7] P. W. Anderson and P. R. Weiss, Rev. Mod. Phys. **25**, 269 (1953).
[8] J. H. Van Vleck, Phys. Rev. **73**, 1249 (1948).
[9] M. Kajnakova, A. Orendachova, M. Orendach, J. Cernak, and A. Feher, Phys. Status Solidi **196**, 282 (2003).
[10] M. Kajňaková, A. Orendáčova, M. Orendáč, J. Černák, M. W. Meisel, and A. Feher, *Proceedings of the 14th Conference of Czech and Slovak Physicists*, Plzeò (2002), p. 270.

Translated by Steve Torstveit

ELECTRONIC PROPERTIES OF METALS AND ALLOYS

Anomalous acoustic transparency under conditions of the tilt effect

N. G. Burma, A. I. Petrishin, N. A. Ryabukha, and V. D. Fil'*

B. Verkin Institute for Low Temperature Physics and Engineering, National Academy of Sciences of Ukraine, pr. Lenina 47, Kharkov 61103, Ukraine
(Submitted July 10, 2003; revised July 23, 2003)
Fiz. Nizk. Temp. **30**, 205–208 (February 2004)

An anomalous acoustic transparency phenomenon is discovered and investigated in high-purity Ga samples under conditions of the tilt effect. This phenomenon is due to resonance coupling of the high-frequency elastic waves with weakly damped electromagnetic eigenmodes of the metal. © *2004 American Institute of Physics.* [DOI: 10.1063/1.1645167]

The interaction of high-frequency sound ($\omega\tau \gg 1$, where ω is the angular frequency of the sound and τ is the relaxation time of the electrons) with ballistic and wave excitations of the plasma in a metal in certain situations can lead to additional effective mechanisms of propagation of elastic strain. If the damping of the fundamental acoustic signal is large, the amplitude of that signal can turn out to be significantly lower than the amplitude of the signals due to additional mechanisms of elastic strain propagation; this leads to the phenomenon of acoustic transparency of the metal.

In the case when the sound is coupled with ballistic excitations, anomalous acoustic transparency can evidently be observed in weak magnetic fields ($qr_H \gg 1$, where q is the wave number and r_H is the radius of gyration of the electrons in the magnetic field **H**) on account of the electron transport of sound[1,2] in metals with flat spots on the Fermi surface (FS).[1)] In such metals the damping of the fundamental acoustic signal in its synchronous motion with electrons of the flat spot is extremely large[3] and increases linearly with the frequency ω, while the damping of the acoustic signals transported by the electrons is determined by relaxation processes and is independent of the frequency of the sound. As a result, starting with a certain sound frequency (or thickness of the sample), it is expected that the amplitude of the fundamental acoustic signal will be small compared to the amplitude of the signals transported by the electrons.

In this paper we present the results of a study of the acoustic transparency of a metal under conditions for the existence of the tilt effect (TE), which was first observed by Reneker on bismuth.[4] The tilt effect is known to be a threshold phenomenon in the resonance absorption of sound in classically high magnetic fields ($qr_H \ll 1$) under conditions of strong temporal dispersion $\omega\tau \gg 1$. The condition of resonance coupling of the electrons with the sound is fulfilled starting at a threshold angle $\varphi_0 = S/V_{H\,\max}$ satisfying the condition

$$qV_H \sin\varphi - \omega = 0, \tag{1}$$

where S is the speed of sound, V_H is the drift velocity of the electrons along **H**, $\pi/2 - \varphi$ is the angle between **q** and **H**, and the transition from the region of angles $\varphi < \varphi_0$ to the region $\varphi > \varphi_0$ is accompanied by a sharp increase in the absorption of sound. The reason why acoustic transparency arises in the tilt effect is presumably that elastic strain is transported by electromagnetic eigenmodes of the metal.

Experiments have been done on samples of gallium prepared from material of grade Ga000 at longitudinal sound frequencies of 50–450 MHz in magnetic fields up to 15 kOe. Under the conditions of the experiment the direction of the wave vector of the sound coincided with the principal axes **a**, **b**, and **c** of the crystal (the [100], [010], and [001] directions, respectively) with an accuracy of $\approx 0.3°$. The thickness of the samples ranged from 0.5 to 5 mm. The experimental setup was a bridge with the sample in one arm. The bridge was automatically balanced with respect to phase and amplitude and worked in a pulsed mode, making it possible to obtain the dependence of the damping α and dispersion of the sound velocity $\Delta S/S$ on the angle φ or on the magnetic field strength.[5] The value of the parameter $\omega\tau$ was determined from the dispersion of the sound velocity in magnetic fields.[6]

The idea for the present study arose in the course of a study of the tilt effect in gallium, when in certain situations a strong change in the shape of the pulse envelope of the acoustic signal was observed at tilt angles $\varphi_{\max}$ ($\varphi_{\max}$ is the tilt angle at which the sound damping is maximum). The situation is reminiscent of the picture of the electron transport of sound,[1] where one observes a change in shape of the acoustic pulse owing to interference of the fundamental acoustic signal with the acoustic precursor pulse generated by it.

Under conditions of the tilt effect the distortion of the envelope of the acoustic signal is manifested most strongly at directions of **H** close to the **a** axis in the cases **q**∥**b** and **q**∥**c** and near the **b** axis for **q**∥**a**. According to gallium band-structure calculations[7] which have been confirmed by numerous experiments, the Fermi surface has rather large flat spots perpendicular to the **a** and **b** axis. Experimentally a flat spot of the Fermi surface with a relative area ~1% was observed in Ga in Ref. 3. The direction of the electron velocity on this flat spot is practically coincident with the **a** direction.

A detailed study of the acoustic transparency was carried

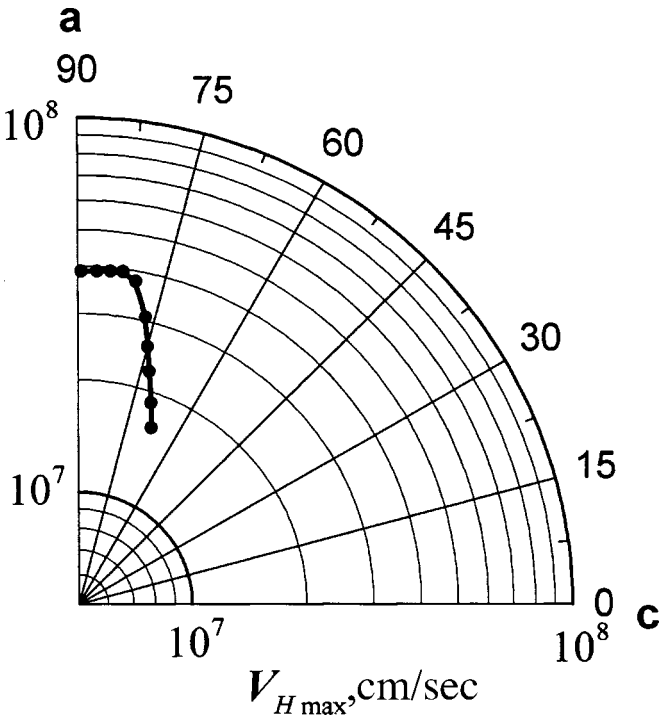

FIG. 1. Angular dependence of the Fermi velocity of the electrons that give the main contribution to the tilt effect for **q**∥**b** in the **ac** plane.

out in the experimental geometry **q**∥**b**, with the angle φ scanned in the **ab** plane. This experimental geometry is convenient because in it one observes a single strong maximum of $\alpha(\varphi)$, and the dependence of the maximum drift velocity on the direction in the crystal, obtained by processing the $\alpha(\varphi)$ curves for this maximum, also partially confirms that there is a significant region of the Fermi surface near the **a** axis where the electron velocity has the same value, equal to 3.8×10^7 cm/s (see Fig. 1).

A specific feature of the experiment in this geometry is that the dependence of $\Delta S/S$ on the angle φ differs strongly from the theoretical dependence. A theoretical study of the tilt effect[8,9] has shown that in ''good'' metals such as gallium under conditions of the tilt effect an important role is played by strain-induced solenoidal electric fields accompanying the propagation of the sound wave, in addition to the direct strain coupling. Figure 2 shows the experimental curve of $\Delta S/S$ as a function of φ, obtained under the conditions $qr_H \ll 1$, $\omega\tau \approx 10$ (solid curve) and the calculated curves for the case of a quadratic electron spectrum.[9] The dot-and-dash curve corresponds to the direct strain coupling, and the dashed curve to the result of a renormalization of that coupling by the solenoidal fields with polarization along the **H** vector. The theoretically predicted result of the renormalization is quite substantial: the rate of growth of $\Delta S/S$ on approach to φ_0 decreases significantly, and the sharp decrease of $\Delta S/S$, with a change of sign, in a small angular region after the transition through φ_0 vanishes. A comparison of the results of the experiment and theory confirms the substantial role of the solenoidal fields under the conditions of our experiment, but only in the region $0<\varphi<\varphi_0$. In the region $\varphi>\varphi_0$, on the other hand, the renormalization of the strain coupling is weakened sharply, apparently because of violation of the condition $(q\delta)^2 \ll 1$ (δ is the skin depth for the

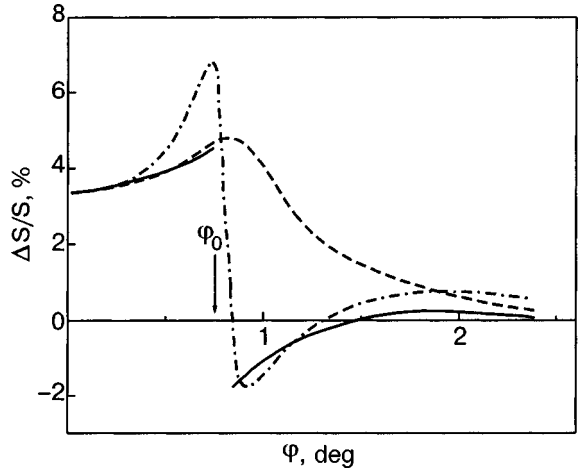

FIG. 2. Comparison of the experimental dependence of $\Delta S/S(\varphi)$ (solid curve) with the curves calculated in the approximation of a quadratic electron spectrum[9] ($\omega/2\pi = 200$ MHz, $\omega\tau = 9.2$, $qr_H \ll 1$). The dot-and-dash line was calculated with only the strain coupling of the electrons with the sound, while the dashed line is that coupling renormalized by the induced solenoidal fields.

electric fields with polarization along **H**). It may be that this situation arises because the existence conditions for electromagnetic modes of the metal are satisfied for $\varphi \geqslant \varphi_0$.

Figure 3 demonstrates the manifestation of the acoustic transparency phenomenon at the lowest sound frequency $\omega/2\pi = 50$ MHz ($\omega\tau = 2.3$). The solid curves show $\alpha(\varphi)$ obtained by automatic recording on a thin sample ($L = 0.92$ mm) and on a thick sample ($L = 3.7$ mm) and the dashed curves show the results calculated for the same value of $\omega\tau$ in the approximation of a quadratic spectrum.

It is seen in Fig. 3 that the acoustic transparency phenomenon is manifested only in the thick sample, where it takes the form of a vanishing of the maximum of $\alpha(\varphi)$; the damping has a lower value at $\varphi \sim \varphi_0$ than at $\varphi = 0$, and, as a result, $\alpha(\varphi)$ is a smooth curve without a maximum. In other words, the acoustic transparency effects ''erode'' the maximum of $\alpha(\varphi)$ in the tilt effect. The gain in amplitude of the

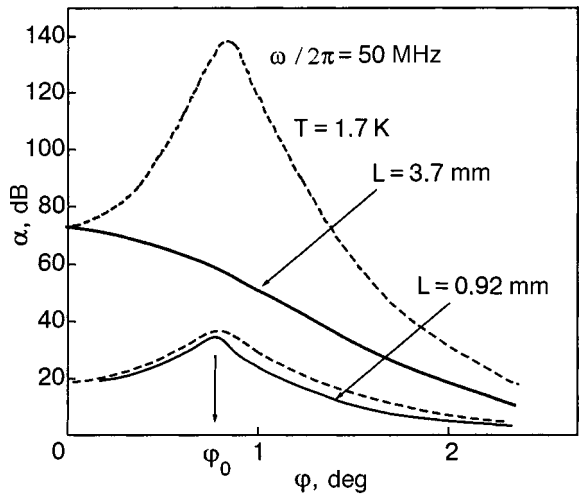

FIG. 3. Angular dependence of the damping of an acoustic signal at $\omega/2\pi = 50$ MHz ($\omega\tau = 2.3$). The solid curves are experimental, the dashed curves calculated in the approximation of a quadratic electron spectrum.[9]

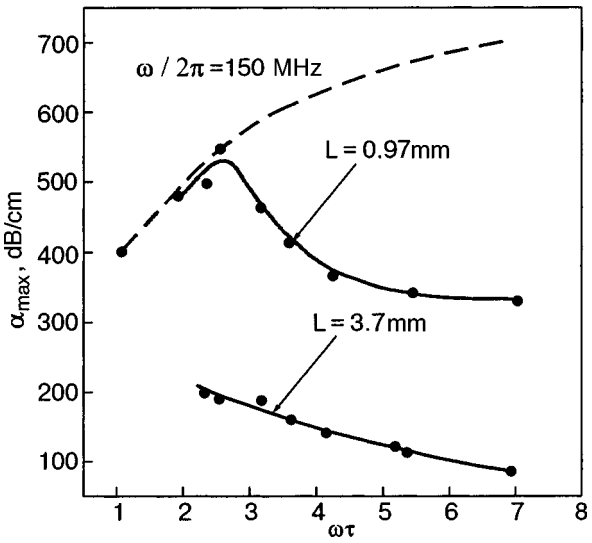

FIG. 4. Damping of the elastic component of a coupled wave as a function of $\omega\tau$ for the thin and thick samples.

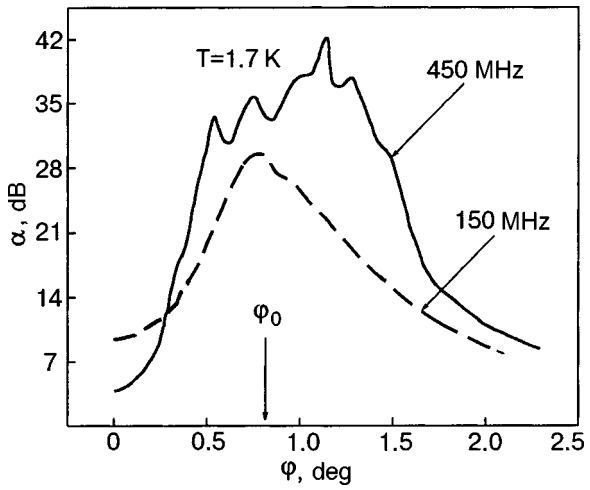

FIG. 5. Angular dependence of the damping of an acoustic signal obtained on the thin sample ($L=0.92$ mm) at sound frequencies of 150 and 450 MHz ($T=1.7$ K, $H=15$ kOe).

elastic wave due to the acoustic transparency effect is about 80 dB at $\varphi\approx\varphi_{\max}$, as can be seen from Fig. 3.

Figure 4 shows the evolution of the efficiency of the acoustic transparency mechanism as a function of $\omega\tau$ for the thin and thick samples at a sound frequency of 150 MHz. The value of τ was varied by changing the temperature of the sample. The dashed curve in the figure shows the results calculated using the results of Ref. 9 for the case of an isotropic quadratic spectrum. In the thin sample the acoustic transparency effect begins to be manifested at $\omega\tau\approx 2.5$, and at a maximum value $\omega\tau=6.8$ the amplitude of the measured signal exceeds its calculated value by more than 30 dB. In the thick sample, in contrast, the acoustic transparency effect is manifested throughout the range of $\omega\tau$, and at $\omega\tau=6.8$ the gain in amplitude of the measured elastic component in comparison with its calculated value in the sound wave is a giant $\sim$240 dB.

Another manifestation of the acoustic transparency effect is the appearance of additional maxima on the $\alpha(\varphi)$ curve. Figure 5 shows the $\alpha(\varphi)$ curves obtained on the thin sample at sound frequencies of 150 and 450 MHz under conditions of maximum manifestation of the transparency effect ($T=1.7$ K). It is seen that while at 150 MHz only a weak second maximum appears on the $\alpha(\varphi)$ curve, at 450 MHz this curve displays a developed structure of additional peaks. Studies showed that the number of these peaks is greater for higher sound frequencies and thicker samples, indicating that they are of an interference nature.

In our view, the set of experimental results described above finds a reasonable explanation in the hypothesis that in the given case a resonance coupling of the sound with an electromagnetic eigenmode of the metal is observed in the tilt-effect regime. At present only one type of electromagnetic wave that can propagate transverse to the magnetic field in a metal is known—the so-called fast magnetosonic wave.[10] However, its velocity is close to the Fermi velocity, and one cannot speak of any resonance coupling of sound with it. As we have emphasized previously, the region of observation of the effects described is geometrically associated with flat spots of the Fermi surface, and it is therefore natural to suppose that an electromagnetic eigenmode in the given case is also due to those formations. It is shown in Ref. 11 that for $H=0$ the electrons of the flat spot form a so-called beam wave, the spectrum of which has both parabolic parts and linear parts and depends on the mutual orientation of the wave vector and the flat spot. It was shown in Ref. 3 that under real experimental conditions in the normal state the beam mode is highly damped, but below the temperature of the superconducting transition its damping falls off, leading to noticeable features in the temperature behavior of the sound velocity and damping. The properties of the beam wave and the features of its coupling with sound in the presence of a magnetic field have not been studied theoretically. Physically it is clear, however, that if **H** is directed along the velocity of the electrons at the flat spot then it will not drive them from the flat spot, and the feature (singularity) in the conductivity of the metal which gives rise to the electromagnetic eigenmode should be preserved.

It can also be expected that in a high magnetic field, because of the vanishing of the transverse components of the conductivity, the spectrum of the beam wave lies in the weak-damping region, unlike the $H=0$ case.

The authors thank E. V. Bezuglyi for a helpful discussion of the results of this study.

*E-mail: fil@ilt.kharkov.ua

[1)]Here and below we use the historical term ''flat spots'' of the Fermi surface. We actually have in mind objects of rather large sizes ($\delta p \gg p_F/qv_F\tau$) on which the projection of the Fermi velocity on a specified direction is practically constant ($\delta v_F/v_F \ll 1/qv_F\tau$). In the case when $|v_F|$ is practically constant on the Fermi surface these requirements lead to geometrically flat objects, although in principle one can imagine a distribution of v_F on the Fermi surface such that the given region will not in any way be distinguished geometrically.

[1] V. D. Fil', N. G. Burma, and P. A. Bezuglyĭ, JETP Lett. **23**, 387 (1976).
[2] E. N. Bogachek, A. S. Rozhavskiĭ, and R. I. Shekhter, JETP Lett. **23**, 230 (1976).
[3] E. V. Bezuglyi, A. M. Stepanenko, and V. D. Fil', Fiz. Nizk. Temp. **13**, 246, 713 (1987) [Sov. J. Low Temp. Phys. **13**, 140, 406 (1987)].
[4] D. H Reneker, Phys. Rev. **115**, 303 (1959).

[5] N. G. Burma, E. A. Masalitin, and A. E. Kabanov, Inventor's Certificate No. 1213410 (USSR) [in Russian].
[6] I. O. Kulik, Zh. Éksp. Teor. Fiz. **47**, 107 (1964) [Sov. Phys. JETP **20**, 73 (1965)].
[7] W. R. Reed, Phys. Rev. **188**, 1184 (1969).
[8] A. P. Korolyuk, M. A. Obolenskiĭ, and V. L. Fal'ko, Zh. Éksp. Teor. Fiz. **59**, 377 (1970) [Sov. Phys. JETP **32**, 205 (1971)]; Zh. Éksp. Teor. Fiz. **60**, 269 (1971) [Sov. Phys. JETP **33**, 148 (1971)].
[9] É. A. Kaner, L. V. Chebotarev, and A. V. Eremenko, Zh. Éksp. Teor. Fiz. **80**, 1058 (1981) [Sov. Phys. JETP **53**, 540 (1981)].
[10] E. V. Bezuglyi, N. G. Burma, E. Yu. Deineka, and V. D. Fil', Fiz. Nizk. Temp. **19**, 300 (1993) [Low Temp. Phys. **19**, 211 (1993)].
[11] E. V. Bezuglyĭ, Fiz. Nizk. Temp. **9**, 543 (1983) [Sov. J. Low Temp. Phys. **9**, 277 (1983)].

Translated by Steve Torstveit

Nonlinear conductance of a quantum contact containing single impurities

Ye. S. Avotina* and Yu. A. Kolesnichenko

B. Verkin Institute for Low Temperature Physics and Engineering, National Academy of Sciences of Ukraine, pr. Lenina 47, Kharkov 61103, Ukraine

(Submitted July 15, 2003)
Fiz. Nizk. Temp. **30**, 209–216 (February 2004)

The conductance of a quantum contact containing single point defects and a potential barrier is investigated theoretically. The dependence of the conductance G on the applied voltage U is obtained for the model of a quantum wire connecting massive banks. The comparative values of the different nonlinear contributions to the conductance due to the interference of electron waves scattered by defects and by defects and the barrier are analyzed. The latter contribution becomes dominant even at extremely small coefficients of reflection of electrons from the barrier. It is shown that the dependence of the transmission coefficient T_{12} on the electron energy E explains the experimentally observed suppression of oscillation of the conductance $G(U)$ when its absolute value is close to the single-quantum value $G_0 = 2e^2/h$. © *2004 American Institute of Physics.* [DOI: 10.1063/1.1645168]

INTRODUCTION

The physical characteristics of conductors with mesoscopic dimensions, such as quantum contacts, wires, rings, and dots, for example, are extremely sensitive to the presence of single defects, which can substantially alter their properties and give rise to new effects that are absent in the pure, ballistic objects. Diverse defects inevitably arise in the preparation of conducting structures, and the study of their influence on the transport characteristics is important in connection with the intensive development of nanoelectronics. On the other hand, the introduction of a controlled number of impurities having definite properties into mesoscopic systems opens up the possibility of varying their kinetic coefficients. A study of the influence of individual impurities on transport properties in mesoscopic systems is also interesting from the standpoint of basic physics, since in that case the scattering of electrons (e.g., Kondo scattering) manifests itself in the most explicit form, unobscured by averaging over a large number of defects, so that detailed information can be obtained from it. These circumstances have attracted interest in the experimental and theoretical study of the properties of conductors of small size containing single defects.

One of the classes of mesoscopic conductors now being studied intensively is that of quantum ballistic contacts. Quantum contacts are microscopic constrictions or wires having diameters comparable to the electron de Broglie wavelength and connecting massive metallic ''banks.'' The conductance G (the first derivative of the current–voltage characteristic, $G=dI/dU$) of such systems is determined by the number N of transverse quantization levels of the electron energy with $\varepsilon_s<\varepsilon_F$ (ε_F is the Fermi energy, $s=1,...,N$) or, as is often said, the number of quantum conducting modes. Each of those modes, according to the Landauer theory,[1,2] contributes to G a single quantum $G_0 = 2e^2/h$, so that the total conductance $G=NG_0$. The value of N can be varied, for example, by varying the diameter d of the contact. Here the function $G(d)$ is a step function with a step equal to the quantum of conductance G_0. This effect was first obtained in necks created on the basis of a two-dimensional electron gas and was later observed in three-dimensional contacts of ordinary metals (see, e.g., the reviews[3,4]). In real contacts the reflection of electrons can be taken into account with the aid of a transmission coefficient of the sth mode, $\tau_s \leqslant 1$, and the conductance in the Ohm's law approximation ($U\to 0$) at low temperatures ($T\to 0$) is described by the Landauer–Buttiker formula[1,2]

$$G = G_0 \sum_{s=1}^{N} \tau_s . \tag{1}$$

The difference of the coefficients τ_s from unity is due to both the shape of the contact and the scattering of electrons. Here if the conductance is determined by a small number of quantum modes, then the presence of single defects can lead to a substantial change in the conductance. A number of papers have been devoted to the theoretical study of this question.[5–12] However, effects nonlinear in the voltage in quantum contacts have been little studied. At the same time, the small size of the contact and, hence, its large resistance make it possible to avoid heating effects at biases eU of the order of tenths of the Fermi energy, making it possible to study highly nonequilibrium electronic states.

The nonmonotonic dependence of the conductance of a quantum contact on the voltage U was first observed experimentally in Ref. 13. This effect was subsequently observed in the experiments of Ref. 14. It was conjectured in Ref. 13 that the cause of this nonmonotonicity might be interference of electron waves. The essence of this effect is as follows. An electron wave with wave vector k_s incident on the contact passes through it with a probability t_s or is reflected with a probability r_s. If a defect is located a distance z_i from the contact, the reflected wave after backscattering on it can return again to the contact. The two waves are coherent and interfere. The corresponding contribution of this process to the total transmission coefficient τ_s depends in an oscillatory manner on the relative phase shift $2k_sz_i$ between the two waves. Since the electron energy and, hence the wave vec-

tors k_s depend on the applied voltage U, varying the latter leads to a nonmonotonic dependence of the conductance $G(U)$. The influence of "dirty" banks on the nonlinear conductance $G(U)$ of ballistic contacts was examined theoretically in Refs. 14 and 15. The authors of Ref. 15 predicted that conductance fluctuations will be suppressed near the edges of the steps of the function $G(d)$, and this effect was subsequently observed experimentally.[14] The study in Ref. 15 was based on a numerical simulation using definite values of the parameters, and for that reason its results cannot be used for analysis of concrete experimental data. In Ref. 14 the scattering-matrix formalism was used to obtain a quite general expression for the nonlinear conductance. Besides the scattering matrix for electrons in the contact the theory also took into account the scattering matrix for backscattering in the banks, and the total probability T_{12} of transmission of an electron from one bank of the contact to another was expressed in terms of the latter matrix. Because the concrete form of the scattering matrices in the formulas for the conductance which were obtained in Ref. 14 is indefinite, it is impossible to estimate the amplitude and characteristic periods of the nonmonotonicities of the function $G(U)$. At the same time, the probability that an electron will again be incident on the contact after scattering by an impurity located a sufficient distance from it at a point $\mathbf{r}_i$ is small, of the order of the solid angle within which the contact is viewed from the point $\mathbf{r}_i$ (Ref. 16). A more realistic situation, it seems, is the interference of electron waves reflected from defects within the contact or in the direct vicinity of it. In Ref. 5 the conductance of a long quantum contact (wire) containing single point defects was analyzed theoretically, and the nonlinear corrections oscillatory in the voltage were found. Such a model ignores one important fact—the finite probability of reflection of electrons even in a pure ballistic contact. Such reflection may be due, for example, to a mismatch of the Fermi velocities when different metals are brought into contact or to nonadiabaticity of the shape of the contact.

In this paper we consider the voltage dependence of the conductance of a quantum wire that contains single point defects (for which no averaging over their positions is done) and a potential barrier cutting across the wire. This model allows one to take into account both the reflection from the plane of the contact (which is described by the coefficient of reflection from the barrier) and also scattering on impurities. The relative simplicity of the model makes it possible to obtain exact analytical expressions describing the dependence of the conductance on the position of the defects.

MODEL AND CALCULATION OF THE TRANSMISSION COEFFICIENT OF ELECTRONS THROUGH THE CONTACT

Consider a contact in the form of a long, narrow channel having a length L much greater than its diameter $d=2R$. The edge of the channel is smoothly (on the scale of the Fermi wavelength λ_F) connected to massive metallic "banks" (the adiabatic approximation[17]), to which a voltage $eU \ll \varepsilon_F$ is applied (Fig. 1). These conditions permit one to neglect the reflection of electrons from the edges of the contact. At the center of the contact ($z=0$) is a potential barrier V, near

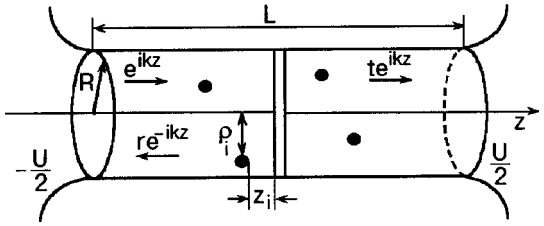

FIG. 1. Model of a quantum contact in the form of a channel of radius R connecting two massive "banks." The barrier and the impurities inside the contact are shown schematically. The arrows indicate the direction of motion of the electrons coming into the contact, reflected by the barrier, and transmitted through it; ρ_i is the distance of the defect from the axis of the contact.

which, at the points $\mathbf{r}_i$, are found several point impurities. The single-electron Hamiltonian of this system is written in the form

$$\hat{H}=\frac{\hat{\mathbf{p}}^2}{2m}+V\delta(z)+g\sum_i \delta(\mathbf{r}-\mathbf{r}_i), \tag{2}$$

where $\hat{\mathbf{p}}$ and m are the momentum operator and the effective mass of the electron, and g is the coupling constant of the electron with the impurities.

Calculation of the conductance of a mesoscopic channel (see, e.g., Ref. 18) reduces to determination of the scattering matrix $\hat{t}(E)$ as a function of the electron energy E. The most general expression for the electric current through the channel has the form

$$I=\frac{2e^2}{h}\int_{-\infty}^{\infty} dE\, T_{12}(E)\left[f_F\left(E+\frac{eU}{2}\right)-f_F\left(E-\frac{eU}{2}\right)\right], \tag{3}$$

$$T_{12}=\mathrm{Tr}(\hat{t}^{\dagger}\hat{t})=\sum_{ss'} T_{ss'}=\sum_{ss'} |t_{ss'}|^2, \tag{4}$$

where $T_{ss'}$ is the probability that an electron belonging to the quantum conducting mode of index s in the left bank of the contact will pass through it and belong to the mode with index s' in the right bank. The summation over s and s' in formula (4) is restricted by the condition $\varepsilon_{s(s')}<\varepsilon_F$. One can diagonalize the matrix $\hat{t}^{\dagger}\hat{t}$ and write the Landauer–Buttiker formula (1) in terms of its eigenvalues τ_s. At temperature $T\to 0$ the expression for the conductance takes the simple form

$$G=\frac{e^2}{h}\left[T_{12}\left(\varepsilon_F+\frac{eU}{2}\right)+T_{12}\left(\varepsilon_F-\frac{eU}{2}\right)\right]. \tag{5}$$

We note that at finite voltages U the conductance of a ballistic contact is determined by two fluxes of electrons moving in opposite directions, with energies differing by an amount eU.[19] Accordingly, the energy of the transverse quantum modes for these groups of electrons also differ by eU. Therefore with increasing diameter of the contact the quantum mode becomes allowed for one direction of the wave vector first, viz., that with the lowest energy. As a result, the conductance jumps by $G_0/2$.[20,21]

The probabilities $T_{ss'}$ can be expressed in terms of the advanced Green's functions $G^{+}(\mathbf{r},\mathbf{r}',E)$ of the electrons (see below). In the adiabatic approximation (far from the edges) the wave functions $\psi_\alpha(\mathbf{r})$ of the electrons in a ballistic chan-

nel in the absence of the barrier ($V=g=0$) can be written in the form

$$\psi_\alpha(r)=\frac{1}{\sqrt{L}}\psi_{\perp\beta}(\mathbf{R})e^{ik_z z}, \tag{6}$$

where $\alpha=(\beta,k_z)$ is the complete set of quantum numbers, consisting of a set of two discrete numbers $\beta=(m,n)$ which specify the energy levels ε_β of the transverse quantization, and the continuous wave number k_z is the projection of the wave vector of the electron on the axis of the contact, $\psi_{\perp\beta}(\mathbf{R})$ is the component of the electron wave function perpendicular to the axis of the contact and can be chosen real, and $\mathbf{r}=(\mathbf{R},z)$. Accordingly, the total energy of the electron is $\varepsilon_\alpha=\varepsilon_\beta+\hbar^2k_z^2/2m$. The functions $\psi_{\perp\beta}(\mathbf{R})$ satisfy zero boundary conditions at the surface of the contact. In the numerical calculations presented below we have assumed for definiteness that the channel has a cylindrical shape. Then the wave functions and energy levels of the transverse quantization of the electrons in a ballistic channel ($L\to\infty$) without the impurities and barrier have the form

$$\psi_{\perp nm}(\rho,\varphi,z)=\frac{1}{\sqrt{\pi R^2}J_{m+1}(\gamma_{mn})}J_m\left(\gamma_{mn}\frac{\rho}{R}\right)e^{im\varphi};$$

$$\varepsilon_{nm}=\frac{\hbar^2\gamma_{mn}^2}{2mR^2}. \tag{7}$$

Here we have used the cylindrical coordinates $\mathbf{r}=(\rho,\varphi,z)$; γ_{mn} is the nth zero of the Bessel function $J_m(x)$.

By factorizing the wave function (6), we can write $G^+(\mathbf{r},\mathbf{r}',E)$ in the form of an expansion:

$$G^+(\mathbf{r},\mathbf{r}',E)=\sum_{\beta\beta'}\psi_{\perp\beta}(\mathbf{R})\psi_{\perp\beta'}(\mathbf{R}')G^+_{\beta\beta'}(z,z'). \tag{8}$$

In accordance with the results of Ref. 22, the transmission probabilities $T_{\beta\beta'}(E)$ are equal to

$$T_{\beta\beta'}(E)=\frac{\hbar^4}{m^2}k_\beta k_{\beta'}|G^+_{\beta\beta'}(z,z',E)|^2,\quad z\to-\infty,\quad z'\to+\infty, \tag{9}$$

where $k_\beta=\sqrt{2m(E-\varepsilon_\beta)}/\hbar$ is the electron wave vector corresponding to the quantized energy level ε_β. In formula (9) we have gone from the classification of electron modes according to index s [formulas (1) and (4)], for which the energies ε_s increase with that index, to a classification according to a set of discrete quantum numbers β.

The Green's function $G_b(\mathbf{r},\mathbf{r}')$ in a channel with a potential barrier in the absence of impurities satisfies the equation

$$G_b(\mathbf{r},\mathbf{r}')=G_0(\mathbf{r},\mathbf{r}')+V\int d\mathbf{R}''G_0(\mathbf{r},\mathbf{R}'')G_b(\mathbf{R}'',\mathbf{r}')|_{z''=0}, \tag{10}$$

where

$$G_0^+(\mathbf{r},\mathbf{r}')=\lim_{\eta\to0}\sum_\alpha\frac{\psi_\alpha(\mathbf{R})\psi_\alpha^*(\mathbf{R}')}{E-\varepsilon_\alpha-i\eta} \tag{11}$$

is the Green's function in the absence of impurities and the barrier. From Eq. (10) we find the coefficients of the expansion (9) of the function $G_b(\mathbf{r},\mathbf{r}',E)$:

$$G^+_{b\beta\beta'}(z,z',E)=-\delta_{\beta\beta'}\frac{im}{\hbar^2k_\beta}\{e^{ik_\beta|z'-z|}+r_\beta e^{ik_\beta(|z|+|z'|)}\}, \tag{12}$$

where the amplitude for reflection from the barrier, r_β, is equal to

$$r_\beta=-\frac{imV}{(\hbar^2k_\beta+imV)}=-i|r_\beta|e^{i\varphi_\beta}. \tag{13}$$

The matrix $T_{\beta\beta'}$ from (9) can be written in the form $T_{\beta\beta'}=T^b_\beta\delta_{\beta\beta'}$, where T^b_β is expressed in terms of the amplitude of the transmitted wave $t_\beta=r_\beta+1=|t_\beta|e^{i\varphi_\beta}$:

$$T^b_\beta=|t_\beta|^2=\left[1+\left(\frac{mV}{\hbar^2k_\beta}\right)^2\right]^{-1}. \tag{14}$$

In the presence of impurities the Green's function $G(\mathbf{r},\mathbf{r}',E)$ that determines the transmission probability (9) must be found from the equation

$$G(\mathbf{r},\mathbf{r}')=G_b(\mathbf{r},\mathbf{r}')+g\sum_i G_b(\mathbf{r},\mathbf{r}_i)G(\mathbf{r}_i,\mathbf{r}'). \tag{15}$$

Equation (15) can be solved exactly for any finite number of impurities i. For this it is necessary to write Eq. (15) at all the values $\mathbf{r}=\mathbf{r}_i$ and solve the system of i linear algebraic equations for the functions $G^+(\mathbf{r}_i,\mathbf{r}')$. As examples, let us solve Eq. (15) for one and two impurities.

For one impurity at the point $\mathbf{r}_1$:

$$G^{(1)}(\mathbf{r},\mathbf{r}')=G_b(\mathbf{r},\mathbf{r}')+G_1(\mathbf{r}_1)G_b(\mathbf{r},\mathbf{r}_1)G_b(\mathbf{r}_1,\mathbf{r}'). \tag{16}$$

For two impurities located at the points $\mathbf{r}=\mathbf{r}_{1,2}$:

$$G^{(2)}(\mathbf{r},\mathbf{r}')=G_b(\mathbf{r},\mathbf{r}')+\frac{G_1(\mathbf{r}_1)G_b(\mathbf{r},\mathbf{r}_1)G_b(\mathbf{r}_1,\mathbf{r}')+G_1(\mathbf{r}_1)G_1(\mathbf{r}_2)G_b(\mathbf{r}_1,\mathbf{r}_2)G_b(\mathbf{r},\mathbf{r}_1)G_b(\mathbf{r}_2,\mathbf{r}')}{1-G_b(\mathbf{r}_2,\mathbf{r}_1)G_b(\mathbf{r}_1,\mathbf{r}_2)G_1(\mathbf{r}_1)G_1(\mathbf{r}_2)}$$

$$+\frac{G_1(\mathbf{r}_2)G_b(\mathbf{r},\mathbf{r}_2)G_b(\mathbf{r}_2,\mathbf{r}')+G_1(\mathbf{r}_1)G_1(\mathbf{r}_2)G_b(\mathbf{r},\mathbf{r}_2)G_b(\mathbf{r}_2,\mathbf{r}_1)G_b(\mathbf{r}_1,\mathbf{r}')}{1-G_b(\mathbf{r}_2,\mathbf{r}_1)G_b(\mathbf{r}_1,\mathbf{r}_2)G_1(\mathbf{r}_1)G_1(\mathbf{r}_2)}, \tag{17}$$

where $G_1(\mathbf{r}_i)=g/1-gG_b(\mathbf{r}_i,\mathbf{r}_i)$.

For a rather large number of impurities the exact expression for the function $G(\mathbf{r},\mathbf{r}')$ becomes extremely cumbersome. If it is assumed that the coupling constant g is small, the expression for the transmission probabilities (9) can be obtained with the use of the Born expansion in powers of g. With accuracy to terms proportional to g^2 we obtain

$$T_{\beta\beta'}=T^b_\beta\delta_{\beta\beta'}+\Delta T_{1\beta\beta'}+\Delta T_{2\beta\beta'}. \tag{18}$$

The first-order correction is equal to

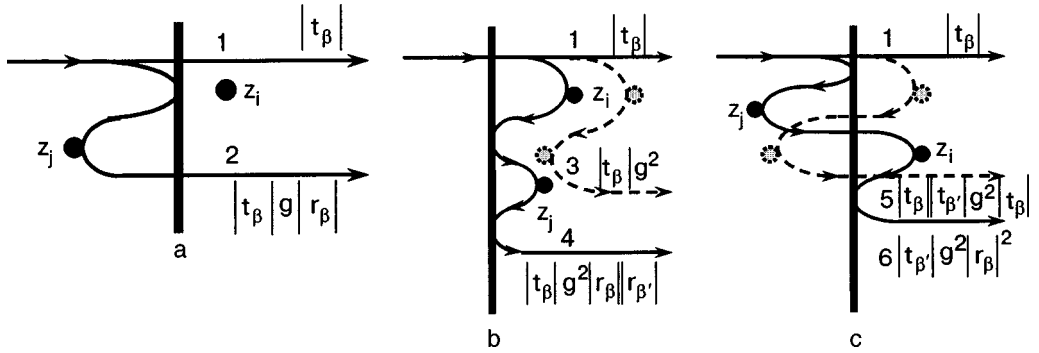

FIG. 2. Schematic illustration of some possible types of electron trajectories in a quantum channel with a barrier and impurities.

$$\Delta T_{1\beta\beta'} = -2\,\delta_{\beta\beta'}\left(\frac{m}{\hbar^2}\right) T_\beta^b g \frac{1}{k_\beta} \sum_i A_{\beta\beta}^{(ii)} |r_\beta| \cos(2k_\beta z_i + \varphi_\beta), \tag{19}$$

where $A_{\beta\beta'}^{(ij)} = \psi_{\perp\beta}(\mathbf{R}_i)\psi_{\perp\beta'}(\mathbf{R}_j)$.

The form of the second-order correction $\Delta T_{2\beta\beta'}$ to the transmission coefficient depends on the position of the defects relative to the barrier. In the case when the impurities are located on different sides of the barrier, $\Delta T_{2\beta\beta'}$ is given by the formula ($z_i<0$, $z_j>0$)

$$\begin{aligned}\Delta T_{2\beta\beta'} = -\left(\frac{gm}{\hbar^2}\right)^2 \frac{1}{k_\beta k_{\beta'}} [-2|t_{\beta'}||t_\beta| \sum_{i\neq j} A_{\beta'\beta'}^{(ij)} A_{\beta\beta}^{(ij)} \{-T_\beta^b \cos((k_\beta + k_{\beta'})(z_j - z_i) + \varphi_\beta + \varphi_{\beta'}) \\ + |r_\beta|^2 \cos((k_\beta + k_{\beta'})(z_j - z_i) + 2\varphi_\beta) + |r_\beta||r_{\beta'}| \cos((k_\beta + k_{\beta'})(z_i + z_j))\} \\ + T_\beta^b \sum_i A_{\beta\beta'}^{(ii)2} \{T_{\beta'}^b + 2|r_\beta| \sin(2k_\beta z_i + \varphi_\beta) + |r_\beta||r_{\beta'}| \cos(2(k_\beta + k_{\beta'})z_i + \varphi_\beta + \varphi_{\beta'})\}]\end{aligned} \tag{20}$$

or in the case when the impurities lie on one side of the barrier ($z_i<z_j$):

$$\begin{aligned}\Delta T_{2\beta\beta'} = -\left(\frac{gm}{\hbar^2}\right)^2 \frac{1}{k_\beta k_{\beta'}} [-2T_\beta^b \sum_{i\neq j} A_{\beta\beta'}^{(jj)} A_{\beta\beta'}^{(ii)} \{-\cos((k_\beta + k_{\beta'})(z_j - z_i)) \\ + 2|r_\beta||r_{\beta'}| \cos((k_\beta + k_{\beta'})(z_j + z_i) + \varphi_\beta + \varphi_{\beta'}) \\ - 2|r_\beta| \sin(k_\beta(z_i + z_j) + k_{\beta'}(z_j - z_i) + \varphi_\beta) + |r_{\beta'}|^2 \cos((k_\beta + k_{\beta'})(z_i - z_j))\} \\ + T_\beta^b \sum_i A_{\beta\beta'}^{(ii)} \{T_{\beta'}^b + 2|r_\beta| \sin(2k_\beta z_i + \varphi_\beta) - 2|r_\beta||r_{\beta'}| \cos(2(k_\beta + k_{\beta'})z_i + \varphi_\beta + \varphi_{\beta'})\}].\end{aligned} \tag{21}$$

These formulas are valid when the value of the total energy of the electrons is not close in value to the energies ε_β of the quantum modes. If that is not the case (i.e., $k_\beta \to 0$), then the transmission coefficient must be calculated using the exact expression for the Green's function.

DISCUSSION OF THE RESULTS

When the reflection of electrons from a barrier in the contact is taken into account, the conductance becomes a complicated nonmonotonic function of the voltage. If the coupling constant g of an electron with the impurity is small, then the electron transmission probability $T_{\beta\beta'}$ in (18) can be obtained in the Born approximation for an arbitrary number of defects (15). In this case the terms in the probability $T_{\beta\beta'}$ (18) with an oscillatory dependence on energy have a clear physical meaning and can be explained in terms of electron trajectories. As we discussed in the Introduction, the presence of such terms is due to the interference of the electron wave passing through the contact without scattering (trajectory *1* in Fig. 2) and the electron waves reflected by the defects and barrier. As an example, Fig. 2 shows several possible electron trajectories. The first correction $\Delta T_{1\beta\beta'}$ (proportional to g) corresponds to the interference between the directly transmitted wave and the wave that undergoes one reflection from an impurity and one reflection from the barrier (trajectory *2* in Fig. 2a). The interference of the trajectories illustrated in Fig. 2b and 2c corresponds to a certain term in the second-order correction $\Delta T_{2\beta\beta'}$, while trajectories *3* and *5* contain two scatterings on impurities, and trajectories *4* and *6* also include two reflections from the barrier. The first and second terms in formula (21) are due to the interference between trajectories *1* and trajectories *3* and *4* in Fig. 2b, respectively. Figure 2c shows trajectories *5* and *6*, the interference between each of which and trajectory *1* cor-

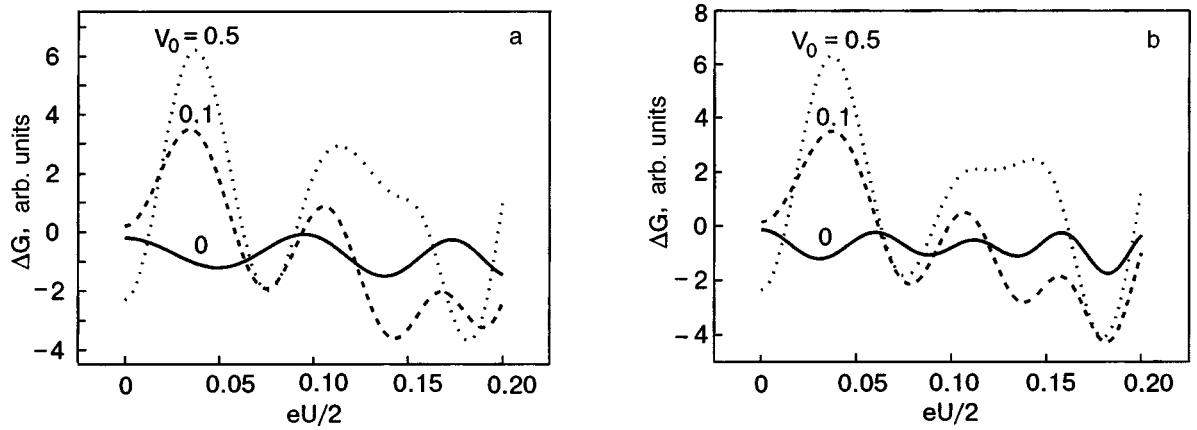

FIG. 3. Dependence of the conductance on $eU/2$ (in units of the Fermi energy) in the presence of two defects in the contact (impurities located on one side (a) and on different sides (b) of the barrier); $\rho_1=\lambda\!\!\!^{-}_F$, $\rho_2=1.5\lambda\!\!\!^{-}_F$, $g_0=0.1$, $R=3\lambda\!\!\!^{-}_F$, $V_0=mV/(\hbar^2k_F)$, $g_0=mg/(\pi R^2\hbar^2k_F)$.

responds to the first and second terms in formula (20). It is interesting to note that the conductance of the contact contains a term proportional to g, which is absent when impurity scattering processes are taken into account with the quantum analog of the collision integral, for example. Although this term vanishes after averaging over positions of a large number of impurities, in a mesoscopic contact with several defects and a barrier it can play a decisive role. The additional phase shift depends on the distance between impurities, their distribution relative to the barrier, the possible variation of the magnitude of the wave vector k_β (the index β of the quantum mode) in scattering on an impurity and also in the reflection of an electron from the barrier. We note that the interaction of an electron with the barrier in the framework of this model does not lead to mixing of the quantum modes. The contribution of the interference terms to the conductance depends substantially on the position of the impurities relative to the axis of the contact, $\mathbf{R}_i$, and is determined by the local density of states for the βth mode at the point $\mathbf{R}_i$: $\nu_\beta(\mathbf{R}_i,E)=m\psi^2_{\perp\beta}(\mathbf{R}_i)/(\hbar^2k_\beta(E))$. Since the transverse wave functions $\psi_{\perp\beta}$ vanish at certain points, the scattering on impurities located near such points contributes little to the conductance of the βth mode. In particular, impurities on the surface do not influence the conductance.

Figure 3 shows the voltage-dependent part of the conductance $\Delta G(U)$ for various values of the barrier potential V and for two impurities located on the same side or on different sides of the barrier (all the numerical calculations were done at zero temperature). These curves show that even at relatively small values of V the contribution corresponding to a single act of scattering on an impurity and reflection from the barrier becomes dominant. For comparison Fig. 4 shows the analogous dependence $\Delta G(U)$ calculated in second-order perturbation theory in the coupling constant g.

Figure 5 shows the dependence $\Delta G(U)$ for a single-mode channel $\beta=(0,1)$ at different values of its radius. At $R=3\lambda\!\!\!^{-}_F$ the energy of the quantum mode ε_{01} is quite far from the Fermi level ε_F, while for $R=2.6\lambda\!\!\!^{-}_F$ it is found near the Fermi level. These dependences clearly demonstrate suppression of the oscillations of $\Delta G(U)$ near the steps where the conductance jumps occur; this agrees with the experimental result of Ref. 14. In the framework of our model this decrease in the conductance oscillations has a natural physical explanation. The coefficient of transmission of an electron through the barrier, T^b_{01} (14), depends on the mode energy ε_β, which, according to formula (7), decreases with increasing radius R. When R approaches the value R_2 corresponding to the entry of the next mode with a higher energy ε_{11} in the channel, the coefficient T^b_{01} increases and the interference contribution due to reflection from the barrier is

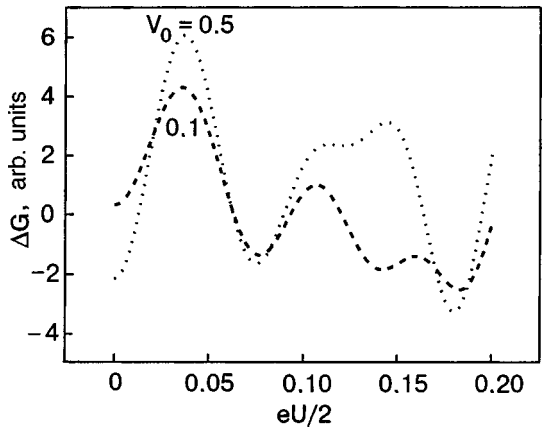

FIG. 4. Dependence of the conductance on $eU/2$ (in units of the Fermi energy) calculated in the linear approximation in the coupling constant g; $\rho_1\equiv\lambda\!\!\!^{-}_F$, $\rho_2=1.5\lambda\!\!\!^{-}_F$, $g_0=0.1$, $R=3\lambda\!\!\!^{-}_F$.

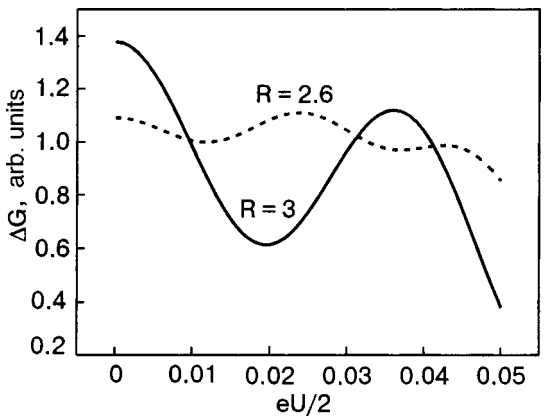

FIG. 5. Dependence on $eU/2$ (in units of the Fermi energy) of the conductance of a single-mode channel ($\beta=(0,1)$) for different values of the radius of the contact (the radius is indicated in units of $\lambda\!\!\!^{-}_F$); $g_0=0.1$, $V_0=0.1$.

minimum. The conductance oscillations are small near $R = R_2$ in the two-mode channel ($R > R_2$) as well, since $T_\beta^b \to 0$ for $E \to \varepsilon_\beta$, as can easily be seen from formula (14).

CONCLUSION

In this paper we have investigated theoretically the nonlinear conductance $G(U)$ of a quantum channel containing single impurities and a barrier. It is shown that the additional phase shift of the wave function, which depends on the distances between impurities or between impurities and the barrier, leads to oscillations of the transmission probability of an electron through the contact as a function of the electron energy E. Upon reflection of the electron from the barrier or transmission through it, the electron wave function also acquires a certain phase $\varphi_\beta(E)$. Increasing the applied voltage U alters the energies of the incoming electrons, leading to a nonmonotonic dependence of $G(U)$. The function $G(U)$ is aperiodic (it cannot be represented by a finite number of Fourier harmonics with respect to the voltage U) because of the complicated dependence of the phase of the wave functions on the energy E. The amplitude of the nonmonotonicities of the conductance $G(U)$ is determined by the distribution of impurities relative to the axis of the contact. Impurities located at points where the local density of electron states for one of the quantum modes vanishes and impurities on the surface of the contact do not influence the contribution to the conductance from that mode. We have shown that the reflection of electrons from a barrier in the contact become the main cause of nonmonotonic behavior of $G(U)$ already at extremely small amplitudes of that reflection (the absolute value of the conductance is close to the value it has in a ballistic contact in the absence of a barrier). The results obtained provide evidence that the energy dependence of the probability of transmission of electrons through the barrier can account for the experimentally observed[14] suppression of conductance oscillations of a single-mode contact having a diameter close to the value corresponding to the entry of the next quantum mode.

In closing the authors expression their gratitude to A. N. Omel'yanchuk for a discussion of the results of this study and for helpful comments.

*E-mail: avotina@ilt.kharkov.ua

[1] R. Landauer, IBM J. Res. Dev. **1**, 223 (1957).
[2] M. Buttiker, Phys. Rev. Lett. **57**, 1761 (1986).
[3] Ya. M. Blanter and M. Buttiker, Phys. Rep. **336**, 1 (2000).
[4] N. Agrait, A. L. Yeyati, and J. M. van Ruitenbeek, Phys. Rep. **377**, 81 (2003).
[5] A. Namiranian, Yu. A. Kolesnichenko, and A. N. Omelyanchouk, Phys. Rev. B **61**, 16796 (2000).
[6] M. E. Flatté and J. M. Byers, Phys. Rev. B **53**, R10536 (1996).
[7] E. Granot, cond-mat/0303347 **v1**, (2003).
[8] M. I. Molina and H. Bahlouli, Phys. Lett. A **284**, 87 (2002).
[9] I. E. Aronov, M. Jonson, and A. M. Zagoskin, Appl. Phys. Rep. **93**, 57 (1994).
[10] Ch. S. Kim, O. N. Roznova, A. M. Satanin, and V. B. Stenberg, Zh. Éksp. Teor. Fiz. **121**, 1157 (2002) [JETP **94**, 992 (2002)].
[11] N. G. Galkin, V. A. Geyler, and V. A. Margulis, Zh. Éksp. Teor. Fiz. **118**, 223 (2000) [JETP **91**, 197 (2000)].
[12] D. Boese, M. Lischka, and L. E. Reichl, Phys. Rev. B **62**, 16933 (2000).
[13] C. Untiedt, G. Rubio Bollinger, S. Vieira, and N. Agrait, Phys. Rev. B **62**, 9962 (2000).
[14] B. Ludoph and J. M. van Ruitenbeek, Phys. Rev. B **61**, 2273 (2000).
[15] D. L. Maslov, C. Barnes, and G. Kirczenow, Phys. Rev. Lett. **70**, 1984 (1993).
[16] Yu. A. Kolesnichenko, A. N. Omelyanchouk, and I. G. Tuluzov, Physica B **218**, 73 (1996).
[17] E. N. Bogachek, A. M. Zagoskin, and I. O. Kulik, Fiz. Nizk. Temp. **16**, 1404 (1990) [Sov. J. Low Temp. Phys. **16**, 795 (1990)].
[18] C. W. J. Beenakker, Rev. Mod. Phys. **69**, 731 (1997).
[19] I. O. Kulik, A. N. Omel'yanchuk, and R. I. Shekhter, Fiz. Nizk. Temp. **3**, 1543 (1977) [Sov. J. Low Temp. Phys. **3**, 740 (1977)].
[20] L. I. Glazman and A. V. Khaetskiĭ, JETP Lett. **48**, 591 (1988).
[21] A. M. Zagoskin, JETP Lett. **52**, 435 (1990).
[22] P. A. Lee and D. S. Fisher, Phys. Rev. B **23**, 6851 (1981).

Translated by Steve Torstveit

LOW-DIMENSIONAL AND DISORDERED SYSTEMS

Vibrational spectrum in the vicinity of a local mode in linear chains with isotopic impurities

M. A. Ivanov,* Yu. V. Skripnik, and V. S. Molodid

G. V. Kurdyumov Institute of Metal Physics, National Academy of Sciences of Ukraine, pr. Vernadskogo 36, Kiev 03142, Ukraine

(Submitted July 15, 2003; revised September 8, 2003)
Fiz. Nizk. Temp. **30**, 216–225 (February 2004)

The vibrational spectrum in the vicinity of the frequency of a local vibration of an isolated light isotopic impurity in a one-dimensional disordered chain containing such impurities is calculated numerically. Chains consisting of 10^8-10^9 atoms, corresponding to macroscopic samples several centimeters in size, are used. A complex hierarchical structure of the spectrum is obtained for this system. The results of the numerical calculations are compared with simple analytical expressions. It is shown that the smoothed density of states in a narrow neighborhood of the local mode can be obtained to sufficient accuracy from arguments based on separating out the nearest neighbor of the chosen impurity atom. It turns out that the expression for the density of states obtained in that manner gives an acceptable result not only outside but also inside the region of concentration broadening of the local mode. © *2004 American Institute of Physics.* [DOI: 10.1063/1.1645169]

1. INTRODUCTION

Determination of the vibrational spectra of disordered systems is a traditional topic in condensed matter physics. Such spectra are of great interest in the study of the properties of crystals at low temperatures, where they determine a wide group of observable physical properties. The problem of the vibrational spectrum of a nonideal crystal reduces to one of solving a system of equations equal in number to the product of the dimensionality times the number of atoms in the system. Since translational symmetry is absent and often there are no other ways of simplifying the problem, various approximate analytical and numerical methods of solution have been developed for the physically most important models of disorder.

Beginning with the pioneering work of I. M. Lifshits,[1,2] many authors have proposed different analytical methods for determining the structure of the vibrational spectrum of disordered systems, often based on comparatively simple model systems. One such widely used model is the linear chain with nearest-neighbor interaction and substitutional disorder. Despite its simplicity, it can describe many properties of real physical objects such as chain crystals and even some optically inhomogeneous media.[3,4] Particular interest in disordered systems with reduced dimensionality arose after the discovery of high-temperature superconductivity.

However, the exact equation[5] from which one can determine the spectrum of such a chain is inconvenient to apply in the general case. Other known approaches to the solution of this problem often assume that there is some small parameter or restrict consideration to some definite spectral intervals. In particular, a wide group of studies has been done on the assumption that there is an isolated impurity center or an isolated defect of the type consisting of a pair of impurities (see, e.g., Refs. 6 and 7).

Numerical modeling is extremely important and useful in the analysis of the spectra of disordered systems. In particular, it can permit one to design an experiment or to check results obtained analytically. Back in the 1960s Dean[8] carried out calculations of the spectra of disordered chains at rather high (0.1–0.5) concentrations of impurities. In spite of the fact that the density of vibrational states could not be analyzed in detail, Dean's studies showed that the high-frequency part of the spectrum in the presence of a light isotopic impurity is very choppy. It was also established that certain spectral lines located near the local mode correspond to the simplest clusters of impurity atoms. In addition, because of the impossibility of calculating chains of sufficient length, cases of low impurity concentrations have not been studied. However, it is just such a case that is of particular interest, since, on the one hand, even extremely low impurity concentrations can in some cases have a substantial influence on the properties of crystals and, on the other hand, it is at low impurity concentrations that one can neglect the indirect interaction between impurities and for which it has been possible to obtain some analytical results.

Today's computational facilities enable one to treat chains in which the number of atoms corresponds to a sample size of several centimeters or more. As a result, one can study the structure of the vibrational spectrum in much greater detail, focusing attention on different spectral intervals, and can include the case of low impurity concentrations. This, in turn, can aid in the construction of an adequate analytical method of determining the spectrum.

This paper is devoted to an analysis of the vibrational spectrum of a disordered chain near a local mode caused by

the presence of light substitutional impurities and to a comparison of the results of a numerical simulation with some analytical results available for such a model system.

2. QUALITATIVE DESCRIPTION OF THE SPECTRUM NEAR THE LOCAL MODE FREQUENCY

Let us consider a disordered chain consisting of two types of atoms interacting only with nearest neighbors. We shall assume that the presence of a defect at one of the sites of a given chain leads only to a change in the mass of the given atom, while the rest of the parameters all remain unchanged. The impurities will be assumed to be distributed randomly with some concentration c, so that this model corresponds completely to the approximation of an isotopic substitutional impurity.

The equations of motion of such a chain of N atoms with fixed ends has the form

$$\beta_n u_{n-1}+(\alpha_n-\omega^2)u_n+\beta_{n+1}u_{n+1}=0, \quad (1)$$

$$n=1,2...N, \quad u_1=u_{N+1}=0,$$

where ω is the vibrational frequency of the atoms, m_n is the mass of the nth atom, $u_n=p_n\sqrt{m_n}$, p_n is the displacement of the nth atom from its position at rest,

$$\alpha_n=\frac{2\gamma}{m_n}, \quad \beta_n=-\frac{\gamma}{\sqrt{m_{n-1}m_n}}, \quad (2)$$

and γ is the bond stiffness.

It is well known that in the case of a light impurity in a one-dimensional system there exists a local mode lying above the maximum frequency of the acoustic band. The frequency of the local mode is determined by the expression

$$1=\nu g_{00}, \quad (3)$$

where g_{00} is a diagonal element of the Green's function in the site representation, and ν is a perturbation. In the case of an isotopic defect

$$\nu=\varepsilon\omega^2, \quad \varepsilon=\frac{m_0-m_d}{m_0}, \quad (4)$$

where m_0 and m_d are the mass of the host and impurity atoms, respectively, ε is the mass defect (for local vibrations to arise it is necessary to satisfy the condition $m_d<m_0$, so that in this case $0<\varepsilon<1$). The solution of equation (3) for the one-dimensional case has the well-known and simple form $\omega_L^2=1/(1-\varepsilon^2)$.

Interaction between impurities leads to splitting of the mode and the appearance of fine structure in the spectrum. For example, the interaction of two impurities leads to splitting of the local mode into two, the distance between their frequencies decreasing with increasing distance between defects. The frequencies of these modes (symmetric and antisymmetric modes, respectively) are given in implicit form by the equations

$$1=\tau^2 g_{0R}^2, \quad \tau=\frac{\nu}{1-\nu g_{00}}, \quad (5)$$

where R is the distance between the impurities of the pair (in units of the interatomic distance). In the case considered, the Green's function g_{0R} has the form[9]

$$g_{0R}=\frac{1}{N}\sum_k \frac{e^{-ikR}}{\omega^2-\omega_k^2}=\frac{(-1)^R(\sqrt{\omega^2}-\sqrt{\omega^2-1})^{2R}}{\sqrt{\omega^2}\sqrt{\omega^2-1}}, \quad (6)$$

where the maximum vibrational frequency of the ideal chain consisting only of atoms of mass m_0 is assumed equal to unity. Thus the frequencies ω_R of the pair modes for impurity atoms separated by a distance R can be determined from the equation

$$\left(\frac{1}{\varepsilon}\sqrt{\frac{\omega_R^2-1}{\omega_R^2}}-1\right)\pm(\sqrt{\omega_R^2}-\sqrt{\omega_R^2-1})^{2R}=0. \quad (7)$$

Below, for obtaining analytic expressions for the density of states in the vicinity of the local mode frequency ω_L we shall use the approximate solution of equation (7) in this region. Here the impurities in a pair will be placed far enough apart that the shift of the pair modes from the initial frequency is substantially less than the distance between it and the band edge. Expanding the left-hand side of (7) about the local mode frequency, we find that the frequency ω_R of these pair modes are distributed almost symmetrically with respect to ω_L and lie a distance away from it given by[9]

$$\Delta(R)=\omega_R^2-\omega_L^2\approx\pm\left(\frac{1-\varepsilon}{1+\varepsilon}\right)^R\frac{2\varepsilon^2}{(1-\varepsilon^2)^2}. \quad (8)$$

In other words, the modes lying a distance Δ from the local mode ($\Delta=\omega^2-\omega_L^2$) correspond to pairs of impurities found a distance apart equal to

$$R\equiv R(\Delta)=\ln\left(\Delta\frac{(1-\varepsilon^2)^2}{2\varepsilon^2}\right)\left(\ln\frac{1-\varepsilon}{1+\varepsilon}\right)^{-1}. \quad (9)$$

Starting from simple qualitative arguments one can easily determine the number of impurity modes that at a low defect concentration fall within a certain neighborhood of the square frequency of the local vibration.[10] The modes corresponding to a pair of impurities separated by a distance greater than the chosen value of R will be split by an amount not exceeding $\Delta(R)$. The probability that the nearest impurity is found a distance greater than or equal to R from some given impurity is

$$P(R)=(1-c)^{2(R-1)}. \quad (10)$$

As a result, by substituting (9) into (10) and neglecting the discreteness, we find that the number of modes N_Δ that fall into a neighborhood of half-width Δ around the square frequency of the local vibration is equal to

$$N_\Delta=NcP(R(\Delta))=Nc\left(\frac{\Delta(1-\varepsilon^2)^2}{2\varepsilon^2}\right)^q, \quad (11)$$

where

$$q=\frac{2\ln(1-c)}{\ln\frac{1-\varepsilon}{1+\varepsilon}}.$$

An expression for the density of states averaged over some frequency interval [the smoothed density of states $\rho(\Delta)$] can be obtained by differentiation of expression (11) with respect to the square frequency:

$$\rho(\Delta)=c^2\left(\left|\frac{\Delta(1-\varepsilon^2)^2}{2\varepsilon^2}\right|\right)^q\left(\left|\Delta\right|\left|\ln\frac{1-\varepsilon}{1+\varepsilon}\right|\right)^{-1}. \tag{12}$$

A formula similar to Eq. (12) but for the electron problem was obtained by Lifshits.[11]

It should be noted that expressions (11) and (12) have in essence been obtained from analysis of the structure of pair modes of the spectrum. Since at a low concentration of impurities the frequency spectrum above the initial acoustic band, except for an extremely narrow neighborhood of the local mode, is formed mainly by just such pair impurity modes, its approximate description by the monotonic function (12) is correct only under the condition that at least several of them fall into the averaging region. In other words, expression (12) is valid in the case when the relative variation of the density of states over the discreteness interval associated with the pair modes is small, i.e., under the condition

$$\frac{1}{\rho(\Delta)}\frac{\partial\rho(\Delta)}{\partial R}\ll 1. \tag{13}$$

When the form of $\rho(\Delta)$ described by expression (12) is taken into account along with the relation between Δ and R, i.e., with the discreteness of the pair modes according to Eq. (8), we find that at low impurity concentrations criterion (13) takes the form

$$-\ln\frac{1-\varepsilon}{1+\varepsilon}\ll 1. \tag{14}$$

Thus expression (12) for the smoothed density of states (and others like it) can be used to some degree or other for description of the states only in the case of local modes lying near the edge of the main band.

We also note that previously in a number of papers[14–18] an analysis of the convergence of the series describing cluster expansions in complexes of interacting impurity centers indicated a region of concentration broadening Δ_c around the local vibration, i.e., a frequency interval $(\omega_L^2\mp\Delta_c)$, within which the spectrum cannot be described by those cluster expansions. The value of Δ_c is determined by the interaction of impurities at the mean distances, i.e.,

$$\Delta_c=\Delta(\chi R_c), \tag{15}$$

where $R_c=1/c$ is the mean distance between impurities, and χ is a numerical coefficient which we take equal to 0.5 in our estimations. Below, in making a comparison of the analytical and numerical results, we shall use Δ_c for analysis of the domains of applicability of the different approaches.

3. NUMERICAL RESULTS

An exact numerical calculation of the spectrum of a disordered crystal of macroscopic size (even for the one-dimensional case) involves a considerable volume of computations. The number of operations necessary to determine all of the vibrational eigenfrequencies of a linear chain is proportional to $N^2/2$. The calculation of the spectrum can be optimized using a theorem of negative eigenvalues proved by Dean.[8,12,13]

According to that theorem, the number of eigenfrequencies lying in an interval $(0,\omega)$ for the model system chosen above with only nearest-neighbor interactions is equal to the number of negative terms in the sequence of values $g_i(\omega^2)$, which are determined by the recursion formula

$$g_i(\omega^2)=(\alpha_i-\omega^2)-\beta_i^2\frac{1}{g_{i-1}(\omega^2)}, \tag{16}$$

where α_i and β_i are scalar quantities defined in relations (2), and the index i goes over all atoms of the chain. Thus the number of operations necessary to determine the number of modes lying in an interval $(0,\omega)$ is proportional to N.

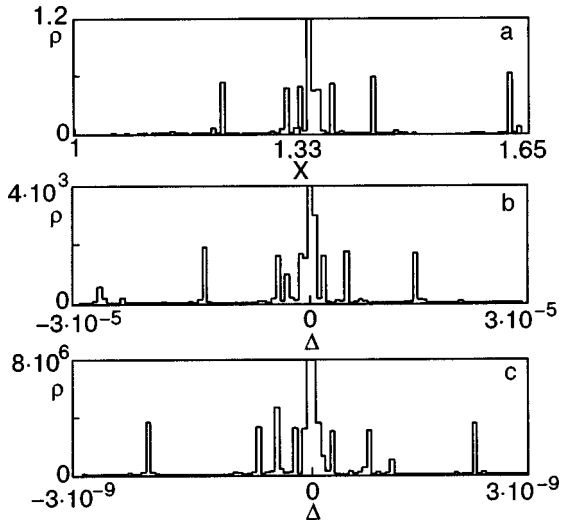

FIG. 1. Structure of the vibrational spectrum near a local level for different magnifications of the frequency scale. The concentration $c=1/20$; $\varepsilon=0.5$; chain length $N=10^8$. The density of states normalized to unity is plotted along the vertical axis and the squares of the frequencies along the horizontal axis. In Fig. 1a the X axis is labeled with the true values of the squares of the frequencies (1 equals the edge of the unperturbed spectrum), while in Figs. 1b and 1c the values are measured from the frequency of the local level.

Figure 1 shows the structure of the spectrum near the local mode frequency for an isotopic impurity with $m=1/2$ in various spectral intervals. In Fig. 1a the distribution of the local mode is shown relative to the band edge $(\omega^2=1)$, and in Figs. 1b and 1c the zero is placed at the vibrational frequency of an isolated impurity. The position of the main levels shown in this figure agree to high accuracy with the solutions obtained using expression (7) for isolated pairs of impurities, including for the levels lying farthest from the unperturbed local mode.

It should be noted that the transition to higher magnification of the scale near the local frequency does not alter the overall form of the spectrum. Such a situation is analogous to that observed for fractal structures. It should also be noted that here, unlike the three-dimensional case, the intensity of the central peak is always much greater than that of the side peaks, even in very close proximity to the local mode of an isolated isotope, in spite of the difference in the step width of the histogram. In this case the density of states increases monotonically as the local mode frequency is approached.

Let us estimate the chain length necessary for obtaining an adequate description of the spectrum above the initial acoustic band. As the chain length increases, new modes will always appear, bringing with them new nuances in the fine structure of the spectrum. Strictly speaking, any spectrum of

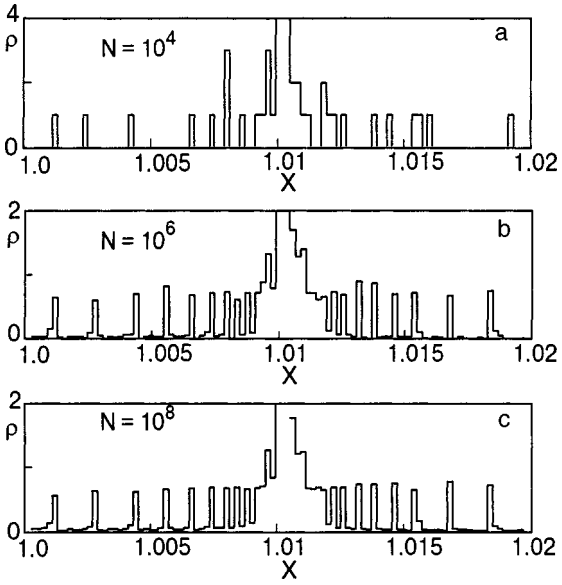

FIG. 2. Structure of the vibrational spectrum near a local level for different values of the number of atoms in the chain, N; here $c=1/100$, $\varepsilon=0.5$. The squares of the frequencies are plotted along the X axis.

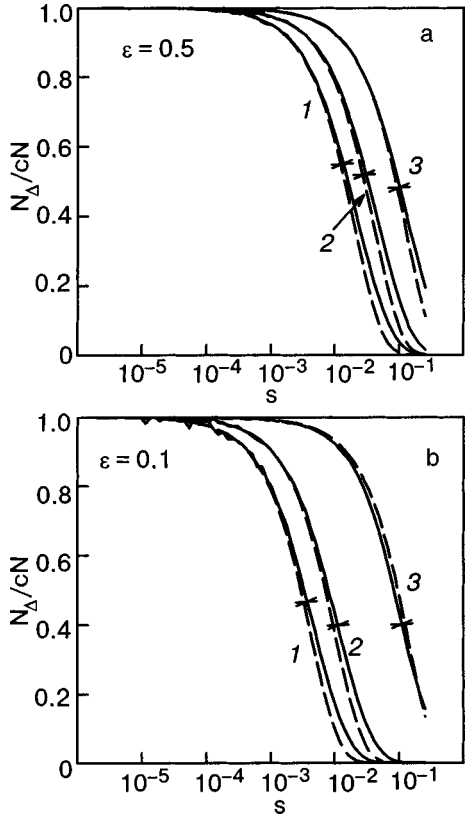

FIG. 3. Number of levels falling into a Δ neighborhood of the local level $(x_L-\Delta,\ x_L+\Delta)$ as a function of the impurity concentration, for $\Delta=10^{-12}$ (*1*); 10^{-6} (*2*), 10^{-2} (*3*). The dashed lines show the calculation according to Eq. (11). $N=10^8$.

a chain of finite length is unique and does not correspond exactly to the spectrum of an infinite system. It was mentioned above that at a low impurity concentration the spectrum above the acoustic band of a chain of heavy atoms consists mainly of pair impurity modes. The probability of pair formation for impurities located close together is proportional to the square of the concentration; consequently, the chain length must be such that the inequality

$$c^2N \gg 1 \tag{17}$$

holds by an extremely wide margin. It will be shown below that the requirements on the chain length become more stringent for the nearest neighborhood of the local vibration, where it is necessary to take widely separated defect pairs into account.

Figure 2 shows how the spectrum depends on the chain length for an impurity mass $m_d=0.9$ and a concentration $c=0.01$. As is seen in Fig. 2a, a chain length of 10^4 atoms is insufficient even to reveal all of the pair modes. At a chain length of the order of 10^6 atoms (Fig. 2b) all the pair modes are present, but their spectral weight changes for different realizations of the chain and contain a substantial noise component. Only for chains of the order of 10^7 and more atoms long (Fig. 2c) does the overall form of the spectrum cease to depend on the chain length and become similar to the spectrum of an infinitely long chain.

In this paper numerical calculations are done for chains consisting of 10^8-10^9 atoms, corresponding to objects several centimeters long. This makes it possibility to obtain statistically reliable and reproducible results conveying the basic features of the spectrum above the initial acoustic band at impurity concentrations above 10^{-3}.

Figure 3 shows, for two values of the impurity mass, the curves obtained numerically for the number of modes (normalized to cN) that fall into a Δ neighborhood of the local vibration as a function of impurity concentration for different values of Δ (the solid curves). The irregular trend of the curves for concentrations of 10^{-4} and less is due to the finite size of the chains generated. The dashed curves are obtained from expression (11). The crosses on the curves denote the concentration values for which the value of Δ_c coincides with the specified value of the interval Δ (the region of concentrations where $\Delta_c<\Delta$ lies to the left).

The best agreement of the analytical and numerical results is observed at a relatively low impurity concentration, when Δ_c is less than or of the order of Δ. However, as can be seen in Fig. 3, good agreement is obtained even in the region where $\Delta_c>\Delta$, and with increasing Δ the agreement of the two results extends to ever higher concentrations. Thus for a one-dimensional chain the results obtained using separation of the closest pair is valid in a narrow neighborhood of the local vibration, with a width less than the concentration broadening of the latter.

In Fig. 4 one can see the good agreement of the smoothed density of states (12) with the calculated density of states for a value of the mass defect satisfying (13). Figures 4a,b,c respectively show the spectra inside and near the boundary and outside the concentration broadening region, respectively. Here small values of the mass defect ($\varepsilon\approx0.01$) were chosen because they make it possible to analyze in greater detail the fine structure of the spectrum near a local mode and accordingly to do a more detailed comparison of the numerical and analytical results.

The numerical results obtained show that the density of states always increases as the frequency of the local vibration is approached. However, according to Eq. (12), such growth

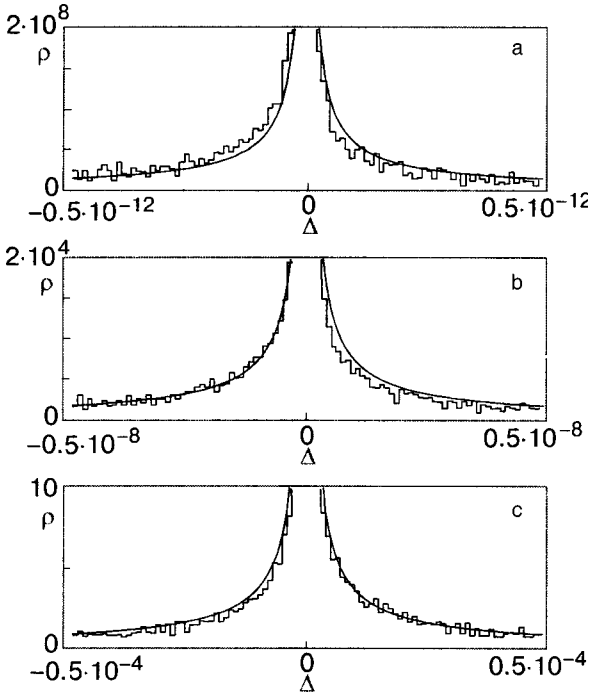

FIG. 4. Comparison of the smoothed spectrum described by expression (12) with the numerically calculated spectrum (for $N=5\times10^8$ and $\varepsilon=0.01$; $c=10^{-3}$) inside (a), near (b), and outside (c) the concentration broadening.

of the density of states should take place only under the condition

$$q<1. \tag{18}$$

Figure 5a shows the region in which condition (18) holds. The lines bounding it can be described approximately by the relation $c\approx\varepsilon$. A calculation for the case $c>\varepsilon$, presented in Fig. 5b, shows that the density of states nevertheless increases as the local mode frequency is approached. This fact is explained by a restructuring of the spectrum starting at $c\approx\varepsilon$, so that expression (12) is no longer valid.

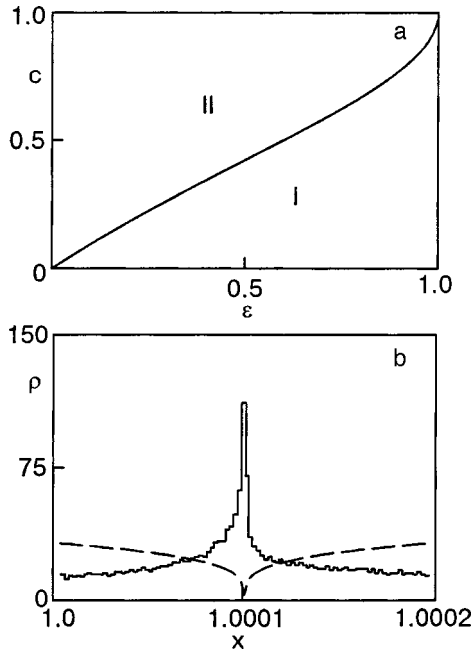

FIG. 5. a—Diagram determining the regions of growth (I) and decay (II) of the density of states (according to expression (12)). b—Behavior of the density of states near a local level for $c>\varepsilon$ ($c=1/80$, $\varepsilon=0.01$). The dashed curve is the analytical calculation (12), the solid line is the result of a numerical calculation for $N=10^8$.

4. MODIFIED EXPANSION IN CONCENTRATIONS

The direct expansion of the thermodynamic quantities in disordered systems in powers of the impurity concentration was proposed by Lifshits.[11,14] When only the terms corresponding to pairs are taken into account and the contribution from clusters containing three or more impurities are neglected, this expansion for the density of vibrational states can be written

$$\rho(\omega^2)=c\,\delta(\omega^2-\omega_L^2)+c^2\sum_R\,[\,\delta(\omega^2-(\omega_R^l)^2)+\delta(\omega^2-(\omega_R^r)^2)-2\,\delta(\omega^2-\omega_L^2)\,]+\ldots, \tag{19}$$

where ω_R^l and ω_R^r are the frequencies of the pair modes lying to the left and right of the local mode frequency. This expansion is equivalent to the so-called unrenormalized cluster expansion[15] and is valid outside the region of concentration broadening.

If one considers only the terms mentioned, then the density of vibrational states will have the form of a ''universal'' function of frequency, determined by the position of the pair modes, which varies with the impurity concentration in proportion to c^2. In the case when the local vibration lies close to the band edge, one can introduce a smoothed density of states, as above, if the summation in formula (19) is replaced by integration:

$$\rho_c(\omega^2)=\frac{c^2}{|\omega_L^2-\omega^2|\left|\ln\dfrac{1-\varepsilon}{1+\varepsilon}\right|}. \tag{20}$$

Figure 6 shows a comparison of $\rho(\omega^2)/c^2$ obtained with the use of expressions (20) and (12). It is seen that they differ appreciably from each other inside the concentration broadening region, in that frequency interval where expression (12) still agrees fairly well with the results of the numerical simulation. It would be interesting to introduce changes in expression (19) such that the results obtained on the basis of that expression would agree with the numerical simulation over a wider range of frequencies.

To obtain better agreement of the numerical and analytical results and to find an interpolation formula for the averaged density of states we shall choose the weight factor in the pair mode not in the form c^2, as was done in (19), but in the next more accurate approximation, in which the combinatorics of the occupation of sites by impurities giving rise to some pair mode or other is taken into account:

$$p(R)=c^2(1-c)^{\gamma R}, \tag{21}$$

where γ is a numerical coefficient. Below we shall consider this coefficient to be a function of R and, moreover, different for pair modes having higher or lower frequencies than that of an isolated local mode. Thus in place of the expansion (19) we get

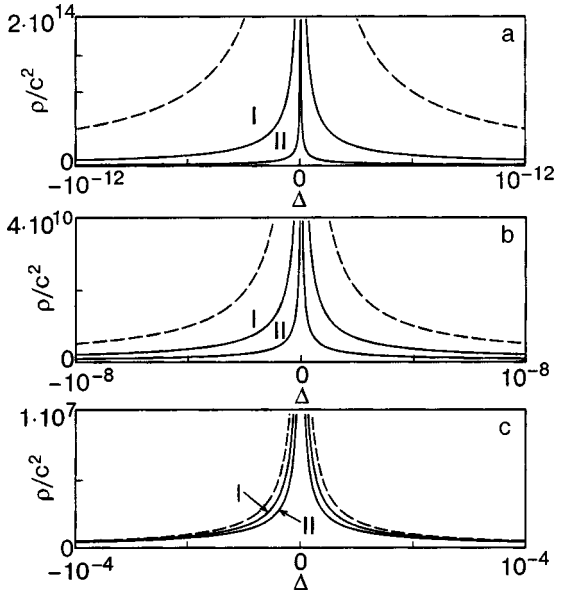

FIG. 6. Comparison of the analytical expressions for the density of states, normalized to c^2, in the neighborhood of a local level. The dashed line is the concentration-independent expression that follows from Eq. (20); the solid curves are calculated according to Eq. (12): for $c=1/1000$ (I) and $c=1/500$ (II) (panels a–c correspond to different values of the scale of the region near the local level); $\varepsilon=0.01$.

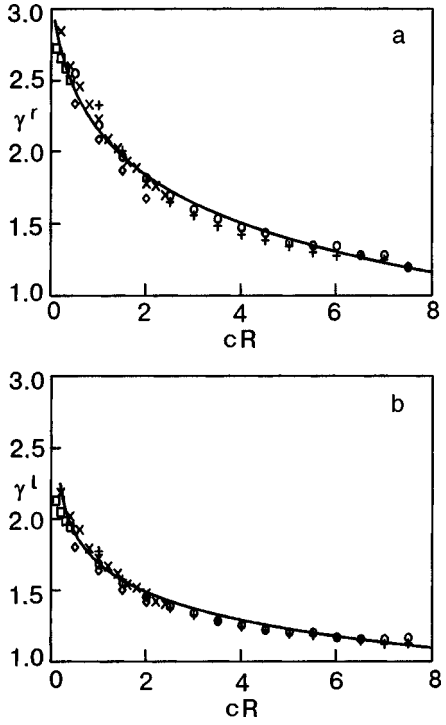

FIG. 7. Dependence of the exponent $\gamma^{l,r}(R)$ on the distance between impurities in a pair (the value of $cR=R/R_c$ is plotted along the horizontal axis) for different values of the mass defect and concentration: $\varepsilon=0.6$, $c=1/20$ ($\diamond$); $\varepsilon=0.6$, $c=1/100$ ($\square$); $\varepsilon=0.9$, $c=1/20$ ($\bigcirc$); $\varepsilon=0.95$, $c=1/100$ ($\times$); $\varepsilon=0.95$, $c=1/20$ ($+$).

$$\rho(\omega^2)=c\,\delta(\omega^2-\omega_L^2)+c^2\sum_R\,[(1-c)^{\gamma^l(R)R}\times\delta(\omega^2-(\omega_R^l)^2)+(1-c)^{\gamma^r(R)R}\delta(\omega^2-(\omega_R^r)^2)+\ldots, \tag{22}$$

where $\gamma^l(R)$ and $\gamma^r(R)$ are the indicated numerical coefficients for the pair modes found to the left and right of the local mode frequency.

It is expected that in a frequency region sufficiently far from the local mode, as a consequence of the exponentially rapid decay of the interaction between impurities, the coefficient $\gamma^{l,r}(R)$ should be equal to three, which meets the simplest requirement that the impurity atom nearest to the pair under consideration be found at a distance greater than the distance between the impurity atoms in that pair. Thus the condition $\gamma^{l,r}(R)=3$ will most likely hold for the impurity modes corresponding to relatively short distances between impurities (but nevertheless sufficiently long in comparison with the interatomic distance). On the other hand, it is interesting to note that for $\gamma^{l,r}(R)=2$, an averaging of expression (22) over a frequency interval corresponding to several pairs of levels will lead to an expression for the smoothed density of states which agrees exactly with (12). Since the latter expression was obtained starting from an analysis of the density of states near the central peak, even though the heuristic discussions also correspond to the singling out of pairs of impurity atoms, one can expect that the value $\gamma^{l,r}(R)=2$ will correspond to impurities located at significantly larger distances from each other (and hence, to a spectral region closer to the central peak).

To determine the dependences $\gamma^{l,r}(R)$, an averaging of the numerical results was done, as in expression (22), over an interval larger than the distance between successive pair modes. The $\gamma^{l,r}(R)$ curves obtained for different values of the concentration and mass defect are shown in Fig. 7. It is seen that the parameter $\gamma^{l,r}(R)$ is independent of the mass defect and impurity concentration if the unit of distance is taken equal to the mean distance between impurity centers, $R_c=1/c$, and decreases monotonically with increasing R. The curves obtained for pair modes lying to the left and right of the local mode frequency, i.e., $\gamma^l(R)$ and $\gamma^r(R)$, are somewhat different. As expected, the value of the coefficient $\gamma^r(R)$ approaches three at small values of R and is approximately equal to two at $R=R_c=1/c$. Analysis of the calculated spectrum to the left of the local mode (between its frequency and the band edge) shows that the values of $\gamma^l(R)$ come out somewhat smaller (by approximately a factor of 1.2 to 2.3), but the general character of the dependence on R remains unchanged.

Thus if the dependence $\gamma^{l,r}(R)$ is taken into account one can, in particular, obtain a more accurate interpolation formula for the density of states than expression (19). Within the concentration broadening band, when $R\gg R_c$, the coefficient $\gamma^{l,r}(R)$ turns out to be less than two. In this region, generally speaking, neither expansion (19) nor interpolation formula (22) is applicable. However, such values of $\gamma^{l,r}(R)$ formally produce agreement between (22) and the calculated spectrum.

5. CONCLUSION

In this paper we have reported a calculation of the vibrational spectra of disordered linear chains containing a number of atoms which corresponds to samples of macroscopic size. Attention is devoted mainly to the detailed examination

of the structure of the spectrum near the local mode frequency of an isolated impurity and to comparison of the numerical results with some simple analytical expressions.

The comparison showed that the smoothed density of states in a narrow neighborhood of the local mode can be obtained to a sufficient degree of accuracy from arguments based on the singling out of the nearest neighbor to a chosen impurity center. It was found that the expression thus obtained for the density of states gives an acceptable result, including inside the region of concentration broadening of the local mode.

At an impurity concentration much less than the mass defect ε, the main contribution to the spectral energy is given by pair impurity modes. Here, in order to describe the density of states at the boundary of the concentration smearing region and in a somewhat closer vicinity of the local mode it is necessary to assign other, concentration-dependent weight factors to the contributions from the pairs of defects in addition to the direct expansion in powers of the concentration.

It is of interest for the future to continue the numerical studies of the vibrational spectra of long, disordered linear chains, particularly to study the fractal hierarchical structure of the local levels and also the spectrum inside the continuous band both for light and heavy substitutional impurities. This method can be used to treat the analogous problem in the presence of a two-parameter impurity center and to introduce a coupling to the immobile substrate that is different for different atoms. That could be applicable for the description of the vibrations of atoms on the surface of a crystal. With further improvements in computing power this method can also be used for analysis of two- and three-dimensional systems.

*E-mail: ivanov@imp.kiev.ua

[1] I. M. Lifshits, Zh. Éksp. Teor. Fiz. **12**, 117 (1942).
[2] I. M. Lifshits, Zh. Éksp. Teor. Fiz. **17**, 1017 (1947).
[3] J. M. Bendickson, J. P. Dowling, and M. Scalora, Phys. Rev. E **53**, 4107 (1996).
[4] Q. Li, C. T. Chan, K. M. Ho, and C. M. Soukoulis, Phys. Rev. B **53**, 15577 (1996).
[5] F. J. Dyson, Phys. Rev. **92**, 133 (1953).
[6] M. A. Mamaluĭ, E. S. Syrkin, and S. B. Fedos'ev, Fiz. Tverd. Tela (St. Petersburg) **38**, 3683 (1996) [Phys. Solid State **38**, 2006 (1996)].
[7] M. A. Mamalui, E. S. Syrkin, and S. B. Fedosev, Fiz. Nizk. Temp. **25**, 976 (1999) [Low Temp. Phys. **25**, 732 (1999)].
[8] P. Dean, Rev. Mod. Phys. **44**, 127 (1972).
[9] A. A. Maradudin, E. W. Montroll, and G. H. Weiss, *Theory of Lattice Dynamics in the Harmonic Approximation*, Academic Press, New York-London (1963).
[10] E. W. Montroll, A. A. Maradudin, and G. H. Weiss, in *Proceedings of the Stevens Institute Many Body Conference*, Interscience (1964).
[11] I. M. Lifshits, Zh. Éksp. Teor. Fiz. **44**, 1723 (1963) [Sov. Phys. JETP **17**, 1159 (1963)].
[12] P. Dean, Proc. R. Soc. London, Ser. A **254**, 507 (1960).
[13] P. Dean, Proc. R. Soc. London, Ser. A **260**, 263 (1961).
[14] I. M. Lifshits, Usp. Fiz. Nauk **83**, 617 (1964) [*sic*].
[15] M. N. Botvinko, M. A. Ivanov, and Yu. G. Pogorelov, Zh. Éksp. Teor. Fiz. **70**, 610 (1976) [Sov. Phys. JETP **43**, 317 (1976)].
[16] I. M. Lifshits, S. A. Gredeskul, and L. A. Pastur, *Introduction to the Theory of Disordered Systems*, Wiley, New York (1988), Nauka, Moscow (1982).
[17] M. A. Ivanov and Yu. V. Skripnik, Fiz. Tverd. Tela (Leningrad) **32**, 2965 (1990) [Sov. Phys. Solid State **32**, 1722 (1990)].
[18] M. A. Ivanov and Yu. V. Skripnik, Fiz. Tverd. Tela (St. Petersburg) **34**, 351 (1992) [Phys. Solid State **34**, 188 (1992)].

Translated by Steve Torstveit

Electron diffraction study of the structural transformations in free argon clusters

O. G. Danylchenko,* S. I. Kovalenko, and V. N. Samovarov

B. Verkin Institute for Low Temperature Physics and Engineering, National Academy of Sciences of Ukraine, pr. Lenina 47, Kharkov 61103, Ukraine

(Submitted July 23, 2003; revised September 3, 2003)
Fiz. Nizk. Temp. **30**, 226–232 (February 2004)

An electron diffraction technique is used to study the structure of clusters formed in an isentropically expanding supersonic argon jet. The formation of the hcp phase with increasing cluster size is reliably detected for the first time. Observations are made for mean cluster sizes $\bar{N}$ in the range from 1×10^3 to 8×10^4 atoms/cluster. An analysis of the shape of the diffraction peaks is carried out. It is found that in the range $\bar{N}\leqslant 2\times10^3$ atoms/cluster, where the clusters are icosahedral, the profiles of the diffraction peaks are well approximated by a Lorentzian. For fcc clusters with $\bar{N}\geqslant 3\times10^3$ atoms/cluster a better approximation is the standard Gaussian function. In the case $\bar{N}\geqslant 1\times10^4$ atoms/cluster one observes peaks of the hcp phase in addition to the fcc peaks. The intensity of the hcp peaks increases with increasing cluster size, and for $\bar{N}\approx 8\times10^4$ atoms/cluster, the (110), (101), (103), and (202) peaks, characteristic only for the hcp phase, are clearly registered in addition to the fcc peaks. A possible mechanism for the formation of the hcp structure in Ar clusters is proposed. © *2004 American Institute of Physics.* [DOI: 10.1063/1.1645170]

The problem of the formation of hcp–fcc structure in solidified rare gases first came up quite long ago. The essence of this problem is as follows. According to the results of x-ray studies, rare gases (except for helium) in bulk samples crystallize in an fcc lattice. This experimental fact is nontrivial, since a calculation in the approximation of a pair interaction of the atoms (which works rather well for describing the thermodynamic properties of atomic cryocrystals) predicts that the hexagonal close-packed (hcp) structure is stable.[1]

It should be noted, however, that in the case of small particles, when the contribution of the surface energy becomes comparable to the bulk component of the free energy of the system, the formation of the hcp structure is, in principle, possible. This is due to the circumstance that, according to the theoretical notions,[2] the transition from fcc to hcp stacking of the atoms leads to a slight lowering of the surface energy at faces perpendicular to the (111) face, as a result of the increase in the density of surface atoms. Therefore the formation of an hcp phase in thin films and small atomic aggregations of rare gases has long seemed quite probable but has been in need of an experimental check. Observations made previously[3–5] on highly disperse condensed films of Ar, Kr, Xe and Ne have shown that heating them to presublimation temperatures (amounting to about 1/3 of the melting temperature) is always accompanied by intense recrystallization. As a result of that process rather large crystallites form, not only with the fcc but also with the hcp structure.

However, for films condensed on a substrate the results of observations are influenced by a number of poorly controlled factors, including the high probability of quenching of a nonequilibrium state in the sample, contamination of the specimens by impurities of residual gases, and also the interaction of the particles being deposited with atoms of the substrate. For investigation of size effects it is more correct to use clusters free of a substrate, formed in a supersonic gas jet flowing into vacuum. Such objects are free of the above-listed shortcomings typical of condensed films.

The dependence of the structure of Ar clusters on their size has been investigated in a number of experimental studies,[6–8] but reliable evidence of fcc–hcp transformations has not been obtained. The reason is that the objects of study have been atomic aggregations of comparatively small size, containing from a few tens to $(2-3)\times10^3$ atoms/cluster. As a result of a comparison of the observed diffraction patterns with the interference functions calculated with the aid of a computer modeling, the authors have established the following. Small clusters with mean sizes $\bar{N}$ not greater than 10^2 atoms/cluster have an amorphous or polycrystalline structure. In the case when $\bar{N}$ is between 10^2 and 2×10^3 atoms/cluster a multilayer icosahedral stacking of the atoms is realized. According the electron diffraction data,[8] Ar clusters with mean sizes greater than 3×10^3 atoms/cluster have the fcc structure with stacking faults, the density of the latter decreasing with increasing $\bar{N}$. By computer modeling of the diffraction pattern the authors of Ref. 9 came to the conclusion that one of the possible reasons for the poor resolution of the fcc peaks (111) and (200) in crystalline clusters might be the presence in them of not only the fcc phase but also of extremely small, randomly oriented regions with the hcp structure. However, an experiment that would unambiguously confirm the presence of the hcp phase in argon clusters has not been done.

The problem addressed in the present electron diffraction study is to investigate the structure of free Ar clusters over a wide range of mean cluster sizes with the goal of detecting the hcp phase in them. This study has taken a qualitatively

new approach to doing the experiments and processing the data obtained.

EXPERIMENTAL TECHNIQUE

The structure of the clusters was studied on an apparatus consisting of a generator of a supersonic cluster beam and an ÉMR-100M electron diffraction unit. The gases from the supersonic jet were pumped out by a condensation pump with liquid hydrogen. A detailed description of the apparatus is given in Ref. 10. Here we note only the key elements of the experiment.

To create a supersonic gas jet a conical nozzle with a throat diameter of 0.34 mm, a cone angle of 8.6°, and an area ratio of the exit section to the throat of 36.7. For a nozzle with these parameters the Mach number at the exist from the nozzle has the value $M_{\text{out}}=8.0$. The region of intersection of the cluster beam and electron beam was a distance of 110 mm from the nozzle exit. At this distance the gas cooling processes are already completed,[11] and the clusters are found in the equilibrium state. The gas pressure P_0 at the nozzle entrance could be varied from 0 to 0.6 MPa, and the temperature T_0 could be varied from 120 K to room temperature.

As the gas flows through the nozzle into vacuum, thermal energy of random motion of the molecules is converted to kinetic energy of directed motion of the supersonic flow. As a result of the isentropic expansion of the jet the gas temperature falls and the gas is transformed into a supersaturated vapor, and hence conditions of homogeneous nucleation are created, i.e., the formation and growth of clusters of the condensed phase.

Since the expansion of the gas is isentropic, the state of the jet is determined by the equation of the adiabat:

$$P_0 T_0^{\gamma/(1-\gamma)} = \text{const}, \tag{1}$$

where $\gamma = C_p / C_V$ is the ratio of specific heats of the gas at constant pressure and constant volume, respectively. In the case of an ideal gas one has $C_V = \frac{i}{2}R$ and $C_P = C_V + R$, where i is the number of degrees of freedom of a molecule of the gas and R is the universal gas constant. For a monatomic gas such as argon one has $i=3$.

Usually in experiments the two parameters P_0 and T_0 are varied. Using relation (1), one can reduce the situation to a single parameter—the equivalent pressure P_{eq}. Then the values of $\overline{N}$ corresponding to different P_0 and T_0 must be referred to a single temperature. In this study all the observations were referred to $T_0 = 200$ K, and therefore the expression for the equivalent pressure has the form $P_{\text{eq}} = P_0 (T_0/200)^{\gamma/(1-\gamma)}$. It should be noted that the calculation of P_{eq} was done using the value of the exponent $\gamma/(1-\gamma) = -2.29$ established previously for Ar by the authors of a mass spectrometric study.[12] (This value is somewhat smaller in absolute value than the value -2.5 characteristic for an ideal gas.) Subsequently all of the diffraction patterns obtained were referred to an equivalent pressure with an exponent of -2.29.

The size of the clusters, their flux density, and size distribution are specified by the temperature T_0, pressure P_0, and nozzle parameters and by the thermodynamic properties of the gas. For a fixed nozzle geometry the size of the clusters of a given gas and their flux density increase with increasing P_0 and decreasing T_0 (Ref. 12). The temperature of the clusters depends on the species of atoms, and for a supersonic argon jet it is around 38 K.[10] The characteristic mean linear size of the clusters in the approximation of spherical cluster shape is $\delta = a\sqrt[3]{3\overline{N}/2\pi}$ (where a is the lattice parameter of crystalline argon, $\overline{N}$ is the mean number of atoms in a cluster) was obtained as follows.

For clusters with $\overline{N} \geqslant 1\times 10^3$ atoms/cluster the value of δ was found with an accuracy of 10% or better from the total broadening of the diffraction peaks with the use of the Selyakov–Scherrer relation.[13] The correctness of applying the Selyakov–Scherrer relation to crystalline clusters with the fcc structure and $\overline{N} > 10^3$ atoms/cluster has been confirmed by calculations done by the authors of Ref. 14. In addition, in Ref. 8 a comparison of the values of δ measured by independent methods was done: electron diffraction with the use of the Selyakov–Scherrer relation and electron microscopy. Measurements were made on gold island films obtained by the thermal evaporation of Au in high vacuum with deposition on an amorphous carbon film substrate. The values of δ obtained by the two methods were in good agreement, with a disparity of 10% or less.

In the case of clusters with $\overline{N} \leqslant 3\times 10^3$ atoms cluster the value of δ was found by the following technique. In Ref. 10 it was shown by an electron diffraction method that for rare gases with $\overline{N}$ in the range from 1×10^4 to 10^3 atoms/cluster the relation $\overline{N} = \kappa P_0^{1.83}$ holds well for $T_0 = \text{const}$. We note that the mass spectrometric technique for supersonic jets of rare gases[15] has shown that this relation holds even for clusters with $\overline{N} = 10^2 - 10^3$ atoms/cluster. Therefore, by determining the parameter κ for large clusters one can, by specifying P_0, i.e., P_{eq}, establish the value of $\overline{N}$ for small clusters.

With the goal of obtaining a large set of data for a single experiment we used photographic registration of the diffraction pattern. For this we used photographic films designed for nuclear research, with a wide region of linearity of the blackening S as a function of exposure (dose) $Q = I\tau$, where I is the intensity of the electron beam and τ is the exposure time. The electronograms obtained were scanned on a microphotometer with a scanning step of 50 μm. The numerical values of S were processed on a computer to construct the densitometer traces and to isolate the background component of the diffraction patterns, due to incoherent scattering of electrons and to their scattering on gas atoms present in the jet. To separate out the background curve at different parts of the densitometer traces we took the points far from the diffraction peaks and drew through them an approximating curve which was described rather well by the sum of two exponentials $A\exp(-S/r)$ with different parameters A and r.

A densitometer trace before subtraction of the background is shown in Fig. 1a. Figure 1b shows a series of densitometer traces for different equivalent pressures (different values of $\overline{N}$) after subtraction of the background.

The recording of the diffraction patterns was usually limited to values of the diffraction vector $s \approx 6\ \text{Å}^{-1}$ ($s = 4\pi \sin\theta/\lambda$, where θ is the Bragg angle and λ is the electron wavelength).

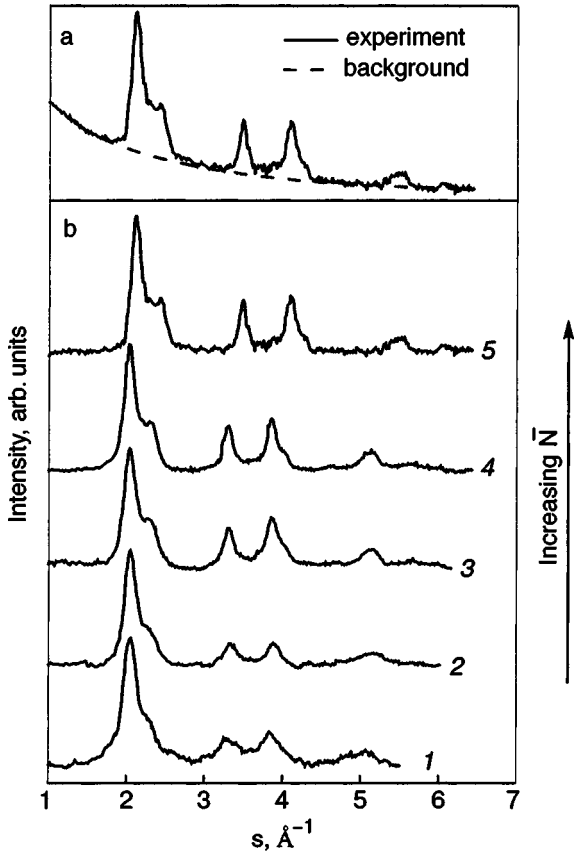

FIG. 1. Densitometer traces for free clusters of argon with $\bar{N}\approx 22.5\times 10^3$ atoms/cluster ($P_{eq}=0.7$ MPa). The dashed curve shows the background component of the diffraction pattern (a). The diffraction patterns after subtraction of the background, for cluster beams with different $\bar{N}$ [10^3 atoms/cluster]: 1.35 ($P_{eq}=0.15$ MPa) (*1*); 2.3 ($P_{eq}=0.2$ MPa) (*2*); 4.8 ($P_{eq}=0.3$ MPa) (*3*); 8.2 ($P_{eq}=0.4$ MPa) (*4*); 22.5 ($P_{eq}=0.7$ MPa) (*5*) (b).

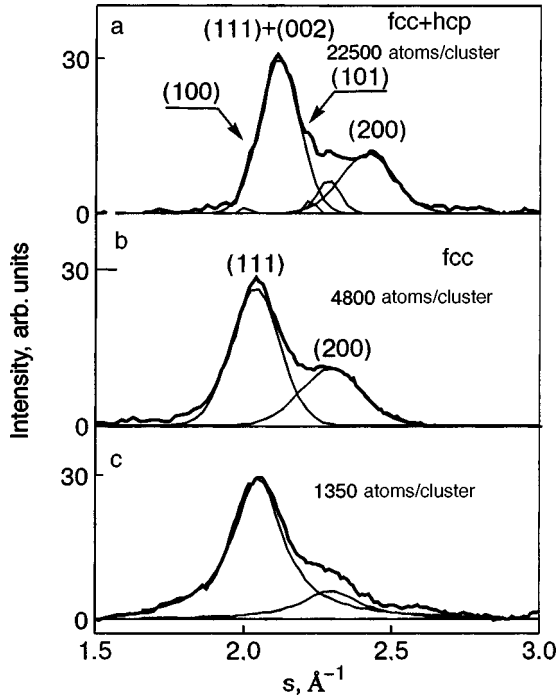

FIG. 2. Fragments of the diffractograms for $\bar{N}\approx(1.35, 4.8, \text{and } 22.5)\times 10^3$ atoms/cluster, approximated by smoothed Gaussian (a,b) and Lorentzian (c) functions. The experimental curves are shown by heavy lines, and the Lorentzian and Gaussian contours by fine lines. The combined model curves coincide with the experimental curves to an accuracy of 3–5%.

RESULTS AND DISCUSSION

Figure 1b shows a series of diffraction patterns corresponding to equivalent pressures at the nozzle entrance, $P_{eq}=0.15$, 0.2, 0.3, 0.4, and 0.7 MPa. The mean size of the clusters corresponding to these pressures are, respectively: $(1.35, 2.3, 4.8, 8.8, \text{and } 22.5)\times 10^3$ atoms/cluster.

It was established previously[7] that in the case $\bar{N}\leqslant(2-3)\times 10^3$ atoms/cluster in argon cluster beams and also in free metal clusters the dominant clusters are atomic aggregations with the icosahedral structure. This assertion is based on the rather good agreement of the positions and relative intensities of the peaks on the experimental diffraction patterns with model interference functions calculated for icosahedral formations of different sizes. The evidence for the icosahedral structure of the small clusters is the more rapid broadening of the diffraction peaks with decreasing linear size of the atomic aggregations than follows from the Selyakov–Scherrer relation and also the fact that the value of the ratio $H_{(311)}/H_{(111)}$ is uncharacteristically low for an fcc structure,[16] where $H_{(311)}$ and $H_{(111)}$ are the heights of the peaks lying in the region of the fcc peaks (311) and (111), respectively. It was determined that the clusters with mean sizes greater than the limit indicated above have the fcc structure with stacking faults, the density of which decreases with increasing $\bar{N}$ (Ref. 8).

In the present study we have for the first time carried out an analysis of the shape of the diffraction peaks with the aid of a computer processing of the experimental results. This analysis was done for cluster beams with $\bar{N}=(1.35, 4.8, \text{and } 22.5)\times 10^3$ atoms/cluster. The results are presented in Fig. 2 in the form of three plots. The intensity on them is expressed in arbitrary units, the intensity of the (111) peak having been scaled to the same value for each curve.

The bottom panel corresponds to clusters with $\bar{N}=1.35\times 10^3$ atoms/cluster. It is seen that the distribution of the intensity in the diffraction peaks in the case of small clusters is well approximated (to an accuracy of around 5%) by a Lorentzian function $a\omega/[\omega^2+4(s-s_0)^2]$, where s_0 is the position of the maximum in units of the diffraction vector. For the highest-intensity peak the parameters of the contour are as follows: $s_0=2.0502$ Å^{-1}, $\omega=0.2011$ Å^{-1}, and $a=5.8715$ Å^{-1}; for the second peak $s_0=2.2928$ Å^{-1}, $\omega=0.2376$ Å^{-1}, and $a=1.3906$ Å^{-1}. Attempts to describe the experimental data by Gaussian curves while maintaining the positions of the peaks give significantly poorer (around 20%) accuracy, and this approximation was completely unsuitable on the ''wings.'' The situation was not improved by varying the parameters of the Gaussian peaks (including their positions).

The good approximation of the experimental intensity distribution by a Lorentzian is indicative of strong lattice distortion, as was noted back by Guinier.[17] A Lorentzian profile of the diffraction peaks is observed in a crystal in the

case of a rather highly nonuniform distribution of the interatomic spacings (of an exponential character).[17] For an ideal crystal a Gaussian function is usually a good approximation of the diffraction peaks.

Modulation of the interplane distances in small clusters in the framework of the most general approach can be a consequence of two factors: first, the influence of the surface on the interatomic interaction and, second, the presence of microstresses in the clusters. However, an analysis[18] of the structural studies showed that the influence of the surface does not extend to the core of the cluster to a meaningful degree. In our opinion, the role of microstresses, which was evidenced in Refs. 7 and 18, is more substantial. Indeed, nonuniformity of the interatomic distances both in the core of the cluster and on its surface is more easily realized in the presence of microstresses. Microstresses can appear in free clusters only when the atomic aggregations have an icosahedral structure. Thus, even when a regular pentagonal bipyramid of seven atoms, constructed by the twinning of regular tetrahedra, is realized, an elastic strain is needed to collapse a gap of 7.35° formed between two neighboring atoms. As the size of the icosahedral formation increases, the elastic stresses grow, ultimately leading to instability of structures with a fivefold symmetry axis. In a multilayer relaxed icosahedron, when the interaction of the atoms is described by a Lennard-Jones pair potential, the flat (111) faces of the ideal icosahedron are distorted. In this case the radial distances between neighboring layers is shortened as one approaches the center of the cluster, and the distance between atoms in the surface layers is larger than in the central layers.[18]

The middle panel in Fig. 2 pertains to larger clusters, with $\bar{N}=4.8\times10^3$ atoms/cluster. As we have said, clusters of this size have the fcc structure. Analysis of the experimental data shows that (and this follows from the plot in the figure) the distribution of the intensity of the diffraction peaks is well (to 5% accuracy) approximated by a standard Gaussian curve $\sqrt{2/\pi}b\{\exp-2(s-s_0)^2/\omega^2\}/\omega$, where ω is the standard deviation. The parameters for the (111) peak are $s_0=2.0396$ Å^{-1}, $\omega=0.1652$ Å^{-1}, $b=5.4622$ Å^{-1}, and for the (200) peak $s_0=2.2951$ Å^{-1}, $\omega=0.2056$ Å^{-1}, and $b=2.8283$ Å^{-1}. We call attention to the fact that the standard deviations ω in this case are somewhat smaller than for clusters of smaller size, the diffraction peaks of which are described by Lorentzian functions.

The Gaussian curve also approximates well the diffraction peaks in the case of clusters with $\bar{N}=22.5\times10^3$ atoms/cluster (see the upper panel in Fig. 2). The approximation presented in the figure was the most optimal for minimization (to 5%) of the disparities between experiment and the model curves. A small shift of the (200) peak to larger angles is observed. In addition, besides the intense fcc peaks, one also observes weak anomalies in the region of diffraction vectors corresponding to the (100) and (101) peaks of the hcp phase. (In a number of cases a maximum is observed between the (101) hcp peak and the (200) fcc peak (see Fig. 2); its origin has not yet been established.) Based on the foregoing facts one can say that the diffraction patterns obtained from clusters with $\bar{N}=22.5\times10^3$ atoms/cluster show evidence of the presence of small traces of the hcp phase along with the predominant fcc phase. Experiments with larger clusters, which will be analyzed below, have confirmed this supposition.

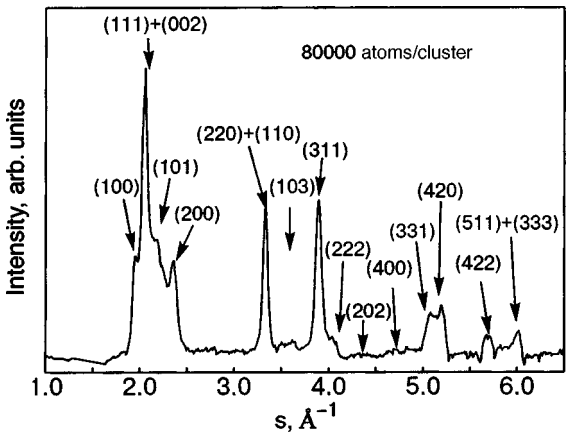

FIG. 3. Diffraction pattern from an argon cluster beam with $\bar{N}=8\times10^4$ atoms/cluster. The maxima for both the fcc and hcp phases are labeled.

It following from what we have said that the results of an analysis of the distribution of the intensity of the diffraction peaks can be used as one more criterion for identifying the structure of clusters. The strong modulation of the interatomic distances causes the Gaussian profile characteristic for regions with constant interatomic distances to be transformed into a Lorentzian profile.

When the equivalent pressure is raised to 1.4 MPa and the mean cluster size increases to $\bar{N}\approx8\times10^4$ atoms/cluster the diffraction pattern changes substantially. A typical densitometer trace for this case is presented in Fig. 3. It is seen that here, along with the set of diffraction peaks of the fcc phase, there are also hcp peaks which are noncoincident with them, viz., (100), (101), and (103), and in the region where the weak hcp maximum (202) should be, one observes a small feature in the intensity distribution. The increase in intensity of the hcp peaks indicates unambiguously that the contribution of the hcp phase in clusters with $\bar{N}\approx8\times10^4$ atoms/cluster has grown. It should be noted that the regions of the hcp phase have have rather large linear dimensions, as is attested to by the comparatively small width of the hcp maxima.

The results obtained suggest the following mechanism of cluster formation. In the first step, after the jet leaves the nozzle, the clusters near its end are found in the liquid state. This view is confirmed by the results of an investigation of clusters of organic compounds in a supersonic jet.[19] As the jet moves away from the end of the nozzle toward the diffraction zone, a cooling of the liquid drops occurs because of intense evaporation of atoms, and there is a transition to the solid state. Small clusters cool faster and solidify earlier than large clusters do. Therefore, small clusters are found in the solid state directly near the nozzle. They can grow further by a mechanism involving the coalescence of icosahedral aggregations with a subsequent condensation of atoms of the gas on steps that have formed as a result of the coalescence and are not yet overgrown.[20,21] This process results in the formation of fcc clusters of medium size containing stacking faults. The large clusters cool slowly, and their crystallization

is completed far from the end of the nozzle. The duration of the crystallization process promotes the formation and growth of a small number of supracritical nuclei of both the fcc and hcp phases. As a result, rather large regions of each phase form in the clusters. The possibility of such a scenario is confirmed by the both the results of observations of recrystallization of highly disperse condensates of heavy rare gases on a substrate and the study by Barrett and co-workers,[22] who noted that the x-ray diffraction patterns of undeformed polycrystalline samples of Ar grown from the liquid phase exhibit peaks of the hcp phase in addition to those of the fcc phase. Plastic deformation of such samples leads to vanishing of the hcp peaks. Some theoretical aspects of the formation of the hcp phase in rare-gas clusters are discussed in Ref. 23.

CONCLUSIONS

1. Our observations have shown that in large clusters of argon containing $\bar{N} \geqslant 2 \times 10^4$ atoms/cluster, rather large regions of the hcp phase form in addition to the fcc phase. The hcp fraction increases with increasing mean cluster size. The data obtained suggest that the hcp phase forms in liquid drops and is not a consequence of a size effect associated with the small size of the solid-state cluster.

2. In small clusters ($\bar{N} \leqslant 2 \times 10^3$ atoms/cluster) an icosahedral structure is realized through rapid freezing of atomic aggregations. Further growth of the small clusters apparently occurs by their coalescence and the subsequent condensation of atoms of the gas on atomic steps that have not been overgrown.

3. We have found that the profile of the diffraction peaks of the icosahedral clusters is described well by a Lorentzian line shape, while the peaks from the fcc clusters have a Gaussian profile. The qualitative change in the profiles of the diffraction peaks is due to the presence in the icosahedral clusters of microstresses inherent to structures with a fivefold symmetry axis. The microstresses cause a strong modulation of the interatomic distances, which vary from the center of the cluster toward its surface. Such modulation causes a transition from the standard Gaussian profile typical for clusters with constant interatomic distances to a Lorentzian.

In closing, the authors express their sincere gratitude to V. V. Eremenko for support of this study.

*E-mail: danylchenko@ilt.kharkov.ua

[1] V. Manzhelii and Yu. Freiman (eds.), *Physics of Cryocrystals*, AIP Press, American Institute Physics, Woodbury, N.Y. (1996).
[2] Yu. F. Komnik, Fiz. Tverd. Tela (Leningrad) **6**, 873 (1964) [Sov. Phys. Solid State **6**, 672 (1964)].
[3] S. I. Kovalenko and N. N. Bagrov, Fiz. Tverd. Tela (Leningrad) **11**, 2724 (1969) [Sov. Phys. Solid State **11**, 2207 (1969)].
[4] S. I. Kovalenko, Candidate's Dissertation [in Russian], FTINT AN USSR, Kharkov (1972).
[5] S. I. Kovalenko, É. I. Indan, A. A. Solodovnik, and I. N. Krupskii, Fiz. Nizk. Temp. **1**, 1027 (1975) [Sov. J. Low Temp. Phys. **1**, 493 (1975)].
[6] I. Farges, M. F. de Feraudy, B. Raoult, and G. Torchet, J. Chem. Phys. **78**, 5067 (1983).
[7] I. Farges, M. F. de Feraudy, B. Raoult, and G. Torchet, J. Chem. Phys. **84**, 3491 (1986); Adv. Chem. Phys. **70**, 45 (1988); D. Holland-Moritz, D. M. Herlach, and K. Urban, Phys. Rev. Lett. **71**, 1196 (1993); K. F. Kelton, G. W. Lee, A. K. Gangopadhyay, R. W. Hyers, T. J. Rathz, J. R. Rogers, M. B. Robinson, and D. S. Robinson, Phys. Rev. Lett. **90**, 195504 (2003).
[8] S. I. Kovalenko, D. D. Solnyshkin, E. A. Bondarenko, and É. T. Verkhovtseva, Fiz. Nizk. Temp. **23**, 190 (1997) [Low Temp. Phys. **23**, 140 (1997)].
[9] B. W. van de Waal, G. Torchet, and M. de Feraudy, Chem. Phys. Lett. **331**, 57 (2000).
[10] S. I. Kovalenko, D. D. Solnyshkin, É. T. Verkhovtseva, and V. V. Eremenko, Fiz. Nizk. Temp. **20**, 961 (1994) [Low Temp. Phys. **20**, 758 (1994)].
[11] J. Koperski, Phys. Rep. **369**, No. 3,177 (2002).
[12] O. F. Hagena and W. Obert, J. Chem. Phys. **56**, 1793 (1972).
[13] S. S. Gorelik, L. N. Rastorguev, and Yu. A. Skakov, *X-Ray Diffraction and Electron-Optical Analysis of Metals* [in Russian], Metallurgizdat, Moscow (1970).
[14] J. W. Lee and G. D. Stein, J. Phys. Chem. **91**, 2450 (1987).
[15] R. Karnboch, M. Yopplen, J. Stapelfeldt, J. Wormer, and T. Moler, Rev. Sci. Instrum. **64**, 2838 (1993).
[16] W. Lee and G. D. Stein, Surf. Sci. **156**, 112 (1985).
[17] A. Guinier, *Théorie et Technique de la Radiocristallographie*, Chapter 13, Dunod, Paris (1956), Fizmatgiz, Moscow (1961).
[18] Yu. I. Petrov, *Clusters and Small Particles* [in Russian], Nauka, Moscow (1986).
[19] L. S. Bartell, J. Phys. Chem. **99**, 1080 (1995).
[20] B. W. van de Waal, J. Chem. Phys. **98**, 4909 (1993).
[21] S. I. Kovalenko, D. D. Solnyshkin, E. T. Verkhovtseva, and V. V. Eremenko, Chem. Phys. Lett. **250**, 309 (1996).
[22] C. S. Barrett, P. Haosen, and L. Meyer, J. Chem. Phys. **40**, 2744 (1964).
[23] É. T. Verkhovtseva, I. A. Gospodarev, A. V. Grishaev, S. I. Kovalenko, D. D. Solnyshkin, E. S. Syrkin, and S. B. Feodos'ev, Fiz. Nizk. Temp. **29**, 519 (2003) [Low Temp. Phys. **29**, 386 (2003)].

Translated by Steve Torstveit

QUANTUM EFFECTS IN SEMICONDUCTORS AND DIELECTRICS

Local exciton states at isoelectronic centers in superlattices

N. V. Bondar'*

Institute of Physics of the National Academy of Sciences of Ukraine, pr. Nauki 46, Kiev 03028, Ukraine
(Submitted June 24, 2003; revised August 27, 2003)
Fiz. Nizk. Temp. **30**, 233–243 (February 2004)

The optical spectrum of strained type-II ZnSe/ZnTe superlattices, both freshly grown and stored for some time, are analyzed with allowance for the formation of $ZnSe_{1-x}Te_x$ mixed layers, having a cluster structure, at their heterointerfaces. The dependence of the hole localization energy on the radius of the clusters of Te atoms is calculated and found to agree well with the experimental data. In the samples stored for some time there is a change in the shape of the photoluminescence band and a monotonic shift of this band to shorter wavelengths. It is shown that the shift is caused by a change in the internal structure of the mixed layer over time and by the formation of local states induced by isoelectronic impurities (Te atoms). © *2004 American Institute of Physics.* [DOI: 10.1063/1.1645171]

1. INTRODUCTION

Numerous experimental studies of superlattices (SLs) with alternating ZnSe and ZnTe layers grown on GaAs substrates have shown that they have a very intense photoluminescence band, attesting that such structures have a high quantum yield of photoluminescence (PL).[1–6] Attempts to explain this effect by radiative recombination of the eigenstates of the ZnSe/ZnTe superlattice run up against a number of difficulties. Chief among these is the fact that superlattices of this type are classed as type–II quantum structures, in which holes created by photoexcitation are localized in the ZnTe layers, and these regions act as potential barriers to electrons. It is well known that the probability of radiative recombination of spatially separated carriers is insignificant in both 3D and 2D structures, and so the intensity of the PL band of these SLs is weak and is rapidly attenuated with increasing thickness of the ZnSe and ZnTe layers and also with increasing temperature T. However, it has been established that, regardless of the thickness of the ZnSe and ZnTe layers, the PL intensity of ZnSe/ZnTe SLs is always very high, and the PL is easily observed all the way up to room temperature.[1–6] X-ray diffraction and optical studies of these objects have established that the source of such intense PL in these SLs is the recombination of excitons localized in the $ZnSe_{1-x}Te_x$ mixed layers formed at the heterointerfaces during growth of the structures.[4,5]

The mixed layers that arise are different from their bulk counterparts, the $ZnSe_{1-x}Te_x$ substitutional solid solutions (SSSs), both in the way they are formed (diffusion of Te atoms out of the plane) and in their internal state, which is a result of the lattice misfit between ZnSe and ZnTe (see below). In spite of this, however, at low concentrations of Te the radiative properties of both systems are mainly determined by small clusters Te_n with $n \leqslant 4$, which are aggregations of atoms in nearest-neighbor sites of the crystal lattice. Localization of excitons on such clusters is so efficient that it completely suppresses all other channels of energy transfer to the radiative and nonradiative recombination centers.[7–11] The reason for this high efficiency of localization is that the $ZnSe_{1-x}Te_x$ SSSs are classed as systems with strong scattering, in which the perturbation of the electronic states due to even isolated Te atoms is sufficient to split off the localized state from the band bottom.[7–13] This property of the system is due to the fact that Te atoms in ZnSe are an isoelectronic impurity and, having a larger volume and mass but smaller electronegativity than the Se atoms, they create an attractive short-range potential for holes in ZnSe. The Coulomb field of the latter traps electrons, leading to the formation of localized excitons.

The authors[7–11] who have studied $ZnSe_{1-x}Te_x$ SSSs with low Te concentrations have found that at $x \leqslant 0.02$ the low-temperature PL band exhibits structure due to the recombination of excitons localized on Te_n clusters with $n \geqslant 2$. It was the opinion of those authors that isolated atoms Te_1 did not create bound states for holes in the band gap of ZnSe. Studies of SSSs with similar concentrations by other groups[1–6] have established that in both 3D and 2D $ZnSe_{1-x}Te_x$ structures the localization of excitons on Te_n clusters occurs starting with $n \geqslant 1$. The values calculated in Ref. 5 for the binding energies of holes at Te_1 and Te_2 in $ZnSe_{1-x}Te_x$ SSSs were 40 and 250 meV, respectively.

Another problem that has remained little studied till now relates to the change of the structure of the $ZnSe_{1-x}Te_x$ mixed layer over time. That problem has a broader aspect, since it bears upon practically all strained quantum structures, and its solution would make it possible to predict the operating parameters of optoelectronic devices based on such materials. The essence of this problem consists in the fact that, because of the lattice misfit ($\sim 7.3\%$) the ZnSe layers are stretched and the ZnTe layers compressed in the growth plane of the SL, and this has a definite influence on the diffusion of Te atoms into the ZnSe layers. The formation of mixed layer occurs in the growth stage of the SL, but this process continues even after the samples are grown, and for that reason the structure of the $ZnSe_{1-x}Te_x$ mixed layer will change over the course of time. This effect was noted by the

authors of Ref. 14, who had studied SLs with very thin ZnSe and ZnTe layers (one or two atomic monolayers or less). As a result, even in the growth stage a certain mixed structure forms which bears no relationship to a SL. The nucleation and evolution of $ZnSe_{1-x}Te_x$ mixed layers and their influence on the band structure of a SL with ZnSe and ZnTe layer thicknesses of a few tens of angstroms have completely escaped notice and have not been studied before.

In this paper we present and analyze the emission spectra of ZnSe(50 Å)/ZnTe(50 Å) type-II SLs recorded both immediately after fabrication of the samples and some time later after storage at room temperature under normal conditions. The feature distinguishing our SLs from the analogous samples studied by other authors is a large thickness of the ZnSe and ZnTe layers. The stretching of the ZnSe layers weakens the bond between Zn and Se, making it easier for Te to diffuse into the ZnSe layers and replace the Se atoms. In addition, the $ZnSe_{1-x}Te_x$ mixed layers are stretched in the growth plane of the SL. The random substitution of the Se atoms by Te leads to a cluster structure of the mixed layers, as a result of which the contour of the PL band exhibits structure consisting of several peaks due to the recombination of excitons localized at small clusters Te_n with $n=1,2,3,4$. In contrast to $ZnSe_{1-x}Te_x$ SSSs with $x<0.01$ or SLs with thin ZnSe and ZnTe layers, the structure appears in the PL band not at helium temperatures but at $T\approx 20$ K; this was apparently observed for the first time in such systems. Using an exciton model in which it is assumed that only the hole is localized at a cluster, while the electron is separated spatially from it by a potential barrier in the conduction band and is held near it by the Coulomb interaction, we calculate the dependence of the energy of localization of a hole $\varepsilon_b^{(n)}$ and exciton ε_x as functions of the radius ρ of the cluster; the calculated localization energies are in good agreement with experiment. By periodically recording the low-temperature PL band of these SL in the course of their storage, we were able to detect a monotonic shift to shorter wavelengths and a subsequent decrease in the half-width of the PL band. This shift is directly related to a change in the internal structure of mixed layer over time and reflects the dynamics of localization of excitons (holes) in them and the formation of local states induced by isoelectronic impurities (Te atoms).

2. EXPERIMENTAL RESULTS

We studied ZnSe/ZnTe SLs obtained by molecular beam epitaxy on GaAs(001) substrates at a growth temperature of 360 °C with a ZnSe buffer layer about 0.3 μm thick. The samples had thicknesses of $30d$, $25d$, and $10d$, where $d=100$ Å is the SL period. The source of excitation of the PL was a He–Cd laser with wavelength $\lambda=325$ nm and average power $P_0\approx 10$ mW.

It should be noted that the form of the reflection and PL spectra is practically independent of the overall thickness of the samples, and therefore in Fig. 1 we show the reflection spectrum (RS) of one of them ($30d$) and the PL band recorded at different T. Although the contour of the reflection spectrum is broadened, as is characteristic for $ZnSe_{1-x}Te_x$ structures, the large amplitude makes it possible to determine the value of the resonance energy ($E_{1s}^0=2521$ meV) of the exciton transition in the mixed layer to rather good accuracy.

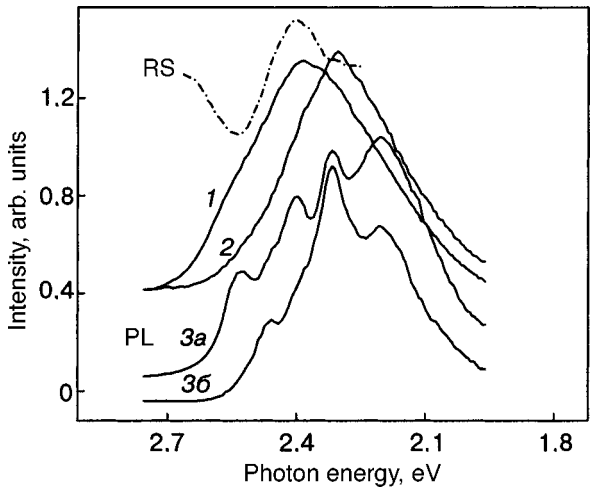

FIG. 1. Reflection spectrum (RS) and photoluminescence spectrum (PL) of a ZnSe/ZnTe superlattice: *1*—5.5 K, *2*—10 K. Lines 3a and 3b were taken at 20 K at different points on the surface.

It is seen in Fig. 1 that E_{1s}^0 lies at the beginning of the short-wavelength part of the PL band at $T\approx 5.5$ K (curve *1*), which is broad (≈ 300 meV at half maximum), structureless, and asymmetric, with an extended long-wavelength wing. When T is increased to 10 K one observes a sharp long-wavelength shift of the band by about 80 meV (curve *2*), and at $T\approx 20$ K a distinct structure appears on it in the region below E_{1s}^0. The structure consists of five peaks, the shortest-wavelength of which (the zeroth peak) coincides in position with E_{1s}^0 (curve $3a$ in Fig. 1). For a more precise determination of the position of these peaks we scanned the laser excitation spot over the surface of the SL at $T\approx 20$ K and recorded the band at different points of the surface (curve $3b$ in Fig. 1). It was found as a result that the peaks lie at distances of 65, 127, 204, and 319 meV from E_{1s}^0 and that their spectral position depends very weakly on the coordinate of the point of excitation on the surface of the SL. It is seen in Fig. 2 that the first three peaks have practically vanished by $T\approx 40$ K (curve *2*) and upon further increase of T a monotonic shift of the fourth peak to longer wavelengths is

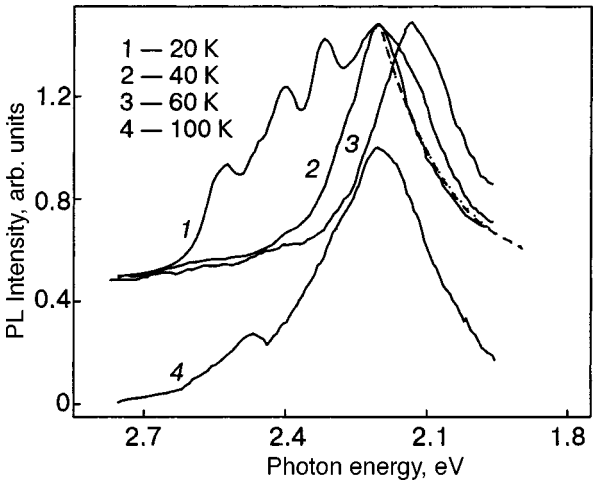

FIG. 2. Temperature dependence of the PL linewidth of ZnSe/ZnTe at $T\approx 20$–100 K; the broken line shows a fit to the long-wavelength part of the band by an experimental dependence.

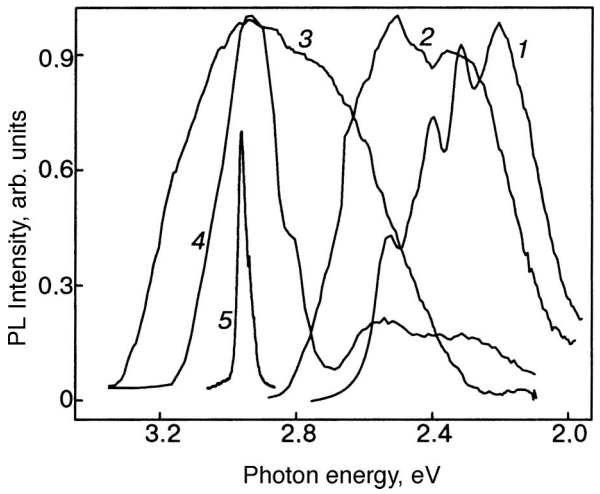

FIG. 3. Change in the shape of the PL band of a ZnSe/ZnTe SL (*1–4*) over time during storage of the samples; *5*—the PL spectrum of a ZnS/ZnSe superlattice.

observed, reaching a value of ~385 meV (relative to E_{1s}^0) at $T \approx 60$ K (curve *3* in Fig. 2). With further increase in temperature at $T > 60$ K the band shifts in the opposite direction, and at $T \approx 100$ K its maximum coincides with the position that it had at $T \approx 40$ K (curve *4* in Fig. 2). We note that when the pump density was decreased the picture remained the same in its overall features, but the broadening of the peaks remained rather large, and it was impossible to make out any distinct structure of the PL band.

Figure 3 shows how the emission spectrum of the SL changes over time when the sample is stored under normal conditions. It was noted that about a year after the SL was grown the PL band (band *2*) began to shift in an unusual way to shorter wavelengths; this was detected over the next several months (band *3*). As a result, it was established that the maximum of the band was stabilized in the region ~2900 meV, and its half width (at half maximum) decreased to ~190 meV (band *4*). Thus over such a time the emission has almost completely vanished from the region 2600–2400 meV, and the band has shifted by ~500 meV in the direction of shorter wavelengths. It is clear that if it were the case that a simple ''mixing'' of the original ZnSe and ZnTe layers to form $ZnSe_{1-x}Te_x$ had occurred, then the direction of the shift of the band would be the opposite of this, as is observed in the SSSs. In the last Section we shall discuss the possible influence of various impurities, oxygen in particular, on this shift, since the SL samples were stored under normal conditions.

3. ENERGY SPECTRUM OF HEAVY EXCITONS IN ZnSe/ZnTe MIXED SUPERLATTICES

Before turning to an analysis of the results, let us calculate the eigenstate energies $E_{hh}(d)$ of the SL, considering only heavy hh excitons and using the model of ideal quantum wells, assuming the presence of ideal interfaces between the corresponding layers of the SL. Then, by comparing the value obtained for $E_{hh}(d)$ with the experimental value, we shall show that the eigenstates of the given SL lies significantly lower in energy than the experimentally observed PL band (Fig. 1). Therefore the PL cannot be due to the radiative recombination of free hh excitons formed by electrons $e1$ and heavy holes $hh1$ from the first subband of their size quantization. In the case of ideal interfaces between layers one has

$$E_{hh}(d) = E_{gSL} + \Theta_e(L) + \Theta_{hh}(L) - \varepsilon_x, \tag{1}$$

where $d = L_1 + L_2$ (from here on the subscripts 1 and 2 refer to ZnSe and ZnTe, respectively), E_{gSL} is the band gap of the SL, $\Theta_e(L)$ and $\Theta_{hh}(L)$ are the energies of electrons and holes in the corresponding potential wells ΔE_c and ΔE_v. If at first we neglect the stress in the ZnSe and ZnTe layers, then, according to the calculation scheme presented in Ref. 15, the unperturbed values of the discontinuities of the conduction band and valence band upon the formation of the SL will be $\Delta E_{0c} = -920$ meV and $\Delta E_{0v} = 1360$ meV, respectively.

The internal stress arising as a result of the lattice misfit between layers brings about a new state of the SL which is characterized by lattice constants in the growth plane $a_\parallel$ and in the normal direction $a_\perp^{1,2}$ which are different from those in the bulk, $a_{1,2}$. These values can be written in analytical form by minimizing the expression for the elastic energy of the SL but under the condition that the SL is found in a free-standing state.[15] According to our estimates, this should be the case for the solutions studied here, since their total thickness (≈ 0.3 μm) is greater than the critical thickness, and therefore $a_\parallel$ and $a_\perp^{1,2}$ are given by the following relations:[15]

$$a_\parallel = \frac{a_1 G_1 L_1 + a_2 G_2 L_2}{G_1 L_1 + G_2 L_2}, \tag{2}$$

$$a_\perp^{1,2} = a_{1,2}\left[1 - D_{1,2}\left(\frac{a_\parallel}{a_{1,2}} - 1\right)\right], \tag{3}$$

where $G_{1,2}$ are the elastic moduli, $D_{1,2} = 2C_{11}^{1,2}/C_{12}^{1,2}$, and $C_{11}^{1,2}$ and $C_{12}^{1,2}$ are the elastic constants (see Table I). A scheme for calculation of the band discontinuities ΔE_c and ΔE_v with allowance for the stress in the layers is given in Ref. 15 and was used by us previously for an analogous calculation of $E_{hh}(L)$ in a type-I ZnS/ZnSe SL,[16] and we shall therefore give only the necessary expressions for ΔE_c and ΔE_v with allowance for the features of the SLs studied here. For a quantitative description of the deformation we introduce the strain tensor with diagonal elements:[15]

TABLE I. Material parameters of ZnSe and ZnTe (Ref. 15).

Parameters	ZnSe	ZnTe
$a_{1,2}$, Å	5.6684	6.089
$a_c^{1,2}$, $a_v^{1,2}$, eV	−3.65, 1.67	−5.83, 0.79
$E_{g1,2}$, eV	2.823	2.39
$C_{11}^{1,2}$, $C_{12}^{1,2}$, Mbar	0.859, 0.506	0.713, 0.407
$b_{1,2}$, eV	−1.2	−1.26
$G_{1,2}$	1.447	1.311
$\Delta_0^{1,2}$, eV	0.143	0.91

$$\varepsilon_{xx}^{1,2}=\varepsilon_{yy}^{1,2}=\frac{a_{\parallel}}{a_{1,2}}-1, \quad \varepsilon_{zz}^{1,2}=\frac{a_{\perp}^{1,2}}{a_{1,2}}-1. \tag{4}$$

Then ΔE_c is determined by the following relation:

$$\Delta E_c=\Delta E_{0c}+a_c^1\frac{\Delta\Omega_1}{\Omega_1}+a_c^2\frac{\Delta\Omega_2}{\Omega_2}, \tag{5}$$

where $\Delta\Omega_{1,2}/\Omega_{1,2}=\varepsilon_{xx}^{1,2}+\varepsilon_{yy}^{1,2}+\varepsilon_{zz}^{1,2}$ are the relative changes in the volumes of the respective unit cells, and $a_c^{1,2}$ are the isotropic deformation potentials of the conduction band. The stress arising in the layers leads to lifting of the degeneracy at the point $\mathbf{k}=0$ of the valence bands of ZnSe and ZnTe, which are split into heavy-hole $E_{vhh}^{1,2}$ and light-hole $E_{vlh}^{1,2}$ subbands:[15]

$$E_{vhh}^{1,2}=E_v^{1,2}-\frac{1}{2}\,\delta E_{001}^{1,2}, \tag{6}$$

$$E_{v1h}^{1,2}=E_v^{1,2}-\frac{1}{2}\left\{\Delta_0^{1,2}-\frac{1}{2}\,\delta E_{001}^{1,2}-\left[(\Delta_0^{1,2})^2-\Delta_0^{1,2}\delta E_{001}^{1,2}+\frac{9}{4}(\delta E_{001}^{1,2})^2\right]^{0,5}\right\}, \tag{7}$$

$\delta E_{001}^{1,2}=2b_{1,2}(\varepsilon_{zz}^{1,2}-\varepsilon_{xx}^{1,2})$ and $E_v^{1,2}=E_{0v}^{1,2}+a_v\Delta\Omega_{1,2}/\Omega_{1,2}$, and $a_v^{1,2}(b_{1,2})$ are the isotropic (uniaxial) deformation potentials of the valence bands. However, in ZnSe, the unit cells of which are elongated in the SL growth plane, the maximum of the hh subband lies lower in energy (relative to E_c^1) than the maximum of the lh subband, and by virtue of the difference of the dispersion curves, degeneracy of the valence band of ZnSe sets in again at $\mathbf{k}\neq 0$, where these subbands have common points of intersection. In ZnTe this does not happen, because the subband there moves in the opposite direction as a consequence of the fact that the unit cells of ZnSe are compressed in the growth plane of the SL (see the scheme in Ref. 4). We choose the energy corresponding to the points of intersection of the hh and lh subbands in ZnSe as the reference level and, using (2)–(9) and the data from Ref. 15, we determine the maximum and minimum depths of the potential well for holes in ZnTe and also the maximum and minimum values of the band gap of the SL: $\Delta E_c=-1212$ meV, $\Delta E_v^{\max}=1480$ meV, $\Delta E_{gSL}^{\min}=1280$ meV; and $\Delta E_c=-1212$ meV, $\Delta E_v^{\min}=1202$ meV, $\Delta E_{gSL}^{\max}=1450$ meV. We note that the values found for ΔE_v are in good agreement with the data of Ref. 17, where the results were obtained by a more rigorous method in the framework of the sp^3s^* tight-binding model with allowance for the spin–orbit interaction.

To calculate the values of Θ_e, Θ_{hh}, and ε_x we solve the Schrödinger equation, describing the motion of e and hh in the corresponding layers with allowance for their Coulomb attraction:

$$[\mathcal{H}_e+\mathcal{H}_h+\mathcal{H}_{\rm ex}-V(\rho,z_e,z_h)]\Psi(\rho,z_e,z_h)=E_{hh}(d)\Psi_{\rm ex}(\rho,z_e,z_h), \tag{8}$$

where

$$V(\rho,z_e,z_h)=\frac{e^2}{\varepsilon[\rho_0^2+(z_e-z_h)^2]^{1/2}}, \tag{9}$$

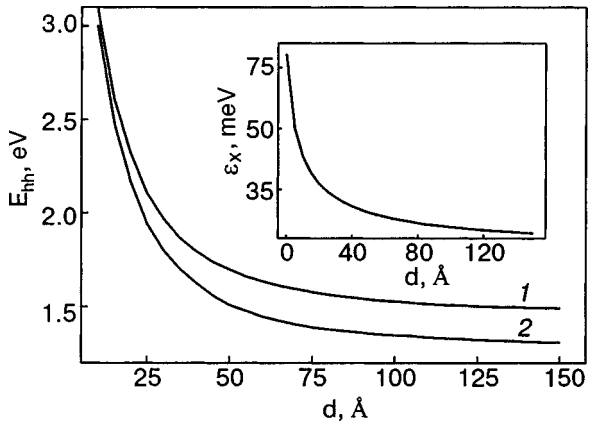

FIG. 4. Dependence of the energy E_{hh} of heavy excitons on the SL period d; the inset shows the dependence of their binding energy ε_x on d.

ρ_0 is the relative distance between carriers in the plane of the well, and ε is the dielectric constant, which, since the values of ε_1 and ε_2 are close, is chosen as $\varepsilon=0.5(\varepsilon_1+\varepsilon_2)$. The wave functions of the electrons and holes in a potential well with finite or infinitely high walls are well known, and therefore the problem of finding $\Theta_j(L)$ is utterly trivial. For calculating ε_x we take the wave function of the relative motion of the electron and hole in the plane of the SL in the form $\varphi(\rho_0,z_e-z_h)=B\exp(-(1/a_x)(z^2-\rho_0^2)^{1/2})$, where B is a normalization coefficient and a_x is the Bohr radius of the exciton, which is treated as a variational parameter. Determination of the exciton binding energy requires minimizing the following expression with respect to variation of a_x:

$$\varepsilon_x(a_x)=\frac{\pi^2\hbar^2}{2\mu a_x}-\langle\Psi_{\rm ex}|\mathbf{H}|\Psi_{\rm ex}\rangle, \tag{10}$$

where μ is the reduced mass of the hh exciton. Figure 4 shows two curves of $E_{hh}(d)$ calculated for $\Delta E_c=1212$ meV: *1*—($\Delta E_{gSL}^{\max}=1450$ meV, $\Delta E_v^{\min}=1202$ meV); *2*—($\Delta E_{gSL}^{\min}=1280$ meV; $\Delta E_v^{\max}=1480$ meV), and the inset shows $\varepsilon_x(d)$. It is seen that $E_{hh}(100)\approx 1550-1350$ meV, i.e., it lies approximately 1000 meV below E_{1s}^0, and therefore the experimental PL band in Fig. 1 cannot be due to the eigenstates of the SL, i.e., to radiative recombination of hh excitons as proposed above. Thus the presence of mixed $ZnSe_{1-x}Te_x$ layers at the heterointerfaces of the SL is practically the only condition that can satisfactorily explain the experimental results.

Let us now estimate the band gap E_g^0 of the $ZnSe_{1-x}Te_x$ mixed layers, taking into account that under the influence of the stresses that have arisen in the ZnSe and ZnTe layers the initial values of the band gaps E_{g1} and E_{g2} are renormalized:

$$E_g^{1,2}=E_c^{1,2}-E_v^{1,2}+\frac{\Delta\Omega_{1,2}}{\Omega_{1,2}}(a_c^{1,2}-a_v^{1,2}), \tag{11}$$

from which we obtain the new values $E_g^1=2667$ meV and $E_g^2=2589$ meV (E_{g1} and E_{g2} are given in Table I). Assuming that the energy of the resonance transition in the mixed layers is given to sufficient accuracy by the value of E_{1s}^0, we obtain $E_g^0=E_{1s}^0+\varepsilon_x=2542$ meV, where $\varepsilon_x\approx 21$ meV is the exciton binding energy in bulk ZnSe. It is clear that if the renormalization is not taken into account, the initial ZnTe layers will be nontransparent to photons formed in the

$ZnSe_{1-x}Te_x$, since $E_{g2}=2391$ meV. The dependence of $E_g^0(x)$ on concentration is determined, as in a SSS, by the following relation:[11,13]

$$E_g^0(x)=xE_g^2+(1-x)E_g^1-bx(1-x) \tag{12}$$

(where $b=1504$ meV is the bowing parameter), from which we obtain the value of the concentration of Te atoms in the mixed layers: $x\sim 0.075$; this value is in fair agreement with the results of Ref. 18, where it was determined for analogous SLs by x-ray structural analysis. Here it should be noted that at large thicknesses of the ZnSe and ZnTe layers and of the SL as a whole, when it reaches a free-standing state, the position of $E_g^0(x)$, in contrast to the SSSs, depends weakly on the Te concentration. This follows already from the fact that in the SSSs one has the value $\Delta E_g=E_{g1}-E_{g2}\approx 430$ meV, whereas in our case it is only 75 meV. This circumstance can explain why the structure in the PL band of the SL is observed even at $x\approx 0.075$ while in bulk SSSs it is smeared even at $x\approx 0.01$.[7–11] It is known that the smearing of the structure is due to the shift of the band edge of the SSSs and to the increase in the radius of the states localized at clusters with $1\leqslant n<3$, as a consequence of which a subsequent merging of these states with the main band occurs; this is absent in the $ZnSe_{1-x}Te_x$ mixed layers.

4. LOCALIZATION OF EXCITONS ON Te CLUSTERS IN $ZnSe_{1-x}Te_x$ MIXED LAYERS

1. Assuming that the structure observed on the contour of the PL band is due to the levels of excitons localized on small clusters of Te atoms, let us consider the features of the formation of bound hole states in $ZnSe_{1-x}Te_x$ mixed layers. Substitution of an atom of the initial semiconductor (ZnSe) introduces a local perturbation $U=V_0-V$, which can give rise to a discrete structure of energy levels in its band gap. The particle spectrum in the presence of the perturbed potential is found from the solution of the one-site Koster–Slater equation with an impurity potential U.[19] For a bound hole state to appear in the band gap of ZnSe it is necessary that the condition $UG(0)>1$ be satisfied, where $G(E)$ is the Green's function of the ideal crystal with the impurity potential ($[G(0)]^{-1}=E_{cr}$) and E_{cr} is the critical value of U at which the bound state appears. Using the relation $E_{cr}=(\pi\hbar)^2/(8m_h^*\rho_1^2)$, where $\rho_1\approx 3.5$ Å is the radius of the first hole bound state (see below), we obtain $E_{cr}=1275$ meV, which is close to the analogous value (1250 meV) obtained in Ref. 11. To calculate U it is necessary to know the values of the ionic potentials of the Te atoms and the ZnSe; one must take into account the screening of the difference of these potentials by the valence electrons of the latter, and the spin–orbit interaction should also be included.[19] Ultimately the value obtained for U in that way will be exactly equal to the value of the discontinuity of the valence bands of ZnSe and ZnTe at the heterointerface:[15]

$$U\equiv\Delta E_v=(E_v^1-E_v^2)+(\overline{V}_{\text{tot}}^1-\overline{V}_{\text{tot}}^2), \tag{13}$$

where $\overline{V}_{\text{tot}}=\overline{V}_H+\overline{V}_{\text{ion}}+\overline{V}_{ECSL}$ is the averaged total potential of the atoms of ZnSe and ZnTe. Since the Te atoms have a larger radius than the Se atoms, the value of U also depends on the strain of the ZnSe layer, and therefore, in order for a bound state to appear, the condition $U/E_{cr}\geqslant 1$ must hold in the entire range of variation of U. To characterize the local distortions of the lattice in the bulk of the samples the parameter $X=R/(R_i-R_h)$ is used, where R_i and R_h are, respectively, the lengths of the unperturbed covalent bonds in the presence and absence of an impurity.[19] In our case we use the quantity $Q=(a_{\|}-a_1)/(a_2-a_1)$, as a result of which we obtain $Q_1=0$, $U(Q_1)=1360$ meV—the unperturbed state, $Q_2=0.475$, $U(Q_2)=1480$ meV—the free-standing state; $Q_3=1$, $U(Q_3)=1560$—the maximum perturbation. One can check that the condition $U/E_{cr}>1$ holds in the entire interval $U(Q_1)-U(Q_2)$. This scheme also gives correct results for other systems, e.g., ZnS(Te) and CdS(Te), in which the localization of excitons on isolated atoms Te_1 is considered a reliably established fact.[12] Using the corresponding parameters for those systems from Ref. 15, we find $U(Q_1)=2230$ meV for ZnS and $U(Q_1)=1330$ meV for CdS (we note that in Ref. 12 a value $U(Q_1)=1320$ meV was obtained for CdS by a fitting procedure), which give $U/E_{cr}>1$. It is known that in ZnS(Se) SSSs the states on isolated Se clusters have never been observed experimentally; this can be confirmed: $U(Q_1)=860$ meV and $U(Q_3)=923$ meV, which give $U/E_{cr}<1$ in the whole range of variation $U(Q_1)-U(Q_3)$. Thus the set of data obtained allows us to state that the localization of a hole on a single Te atom can occur in the $ZnSe_{1-x}Te_x$ mixed layers, and since a cluster with a larger number of atoms also creates a bound state, it is clear that the four main peaks of the PL band are the levels of excitons localized on Te_n clusters ($n=1,2,3,4$) with binding energies of 65, 127, 204, and 319 meV.

2. We consider the features of the PL band shape and its variation in certain temperature intervals. When T is raised to 20 K there are two discrete shifts of the maximum of the PL band to longer wavelengths by distances comparable to the distances between its individual peaks, and a band structure appears, as is seen in Fig. 1. In the interval 20–40 K the latter vanishes completely as a result of the thermal breakup of excitons localized at clusters with $1\leqslant n\leqslant 3$. Further increase of T to 60 K leads to the aforementioned monotonic shift of the band in the long-wavelength direction (see curves *2* and *3* in Fig. 2).

The observed discrete shift of the PL band and its monotonic shift are easily explained if it is taken into account that a cluster of size n has a certain number of spatial configurations, each of which is characterized by an exciton localization energy $\varepsilon_b^{(n)}$ ($\varepsilon_b>0$ is a positive quantity measured from E_{1s}^0 into the band gap of the mixed layer).[7–9] Thus to each cluster there corresponds a region of values $\Delta\varepsilon_b^{(n)}$, the overlap of which leads to the formation of a quasi-continuous tail of the density of localized states. For those clusters for which this overlap does not exist one observes individual exciton levels, as, e.g., on clusters with $1\leqslant n\leqslant 3$ (see Figs. 1 and 2), although for clusters with $n\geqslant 4$ ($\varepsilon_b\geqslant\varepsilon_b^{(4)}$) a quasi-continuous tail of the density of states is formed; otherwise one would observe individual levels of excitons localized on clusters with $n=5,6,7,\ldots$, as is the case for the system ZnS(Te).[12] At $T=40$ K the long-wavelength part of the PL band reflects a form of the density of localized states $g(\varepsilon_b)$ which falls off smoothly into the band gap of the mixed layer by an exponential law $g(\varepsilon_b)\approx\exp[-(\varepsilon_b/\varepsilon_0)]$, (the part of

curve *2* shown by the broken line in Fig. 2), where $\varepsilon_0 \approx 150$ meV is the energy scale of the localized states. Based on the data obtained we can conjecture that the energy $\varepsilon_b^{(4)} = 319$ meV is the mobility threshold of the localized excitons. This energy divides the states localized on clusters with $1 \leqslant n \leqslant 3$ and states belonging to the quasi-continuous tail of the density of states. It was also established in Ref. 10 that in $ZnSe_{1-x}Te_x$ SSSs with $x = 0.13$ the mobility threshold of the localized excitons lies in the vicinity of the energy of localization of a cluster of four Te atoms.

The observed monotonic shift of the PL band as the temperature is increased for $T > 40$ K is due to the tunneling relaxation of excitons (holes) via states of the tail of the density of states with the emission of acoustic phonons. At $T = 60$ K this shift reaches a value ~ 385 meV relative to E_{1s}^0, which approximately corresponds to the energy of localization of a hole on a cluster with $n = 5$. As a result, we obtain the five experimental values: $\varepsilon_b^{(n)} = 65$, 127, 204, 319, and 385 meV for $1 \leqslant n \leqslant 5$, which will be used for comparison of the calculated and experimental $\varepsilon_b^{(n)}(\rho)$ curves. When T is increased further to 100 K, processes involving the absorption of phonons by localized excitons begin to dominate, and as a result, the PL band is shifted to shorter wavelengths, reaching the same spectral position at $T = 100$ K as at $T = 40$ K (curve *4* in Fig. 2). Analogous behavior of the PL band was noted in Ref. 8 (Fig. 2), where $ZnSe_{1-x}Te_x$ SSSs with $x = 5\%$ were studied, i.e., concentrations for which the PL band becomes structureless.

Let us now discuss on a qualitative level the reason why the structure of the PL band in the SLs studied here is manifested at higher temperatures (≈ 20 K), which has been observed for the first time in such SLs. We recall that in SLs with thin ZnSe and ZnTe layers (1–2 monolayers and less) and in SSSs with $x \leqslant 0.01$ the structure of the PL band is clearly observed at helium temperatures.[7,14] Clearly the structureless PL band observed at helium temperatures in our SLs is a consequence of the large thickness of the ZnSe and ZnTe layers. The mutual deformation of these layers splits their degenerate valence bands and thereby increases the depth of the potential well, leading to stronger localization of holes as compared to the bulk SSSs. This, in turn, increases the occupation of exciton levels at clusters with $1 \leqslant n \leqslant 3$, leading to their broadening. When the temperature is raised to 20 K the radiative and nonradiative processes are activated, and an overall decline of the integrated intensity of the PL occurs, as a result of which the structure appears in the band. This can also be used to establish the position of the shortest-wavelength (zeroth) peak of the PL band, which corresponds to E_{1s}^0, and to link it with the recombination of free excitons in the $ZnSe_{1-x}Te_x$ mixed layers. Thus the experimental data obtained allow us to make the quite definite assumption that in systems with lowered dimensionality, i.e., the $ZnSe_{1-x}Te_x$ mixed layers, the processes of cluster formation have the same character as in the bulk SSSs, in spite of the straining (stretching) of the layers of the initial semiconductors due to their lattice misfit.

3. Let us turn to a calculation of the dependence of the hole localization energy on the cluster radius, $\varepsilon_b^{(n)}(\rho)$. As is seen from Sec. 3, the value of the impurity potential localizing the *hh* hole in the $ZnSe_{1-x}Te_x$ mixed layer is $V_0 \equiv \Delta E_v = 1480$ meV. It is usually assumed that the impurity potential $V_0(\mathbf{r})$ contains two parts: a short-range part $V_0(\mathbf{r}) = V_0$ for $r \leqslant \rho$ and a long-range part $V_0(\mathbf{r}) = V_0 f(\rho/r)$, which takes into account the local distortions of the lattice, for $r > \rho$, where $f(\rho/r)$ is some function of r and ρ. In our case such a choice of potential is based on the consideration that, since the Te atoms are larger than the Se atoms, this gives rise to an additional stress field around them and leads to a tail of the potential at $r > \rho$ (Ref. 20). Here $V_0(\mathbf{r})$ has the following form:

$$V_0(r) = \begin{cases} V_0, & r \leqslant \rho, \\ V_0\left(\dfrac{\rho}{r}\right)^3, & r > \rho. \end{cases} \tag{14}$$

In choosing the wave function of the localized state one must take into account the degeneracy of the valence bands of ZnSe and ZnTe, but this degeneracy is lifted as a result of the strain; therefore, starting from the spherical symmetry of the problem and taking into account the character of the localization of a particle at an isoelectronic impurity, we write the wave function of the state in the form[21]

$$\Psi_1(r) = \left(8\frac{\alpha^3}{\pi}\right)^{1/2} j_0(\alpha r)\exp(-\alpha r), \quad r \leqslant \rho, \tag{15a}$$

$$\Psi_2(r) = (4\beta^3)^{1/2}\exp(-\beta r), \quad r > \rho, \tag{15b}$$

where $j_0(\alpha r)$ is the spherical Bessel function and α is a variational parameter. The coefficients in front of the wave functions are obtained from their normalization conditions in the corresponding regions, and the quantity $\beta(\alpha,\rho) = 1/\rho + \alpha[1 - \cot(\alpha,\rho)]$ is obtained from the condition that ψ'/ψ be continuous at $r = \rho$. We find the hole localization energy $\varepsilon_b^{(n)}(\rho)$ by minimizing the expression $\langle \psi(r_h)| -\hbar^2\nabla_h^2/2m_h^* + V(r_h)|\psi(r_h)\rangle$ with respect to α, where $\psi(r_h) = \Psi_1(r) + \Psi_2(r)$. Doing the integration over the spatial coordinate, we obtain the following expressions for the kinetic energy $\mathrm{KE}(\alpha,\rho) = \mathrm{KE1}(\alpha,\rho) + \mathrm{KE2}(\alpha,\rho)$ and the potential energy $\mathrm{PE}(\alpha,\rho)$:

$$\mathrm{KE1}(\alpha,\rho) = -8\frac{\hbar^2\alpha^3}{\pi m_h^*}\int_0^\rho |\psi_1(r)|^2[(1+\alpha r) \times (1 - \alpha r\cot(\alpha r)]dr, \tag{16}$$

$$\mathrm{KE2}(\alpha,\rho) = -2\frac{\hbar^2}{m_h^*}\beta^5\int_\rho^\infty \exp(-2\beta\rho)r^2 dr, \tag{17}$$

$$\mathrm{PE}(\alpha,\rho) = V_0\left[1 - \frac{2 - \cos(2\alpha\rho) + \sin(2\alpha\rho)}{\exp(2\alpha\rho)} + 4\beta^3\rho^3\mathrm{Ei}(2\beta\rho)\right], \tag{18}$$

where $m_h^* = 0.6m_0$ is the effective mass of an *hh* hole, and $\mathrm{Ei}(x)$ is the exponential integral function.

The experimental position of peaks *1–4* of the PL band (see Fig. 1) is given as $\hbar\omega_n = E_g^0 - \varepsilon_b^{(n)}(\rho) - \varepsilon_x(\rho)$, where $\varepsilon_x(\rho)$ is the binding energy of an exciton at the cluster. A cluster that has formed acts as a potential well for a hole and a potential barrier for an electron, which with increasing ρ "feels" a hole charge that is smeared out over the cluster, $q(\rho) = -e(\psi_2(\rho))^2$, and for this reason the Coulomb attraction $V_c(r_e) = eq(\rho)/\varepsilon r_e$ and, hence, $\varepsilon_x(\rho)$ are reduced.[22] In

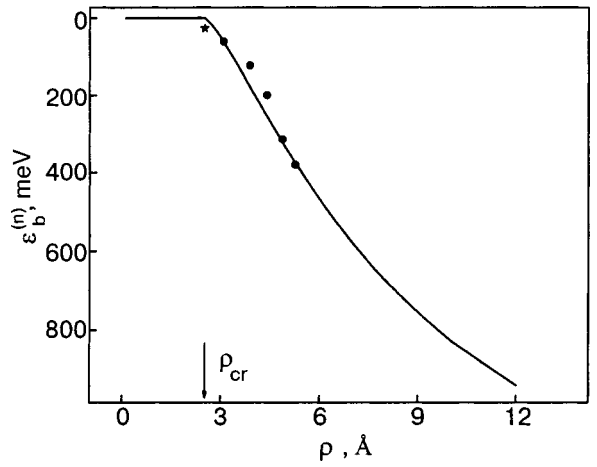

FIG. 5. Dependence of the hole localization energy $\varepsilon_b^{(n)}$ on the cluster radius ρ.

estimating $\varepsilon_x(\rho)$ one must take into account that the wave function of an exciton localized at a cluster must satisfy the boundary condition $\Psi_{ex}(r_3=\rho, r_h)=0$, i.e., it must vanish on the surface of the cluster. This problem was solved in Ref. 22, where in the region $\rho<0.5R_e$, which corresponds to the size of the clusters forming the PL band at small x, the following expression was obtained:

$$\varepsilon_x(\rho)\approx\left[1-0.4\left(\frac{\rho}{R_e}\right)^2\right]E_e, \tag{19}$$

where $E_e=m_e^*e^4/(2\hbar^2\varepsilon^2)$, $R_e=\hbar^2\varepsilon/(m_e^*e^2)$, where $m_e^*=0.17m_0$ is the effective mass of an electron. It is seen from (19) that for $\rho\to 0$ the value of $\varepsilon_x(\rho)\to E_e=26.3$ meV, i.e., it tends toward the value of the binding energy of an electron at a donor in ZnSe. Using equations (16)–(18), we find the radius of the first hole bound state $\rho_1\approx 3.5$ Å, the value of which is comparable to the analogous quantities in the systems ZnS:Te(3.2 Å) and CdS:Te(3.9 Å).[12] The solid line in Fig. 5 shows the calculated $\varepsilon_b^{(n)}(\rho)$ curve, and the points are the experimental values of $\varepsilon_b^{(n)}(\rho)=E_g^0-\hbar\omega_n-\varepsilon_x(\rho)$ with allowance for Eq. (19), where the cluster radius was taken to be $\rho_n=n^{1/3}\rho_1$. Also shown in the figure is the critical size of the potential well $\rho_{cr}\geqslant 2.51$ Å in which a hole bound state with practically zero binding energy is formed; therefore the first experimental point $\varepsilon_x(\rho_{cr})=26.3$ meV is indicated in the figure by a star. If the covalent radii of ZnSe ($r_c=2.45$ Å) and ZnTe ($r_c=2.63$ Å) and the stretching of the $ZnSe_{1-x}Te_x$ layers in the plane of the SL are taken into account, it becomes clear that ρ_{cr} is correlated with these quantities. As we have said, as the number of atoms in a cluster increases, the number of its spatial configurations increases exponentially. In a first approximation each configuration is characterized by a certain averaged spherical wave function $\Psi(r_h)$, as a consequence of which a slight disparity between the experimental and calculated values of $\varepsilon_b^{(2,3)}(\rho_{2,3})$ is observed. With increasing n the shape of the cluster will approach ever closer to spherical, and therefore the states at such clusters will be described most accurately by spherical wave functions.

5. EVOLUTION OF THE EXCITON SPECTRUM OF A ZnSe/ZnTe SUPERLATTICE DUE TO CHANGES IN THE STRUCTURE OF THE MIXED LAYERS

The changes in the shape and spectral position of the PL bands shown in Fig. 3 can be explained by the processes of elastic energy relaxation that take place in practically any strained quantum structure. In our particular case this occurs through an increase in the concentration of Te atoms in the ZnSe layers on account of diffusion. We recall that such a diffusion process is made easier by the fact that the bonding between Zn and Se in the ZnSe layers is weakened on account of the stretching of those layers in the growth plane. In a SSS the growth of the Te concentration leads to a change in the width of the band gap and an increase in the number and mean size of the clusters. The first factor does not play a substantial role in a SL, since $E_g^0(x)$ is determined mainly by the renormalized band gaps of the ZnSe and ZnTe layers. This follows from Fig. 3, where band *2*, recorded in samples stored for some time, is shifted to shorter wavelengths, unlike the long-wavelength shift with increasing concentration observed in $ZnSe_{1-x}Te_x$ SSSs.

The second factor, the increase in the number and mean size of the clusters with increasing concentration leads to overlap of the wave functions of the states localized on them and, as a consequence, to the formation of a percolating cluster. As a result of the appearance of a percolation level for the hole states, the holes can move freely and be trapped in the ZnTe layers; therefore, the localization in the mixed layer falls off. This explains the rather unusual phenomenon of practically complete disappearance of the emission from the region 2600–2400 meV (bands *2* and *3* in Fig. 3). However, the emission does not simply vanish from the indicated region—the PL bands shift monotonically to shorter wavelengths, into a region which is significantly greater than even the band gap of bulk ZnSe (2823 meV). We note that between bands *2* and *3* there exist several more bands that we recorded at different times, showing a smooth transition between them, but they have been left out of Fig. 3 to avoid clutter. The short-wavelength shift of the PL band is about 500 meV and is accompanied by a narrowing of the band to 190 meV at half maximum (band *4*).

For a qualitative explanation of the observed short-wavelength shift of the band we show for comparison in Fig. 3 the PL band (*5*) of a type-I superlattice ZnS(60 Å)/ZnSe(20 Å) which we studied previously, in which the excitons are localized in the ZnSe layer.[16] Comparing the spectral positions of the PL bands *1*, *2*, *3*, and *5*, we can draw the following conclusions. The freshly grown ZnSe/ZnTe SLs and SSSs with low Te concentrations have practically the same emission properties, which are due to localization of the excitons at isolated traps and clusters. This is confirmed by the similar shape of the PL bands and the coincidence of their spectral positions.[7,14] However, as time goes on, the thickness of the mixed layers increases and, accordingly, the thickness of the ZnSe layers dencreases. The energy of size quantization of the electrons localized in the latter begins to exceed their binding energy at isolated traps and clusters, and, as a result, the PL band is shifted monotonically to shorter wavelengths. Thus a periodic structure with alternating ZnSe and ZnTe layers after a certain time begins to ac-

quire the characteristic features of a quantum structure, in which the short-wavelength shift of the PL band is due to size quantization of the motion of one or both of the carriers in the exciton.

A calculation shows that the fact that the size quantization energy of the electrons exceeds the binding energy at isoelectronic traps in the mixed layers begins to be the dominant factor at ZnSe thicknesses $L<30$ Å. The hole states are not affected by the sizes of the ZnSe layers on account of their strong localization. This model of the exciton was considered in Ref. 23, where the energy of a local exciton state induced by isoelectronic traps of vanishingly small radius was calculated as a function of the width of the quantum layer (ZnSe) and for various positions of the impurity at it. It is seen from Fig. 3 that the shift of the PL band relative to E_{1s}^0 is $\varepsilon_1=500$ meV, which can be written as follows: $\varepsilon_1=(\hbar t_1)^2/(2m_e^* L_1^2)$, where t_1 is the first root of the equation relating the width L_1 of a quantum layer to its width ΔE_c and the mass ratio of the electrons in ZnTe ($m_b^*=0.13m_0$) and in ZnSe:[24]

$$\tan\left(\frac{t_1}{2}\right)=\left(\frac{m_e^*}{m_b^*}\right)^{1/2}\left[\frac{q^2-t_1^2}{t_1^2}\right]^{1/2}, \tag{20}$$

where $q^2=2m_e^* L_1^2 \Delta E_c/\hbar^2$. Since $\Delta E_c=1212$ meV, we can without loss of generality set $\Delta E_c\to\infty$ and $t_1=\pi$, whereupon we obtain $L_1\approx 20$ Å and $L_x\approx 30$ Å.

It should be noted that the results of the calculation are only estimates, for the following reasons. As a result of the diffusion of Te atoms into the ZnSe layers a smearing of the heterointerface occurs, and one can therefore no longer represent the ZnSe layer in the form of a square potential well; more likely the potential well should be written as $V=-V_0/f(r)$, where $f(r)$ is a function describing the smearing of the boundaries of the quantum layer and which has the following properties: $f(r=0)=1$ at the center of the layer, and $f(r)\to\infty$ with increasing r. It is clear that the position of the size quantization level of a particle in such a potential will differ from that in the usual square well with sharp interfacial boundaries.[23] The smearing of the heterointerfaces leads to strong fluctuations of the thickness of the ZnSe layer and, as a consequence, to fluctuations of the energy level of electrons in it; this leads to strong broadening of the PL band, which can be seen in Fig. 3. Although fluctuations of the thickness of the ZnSe layers in ZnS/ZnSe SLs also occur, they are considerably smaller, as can be seen from a comparison of PL bands *4* and *5*.

CONCLUSION

Let us conclude by discussing the possible influence of oxygen on the SL spectra obtained, since the samples were stored under normal conditions at room temperature. According to its position in the periodic table, oxygen is an isoelectronic acceptor with respect to both ZnSe and ZnTe. However, in the ZnSe:O system the PL band ($I_1=2.791$ eV), which is due to the recombination of excitons bound to O atoms, is not dominant in the spectrum, and a number of other bands (I_2, I^d, etc.; see Ref. 25 for details) are observed in addition to it. It is clear that these bands to not appear at all in the SL spectra shown. In contrast to ZnSe, in ZnTe oxygen plays a substantial role, and even at low oxygen concentrations an appreciable rearrangement of the original exciton spectrum of ZnTe occurs wherein an isolated band due to the recombination of excitons on O clusters of different shape appears.[25] However, in that case the PL band is shifted into the energy region 2.2–1.8 eV, which likewise has no effect on the spectra of the SLs studied here. Thus it is clear that the change in the internal structure of a ZnSe/ZnTe SL due to the influence of relaxation processes, which lead to a lowering of the elastic energy in the system, is the main source of rearrangement of the emission spectra of the given SRs.

*E-mail: jbond@iop.kiev.ua

[1] N. Takojima, F. Iida, K. Imai, and K. Kumazaki, J. Cryst. Growth **138**, 633 (1994).
[2] S. Nakashima, A. Wada, H. Fujiyasu, M. Aoki, and H. Yang, J. Appl. Phys. **62**, 2009 (1987).
[3] H. Kuwabara, H. Fujiyasu, M. Aoki, and Sh. Yamada, Jpn. J. Appl. Phys. **25**, L707 (1986).
[4] M. Kobajashi, N. Mino, H. Katagiri, R. Kimura, M. Kanagi, and K. Takahashi, J. Appl. Phys. **60**, 773 (1986); C. D. Lee, H. K. Kim, H. L. Park, C. H. Chung, and S. K. Chang, J. Lumin. **48–49**, Part 1, 116 (1991).
[5] J. J. Davies, Semicond. Sci. Technol. **3**, 219 (1988); T. Yao, M. Kato, J. J. Davies, and H. Tanino, J. Cryst. Growth **86**, 552 (1988).
[6] D. Lee, A. Mysyrowicz, A. V. Nurmikko, and B. J. Fitzpatrick, Phys. Rev. Lett. **58**, 1475 (1987).
[7] A. Yu. Naumov, S. A. Permogorov, A. N. Reznitskiĭ, V. Ya. Zhulaĭ, V. A. Novozhilov, and G. T. Petrovskiĭ, Fiz. Tverd. Tela (Leningrad) **29**, 377 (1987) [Sov. Phys. Solid State **29**, 215 (1987)].
[8] A. N. Reznitskiĭ, S. A. Permogorov, and A. Yu. Naumov, Izv. AN SSSR Ser. Fiz. **52**, 691 (1988); **49**, 2019 (1985).
[9] S. Permogorov, A. Reznitsky, A. Naumov, H. Stolz, and W. von der Osten, J. Phys.: Condens. Matter **1**, 5125 (1989).
[10] A. A. Klochikhin, S. G. Ogloblin, S. A. Permogorov, A. Reznitsky, S. Klingshirn, V. Lysenko, and J. M. Hvan, JETP Lett. **72**, 320 (2000).
[11] A. A. Klochikhin, S. A. Permogorov, and A. N. Reznitskiĭ, Zh. Éksp. Teor. Fiz. **115**, 1039 (1999) [JETP **88**, 574 (1999)].
[12] O. Goede and W. Heimbrodt, Phys. Status Solidi B **135**, 795 (1986); D. Hennig, O. Goede, W. Heimbrodt, and R. Muller, *ibid.* **105**, 543 (1981).
[13] K. Dhese, J. Goodwin, W. E. Hadston, J. E. Nicholls, J. J. Davies, B. Cockayne, and P. J. Wright, Semicond. Sci. Technol. **7**, 1210 (1992).
[14] I. L. Kuskovsky, C. Tian, G. F. Neumark, J. E. Spanier, I. P. Herman, W. C. Lin, S. P. Guo, and M. C. Tamargo, Phys. Rev. B **63**, 155205 (2001).
[15] Ch. van der Walle, Phys. Rev. B **39**, 1871 (1989); A. Oteish and R. J. Needs, *ibid.* **45**, 1317 (1992).
[16] N. V. Bondar', V. V. Tishchenko, and M. S. Brodin, Fiz. Tekh. Poluprovodn. **34**, 588 (2000) [Semiconductors **34**, 568 (2000)]; N. V. Bondar', Fiz. Tverd. Tela (St. Petersburg) **42**, 1486 (2000) [Phys. Solid State **42**, 1529 (2000)].
[17] F. Malonga, D. Bertho, C. Jouanin, and J.-M. Jancu, Phys. Rev. B **52**, 5124 (1995).
[18] K. Suzuki, K. Wundke, G. Bley, U. Neukirch, J. Gutowski, N. Takojima, T. Sawada, and K. Imai, Phys. Status Solidi B **202**, 1013 (1997).
[19] V. K. Bazhenov and V. I. Fistul', Fiz. Tekh. Poluprovodn. **18**, 843 (1984) [Sov. J. Semicond. **18**, 1345 (1984)]; J. J. Hopfield, D. G. Thomas, and R. T. Lynch, Phys. Rev. Lett. **17**, 312 (1966); A. Baldereshi, J. Lumin. **7**, 79 (1973).
[20] A. van Vechten and J. C. Phillips, Phys. Rev. B **2**, 2160 (1970).
[21] S. H. Sonh and Y. Hamakawa, Phys. Rev. B **46**, 9452 (1992).
[22] U. E. H. Laheld and P. C. Hemmer, Phys. Rev. B **39**, 1871 (1989); U. E. H. Laheld, P. C. Hemmer, and F. B. Pedersen, *ibid.* **48**, 4659 (1993); **52**, 10739 (1994).
[23] L. D. Landau and E. M. Lifshitz, *Quantum Mechanics: Non-Relativistic Theory*, 3rd ed., Pergamon Press, Oxford (1977), Nauka, Moscow (1989).
[24] A. A. Pakhomov, K. V. Khalipov, and I. N. Yassievich, Fiz. Tekh. Poluprovodn. **30**, 1387 (1996) [Semiconductors **30**, 730 (1996)].
[25] K. Akimoto, T. Miyajima, and Y. Mori, Phys. Rev. B **39**, 3138 (1989).

Translated by Steve Torstveit

QUANTUM LIQUIDS AND QUANTUM CRYSTALS

Topology and solid-state physics (Review)*

A. M. Kosevich**

B. Verkin Institute for Low Temperature Physics and Engineering, National Academy of Sciences of Ukraine, pr. Lenina 47, Kharkov 61103, Ukraine

(Submitted July 7, 2003)
Fiz. Nizk. Temp. **30**, 135–162 (February 2004)

The topological aspect of the dynamics of electrons in a crystal (band electrons) and of crystal lattice vibrations (phonons) is discussed. The main features of the dynamics of conduction electrons in metals are connected with the shape of their Fermi surface, which is different from that for free electrons. It is demonstrated that the behavior of band electrons under the influence of external electric and magnetic fields depends strongly on the topology of the Fermi surface. Various examples of such a dependence (calculation of the periods of quantum oscillations, magnetic breakdown, features of the magnetoresistance, Bloch oscillations) are adduced and discussed. The features of the dynamics of phonons are manifested in singularities of the density of vibrational states (van Hove singularities), which are directly related to a change in the topology of the constant-frequency surfaces. The presence of a topological invariant that changes by a jump upon a change in topology of the constant-frequency surface is pointed out. The origin of the so-called phase transition of order two and a half is discussed. © *2004 American Institute of Physics.* [DOI: 10.1063/1.1645161]

1. INTRODUCTION

The quantitative description of processes and observable physical phenomena requires the use of mathematical methods. The more complex the nature of the phenomenon, to more powerful the mathematical methods that are used to describe it. Delving into the details of physical processes requires that theoretical physicists employ ever more refined methods of calculation.

However, there are branches of mathematics that help one to understand not the details of some physical phenomena (as would be important, in particular, for discussing specific experimental data) but rather some general relations that unify the physical relationships obtained in many different kind of experiments. Well-known examples in solid-state physics are group theory and the theory of symmetry. They make it possible to systematize in a rather general way the expected and observed effects without having to write out the corresponding equations in concrete form, knowing only the symmetry of the crystalline objects and the set of mathematical entities (vectors, tensors, etc.) used for describing the physical phenomena in question.

An example of a general type of assertion based only on symmetry properties is the following statement in the dynamics of any periodic structure: an oscillation frequency of any physical nature (or the energy of any elementary excitation) in such a system is a periodic function of the wave (or quasi-wave) vector with a period determined by the structure of the reciprocal lattice and is equal in order of magnitude to $2(\pi/a)$, where a is the spatial period of the system under discussion.

Another type of general systematization of physical phenomena in crystalline objects can be obtained using another branch of mathematics—topology. Although topology is a younger science than physics, its methods and ideas have penetrated into many areas of theoretical physics and enable one to formulate some rather important physical relations of a general character. Topological derivations are especially valuable when the equations of the physical fields have a complicated mathematical structure and do not admit simple general solutions. Descriptions of how topological conclusions are used in field theory, in the theory of phase transitions, the theory of the superfluid phases of ^{3}He, nonlinear dynamics, etc. can be found in the books by Nakahara[1] and Monastyrskiĭ.[2] In condensed matter physics, however, only two aspects are actually discussed: first, the topology of the order parameter in systems undergoing phase transformations, and, second, the classification of possible forms of such nonlinear objects as solitons, vortices, dislocations, disclinations, monopoles, etc.

We wish to call attention to another point of view on a problem that reflects the original understanding of topology. From our point of view (regarding the use of topology in the problems discussed below), topology refers to the geometry of curved lines (trajectories) and surfaces. Can these objects be systematized? A curved line in a 2D or 3D space can be either closed or unclosed; a closed curve can have nodes or not. If those curves are classical trajectories of a particle, then its quantum properties will be different depending on which class of curves the trajectory belongs to. Surfaces (2D manifolds in a 3D space) can contain holes (breaks in continuity) or can be continuous; the surfaces can be closed (like spheres) or open (like a hyperboloid of one sheet); surfaces can be self-intersecting. The characteristic surfaces in solid-state physics are constant-frequency or constant-energy sur-

faces in **k** space; in the electron theory of metals the Fermi surface most often comes to mind. It turns out that a change in topology of a constant-frequency surface (a transformation from a closed to an open surface) at a certain frequency leads to the appearance of features in the density of vibrational states at that frequency—van Hove singularities. Metals with Fermi surfaces of different topology have different asymptotics of their low-temperature magnetoresistance at high magnetic fields.

Substantial progress in elucidating the role of the topological properties of the characteristic surfaces in crystal physics has been reached thanks to the work of I. M. Lifshits and his scientific school (his students and successors). Their work underlies the branch of theoretical condensed matter physics discussed in this review. The interweaving of the classical concepts of particle trajectories, the topological properties of trajectories and constant-energy surfaces, and also the quantum nature of the laws of motion of microparticles is, to the author, the most engaging part of those studies. And although the first studies cited in this review were done over half a century ago, interesting results have been obtained in recent years, demonstrating the inexhaustibility of the problem. The author considers himself to be a direct student of I. M. Lifshits and dedicates this review to the memory of his teacher.

2. GEOMETRY AND TOPOLOGY OF THE FERMI SURFACE OF THE ELECTRON GAS IN METALS

2.1. Dynamics of conduction electrons and the Fermi surface

The terms ''electron gas'' and ''electron dynamics'' are basic concepts in the branch of theoretical solid-state physics known as the electron theory of metals. This theory is based on the concept that the electrical conduction of a metal and its interaction with the electromagnetic field are due to the presence of a collective of atomic electrons which for a variety of reasons behaves as a gas capable of flowing through the crystal lattice. As stated in words, this concept, which was formulated a century ago by Drude, remains unchanged to this day. Now not only do we understand in general terms the reasons for the validity of such a simple model, but it is also clear that the dynamics and kinematics of electrons in a crystal must be substantially altered in comparison with those for an electron in vacuum.

The reason why the model of a gas of noninteracting electrons can be employed with confidence is that at low temperatures the majority of electrons, obeying the thermodynamic requirement of minimization of the energy of the system, densely occupy the low-lying energy levels, filling the individual states in pairs (with opposite spins) and becoming incapable of participating in any motion (which inevitably involves a transition from one state to another). The remaining electrons can be considered to have been pulled out of this ''dead sea'' and represent Fermi elementary excitations of the whole electron system. It is completely admissible to treat the set of these excitations as an ideal Fermi gas. The energy per particle separating the occupied and unoccupied electronic states is called the Fermi energy. In a literal sense such a clear separation of electronic states is possible only at absolute zero ($T=0$), but if the thermal energy of an electron (the temperature T in energy units) is small compared to the Fermi energy, then a narrow energy region (with a width of the order of T) containing only partially filled electronic states will arise near the Fermi energy. It is the electrons in these states that actively participate in all the processes involving the motion of electrons. The lower the temperature, the greater the confidence with which one can say that only electrons with the Fermi energy participate in physical processes.

Thus we have agreed to consider electrons with energies close to the Fermi energy as free particles forming an ideal Fermi gas. The main dynamical variable of a free particle is its momentum **p**. In a quasiclassical approximation the position of an electron in space is specified by its coordinate **x**. The coordinates **x** and **p** are a pair of canonically conjugate variables specifying the instantaneous state of the particle in classical mechanics. In the absence of external fields the energy ε of an electron depends only on **p**: $\varepsilon=\varepsilon(\mathbf{p})$, and this dependence is called a dispersion relation. For a free electron $\varepsilon=p^2/(2m_0)$, where m_0 is the mass of the electron, and we speak of a quadratic dispersion relation. An equal-energy or ''constant-energy'') surface is a geometric mapping of the dispersion relation. A constant-energy surface is a surface in **p** space specified by the condition

$$\varepsilon(\mathbf{p})=\varepsilon=\text{const}. \tag{1}$$

For a free electron this is a sphere of radius $p=\sqrt{2m_0\varepsilon}$.

The constant-energy surface corresponding to the Fermi energy ε_F is called the Fermi surface. For a gas of free electrons it is a sphere of radius $p_F=\sqrt{2m_0\varepsilon_F}$. At $T=0$ all states inside the Fermi surface are occupied, and therefore for a fixed number of electrons the volume inside the Fermi sphere and, hence, the Fermi energy ε_F are uniquely related to the number of electrons:

$$N=2\frac{V\Omega(\varepsilon_F)}{(2\pi\hbar)^3}=\frac{8\pi Vp_F^3}{3(2\pi\hbar)^3}=\frac{\pi(2m_0)^{3/2}}{3(2\pi\hbar)^3}\varepsilon_F^{3/2}, \tag{2}$$

where $\Omega(\varepsilon_F)$ is the volume in **p** space inside the Fermi sphere, and the factor of 2 takes into account the two possible values of the electron spin. It follows from (2) that

$$p_F^3=3\pi^2\frac{N}{V}\hbar^3. \tag{3}$$

If we write $N/V=1/a^3$, where a is introduced as the average distance between electrons, relation (3) to good accuracy reduces to the estimate

$$p_F=\hbar(\pi/a). \tag{4}$$

We note that estimate (4) does not contain any of the parameters of the free-electron dispersion relation. This is an extremely important circumstance, since it raises the question of to what degree the calculation (2), which is based on the concept of a gas of free particles with a quadratic dispersion relation, can be used to discuss the properties of electrons in a crystalline metal. In fact, in a periodic structure, such as any single crystal, the momentum **p** is a convenient dynamical variable—its role is played by the quasimomentum, and the energy of an elementary excitation, the role of which we confer on the electron, becomes a periodic function of the quasimomentum with the period of the reciprocal

lattice. Consequently, the dispersion relation of an electron in a metal must be a more complex (and necessarily anisotropic) function of the quasimomentum, and the Fermi surface can therefore acquire a shape that is very unlike a sphere. Nevertheless, the characteristic radius of the Fermi surface is estimated correctly by formula (4). The point is that, in the calculation of (2) we were interested only in the number of states occupied by electrons, which is actually determined by the number of degrees of freedom of all the electrons. In distributing the states corresponding to these degrees of freedom over ''cells'' of the phase space, we will have filled some volume of phase space invariant with respect to the choice of the concrete description of the single-particle states.

Let us turn to the question of the shape of the Fermi surface of the electrons in a crystal and what determines that shape, and discuss the possible manifestations of the shape of the constant-energy surface in the electron dynamics. The motion of an electron in a magnetic field is the most sensitive to this shape.

Let us consider the dynamics of an electron with a dispersion relation $\varepsilon=\varepsilon(\mathbf{p})$ in a uniform magnetic field $\mathbf{B}$. The pair of Hamilton's equations of classical dynamics of the electron have the form

$$\frac{d\mathbf{p}}{dt}=\frac{e}{c}[\mathbf{v}\times\mathbf{B}],\quad \mathbf{v}\equiv\frac{d\mathbf{x}}{dt}=\frac{\partial\varepsilon}{\partial\mathbf{p}}. \tag{5}$$

Choosing the z axis along the direction of $\mathbf{B}$, we obtain the following system of equations of motion:

$$\frac{dp_x}{dt}=\frac{eB}{c}v_y,\quad \frac{dp_y}{dt}=-\frac{eB}{c}v_x,\quad \frac{dp_z}{dt}=0, \tag{6}$$

which have two integrals of the motion:

$$\varepsilon(\mathbf{p})=\text{const},\quad p_z=\text{const}. \tag{7}$$

The pair of conditions (7) determines the trajectory of the electron in $\mathbf{p}$ space—it is the curve of the intersection of the surface $\varepsilon(\mathbf{p})=\text{const}$ and the plane $p_z=\text{const}$ (Fig. 1). It follows from Eq. (6) that the projection of the electron trajectory in $\mathbf{x}$ space is similar to the trajectory (7). Indeed, we rewrite the first two equations of (6) in the form

$$\frac{dp_x}{dt}=\frac{eB}{c}\frac{dy}{dt},\quad \frac{dp_y}{dt}=-\frac{eB}{c}\frac{dx}{dt}. \tag{8}$$

Relations (8) show that the projection of the trajectory in $\mathbf{x}$ space on the xoy plane is indeed similar to that in $\mathbf{p}$ space, but rotated by 90° in relation to the coordinate axes ox and oy (Fig. 2). The coincidence of the directions of the electron velocity vector can also be noted in Fig. 2.

Analysis of the equations of motion (6) and inspection of Fig. 2 lead to the conclusion that the electron executes cyclic motion in a magnetic field, revolving along a closed trajectory (in the case of a free electron this would be motion along a circle). The frequency of this cyclic motion is easily calculated. It follows from (6) that the velocity of the electron's motion along the trajectory in $\mathbf{p}$ space is given by

$$\frac{dp_l}{dt}=\frac{eB}{c}v_\perp, \tag{9}$$

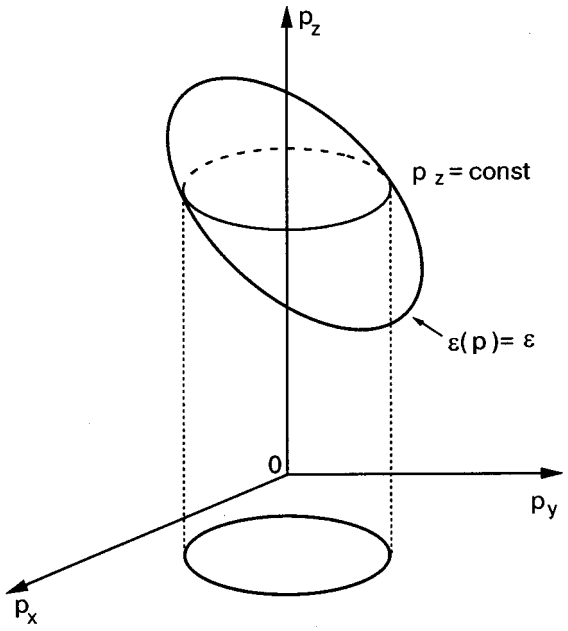

FIG. 1. Trajectory of an electron in $\mathbf{p}$ space and its projection on a plane perpendicular to the magnetic field.

where $v_\perp$ is the projection of the electron velocity on the plane perpendicular to the magnetic field $\mathbf{B}$. Relation (9) generates a chain of equations

$$dt=\frac{c}{eB}\frac{dp_l}{v_\perp},\quad t=\frac{c}{eB}\int\frac{dp_l}{v_\perp},\quad \Delta t=\frac{c}{eB}\oint\frac{dp_l}{v_\perp}, \tag{10}$$

where the integral is evaluated along the electron trajectory, Δt is the period of the cyclic motion of the electron, and the last integral is taken over the whole closed trajectory. Knowing Δt, we determine the frequency of the cyclic motion of the electron: $\omega_c=2\pi/\Delta t$. This the cyclotron resonance frequency in a magnetic field for an electron in a crystal. However, this frequency is customarily written in the form $\omega_c=eB/mc$, where m is the electron mass. Consequently, the cyclotron mass of the electron in a crystal depends on its trajectory and is a function of state and not a numerical characteristic (as in the case of a free electron, where $m_c=m_0=\text{const}$). It is not hard to get the geometric sense of this characteristic of the electron. One need only calculate the change in area bounded by an electron trajectory on the plane $p_z=\text{const}$ upon a small increase $\delta\varepsilon$ in the electron energy:

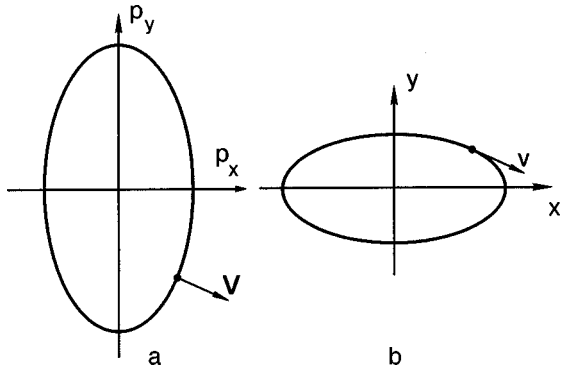

FIG. 2. Trajectory of an electron in $\mathbf{p}$ space (a) and in $\mathbf{x}$ space (b).

$$\delta S = \oint \delta p_\perp \, dp_l = \oint \frac{dp_l}{v_\perp} \, \delta\varepsilon \, . \tag{11}$$

Here the integral is evaluated over the closed trajectory of the electron. Comparing the expression for Δt in (10) with (11), we find

$$\Delta t = \frac{c}{eB} \frac{\partial S}{\partial \varepsilon}, \tag{12}$$

where the function $S = S(\varepsilon, p_z)$ is the aforementioned area bounded by the electron trajectory on the plane $p_z = \text{const}$. Thus the effective cyclotron mass of the electron is given by the expression[3]

$$m_c = m_c(\varepsilon, p_z) = \frac{1}{2\pi} \frac{\partial S}{\partial \varepsilon}. \tag{13}$$

In light of what we have said above, for electrons in a metal formula (13) has actuality on the Fermi surface $\varepsilon = \varepsilon_F$. This means that the area of the cross section of the Fermi surface on the plane $p_z = \text{const}$ and its dependence on the Fermi energy have direct physical meaning—the derivative in (13) is an experimentally measurable quantity.

2.2. Geometry of the Fermi surface in a crystal

The circumstance that the constant-energy surfaces for electrons in a crystal can have shapes that differ strongly from spherical was obvious from the time the electron theory of metals first appeared, as the figures for the constant-energy surfaces in the well-known monograph of Bethe and Sommerfeld[4] attest. It was understood that, by virtue of the complex structure of the electron spectrum of crystals, there can exist a great diversity of Fermi surfaces of the most unusual shapes, some of which are described in the book by Lifshits, Azbel', and Kaganov.[3] But for a long time it remained unclear whether the shape of the Fermi surface in a given metal could be predicted even as far as its general traits. Only the lucid and rather simple arguments of Harrison[5] made it possible to clarify, first, why an expected shape of the Fermi surface appears in a given metal and, second, the possibility of several Fermi surfaces (more precisely, several different sheets of a multiply connected Fermi surface) coexisting in the same metal.

Let us illustrate Harrison's method by the example of a 2D square lattice, considering it as some symmetric cross section of a 3D lattice. The unit cell in the reciprocal lattice is usually chosen such that the point $\mathbf{k} = 0$ lies at its center (the main square in Fig. 3a and the square in Fig. 3b). However, it could also be chosen differently (a dashed square in Fig. 3c or 3d). Starting from the density of electrons in the metal under discussion, we determine the radius of the Fermi surface (4) (if there is one conduction electron for each atom in the crystal, this radius will be of the same order of magnitude as the size of the unit cell). We draw a circle of that radius around the coordinate origin in Fig. 3a; this will be the cross section of the Fermi surface. Since the energy of an electron in a crystal is a periodic function of the quasimomentum, such circles should also be drawn around each site of the reciprocal lattice. Then a system of intersecting lines (Fermi surfaces) appears in which each point of intersection is a point of degeneracy. It is clear that the points of degeneracy arose by virtue of the primitive model representation of a circular (spherical) shape of the constant-energy surfaces and must be regarded as the result in zeroth approximation. When practically any physical circumstances are taken into account in the next approximation the degeneracy will be removed, and all of the points of intersection of the graphs of the constant-energy surfaces will be shifted slightly. On a plane of the reciprocal lattice an ornament of several closed lines appears. Part of them are conveniently placed in a unit cell of the first type, and part of them in a cell of the second type. Usually they pertain to different (first, second, third,

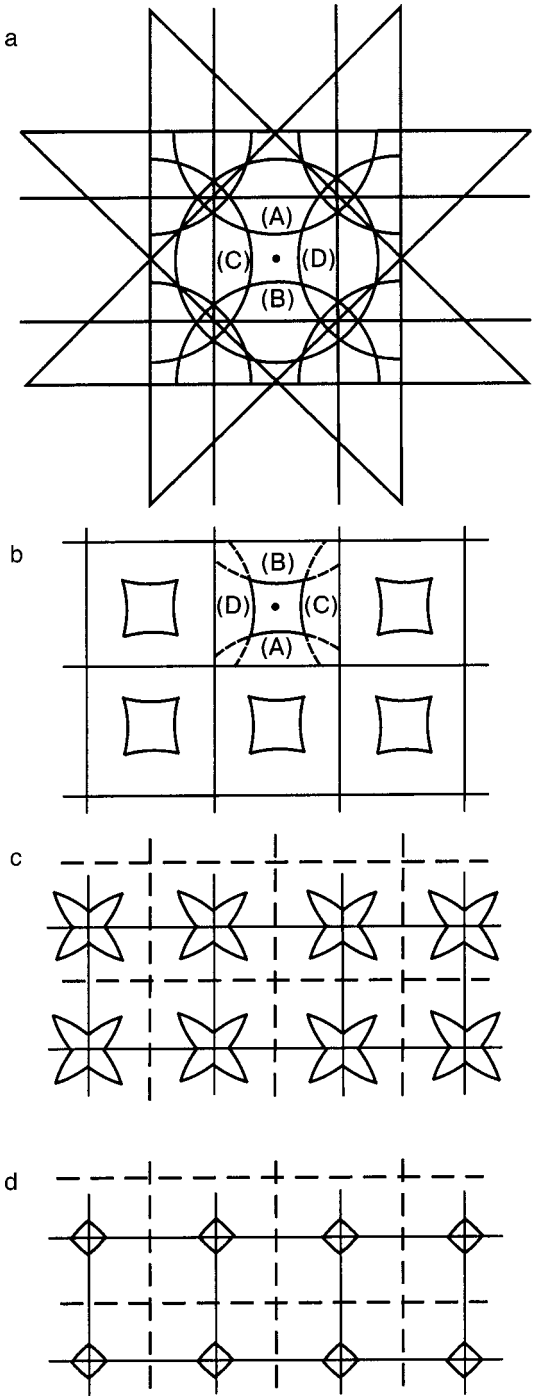

FIG. 3. Construction of the Fermi surface for a square lattice: spheres in the zeroth approximation (a); sheets of the Fermi surface which are situated in different Brillouin zones (b,c,d).

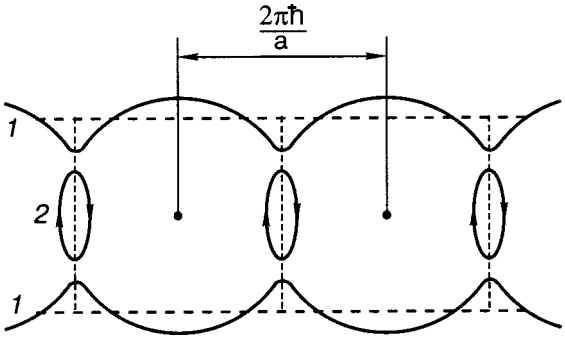

FIG. 4. Two types of electron trajectories on a highly anisotropic Fermi surface: open (*1*) and closed (*2*)

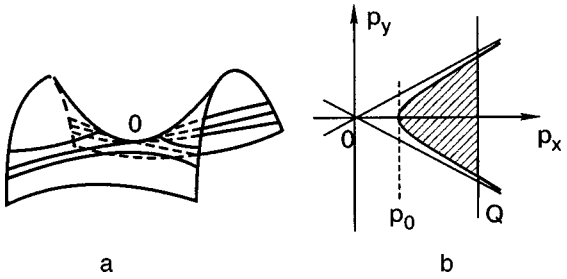

FIG. 6. Trajectories of an electron in the vicinity of a saddle point: the saddle point *O* on the Fermi surface (a); trajectories close to the saddle point (b).

etc.) Brillouin zones and are taken to be different sheets of the Fermi surface.

A somewhat different system of sheets of Fermi surfaces arises in an anisotropic crystal (Fig. 4). After the degeneracy is lifted there will not only be closed lines but also lines threading through the whole reciprocal lattice—cross sections of *open Fermi surfaces*. Consequently, there can exist two topologically different types of Fermi surfaces—closed and open.

If the plane in Fig. 4 is perpendicular to the external magnetic field, then the two types of cross sections of the Fermi surface will lead to two types of electron trajectories in a magnetic field: closed (typical for a free electron) and open, i.e., traversing all of reciprocal space. The latter means that in ordinary coordinate space in the plane perpendicular to the magnetic field the electron executes unbounded motion—it goes off to infinity. It is clear that such a situation is possible only for electrons in a crystal and demonstrates the manifestation of the features of the topology of the Fermi surface in the dynamics of the electrons.

Naturally, only closed cross sections can arise on closed Fermi surfaces, and therefore the corresponding electrons will move along closed (cyclic) trajectories in a magnetic field. On open Fermi surfaces both closed and open crystals are possible. Figure 5 shows various cross sections of a surface having the form of a corrugated cylinder with its axis along the op_x axis. The lines of these cross sections determine electron trajectories with different values of the momentum p_z in the magnetic field. Trajectories of type *1* are open trajectories corresponding to infinite motion of the electron (corresponding to small p_z), while trajectories of type *2* are closed trajectories. The two types of trajectories are separated by an open trajectory (the *separatrix*, which passes through the saddle point on the Fermi surface and therefore has points of self-intersection at the boundaries of the Brillouin zone. These points are singular points because at them the group velocity (equal to the gradient in **p** space) is directed strictly along the normal to the plane of section and, consequently, the projection of the electron velocity on that plane vanishes. The electron at this point should be at rest, but in its motion along such a trajectory it approaches the saddle point only asymptotically (for $t\to\infty$). The forced stopping of an electron at the saddle point means that its mass goes to infinity. From a mathematical standpoint the trajectory passing through the saddle point has a singular mass.

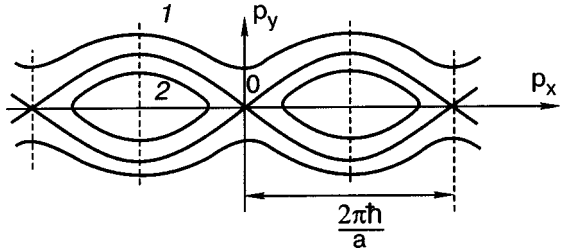

FIG. 5. Different types of electron trajectories: open (*1*) and closed (*2*), corresponding to cross sections of a Fermi surface in the form of a corrugated cylinder on $p_z=\text{const}$ planes for different p_z.

In the previous Section it was shown that the effective mass of an electron in a magnetic field is determined as a function of energy ε by formula (13), where S is the cross-sectional area of the constant-energy surface. If one goes from the Fermi energy ε_F to an energy exceeding it by an amount $\Delta\varepsilon$, i.e., to $\varepsilon=\varepsilon_F+\Delta\varepsilon$, then at the same p_z the singular trajectory will be replaced by a nearby closed cyclotron trajectory of type *2*. Figure 6a shows portions of trajectories of the different types near a saddle point. The anomaly of the trajectory of the second type is due to the presence of the close-lying saddle point, and therefore the singularity results from the energy dependence of only that part of the area ΔS which is enclosed by the part of the trajectory near that point. In the leading approximation the part of the cyclotron trajectory of interest to us can be taken as the hyperbola

$$\frac{p_x^2}{2m_1}-\frac{p_y^2}{2m_2}=\Delta\varepsilon, \tag{14}$$

where $m_i>0$ $(i=1,2)$ are characteristics of the corresponding curvatures of the Fermi surface (the trajectory passing through the saddle point can be replaced by the asymptotes of the hyperbola). The quantity ΔS can be calculated as the area bounded by the hyperbola and the straight line $p_x=Q=\text{const}$, where Q is chosen a small (but finite) distance away from the saddle point (see Fig. 6b). Then

$$\Delta S = 2m_2\int_{p_0}^{Q}\left(\frac{p_x^2}{2m_1}-\Delta\varepsilon\right)^2 dp_x$$
$$= 4\sqrt{m_1m_2}\,\Delta\varepsilon\int_1^{x(\Delta\varepsilon)}\sqrt{x^2-1}\,dx, \tag{15}$$

where $p_0=\sqrt{2m_1\Delta\varepsilon}$ and $x(\Delta\varepsilon)=Q/\sqrt{2m_1\Delta\varepsilon}$. Then in the leading approximation the cyclotron mass of an electron on a trajectory close to the singular trajectory is equal to[3]

$$m_c=\frac{(m_1m_2)^{1/2}}{\pi}\ln\frac{\varepsilon(Q)}{\Delta\varepsilon}, \tag{16}$$

where $\varepsilon(Q)=Q^2/(2m_1)$. Thus as the saddle point is approached, the effective mass of the electron increases logarithmically. Consequently, the period of gyration of the electron in the magnetic field (its cyclotron period) increases to infinity, and the motion along a trajectory passing through the saddle point become similar to motion along an open trajectory—the electron takes an infinite time to traverse the trajectory.

2.3. Quantum magnetic oscillations and the shape of the Fermi surface

A direct reflection of the shape of the Fermi surface is found in the *de Haas–van Alphen effect*, which is among the most interesting of macroscopic quantum phenomena. It is manifested in an oscillatory dependence of the magnetization of a metal on the strength of the magnetic field. This effect, discovered in 1930 by the Leiden physicists for whom it is named, has a surprising distinction: the de Haas–van Alphen effect is amenable to theoretical interpretation in all its details. A detailed description of the history of the discovery of this effect and its observation over the course of many decades and an assessment of its role in the experimental determination of the electronic spectrum of metals is found in the monograph by Shoenberg.[6] For us it is important that it is a purely quantum phenomenon, due to the quantization of the electron motion in a magnetic field.

We perform a quasiclassical quantization of the electron motion along a closed orbit. It is known that the magnetic flux Φ enclosed by the electron orbit is quantized:

$$\Phi=\phi_0 n,\quad n=0,1,2,...;\quad \phi_0=\frac{2\pi\hbar c}{e}, \tag{17}$$

where ϕ_0 is the magnetic flux quantum. If A denotes the area enclosed by the projection of the electron orbit on the xy plane, perpendicular to the magnetic field **B**, then one can write $\Phi=BA$. But according to (8) the area A is proportional to the cross-sectional area of the constant-energy surface $\varepsilon(\mathbf{p})=\varepsilon=\text{const}$ on the plane $p_z=\text{const}$:

$$A=\left(\frac{c}{eB}\right)^2 S(\varepsilon,p_z),$$

and therefore the following quantization rule arises:

$$S(\varepsilon,p_z)=\frac{2\pi\hbar eB}{c}(n+\gamma),\quad n=0,1,2,..., \tag{18}$$

where γ is a parameter having a value of the order of unity. Formula (18), which was first proposed by Onsager,[7] gives the dependence of the electron energy on the quantum numbers n and p_z: $\varepsilon=\varepsilon_n(p_z)$, from which one can construct the thermodynamics of the electron gas in a magnetic field.

The quantization of the electron motion along trajectories close to the separatrix in Fig. 4 (or, in other words, close to a self-intersecting trajectory) requires special study. Let us consider the electron orbits into which the separatrix in Fig. 4 is transformed either upon a small deviation of the magnetic field from the z axis or upon a small change in the value of p_z. We shall discuss the case when there are two closed trajectories enclosing a cross section of the Fermi surface, of the type indicated by the shading in Fig. 7. The quasiclassical quantization in such a case was investigated by Azbel'.[8] If the trajectories *1* and *2* in Fig. 7 have parts that are close, then the effective value of γ will depend strongly on the number n, and near the self-intersecting trajectory the distance between energy levels oscillates with variation of the magnetic field.

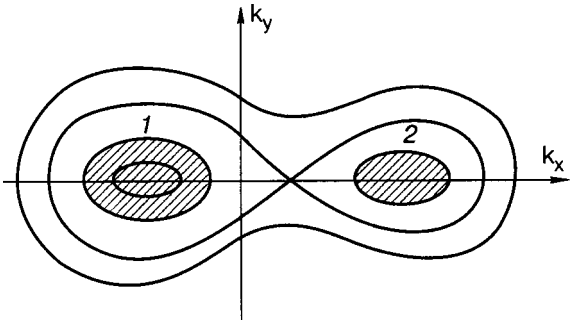

FIG. 7. Magnetic orbits in the vicinity of a separatrix in the form of a figure eight.

In the papers by Lifshits and Kosevich[9] the magnetization of the electron gas was calculated at low temperatures and an expression was obtained for the oscillatory part of the magnetization of the metal. This expression can be represented schematically in the form

$$\Delta M_{\text{osc}}=M_0(B,T)\cos\left(\frac{c\hbar S_m(\varepsilon_F)}{eB}-\gamma\right)\cos\left(\frac{\pi g}{2}\frac{m_c}{m_0}\right), \tag{19}$$

where M_0 is a smoothly varying (with B) amplitude of the oscillations, $S_m(\varepsilon_F)$ is the area of the extremal cross section of the Fermi surface on the plane $p_z=\text{const}$, m_c is the effective cyclotron mass of an electron in the metal, m_0 is the mass of a free electron, and g is the gyromagnetic ratio, which determines the spin magneton of the electron (for a free electron $g=2$). The main characteristic of the de Haas–van Alphen effect is the period of the oscillations. In the inverse magnetic field it is given by

$$\Delta\left(\frac{1}{B}\right)=\frac{2\pi|e|\hbar}{cS_m}. \tag{20}$$

This period is independent of the magnetic field (see Fig. 8) and also independent of temperature (!). In terms of the field itself, under the condition $\Delta B\ll B^2$ one has

$$\Delta(B)=\frac{2\pi e\hbar}{cS_m}B^2, \tag{21}$$

i.e., at high fields the period is proportional to the square of the magnetic field.

If the Fermi surface is convex, then there is only one extremal cross section (a maximum). If the surface is nonconvex there may be several of them (Fig. 9). Consequently, the experimentally observed dependences for M_{osc} can have the form of a superposition of several oscillatory curves.

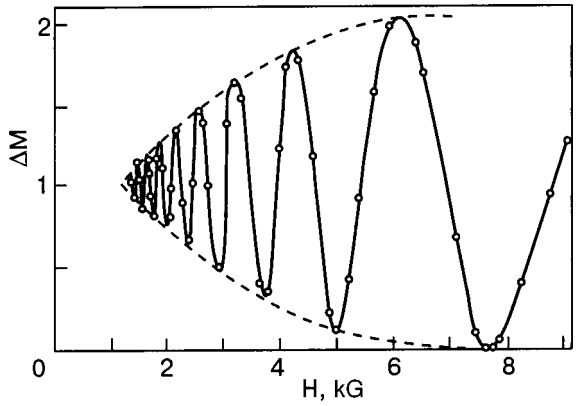

FIG. 8. Oscillations of the magnetization of a Bi single crystal (Shoenberg, 1938).

A set of cross sections of the Fermi surface and, hence, of oscillation periods arises in quasi-two-dimensional conductors, for which the Fermi surfaces typically have the form of corrugated cylinders. If the magnetic field **B** is directed along the axis of the cylinder, then two types of extremal cross sections (minimum and maximum) are possible. If the direction of **B** deviates from the axis of the cylinder by some angle θ (see Fig. 10), then there arises a continuous set of cross sections whose areas increase with increasing angle θ. It is easy to see that the areas of the extremal cross sections will increase in proportion to $\tan\theta$ $(0<\theta<\pi/2)$, and this will lead to an inverse dependence on $\tan\theta$ of the periods of the quantum oscillations in the inverse magnetic field (20). For $\theta=\pi/2$ a cross section threading through the whole momentum space arises, and its contour becomes an open trajectory of the type like curve *1* in Fig. 5; the corresponding quantum oscillations then vanish.

The amplitude of the oscillations have the simplest dependence on T at not very low temperatures $T>\hbar\omega_c$, where $\omega_c=eB/(m_c c)$ is the cyclotron frequency, when

$$M_0\sim\exp\left(-\frac{2\pi^2 T}{\hbar\omega_c}\right). \tag{22}$$

Thus the three separated factors in Eq. (19) make it possible to determine the three most important characteristics of the electron system: a) from the periods of the oscillations one can determine the extremal cross sections of the Fermi surface for different directions of the magnetic field (the dimensions of the projection of the Fermi surface on different planes), b) from the temperature dependence (22) one can determine the effective electron masses on the extremal trajectories and, finally, c) the last cofactor tells about the gyromagnetic ratio for an electron in the metal. All of these possibilities have been used successfully in numerous experiments, and formula (19) is highly valued by those who investigate the electronic properties of metals. The Fermi surfaces of many metals have been studied and an atlas of Fermi surfaces has even been compiled on the basis of formula (19). Such an atlas, prepared by Yu. P. Gaidukov, was first published as a proposal in Ref. 3. In Shoenberg's book[6] formula (19) is called the Lifshits–Kosevich (LK) formula, a name that is used repeatedly in original papers and reviews, including the book by Wosnitza.[10]

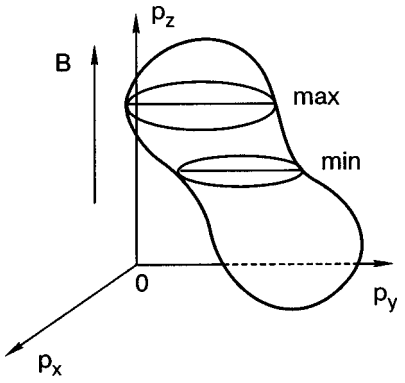

FIG. 9. Two types of extremal single crystals of a nonconvex Fermi surface.

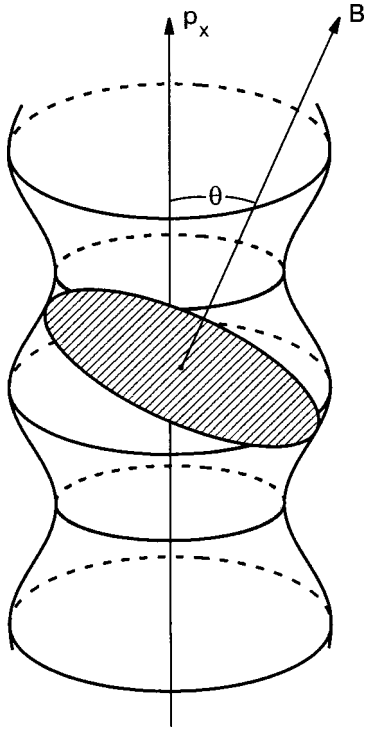

FIG. 10. Cross section of a Fermi surface in the form of a corrugated cylinder, in relation to the direction of the magnetic field.

From the standpoint of geometry, item ''a)'' is the most interesting possibility, since it entails a statement of the problem of determining the shape of the Fermi surface from a set of extremal cross sections for various orientations of the secant plane (Fig. 11). This question was posed in the form of an inverse problem and solved by Lifshits and Pogorelov.[11] It was shown that if the surface has a center of symmetry and any ray drawn from the center intersects the surface at only one point (there are no folds on the surface), then the shape of the surface can be reconstructed uniquely from the dependence of the area of the central cross section on the direction of the normal to this cross section. Unfortunately, as far as we know, this result is not being used to reconstruct the Fermi surface from experimental data, since the attention of researchers has been focused on searching for and identifying the unusual sheets, Fermi surfaces that do not satisfy the conditions of the Lifshits–Pogorelov theorem.

In addition to the de Haas–van Alphen effect, quantum magnetic oscillations are characterized by the Shubnikov–de

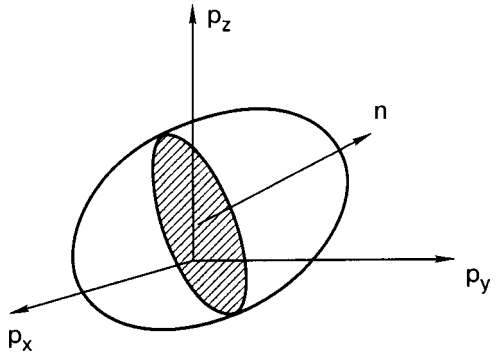

FIG. 11. Cross section of the Fermi surface, in relation to the direction of the magnetic field.

Haas effect—oscillatory dependence of the magnetoresistance of a metal on the magnetic field. Since the physical nature of the latter effect is the same, measurements of the magnetoresistance yield the same periods as for the de Haas–van Alphen effect.[12] Magnetoresistance oscillations are easily observed not only in conventional metals but also in organic conductors (Fig. 12) and thus can be used to study their electronic spectra.

2.4. Magnetic breakdown

In discussing the periods of the quantum oscillations in the case of a complex Fermi surface, we start from the fact that if there are several different extremal cross sections or cross sections of different sheets of the Fermi surface, then the experimental plot will be a superposition of several independent curves with independent periods. In other words, it is assumed that the motion of an electron along each of the closed orbits shown in Fig. 3b or in Fig. 4 is completely independent of the presence of a nearby trajectory of another type. But the Lorentz force can lead to transitions from one trajectory to another. In fact, that can occur if different classical trajectories approach each other very closely. The phenomenon due to these transitions is called *magnetic breakdown*.[13]

The essence of magnetic breakdown is easily illustrated by examining Figs. 4 and 13. In a weak magnetic field the motion of an electron along a small orbit of type *2* in Fig. 13

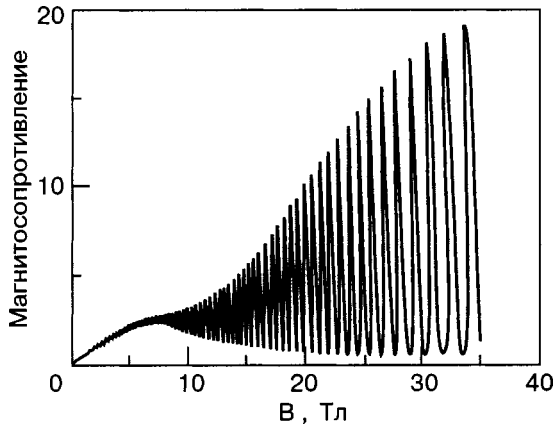

FIG. 12. Oscillations of the magnetoresistance of the organic conductor α-$(ET)_2TlHg(SeCN)_4$ at $T=80$ mK.[10]

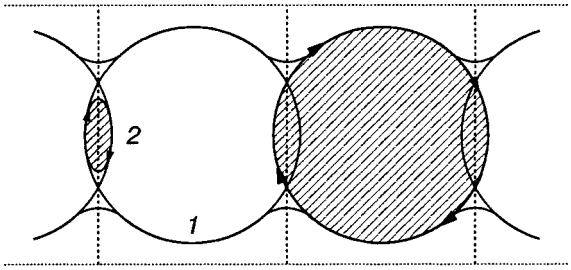

FIG. 13. Diagram explaining the nature of magnetic breakdown: an electron ''hops'' from the small orbit to the large orbit.

gives rise to the de Haas–van Alphen effect with large periods. However, an electron on a closed trajectory of small size at some times comes very close to an open trajectory of type *1*. If the magnetic field exceeds a certain limiting value, then the electron at that time hops ''by inertia'' to the trajectory *1* (see Fig. 13) and then, moving along the latter, ''slips into'' a short part of a second trajectory of type *2*, emerging as a result on a closed trajectory of large radius. This leads to a decrease in the period of the quantum oscillations.

The magnetic breakdown result can be interpreted another way: an electron moving along an open trajectory of type *1* which threads all of reciprocal space goes over to a closed trajectory, the area of which is shaded in Fig. 13. Consequently, a high magnetic field can alter not only the size but also the topology of the electron trajectories.

It is clear that the phenomenon described goes beyond the framework of the classical dynamics of particles with a definite trajectory. The transition (or nontransition) to another trajectory occurs with a certain quantum probability. Therefore, magnetic breakdown is a rather complex quantum process that can lead to a rearrangement of the electronic spectrum of a metal in a high magnetic field. An exposition of the theory of magnetic breakdown may be found in the book by Lifshits *et al.*[3] and in several reviews.[14]

Magnetic breakdown is manifested in oscillatory effects only as a jumplike change in the oscillation period when the magnetic field reaches a limiting (breakdown) value, at which the electrons hop from one closed trajectory to another or in the vanishing of oscillations if the second trajectory encloses such a large area that the period of the oscillations and their amplitude become vanishingly small.

The presence of magnetic breakdown modifies the quantization rule (18). The area $S(\varepsilon,p_z)$ appearing in this formula is that of the closed electron trajectory lying within one unit cell of **p** space. In the leading approximation, when relation (18) is valid, the motion along such a trajectory is autonomous and is insensitive to the periodic dependence of the energy on the quasimomentum. However, in an extended band scheme there are analogous orbits in all cells of the reciprocal lattice—the energy levels obtained from (18) are continuously degenerate [the parameter of this degeneracy is known: it is one of the coordinates of the center of the electron orbit in **x** space; we denote it as $y_0=-cp_x/(eB)$]. On the basis of magnetic breakdown concepts, one should postulate a small tunnel coupling between the motions along these orbits, which lifts the degeneracy of the n levels obtained from (18).

Zil'berman[15] showed on the basis of other arguments

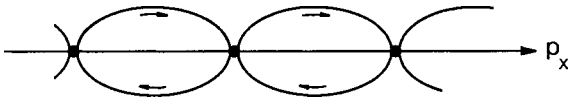

FIG. 14. Chain of magnetic-breakdown orbits in a highly anisotropic metal.

that taking the quantum corrections to the quasiclassical result into account leads to the conclusion that the parameter γ in (18) becomes dependent on the position of the center of the electron orbit within the unit cell of the metal:

$$\gamma = \frac{1}{2} + \delta\gamma_n(p_x),$$

and the level smearing $\delta\gamma$ is small, of the order of the ratio of the lattice constant a to the minimum cyclotron radius of the electron: $\varepsilon = a\sqrt{eB/(c\hbar)} \ll 1$ (usually $\delta\gamma \sim \varepsilon^2$).

The influence of tunneling effects on the electronic spectrum is, of course, enhanced if the trajectories under discussion have close-lying (almost touching) parts. An example of such a system is a chain of closed electron trajectories in a magnetic field (Fig. 14), linked by centers of magnetic breakdown (the small dark circles at the Brillouin zone boundaries). In terms of magnetic breakdown the motion of an electron along the main part of the orbit is classical, while at the magnetic-breakdown center a probability $w = \rho^2(B)$ of tunneling to a neighboring closed trajectory arises. As was shown previously,[16] one usually has

$$\rho = \exp(-B_0/2B) \ll 1,$$

where B_0 is called the breakdown field (it is determined by the effective potential barrier separating the trajectories in the magnetic field). A calculation of the energy of the stationary states in a chain of circular orbits of the type shown in Fig. 14 with the magnetic-breakdown tunneling taken into account leads to the result[17]

$$\delta\gamma_n = \frac{(-\mathbf{1})^n}{\pi} \arcsin\left(\rho \cos\frac{ap_x}{\hbar}\right),$$

which in the case $\rho \ll 1$ reduces to a typical one-dimensional dispersion relation

$$\gamma_n(p_x) = \frac{(-\mathbf{1})^n}{\pi} \rho \cos\frac{ap_x}{\hbar}.$$

The broadening of the electron energy levels as a result of magnetic breakdown no doubt affects the amplitude of the quantum oscillations, leading to an additional decrease in amplitude with increasing magnetic field.

2.5. Band electrons in an electric field and Bloch oscillations

The diversity of the shapes of constant-energy surfaces, the Fermi surfaces in particular, which lead to features of the quantum oscillations is in the final analysis due to the periodic dependence of the energy of a band electron on its quasimomentum. A peculiar manifestation of this dependence is observed in the behavior of an electron under the influence of a uniform static electric field **E**.

In the quasiclassical approximation the electron dynamics is determined by the usual equation

$$\frac{d\mathbf{p}}{dt} = e\mathbf{E} \tag{23}$$

with the usual Hamiltonian definition of the velocity:

$$\mathbf{v} = \frac{\partial\varepsilon}{\partial\mathbf{p}}, \tag{24}$$

where $\varepsilon = \varepsilon(\mathbf{p}) = \varepsilon(\mathbf{p}+\mathbf{G})$, with **G** being a reciprocal lattice vector in **p** space.

We direct the vector **E** along the ox axis and adopt the simplest dependence $\varepsilon = \varepsilon(p_x)$:

$$\varepsilon = \varepsilon \sin\frac{ap_x}{\hbar}; \quad v = \frac{a\varepsilon_0}{\hbar}\cos\frac{ap_x}{\hbar}; \tag{25}$$

then it follows from (23) that $p_x = eEt$, which immediately gives a periodic time dependence of the electron velocity:[18]

$$v_x = v_0(t) \equiv \frac{a\varepsilon_0}{\hbar}\cos(\omega_B t). \tag{26}$$

The frequency $\omega_B = eEa/\hbar$ is called the *Bloch frequency*.

The point is that from a quantum point of view the presence of a definite frequency means that discrete levels, with an energy difference $\Delta\varepsilon = \hbar\omega_B$, are present in the electron spectrum. What reason can there be for this value of $\Delta\varepsilon$ to be selected in a uniform field? By virtue of the uniformity of the field, there can be no preferred value of ε. Therefore, the necessary discreteness can only be due to an equidistant discrete spectrum of the type

$$\varepsilon = \varepsilon_0 + n\hbar\omega, \quad n = 0, \pm 1, \pm 2, \ldots .$$

This equidistant spectrum and especially its manifestation in optical experiments[19] is called the *Wannier–Stark ladder*. It turns out that the distance between ''rungs'' of this ladder in the case of an electron in a uniform electric field determines the Bloch frequency of the oscillations: $\omega = \omega_B$. A brief account of the quantum theory of Bloch oscillations can be found in a review.[20]

At reasonable values of the electric field the frequency of the Bloch oscillations of an electron in a metal is many orders of magnitude smaller than the electron collision frequency even in extremely pure metals (in other words, the oscillation period is much longer than the relaxation time τ in the metal, and the amplitude of the Bloch oscillations is much greater than the electron mean free path).[3] Therefore, in calculating the electrical resistance of conductors and in other analogous cases the periodic character of the electron motion may be ignored if it is kept in mind that on small parts of its path the motion of an electron is translational. For a long time it was considered that Bloch oscillations are an extremely curious physical phenomenon but one that is of only theoretical interest.

The situation changed fundamentally when a technology was developed for preparing perfect semiconductor superlattices with structure periods much greater than the lattice constant. Since in such structures the reciprocal lattice period is strongly reduced and the electron energy spectrum is broken up into narrow subbands, the Bloch oscillations corresponding to them have rather high frequencies (the obvious condition $\omega_B\tau \gg 1$ becomes attainable), affording a real opportunity for generating and observing these oscillations. Recently

direct observations of Bloch oscillations of an electron current in the bulk of semiconductor superlattices have been made (the first direct experiments of this type were apparently carried out in Refs. 21 and 22).

The experimental possibility of ''sensing'' the periodicity of the electron energy in a semiconductor superlattice was first pointed out by Esaki and Tsu.[23] Their arguments and a calculation done in the relaxation-time approximation reduce to the following. If relaxation did not occur, then the time dependence of the electron energy would be determined by formula (26), where now a is the superlattice period. Taking dissipative processes (relaxation) into account forces one to consider that the real change in the electron velocity occurs more slowly (is damped):

$$dv_x = \exp(-t/\tau)dv_0. \tag{27}$$

It follows from (27) that

$$v_x(t) = \int \exp(-t/\tau)dv_0(t) = \int_0^t \frac{dv_0}{dt'}\exp(-t'/\tau)dt'. \tag{28}$$

Thus it turns out that

$$v_x(t) = eE\int_0^t \frac{\partial^2\varepsilon}{\partial p_x^2}\exp(-t'/\tau)dt' = \frac{eE}{m(0)}\int_0^t \cos(\omega_B z')\exp(-z'/\tau)dz', \tag{29}$$

where $m(0)^{-1} = \partial^2\varepsilon/\partial p_x^2$ is the inverse effective mass of an electron at $p_x = 0$.

For long times ($t \gg \tau$) one can set $t = \infty$ at the upper limit in (29), and then one gets the well-known formula of Esaki and Tsu[23] for the steady-state mean velocity of an electron in a semiconductor superlattice:

$$\langle v\rangle = v_x(\infty) = \frac{\omega_B\tau}{1+(\omega_B\tau)^2}\frac{a\varepsilon_0}{\hbar}. \tag{30}$$

In weak fields (when $\omega_B\tau \ll 1$) Eq. (30) implies the standard linear dependence of the mean electron velocity on the field,

$$\langle v\rangle = \frac{e\tau}{m(0)}E, \tag{31}$$

which explains the electrical conductivity in weak electric fields. In a strong electric field ($\omega_B\tau \gg 1$), attainable in semiconductor materials, Eq. (30) implies that the mean velocity is a decreasing function of E (which is impossible in metals):

$$\langle v\rangle = \frac{\varepsilon_0}{e\tau}\frac{1}{E}, \tag{32}$$

and that leads to a negative differential conductance of the semiconductor superlattice.

Bloch oscillations, as we have said, can occur at times shorter than the relaxation time and in sufficiently strong electric fields, i.e., under the condition $1/\omega_B \ll t \ll \tau$. In the limit $\tau = \infty$ expression (29) goes over to formula (26). At large but finite τ formula (29) describes Bloch oscillations of an anharmonic form.

The electrodynamics of semiconductor superlattices is now an independent branch of physics,[24] the content of which touches only lightly on our theme.

2.6. Topology of the Fermi surface and the low-temperature magnetoresistance of metals

The above-described quantum oscillation effects in metals undoubtedly provide a beautiful demonstration of the quantum nature of magnetism, and the diverse forms of their manifestation confirm the complexity of the Fermi surface in metals. However, only closed electron orbits contribute to the observed quantum oscillations. We have mentioned that if, when the direction of the magnetic field is changed, an electron orbit on an open Fermi surface becomes very large and in the limit is transformed to an unclosed trajectory, then the quantum oscillations vanish. The latter circumstance makes it possible to determine the direction in which the Fermi surface is open. However, the specifics of the electron dynamics in motion along open trajectories are reflected in a study of other phenomena.

The dynamics of electrons on open trajectories is clearly manifested in features of those macroscopic properties of metals which can be described without invoking the quantum mechanics of a particle with an arbitrary dispersion relation but which are sensitive to the shape of the classical trajectories of the current carriers. Foremost among such properties are the galvanomagnetic properties of metals in high magnetic fields. The topological aspect of the theory of galvanomagnetic phenomena in metals at low temperatures has become the subject of a deep mathematical analysis.[25]

However, we are not interested in the details of the mathematical analysis but with the physical inferences relating observable phenomena with the geometry of the Fermi surface.

The theme stated by the heading of this subsection has been exhaustively discussed in a splendid review article,[26] and we can therefore limit the discussion here to some general qualitative remarks. It need only be said that that review[26] and the aforementioned monograph[3] give a complete exposition of the theory of low-temperature galvanomagnetic properties of metals in high magnetic fields, when the topological features of the Fermi surfaces are manifested in full measure. In its day this theory was called the LAK theory, after the initial letters of the names of its creators, Lifshits, Azbel', and Kaganov.

At sufficiently high magnetic fields the cyclotron frequency is so large that at low temperatures an electron during its mean free time will go around any closed trajectory within the Brillouin zone many times, and it therefore traverses many unit cells in the reciprocal space, moving along an open trajectory. It is this circumstance that makes it possible for ''openness'' of the electron trajectories to be manifested in the macroscopic properties of a metal.

The value of the electric field in a metal is very small, and therefore in a leading approximation the dynamics of the electron is determined by the shape of its trajectory in the magnetic field. The electric field can be taken into account as a small perturbation that makes the electron jump from one trajectory to another. An exception is the situation in which the magnetic field **B** and electric field **E** are mutually perpendicular. Then all of the electrons on the closed trajectories are entrained into Hall drift with a constant macroscopic velocity $\langle v\rangle = cE/B$. The Hall drift for electrons on open trajectories looks somewhat different, but we will mainly be

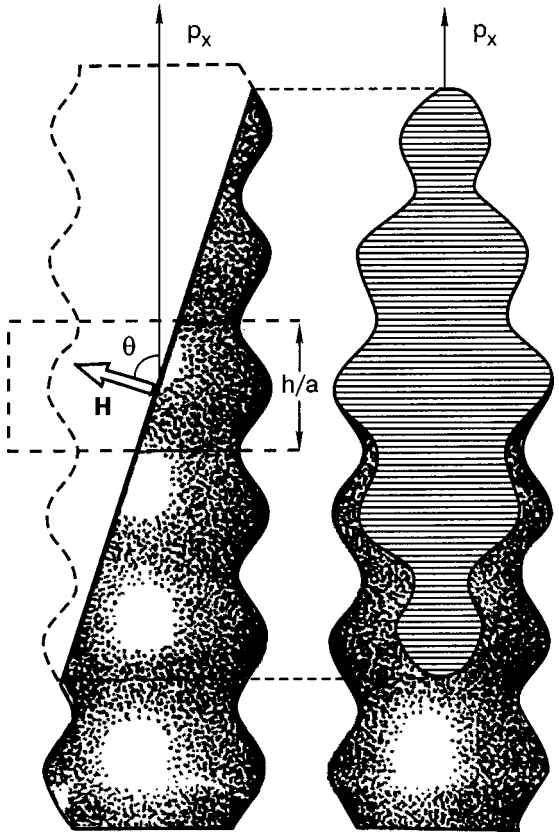

FIG. 15. Long trajectory on a Fermi surface in the form of a corrugated cylinder.

interested not in the Hall but in the diagonal element ρ_{xx} of the resistivity as a function of the direction of the magnetic field. A detailed analysis of the different situations and different possibilities in the dynamics of electrons on open Fermi surfaces was given in Refs. 27 and 28 and analyzed in the monograph cited as Ref. 29. We shall limit consideration to the simplest version.

Let us consider a metal for which the Fermi surface is a corrugated cylinder (of the type illustrated in Fig. 10 or 15). A model dispersion relation that gives such a Fermi surface is

$$\varepsilon(\mathbf{p})=\Delta\sin^2\frac{bp_x}{2}+\frac{p_y^2+p_z^2}{2m}, \tag{33}$$

where $\varepsilon_F>\Delta$. The magnetic field direction is close to the z axis.

The cross section of such a Fermi surface on the $p_z=0$ plane is shown in Fig. 5. It is clear that if the magnetic field is strictly parallel to the z axis, then open trajectories arise for $|p_z|<p_1$. However, if the magnetic field deviates from the z axis by a finite angle θ, then the trajectories become closed (see Fig. 15). But at small angle $\theta\ll 1$ the trajectories, although closed, are very extended, and therefore the length of the trajectory can be much greater than the reciprocal lattice period $2\pi/b$.

If the corresponding length of a trajectory in coordinate space begins to exceed the mean free path of an electron in the metal, then such a trajectory will be manifested in the kinetics as open. Recalling the relationship between the parameters of the electron trajectories in the coordinate and reciprocal spaces (8), we can easily estimate the limiting angle as that value for which the quantity $2\pi c/(beB\theta)$ is comparable to the electron mean free path. Inside the estimated angular interval are extended closed orbits on which the electrons are unable to execute cyclotron motion. As a result, for those electrons $\langle v_x\rangle=0$, while at the same time $\langle v_y\rangle\neq 0$. The latter circumstance leads to a sharp increase in ρ_{xx} in the vicinity of $\theta=0$ (see Fig. 16).

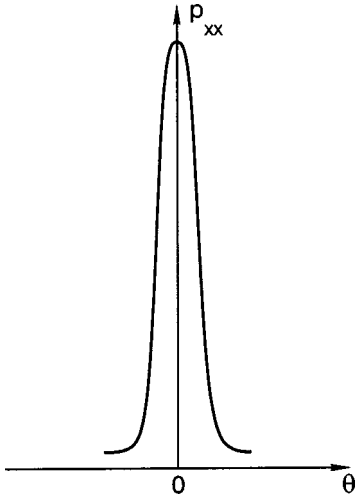

FIG. 16. Singular dependence of the magnetoresistance of a metal with a Fermi surface in the form of a corrugated cylinder on the direction of the magnetic field.

If the Fermi surface is more complex than a corrugated cylinder, e.g., if it is like that shown in Fig. 17, then the orientation of the topological features can be illustrated with the aid of a stereographic projection (Fig. 18). The center of the circle corresponds to the normal in Fig. 17, and the boundary of the circle to $\theta=\pi/2$. The shaded areas show regions in which one encounters open trajectories. The solid lines from the center to the boundary and the circle $\theta=\pi/2$ itself correspond to open trajectories, which arise when the field is rotated in one of the principal planes. The points at the center and on the circumference correspond to directions in which again only closed trajectories are encountered; the dashed lines delimit the region of trajectories which, although closed, extend for many reciprocal lattice periods.

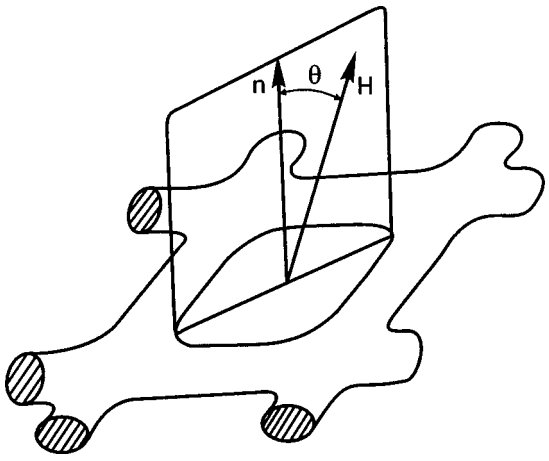

FIG. 17. An open Fermi surface of complex shape.

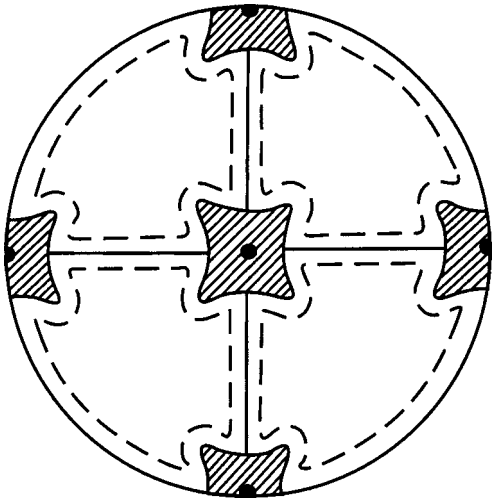

FIG. 18. Stereographic projection of the directions of the magnetic field for which open trajectories are possible.

A peculiar manifestation of the band motion of electrons in a magnetic field, which affords another opportunity for studying the geometry of the Fermi surface, is demonstrated by the classical size-effect oscillations of the magnetoresistance in a conducting superlattice. If the superlattice is a 1D structure with a macroscopic period b along the x axis, then in the single-band approximation the electron can be assigned a dispersion relation of the type (33). We assume that the external magnetic field is directed along the z axis, and we consider classical electron trajectories in the xoy plane. From all we have said it is clear that resonance features appear in the dynamics of an electron gas when the size of the Fermi orbit of an electron along the ox axis in that plane is a multiple of the period b. The corresponding calculations of the low-temperature magnetoresistance of such a system and a bibliography can be found in Ref. 30.

We note that the classical oscillations described are an analog of the magnetoacoustic oscillations predicted by Pippard (see, e.g., Ref. 29). We are talking about a geometric resonance arising when a monochromatic longitudinal acoustic plane wave traverses a metal perpendicular to an external magnetic field. The wave of compression and rarefaction creates a moving periodic structure. Since the velocity of an electron is significantly higher than the speed of sound, it perceives this wave as a slowly moving superlattice with a period equal to the acoustic wavelength. A resonance effect arises when the size of the electron orbit along the direction of propagation of the wave is equal to a whole number of wavelengths. The anisotropy of the effect in relation to the direction of propagation of the sound wave makes it possible to judge the shape of the electron trajectory in the magnetic field.

Additional information about the details of the Fermi surface and the effective masses of the electron can also be obtained from an analysis of the Azbel'–Kaner cyclotron resonance.[31,32] However that effect is due to the high-frequency properties of metals, an analysis of which would be the subject of a separate publication. Therefore, while appreciating the enormous importance of the Azbel'–Kaner effect in the electron theory of metals, here we shall only mention it in passing.

2.7. Berry phase and the topology of trajectories in a magnetic field

Completing our discussion of the problems relating to the topology of electron trajectories in a magnetic field, let us mention the profoundly quantum effect of Berry's geometric phase[33] in magnetic oscillation phenomena. The question concerns the discussion of the parameter γ in formula (18), which influences the phase of the magnetization oscillations (19). A calculation of γ by the WKB method was first carried of these in Ref. 15, and later a more rigorous calculation was done in Ref. 34 for a single-band electron spectrum. In particular, the calculation of Ref. 34 confirmed the special contribution to γ from self-intersecting electron trajectories (like the separatrix in Fig. 5), described previously in Ref. 8.

Let us now say a few general words about the circumstances requiring that the Berry phase be taken into account. It is known that the local instantaneous value of the phase of the wave function is not measurable (only its gradients and time derivative are locally measurable). We write the wave function in the form

$$\psi(\mathbf{x},t)=|\psi|\exp(i\varphi(\mathbf{x},t)).$$

It is assumed that $\psi(\mathbf{x},t)$ is a single-valued function of the coordinates and time. However, the phase $\varphi(\mathbf{x},t)$ need not be single-valued, but its variation along any closed contour must be a multiple of 2π. In the case of interest to us, that of an electron in a static magnetic field directed along the z axis, when $p_z=\text{const}$, $\varepsilon=\text{const}$, the dependence of the phase on x and y is important:

$$\varphi=\frac{p_z z-\varepsilon t}{\hbar}+\varphi_0(x,y).$$

The condition formulated above takes the form

$$\oint\frac{\partial\varphi_0}{\partial x_\alpha}\,dx_\alpha=2\pi n,\quad n=0,1,2,\ldots,\ (\alpha=1,2)\ , \tag{34}$$

where the integration is done along any closed contour in the (x,y) plane.

The phase of a quasiclassical wave function is determined by the classical action S for the system under study: $\varphi=(1/\hbar)S$. In a magnetic field the action S acquires an additional term,

$$\delta S_0=\frac{e}{c}\int_0^{\mathbf{x}}\mathbf{A}d\mathbf{x}, \tag{35}$$

where $\mathbf{A}$ is the vector potential, and therefore a closed electron trajectory Γ should satisfy the following condition, which drives from (34):

$$\frac{e}{\hbar c}\oint_\Gamma\mathbf{A}\,d\mathbf{l}=2\pi n,\quad n=0,1,2,\ldots\ . \tag{36}$$

Condition (36) is equivalent to the quasiclassical quantization of the magnetic flux (16). Relation (36) underlies the Aharonov–Bohm effect[35] and explains the quantization of circular electron orbits in the field of a singular vector potential.[36] What seems strange about this effect is the following. An infinitely thin (in the limit) rectilinear solenoid creates a magnetic field Φ_0 localized along the z axis, while in the surrounding space it creates a vector potential $\mathbf{A}$ with

a single nonzero angular component $A_\theta = \Phi_0/(2\pi r)$, where $r^2 = x^2 + y^2$. Although such a vector potential does not generate a magnetic field in the surrounding space ($\operatorname{curl} A = 0$, $r \neq 0$), an electron constrained to move (e.g., by a special distribution of the electric potential) along a closed trajectory Γ that encloses the z axis nevertheless ''feels'' the presence of the magnetic flux, since its trajectory obeys condition (36).

This is a nonlocal topological effect. There is no physical field of magnetic origin acting locally on the electron at any point $z \neq 0$. The entire trajectory functions as a whole. That trajectory Γ has the feature that the forced motion of the electron takes place in a doubly connected plane (x,y) (its simply connected nature is destroyed by the presence of a localized magnetic flux piercing the plane at the point $x = y = 0$). The Aharonov–Bohm effect was in fact the first physical realization of what later became attributed to a manifestation of the Berry phase.

In Ref. 33, Berry made an extremely important observation that led to a discovery with far-reaching consequences. Suppose that the Hamiltonian and action of a quantum system depend on some set of continuous parameters, which may be called the *space of parameters* **R**. Then the phase of the wave function of that system will also depend on those parameters. For an electron in a crystal the parameter space might be the Brillouin zone in **k** space, for example.[37] If the parameters **R** undergo adiabatic changes and vary slowly in time, $\mathbf{R}(t)$, in such a way that at the end of some cyclic process at $t = T$ they return to their initial values $\mathbf{R}(T) = \mathbf{R}(0)$, then the phase of the wave function obtains an additional change $\delta\beta$ that is not related to an increment of the classical action. The increment $\delta\beta$ was called the *geometric phase*, and that is the Berry phase. The total phase advance along any closed contour in the parameter space must obey a condition of the type (34):

$$\delta\varphi \equiv \frac{1}{\hbar}\delta S_0 + \delta\beta = 2\pi n, \quad n = 0,1,2,\ldots . \tag{37}$$

It is not hard to obtain a formal expression for the Berry phase. Let $\mathcal{H}(\mathbf{R}(t))$ be the Hamiltonian and $|\psi(t)\rangle$ be the wave function—the state vector of the system (we follow the original paper[33] and use the Dirac notation). The evolution of $|\psi(t)\rangle$ is described by the Schrödinger equation

$$i\hbar\left|\frac{\partial\psi(t)}{\partial t}\right\rangle = \mathcal{H}(\mathbf{P}(t))|\psi(t)\rangle. \tag{38}$$

At a fixed time we obtain the eigenfunctions and eigenvalues of the Hamiltonian $\mathcal{H}(\mathbf{R})$, where $\mathbf{R} = \mathbf{R}(t)$:

$$E_n(\mathbf{R})|n(\mathbf{R})\rangle = \mathcal{H}(\mathbf{R}|n(\mathbf{R})\rangle. \tag{39}$$

We assume that the spectrum $E_n(\mathbf{R})$ is discrete and nondegenerate. According to Ehrenfest's quantum adiabatic hypothesis, a system found at the initial time in a state with n energy levels will be found in the same state during adiabatic evolution, although the state itself and the level $E_n(\mathbf{R})$ will vary with time. Therefore the wave function of the system at any time can be written in the form[38]

$$|\psi(t)\rangle = \exp\left(\frac{-i}{\hbar}\int_0^t E_n(\mathbf{R}(t))dt'\right) \times \exp(i\beta_n(t))|n(\mathbf{R}(t))\rangle, \tag{40}$$

where the first exponential factor is the usual phase factor, the last factor $|n(\mathbf{R}(t))\rangle$ is a single-valued function of the parameters $\mathbf{R}(t)$, and the second exponential factor, which arises naturally in Eq. (40), is the key element in the analysis, since the phase $\beta_n(t)$ is not necessarily a single-valued function of $\mathbf{R}(t)$. Therefore in a cyclic process it can happen that $\beta_n(T) \neq \beta_n(0)$.

Substituting (40) into (38), we easily obtain an equation for $\beta_n(t)$:

$$\frac{d\beta_n(t)}{dt} = i\left\langle n(\mathbf{R}(t))\left|\frac{\partial n(\mathbf{R}(t))}{\partial t}\right\rangle\right. . \tag{41}$$

Let us calculate the increment to β_n upon an adiabatic variation along some closed contour C in the parameter space, so that $\mathbf{R}(T) = \mathbf{R}(0)$:

$$\beta_n(T) = i\oint_C \left\langle n(\mathbf{R})\left|\frac{\partial n(\mathbf{R})}{\partial \mathbf{R}}\right\rangle\right. d\mathbf{R} . \tag{42}$$

Since the functions $|n\rangle$ are normalized ($\langle n|n\rangle = 1$), the quantity $\langle n|(\partial n/\partial t)$ is purely imaginary, which guarantees that the phase $\beta_n(T)$ is real. If we take $\beta_n(0) = 0$, then $\beta_n(T)$ is the geometric (Berry) phase.

Consider the geometric phase for an electron moving in a crystal along some closed orbit Γ in **k** space. As we have said, the Brillouin zone in this case can play the role of the parameter space, with $\mathbf{R} = \mathbf{k}$.

Suppose that at time t the electron has an energy from the band s. Then its wave function has the form (we return to the usual notation for the wave function)

$$|s\rangle = u_{s\mathbf{k}}(\mathbf{x})\exp(i\mathbf{k}\cdot\mathbf{x}), \tag{43}$$

where $u_{s\mathbf{k}}(\mathbf{x})$ is the Bloch amplitude, periodic in space. The Bloch amplitude and the electron energy $\varepsilon_s(\mathbf{k})$ are the eigenfunctions and eigenvalues of a stationary equation of the type (39) at time t. The quasi-wave vector **k** enters this equation as a parameter. For example, in a magnetic field $\mathbf{k}(t) = \mathbf{k} - (e/\hbar c)\mathbf{A}(t)$. Therefore upon an adiabatic variation of the physical conditions one should set

$$|s,t\rangle = u_{s\mathbf{k}}(t)\exp(i\mathbf{k}\cdot\mathbf{x}), \tag{44}$$

assuming that the quasi-wave vector in the exponential factor $\exp(i\mathbf{k}\cdot\mathbf{x})$ is independent of time. The slow dependence on time is contained in the Bloch amplitude and energy $\varepsilon_s(\mathbf{k}(t))$. Taking this last observation into account, we substitute (44) into (42):

$$\beta_n(T) = i\oint_\Gamma d\mathbf{k}\int u^*_{n\mathbf{k}}(x)\frac{\partial u_{n\mathbf{k}}(\mathbf{x})}{\partial \mathbf{k}}\,d^3x . \tag{45}$$

This is the geometric phase of an electron executing cyclic motion in a magnetic field. Curiously,[34] the integral

$$\Omega(\mathbf{k}) = i\int u^*_{s\mathbf{k}}(\mathbf{x})\frac{\partial u_{s\mathbf{k}}(\mathbf{x})}{\partial \mathbf{x}}\,d^3x \tag{46}$$

coincides with the diagonal element of the matrix

$$\Omega_{ss'}(\mathbf{k}) = i \int u^*_{s\mathbf{k}}(\mathbf{x}) \nabla_k u_{s'\mathbf{k}}(\mathbf{x}) d^3x, \tag{47}$$

which determines the so-called periodic part of the coordinate operator in the **k** representation, which is responsible for the interband transitions (see, e.g., Ref. 39):

$$\hat{\mathbf{r}} = i \frac{\partial}{\partial \mathbf{k}} + \hat{\Omega}(\mathbf{k}) . \tag{48}$$

Thus it can be considered that the Berry phase has called attention to the second term in the coordinate operator (48) in a spatially periodic structure.

Finally, let us return to the quantization rules (37) and the discussion of the γ term in formula (18). If the corresponding electron orbits with different n in a magnetic field are not very close to each other and their shape is substantially different from that of the self-intersecting orbits, then, as was shown in Ref. 15 and confirmed in Ref. 39, the parameter γ always has the value

$$\gamma = \frac{1}{2}. \tag{49}$$

This is the value usually used in discussing quantum oscillations in metals.[6] Consequently, upon quantization of the electron motion in a magnetic field under the conditions indicated above, the value of δS_0 to be used in (37) is

$$\delta S_0 = 2\pi \left(n + \frac{1}{2} \right) \hbar. \tag{50}$$

Thus the constant γ in formula (18) is equal to

$$\gamma = \frac{1}{2} - \frac{1}{2\pi} \Delta\beta, \tag{51}$$

where $\Delta\beta = \beta(T) - \beta(0)$ is the advance of the geometric phase in a complete turn of the electron along its closed trajectory in the magnetic field.

The possibility of using formula (51) and the consequences of doing so are discussed in Ref. 40. A nonzero Berry phase is usually due to degeneracy of the electronic states. Degeneracy, i.e., the touching or intersection of constant-energy surfaces (sheets of the Fermi surfaces) can be of two types: 1) caused by symmetry, in which case it occurs either at points of symmetry or along axes of symmetry in the Brillouin zone; 2) along lines of *accidental degeneracy*.[41] Analysis of the geometry of the Fermi surface shows that lines of symmetry-related and accidental contact should exist in many metals. Figure 19 shows the peculiar shapes of the Fermi surfaces in various metals in which the features under discussion are found. To calculate the value of γ we use a result obtained back in 1962.[42] It turns out that if a trajectory Γ encloses a line of degeneracy, then the geometric phase $\Delta\beta$ along it is largely determined by the character of the dependence of the energy splitting on the distance of the point **k** from the indicated line. If the splitting of the energy bands increases linearly with that distance, then the integral (45) giving the geometric phase $\Delta\beta$ is equal to

$$\Delta\beta = \pm\pi, \tag{52}$$

where the sign depends on the direction of integration in (45).

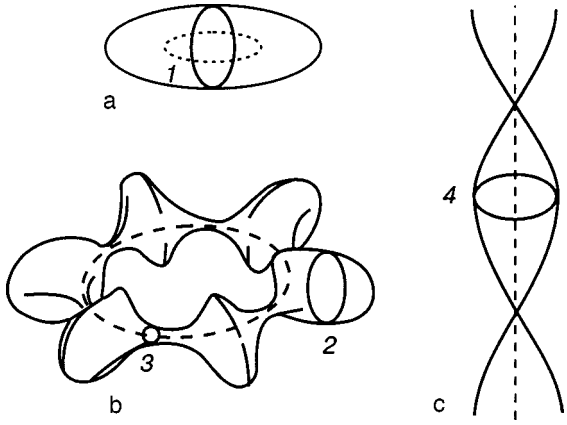

FIG. 19. Schematic illustration of Fermi surfaces for certain metals which have lines of degeneracy in the electron spectrum: electron "lenses" for Zn and Cd (a); the hole "monster" for Be and Mg (b); the self-intersecting Fermi surface for graphite (c). The dashed lines show lines of degeneracy.

The stated conditions hold in the vicinity of a line of accidental degeneracy and also near a line of degeneracy coinciding with a threefold symmetry axis (trajectories *3* and *4* in Fig. 19b, c). Therefore, for the indicated trajectories

$$\gamma = 0; \tag{53}$$

$\gamma = 1$ and $\gamma = 0$ are equivalent.

If the energy splitting near a line of degeneracy increases quadratically with increasing distance of the point **k** from that line, then

$$\Delta\beta = 0. \tag{54}$$

Consequently, in this case, and also for trajectories Γ that do not enclose lines of degeneracy (or which enclose an even number of lines of degeneracy—trajectories of the type *1* and *2* in Fig. 19a, b),

$$\gamma = \frac{1}{2}.$$

Summarizing, we note that the described role of the Berry phase is of a purely topological character and depends on neither the form of $\varepsilon(\mathbf{k})$ in the vicinity of the line of degeneracy nor on the linear dimensions of the trajectory Γ. The result depends only on whether that trajectory encloses a line of singularity for the Bloch wave function (in which case $\gamma = 0$) or does not enclose such a line (in which case the usual value $\gamma = 1/2$ obtains). As we have said, experimental measurement of the phase shift of quantum oscillations in the metals mentioned above makes it possible in principle to distinguish the presence of lines of degeneracy in their energy spectrum.

3. TOPOLOGY OF THE CHARACTERISTIC SURFACES IN THE DYNAMICS AND THERMODYNAMICS OF QUASIPARTICLES IN CRYSTALS

3.1. Geometry of constant-energy (constant-frequency) surfaces and the asymptotics of the scattered waves

In discussing the geometry and topology of Fermi surfaces we start from the fact that for Fermi particles (such as electrons) at low temperatures the region near a single surface is important, viz., that which corresponds to the Fermi

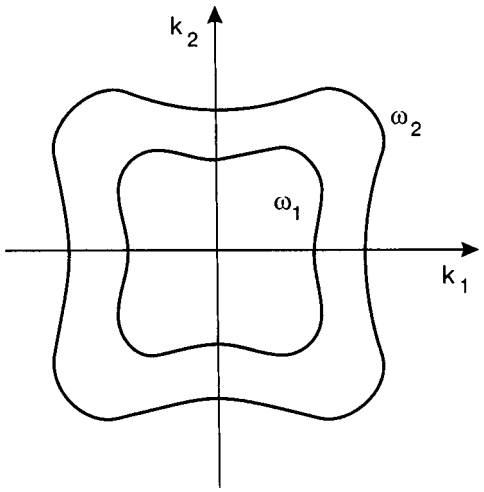

FIG. 20. Cross section of a nonconvex constant-frequency surface for acoustic oscillations in a cubic lattice.

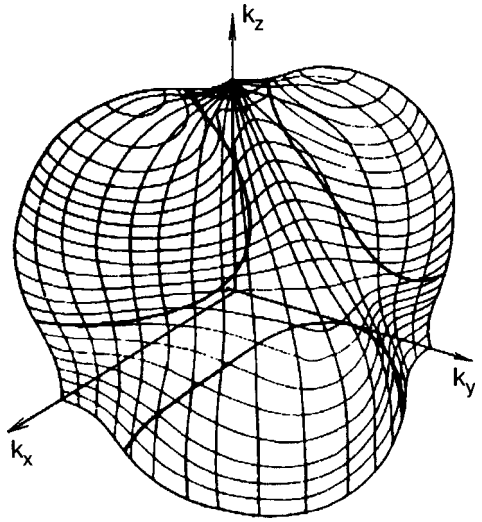

FIG. 21. Consant-frequency surface for one of the branches of vibrations of the Ge crystal.

energy. For Bose particles (such as photons in a medium, phonons, and magnons) there is no single characteristic preferred energy (frequency). Therefore it is of interest to study the dynamics of such particles (quasiparticles) at all possible energies. The thermodynamics of a gas of such particles is extremely sensitive to temperature, and its features reflect the singularities of the density of states of Bose particles.

As in the case of electrons, the main dynamical characteristic of any particles is the dispersion relation, i.e., the dependence of the energy ε of the particle on the quasimomentum **p**. In the case of phonons one usually considers the dependence of the square of the frequency, $\varepsilon=\omega^2$, on the quasi-wave vector. Here, of course, it is understood that $\mathbf{p}=\hbar\mathbf{k}$.

Since the features of the manifestation of the complex form of the electron Fermi energy were discussed in detail in Section 1, now we shall, for the sake of definiteness, speak of phonons. As in the case of electrons, all of the qualitative arguments are conveniently linked to the geometry of the constant-frequency surface $\omega(\mathbf{k})=\omega=\text{const}$. At low frequencies and long wavelengths ($ak\ll 1$), when the dispersion relation is $\omega=ck$, the constant-frequency surfaces are closed. However, since the sound velocity s in a crystal depends on the direction of the wave vector **k**, even for long-wavelength oscillations the constant-energy surface can be nonconvex. The parts on which the cross section of the constant-frequency surface is convex are separated from the parts on which it is concave by points of zero curvature of the cross section (Fig. 20). In a three-dimensional **k** space the convex parts of the constant-frequency surface are separated from the concave parts by lines along which the Gaussian (total) curvature vanishes. Figure 21 illustrates one octant of the constant-frequency surface of the Ge single crystal. The heavy lines in Fig. 21 are lines of zero Gaussian curvature separating the convex and concave parts of the surface.

By virtue of the periodicity of $\omega(\mathbf{k})=\omega(\mathbf{k}+\mathbf{G})$, where **G** is a reciprocal lattice vector, the closed surfaces described must repeat periodically in **k** space. Figure 22 shows a cross section of the reciprocal lattice on the plane $k_z=0$; the cross sections of these surfaces are situated at the points $k_1=(2\pi/a_1)n_1$, $k_2=(2\pi/a_2)n_2$, where $n_1,n_2=0,\pm 1,\pm 2,\ldots$. The points $k_1=\pi/a_1$, $k_2=\pi/a_2$ correspond to the maximum frequency $\omega=\omega_{\max}$. The constant-frequency surfaces around it are also closed (ellipsoids). Between the two types of closed surfaces is a layer of open constant-frequency surfaces ($\omega_1<\omega<\omega_2$ in Fig. 22). Usually the surface separating the open and closed surfaces has a *conical point*, in the vicinity of which the constant-frequency surfaces have the form shown in Fig. 23, i.e., they resemble hyperboloids. In the scheme in Fig. 22 the conical points are points of the type $k_1=0$, $k_2=\pi/a_2$ or $k_1=\pi/a_1$, $k_2=0$.

The shape of the constant-frequency surface is extremely important in studying the propagation of quasiparticles. The phonon group velocity is given by $\mathbf{v}=\partial\omega/\partial\mathbf{k}$, and therefore its direction for a nonspherical constant-frequency surface in the general case is noncoincident with the direction of **k**. The interrelationship of the directions is determined geometrically by the shape of the constant-frequency surface $\omega(\mathbf{k})=\text{const}$, since the vector **v** is always normal to a surface of constant frequency level (see Fig. 24). To each wave vector **k**

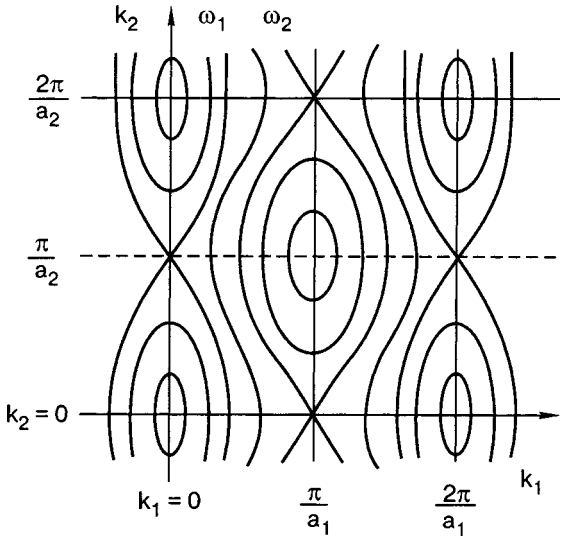

FIG. 22. Scheme of the cross sections of the constant-frequency surfaces on the plane $k_z=0$.

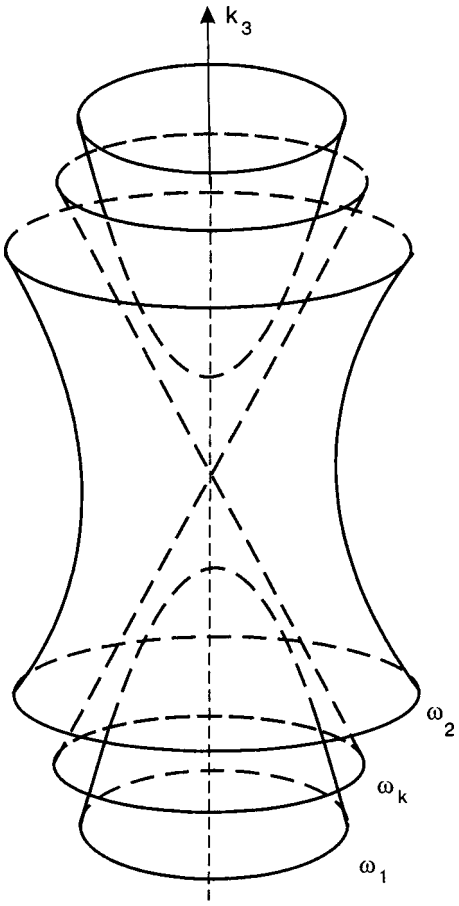

FIG. 23. Form of the constant-frequency surface near a conical point.

at a fixed frequency there corresponds a single velocity **v**. However, to a specified direction of the group velocity **v** (i.e., to a specified direction of the energy transfer $\mathbf{n}=\mathbf{v}/v$) there can correspond several wave vectors **k** ($\mathbf{k}_1$, $\mathbf{k}_2$, and $\mathbf{k}_3$ in Fig. 24), i.e., several waves with different directions of propagation of the phase of the wave (the wave front).

Suppose that we are studying a quasiparticle of arbitrary dispersion relation emitted (or scattered by a point defect) at the coordinate origin, and we are interested in its asymptotic behavior at large distances. Such a statement of the problem was proposed by I. M. Lifshits,[43] who showed that the intensity of the wave function in this case is conveniently characterized by the integral

$$J(r,\varepsilon)=\oint_{\varepsilon(\mathbf{k})=\varepsilon}\frac{\exp(i\mathbf{kr})\,dS_{\mathbf{k}}}{|\nabla_k\omega^2(\mathbf{k})|}. \tag{55}$$

The asymptotic behavior of the integral (55) for $r\to\infty$ is characterized by the following. First, the number of waves in a direction **n** is determined by the number of points of tangency of the constant-energy surface with a plane perpendicular to the direction of **n** (points $\mathbf{k}_1$, $\mathbf{k}_2$, and $\mathbf{k}_3$ in Fig. 24). Second, the intensity (55) at each point of tangency (or "reference point") ν depends on the total (Gaussian) curve K_ν of the surface at that point ($K_\nu=\alpha_1\alpha_2$, where α_1 and α_2 are the principal curvatures). If $K_\nu>0$ the corresponding point is called *elliptical*, and if $K_\nu<0$ it is called *hyperbolic*.

All points of a convex surface are elliptical. If the surface is not convex (but of the type shown in Fig. 21), then it has parts of different types (elliptical or hyperbolic). But the parts of the constant-frequency surface of first and second types are separated by lines along which one of the coefficients (α_1 or α_2) vanishes. These are called *lines of parabolic points*. Finally, at the intersection of lines of parabolic points there are "flat spots" where $\alpha_1=\alpha_2=0$.

Let us begin with an analysis of the asymptotic form of the integral (55) in the case when the reference points are elliptical or hyperbolic points. The asymptotic expression for (55) in this case is[43]

$$J(r,\varepsilon)=\frac{2\pi}{r}\sum_{\nu}\frac{\exp\left(i\mathbf{k}_\nu\mathbf{r}\pm i\,\frac{\pi}{4}\pm\frac{\pi}{4}\right)}{|\nabla\varepsilon(\mathbf{k})|\sqrt{|K_\nu|}}, \tag{56}$$

where the signs in the argument of the exponential function are determined by the signs of the principal curvatures α_1 and α_2. The intensity (56) is typical for a diverging spherical wave: $J\sim 1/r$.

Thus the scattered wave is, generally speaking, a superposition of several diverging waves. Each of these waves has its own shape and its own propagation velocity. An idea of the spatial distribution of the scattered waves can be got by studying the so-called *wave surface*. The wave surface in coordinate space is in a certain sense the polar opposite of the constant-frequency surface and is constructed as follows. From the position of a defect (point *O* in Fig. 25) a ray is constructed in the direction of **n**, and along it the length $r=1/(\mathbf{n}\cdot\mathbf{k}_\nu)$ is marked off, where $\mathbf{k}_\nu=\mathbf{k}_\nu(\mathbf{n})$ are the reference points. If the constant-frequency surface is convex, then there is a single reference point, with $\mathbf{n}\cdot\mathbf{v}_\nu>0$. If the constant-frequency surface is nonconvex, then there can be several such points. In the latter case, folds and cusps appear on the wave surface. The tangent plane in the vicinity of each reference point generates its own part of the wave surface. At the boundary of adjacent folds there is a transition from regions of elliptical points on the constant-frequency surface to regions of hyperbolic points. The boundaries are lines of parabolic points ($K_\nu=0$). There is always a continuous manifold of directions (conical surface) corresponding to $K_\nu=0$. These directions are shown by the straight lines OS_1 and OS_2 in Fig. 25; at the points S_1 and S_2 a pair of parts of

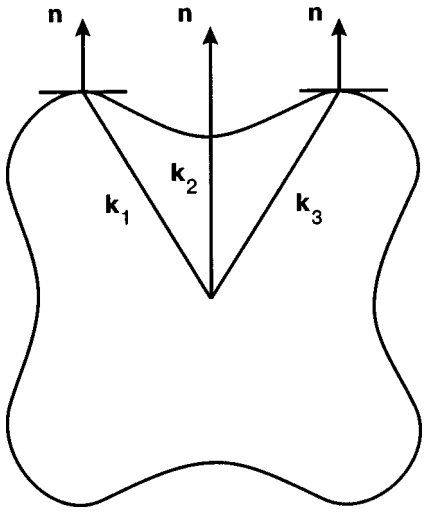

FIG. 24. Reference points on the constant-frequency surface, corresponding to the direction **n**.

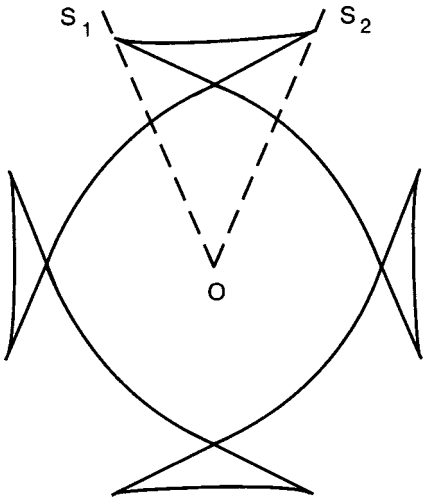

FIG. 25. Cross section of the wave surface on which the rays OS_1 and OS_2 delimit a "fold."

the wave surface comes together and breaks apart. In catastrophe theory a classification of such singularities is carried out: in respect to the scattering of elastic waves in crystals it has been made clear that the only types of catastrophes possible are the folds and cusps. The "catastrophe" lies in the fact that the energy flux density in the indicated directions, calculated formally with the use of Eq. (56), goes to infinity $(K_\nu=0)$. Indeed, at those points (more precisely, on the corresponding conical surfaces) a change in the asymptotic behavior of the scattered wave occurs—a decrease in the power to which the distance r is raised in the denominator of the expansion of the function $J(\mathbf{r},\varepsilon)$.

Let us consider as an example the simplest parabolic point k_0, in the vicinity of which the function $h=\mathbf{k}\cdot\mathbf{n}$ has the expansion

$$h=\mathbf{k}_0\cdot\mathbf{n}_0+\frac{1}{2}\alpha\xi_1^2+\beta\xi_2^3, \tag{57}$$

where $\mathbf{n}_0$ is a unit vector in the direction for which the reference planes are tangent to the constant-frequency surface at the parabolic point $\mathbf{k}_0$ (we have chosen the coordinate lines ξ_1 and ξ_2 along the principal directions of curvature of the constant-frequency surface). In this case we obtain[44] instead of (56)

$$J(r,\varepsilon)=\frac{\sqrt{6\pi\Gamma}(4/3)}{r^{5/6}}\frac{\exp\left(i\mathbf{k}_0\cdot\mathbf{r}\pm i\frac{\pi}{4}\right)}{|\nabla\omega^2(\mathbf{k}_0)||\alpha|^{1/2}|\beta|^{1/3}}. \tag{58}$$

Using (58) to calculate the asymptotics of the Green's function and then the energy flux density, we find that the latter is proportional to $1/r^{5/3}$. If there are no other singularities on the line of parabolic points, then on average one has in order of magnitude $|\alpha|\sqrt{|\beta|}\sim K^*$, where K^* is the Gaussian curvature at an arbitrary (nonpreferred) point of the constant-frequency surface. Therefore, the energy flux density along the direction $\mathbf{n}_0$ at large r "catastrophically" exceeds the energy flux density from the other points, in the ratio $r^{1/3}/|\beta|^{1/6}$.

However, the solid angle within which this energy flux density exists decreases with increasing r. Indeed, consider the scattered wave in a direction $\mathbf{n}$ that deviates from $\mathbf{n}_0$ by an angle θ_2 (along ξ_2). Then the reference point is shifted by an amount $\delta\xi_2$ determined by the relation $\theta_2=3\beta(\delta\xi_2)^2$. At the new reference point the Gaussian curvature has the value $K=6\alpha\beta\delta\xi_2$. Comparing expression (56), in which this Gaussian curvature is used, with expression (58) for a parabolic reference point, one can see that they become of the same order of magnitude for $\delta\xi_2\sim 1/(|\beta|r)^{1/3}$. Consequently, the angle within which energy is radiated with elevated intensity can be estimated as $\delta\theta_2\sim|\beta|^{1/3}/r^{2/3}$. We see that the angle $\delta\theta_2$ decreases with increasing r faster than the energy density increases. Therefore the total energy flux into the angle $\delta\theta_2$ falls off with distance in proportion to $1/r^{1/3}$, which completely compensates the effect of the increased flux density.

Finally, let us calculate the contribution to the integral (55) due to a "flat spot," where one has the expansion

$$h=\mathbf{k}_0\cdot\mathbf{n}_0+\beta_1\xi_1^3+\beta_2\xi_2^3.$$

Without repeating the calculation of Ref. 45, we can immediately write down the corresponding part of the integral[45] (1):

$$J(r,\varepsilon)=\frac{3\left[\Gamma\left(\frac{4}{3}\right)\right]^2}{r^{2/3}}\frac{\exp(i\mathbf{k}_0\cdot\mathbf{r})}{|\nabla\omega^2(\mathbf{k}_0)||\beta_1\beta_2|^{1/3}}. \tag{59}$$

In this case the energy flux density in the scattered wave exceeds that under ordinary conditions by the ratio $r^{2/3}/|\beta_1\beta_2|^{1/6}$. Accordingly, the solid angle in which the flux is concentrated with such a density decreases with distance in proportion to $|\beta_1\beta_2|^{1/3}/r^{4/3}$.

The presence of flat spots and lines of parabolic points on the constant-frequency surface for phonons gives rise to *phonon focusing*. This phenomenon consists in the fact that the point generation of phonons in a single-crystal sample gives rise to elastic wave propagation characterized by sharp focusing along selected directions associated with these singular lines and points on the constant-frequency surface. A detailed analysis of phonon focusing and its experimental implementation is the subject of a series of papers by Every,[46] with which one can become acquainted in the book by Wolfe.[47]

An analogous phenomenon can be observed in a study of the propagation of electrons in sufficiently pure metals (e.g., the mean free path of the electron in a metal film must be greater than the thickness of the film). It was predicted in Ref. 48 that the point excitation (generation) of electrons on one surface of a slab leads to electron flows which, when detected on the opposite surface of the slab, are also characterized by focusing along the same kinds of directions. The focusing of electrons was detected experimentally in Ref. 49.

Curiously, the phonon features due to the shape of the constant-frequency surfaces can be manifested even in the lowest-frequency (sonic) region of the frequency spectrum. Indeed, for certain relations between the elastic constants the corresponding cross section of the acoustic constant-frequency surfaces can be convex or concave. In turn, the property of convexity of nonconvexity of these surfaces determines, for example, the character of the decay of surface (Rayleigh) waves with depth in the crystal. For ordinary

Rayleigh waves the amplitude falls off monotonically with increasing distance from the surface. In an anisotropic medium such as a crystal, however, the amplitude of the so-called generalized Rayleigh waves falls off nonmonotonically (in an oscillatory manner).

As an example, let us consider a situation which is easily discussed with the aid of Fig. 24. Suppose that the plane of the figure is the central secant plane (k_z,k_x), with the oz axis (normal to the surface) directed horizontally and the ox axis vertically, and that a surface wave is propagating along this direction, indicated by the vector **n** in the figure. At a fixed frequency ω the vectors $\mathbf{k}_1$ and $\mathbf{k}_3$ in Fig. 24 indicate points of tangency of the plane $k_z=\text{const}$ to the constant-frequency surface. The character of the surface waves is determined by the dispersion relation in the vicinity of these points.

A cross section of the constant-frequency surface near the point of tangency $\mathbf{k}=\mathbf{k}_0$ (where $\mathbf{k}_0$ coincides with $\mathbf{k}_1$ or $\mathbf{k}_3$) can be written in the form

$$k_x=k_x^0-\alpha^2(k_z-k_z^0)^2,\quad \omega(k_x^0,0,k_z^0)=\omega.$$

A surface wave has a wave vector component k_x somewhat greater than k_x^0 $(k_x>k_x^0)$, and therefore

$$k_z=k_z^0\pm i\kappa,\quad \kappa=\frac{(k_x-k_x^0)^{1/2}}{\alpha^2}.$$

Using the standard representation for a surface wave with the use of a complex-valued k_z, we see that it falls off nonmonotonically with depth z:

$$u=u_0\exp[(-\kappa+ik_z^0)z]\mathrm{e}^{ik_x-i\omega t}.$$

Since the nonmonotonicity of the z dependence is uniquely related to a nonzero value of k_z^0, nonconvexity of a cross section of the constant-frequency surface is a sufficient condition for the existence of a generalized Rayleigh wave. A detailed discussion of the problem can be found in Refs. 50.

3.2. Density of vibrational states in a crystal and van Hove singularities

The distribution of the vibrations of the crystal over frequencies is conveniently characterized by the so-called density of vibrations $g(\varepsilon)$, where $\varepsilon=\omega^2$ (the latter means that we are talking about the distribution over the squares of the frequencies):

$$g(\varepsilon)=\frac{V}{(2\pi)^3}\oint\limits_{\omega^2(\mathbf{k})=\varepsilon}\frac{dS_{\mathbf{k}}}{|\nabla_{\mathbf{k}}\omega^2(\mathbf{k})|},\tag{60}$$

where V is the volume of the crystal and the integration is over the sureferenceace $\omega^2(\mathbf{k})=\varepsilon$.

Since the band of allowed frequencies is restricted $(0<\varepsilon<\omega_m^2$, and $g(\varepsilon)\equiv 0$ for $\varepsilon<0$ and $\varepsilon>\omega_m^2)$, the function $g(\varepsilon)$ loses analyticity at the band edges. For $\omega\ll\omega_m$ in the isotropic approximation we have $\omega^2=s^2k^2$, and therefore Eq. (60) gives

$$g(\varepsilon)=\frac{V}{(2\pi)^2s^3}\sqrt{\varepsilon},\quad \varepsilon\ll\omega_m^2.\tag{61}$$

For $\omega_m-\omega\ll\omega_m$ one can usually write (as near points of a maximum of a function):

$$\omega^2=\omega_m^2-\gamma_1^2k_1^2-\gamma_2^2k_2^2-\gamma_3^2k_3^2,\tag{62}$$

where **k** is measured from the point in the Brillouin zone at which $\omega=\omega_m$. However, because we are interested in topologically equivalent situations, Eq. (62) can be simplified to

$$\omega^2=\omega_m^2-\gamma^2k^2.\tag{63}$$

Substituting (63) into (60), we get

$$g(\varepsilon)=\frac{V}{(2\pi)^2\gamma^3}\sqrt{\omega_m^2-\varepsilon},\quad \omega_m^2-\varepsilon\ll\omega_m^2.\tag{64}$$

Comparing (61) and (64), we see that $g(\varepsilon)$ vanishes at the ends of the band of eigenfrequencies by a singular law:

$$g(\varepsilon)=\text{const}\sqrt{|\varepsilon-\varepsilon^*|},\tag{65}$$

where ε^* is one of the boundaries of the continuous spectrum of frequencies squared.

Besides boundaries of the continuous spectrum, singularities of the density of states are manifested at values of ε separating parts of the surface with different topology. It was mentioned above that the presence of a conical point serves as a indicator of the corresponding surface—the separatrix. Examining Fig. 23, we easily see that near the conical point $\omega=\omega_k$ the transformation of the closed constant-frequency surfaces to open surfaces occurs continuously. However, it is important that this continuous transformation is accompanied by a change in the topology of the surfaces. But the topology of a surface, like its symmetry, cannot change continuously. The transition from closed to open surfaces is in principle a jumplike process and must therefore be characterized by a corresponding change of some topological parameter of the surface. Such a parameter does indeed exist, and it is called the topological invariant of Euler (or the Euler characteristic).

The topological invariant of Euler for the surface $\omega(\mathbf{k})=\omega=\text{const}$ can be written in the form

$$\chi(\omega)=\frac{1}{4\pi}\int K(\mathbf{k})dS_k,\tag{66}$$

where the integration is over the whole surface, dS_k is an element of surface area, and $K(\mathbf{k})$ is its Gaussian (or total) curvature at the point **k**. The Gaussian curvature is defined in terms of the partial derivatives of the function $\omega=\omega(\mathbf{k})\equiv\omega(k_x,k_y,k_z)=\omega(k_1,k_2,k_3)$ by the following formula:

$$K(\mathbf{k})=\frac{1}{v^4}\begin{vmatrix} v_{1,1} & v_{1,2} & v_{1,3} & v_1\\ v_{2,1} & v_{2,2} & v_{2,3} & v_2\\ v_{3,1} & v_{3,2} & v_{3,3} & v_3\\ v_1 & v_2 & v_3 & 0\end{vmatrix},\tag{67}$$

where v_i is the group velocity vector, $v_{i,j}=\partial v_i/\partial k_j=\partial^2\omega/(\partial k_i\partial k_j)$, $i,j=1,2,3$.

In using Eq. (66) for the characteristic of the constant-frequency surfaces it should be kept in mind that they repeat periodically over all of reciprocal space. The topological invariant will be understood to be the integral (66) calculated over that part of the constant-frequency surface which is found in a single unit cell of **k** space.

Near the conical point the dispersion relation in the simplest case has the form

$$\omega(\mathbf{k}) = \omega_k + \gamma_1^2(k_1^2 + k_2^2) - \gamma_3^2 k_3^2, \tag{68}$$

where $\mathbf{k}$ is measured from the conical point. In the vicinity of that point one has

$$K(\mathbf{k}) = \frac{(\gamma_1\gamma_2\gamma_3)^2(\omega_k - \omega)}{[(\gamma_1^2 k_1)^2 + (\gamma_2^2 k_2)^2 + (\gamma_3^2 k_3)^2]^2}. \tag{69}$$

At the conical point itself ($\omega = \omega_k$ and $k_1 = k_2 = k_3 = 0$) the Gaussian curvature (69) is singular, but off that point the constant-frequency surfaces are regular and the curvature K does not have singularities. We assume that the other singular points on the constant-frequency surface are far from the selected conical point. Then for $\omega \to \omega_k$ the singular behavior of the invariant $\chi(\omega)$ due to the appearance of the conical point should be determined by the integration in (66) over a small neighborhood of that point.

Having a clear idea of the surfaces near the conical point [Fig. (23)], for $\omega \to \omega_k$ we can easily do the calculations proposed in Ref. 51. For frequencies $\omega < \omega_k$ they give hyperboloids of two sheets:

$$\delta\chi(\omega) = 1 - \frac{\gamma_3}{\sqrt{\gamma_1^2 + \gamma_3^2}}. \tag{70}$$

For frequencies $\omega > \omega_k$ we obtain hyperboloids of one sheet:

$$\delta\chi(\omega) = -\frac{\gamma_3}{\sqrt{\gamma_1^2 + \gamma_3^2}}. \tag{71}$$

Comparing (70) and (71), we see that in the presence of a conical point on the constant-frequency surface the topological invariant $\chi(\omega)$ changes exactly by unity upon a change in frequency (for each conical point per unit cell of the reciprocal lattice).

For mathematicians that statement may be trivial, but for physicists it is important that there exists a definite topological invariant, which makes it possible to monitor the relationship between the qualitative features of the constant-frequency surfaces and the analytical model description of them.

The presence of a jump in the frequency dependence $\chi(\omega)$ should naturally be reflected in the analytical properties of the density of states in the vicinity of the frequency ω_k. The features of the density of states generated by the dispersion relation (68) are straightforwardly calculated, and the corresponding calculations are reported in Refs. 45 and 51. Let us summarize them.

If $\varepsilon_k = \omega_k^2$ is the square of the frequency at the critical point, and if values $\varepsilon < \varepsilon_k$ correspond to closed constant-frequency surfaces and $\varepsilon > \varepsilon_k$ correspond to open ones, then for $\varepsilon \to \varepsilon_k$ we have

$$g(\varepsilon) = \begin{cases} g(\varepsilon_k) - A^2\sqrt{\varepsilon_k - \varepsilon} + O(\varepsilon_k - \varepsilon), & \varepsilon < \varepsilon_k; \\ g(\varepsilon_k) + O(\varepsilon - \varepsilon_k), & \varepsilon > \varepsilon_k, \end{cases} \tag{72}$$

where $A^2 = \text{const}$, and $O(x)$ is a small quantity of order x (for $x \to 0$).

The frequency giving a square-root feature of the type in (72) is called an *analytical critical point of type S*. In the spectrum of a 3D crystal there exist at least two critical points of type S. In Fig. 22 the two separatrices with conical points $\varepsilon = \omega_1^2$ and $\varepsilon = \omega_2^2$ bound a layer of open constant-frequency surfaces.

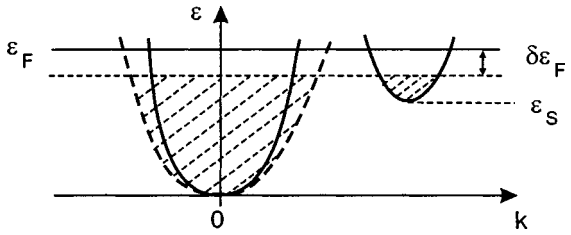

FIG. 26. Scheme of the electron spectrum of a metal with two groups of conduction electrons.

Type-S singularities generated by a change in topology of the constant-frequency surfaces and features at the boundaries of the continuous spectrum are called *van Hove singularities*.

3.3. Electronic phase transition of order $2\frac{1}{2}$

Van Hove singularities are weakly manifested in the thermodynamics of the crystal lattice, since the thermodynamic characteristics are expressed by integrals over all frequencies, and square-root singularities of the density of states cannot lead to any noticeable effects in them. Matters are different in the thermodynamics of the electron gas in metals, which at low temperatures have a characteristic energy—the Fermi energy. And if for physical reasons the energy ε_k at the singular point is close to ε_F and depends so strongly on some continuous parameters that the difference $\varepsilon_F - \varepsilon_k$ can pass through zero, then there arises the possibility of a change in topology of the Fermi surface. Then upon a change in the indicated parameter one should expect anomalies of the thermodynamic characteristics of the electron gas.[52]

Such a continuous parameter can be high-pressure hydrostatic compression. In view of the low compressibility of metals, one might assume that observation of the effect would require enormous pressures. However, there is a situation in which the required pressures are not so large.

Consider a metal for which the Fermi surface has two sheets: large and small, i.e., two groups of electrons: numerous and anomalously few. Such a metal is interesting from the standpoint of observation of the de Haas–van Alphen effect, since the cross sections of the small sheet of the Fermi surface will give large and easily observed periods of the quantum oscillations. In a one-electron scheme the electron energy spectrum can be characterized by the following picture[53] (see Fig. 26). Here ε_F is the Fermi energy, equal to the chemical potential ζ_0 measured from the bottom of the band of the large electron group in the absence of pressure (analogously, $\zeta_s = \varepsilon_F - \varepsilon_s$ is the chemical potential measured from the bottom ε_s of the anomalously small group of electrons). At a small strain (compression) under hydrostatic pressure p the shift $\delta\varepsilon_F$ is proportional to p, and for the main group of electrons

$$\frac{|\delta\varepsilon_F|}{\zeta_0} \sim \frac{p}{G}, \tag{73}$$

where G is the shear modulus. Finally, $p/G \ll 1$, but by virtue of the anomalous smallness of the second group of electrons ($\zeta_s \ll \varepsilon_F$) the value of $\delta\varepsilon_F$ can be comparable to ζ_s. In any case the study of the de Haas–van Alphen effect under pressure[54] demonstrates the possibility of changing the oscillation periods by an amount comparable to the period itself. But that means that at high but reasonable pressures one can achieve the condition $|\delta\varepsilon_F| > \zeta_s$. Since under compression of the crystal, by virtue of the invariance of the number of electrons belonging to it, the volume in **k** space expands, one expects that $\delta\varepsilon_F < 0$. Consequently, at the time when ε_F falls below ε_s the small closed surface vanishes, and therefore the term of the type (61) in the density of states vanishes with a singular dependence:

$$g_s(\varepsilon) = \begin{cases} 0, & \varepsilon < \varepsilon_s; \\ VA^2\sqrt{\varepsilon - \varepsilon_s}, & \varepsilon > \varepsilon_s, \end{cases} \tag{74}$$

where $A^2 = \text{const}$.

Let us consider an electron gas with the energy spectrum described above at a temperature of absolute zero. Then the free energy of the gas is equal to its internal energy:

$$F(V) = E(V) = \int_0^{\varepsilon_F} \varepsilon g(\varepsilon) d\varepsilon. \tag{75}$$

We single out in (75) that part of F which is generated by the anomalously small group of electrons:

$$F_s(V) = VA^2 \int_{\varepsilon_s}^{\varepsilon_F} \varepsilon \sqrt{\varepsilon - \varepsilon_s}\, d\varepsilon.$$

The pressure in the system also includes a singular part:

$$p_s = -\frac{\partial F_s}{\partial V} = \begin{cases} 0, & \varepsilon_F < \varepsilon_s; \\ -A^2 \int_{\varepsilon_s}^{\varepsilon_F} \varepsilon \sqrt{\varepsilon - \varepsilon_s} d\varepsilon, & \varepsilon_F > \varepsilon_s. \end{cases} \tag{76}$$

The transition from the region $\varepsilon_F < \varepsilon_s$ to the region $\varepsilon_F > \varepsilon_s$ corresponds to the appearance of a new sheet of the surface $\varepsilon(\mathbf{k}) = \varepsilon_F$. Here ε_F is a function of the external parameter that determines the singularity in question. In the case of hydrostatic compression this parameter is the volume: $\varepsilon_F = \varepsilon_F(V)$. Therefore the singular part of the compressibility κ (the second derivative of the free energy) can be written in the form

$$\kappa_s = \frac{\partial p_s}{\partial V} = \begin{cases} 0, & \varepsilon_F < \varepsilon_s; \\ -A^2 \varepsilon_F \sqrt{\varepsilon_F - \varepsilon_s} \dfrac{d\varepsilon_F}{dV}, & \varepsilon_F > \varepsilon_s. \end{cases} \tag{77}$$

We see that the second derivative of F at the point $\varepsilon_F = \varepsilon_s$ has a vertical kink, and the third derivative goes to infinity as $|\varepsilon_F - \varepsilon_s|^{-1/2}$. Thus at $T = 0$ there is a singularity at the point $\varepsilon_F = \varepsilon_s$, which according to the Ehrenfest terminology can be nominally called a phase transition of order $2\frac{1}{2}$. For $T \neq 0$, however, the singularity at $\varepsilon_F = \varepsilon_s$ is smeared out, and so there is no true phase transition, although a certain anomaly exists at $\varepsilon_F = \varepsilon_s$.

A peculiar manifestation of an electronic topological phase transition is realized if the phase transition of order $2\frac{1}{2}$ coincides with a superconducting phase transition. Since the transition of a metal to the superconducting state is a true phase transition, the ''interference'' in the thermodynamics of the superconducting transition from the situation described above is undoubtedly of interest.

We have called attention to the fact that electrons in a metal can be separated into groups with strongly different Fermi surfaces and dynamical properties. In the process of the electron–topological phase transition, one or several small groups of electrons can appear or disappear. Here many physical characteristics of the metal change sharply: the value and anisotropy of the electrical conductivity, magnetoelastic effects, and the Hall effect. A theoretical treatment of the interesting physical phenomena that arise under such conditions was proposed by Bar'yaktar and Makarov.[55] Their paper[55] gave a splendid explanation of the features of the influence of pressure on the superconducting transition in thallium, observed experimentally at about the same time.[56] A detailed review of the experimental and theoretical research done by physicists in Kharkov on the manifestation of topological features of the electron spectrum in the superconducting characteristics of a metal has been published in Ref. 57.

The electron–topological features at the superconducting phase transition under high pressure can even lead to an appreciable change in the vibrational spectrum of the crystal owing to the strong electron–phonon coupling. Something similar is observed in the high-temperature superconductor MgB_2. The electron and phonon spectra of this crystal have certain peculiarities. First, there are two different groups of conduction electrons: a large group of electrons with properties typical for a 3D electron gas, and a small group with practically 2D dynamics, the dispersion relation of which is analogous to (33) and the Fermi surface of which is close to a cylinder—a situation similar to that which was analyzed in the discussion of Fig. 25; second, the electron–phonon coupling that brings about the Cooper pairing of the electrons is mainly due to just *one* phonon mode, corresponding to motion of the boron atoms in the basal plane.[58] The strong coupling of this vibrational mode with the small group of electrons makes it extremely sensitive to the state of the small group of electrons: when the small group of electrons vanishes upon a change in pressure, a kink appears on the corresponding experimental curves relating to the state of the vibrational system, develops a kink (a rather complete bibliography on this topic can be found in Ref. 59 and in an upcoming review article[60]).

The author thanks Oksana Charkina and Aleksandr Kotlyar for assistance in preparing the manuscript and illustrations, respectively, and is deeply grateful to V. G. Peschansky, V. M. Gvozdikov, and S. S. Syrkin for helpful discussions and to I. K. Yanson for valuable comments.

*Based on lectures delivered by the author at the International Conference on Topology in Condensed Matter Physics, Dresden, MPIPKS (March 13–July 31, 2002)

**E-mail: kosevich@ilt.kharkov.ua

[1] M. Nakahara, *Geometry, Topology, and Physics*, Inst. Physics Publishing, Bristol (1990).

[2] M. Monastyrskiĭ, *Riemann, Topology and Physics* [in Russian], PAIMS, Moscow (1990).

[3] I. M. Lifshits, M. Ya. Azbel', and M. I. Kaganov, *Electron Theory of*

Metals, Consultants Bureau, New York (1973), Nauka, Moscow (1971).
[4] A. Sommerfeld and H. A. Bethe, ''Electrontheorien der Metalle,'' in *Handbuch der Physik*, Vol. 24, Part 2, edited by H. Geiger and K. Scheel, Springer-Verlag, Berlin (1933), p. 333; Russian translation *Electron Theory of Metals*, ONTI (1938).
[5] W. A. Harrison, *Pseudopotentials in the Theory of Metals*, New York (1966), Mir, Moscow (1968).
[6] D. Shoenberg, *Magnetic Oscillations in Metals*, Cambridge University Press, Cambridge (1984), Mir, Moscow (1986).
[7] L. Onsager, Philos. Mag. **43**, 1006 (1952).
[8] M. Ya. Azbel', Zh. Éksp. Teor. Fiz. **39**, 1276 (1960) [Sov. Phys. JETP **12**, 891 (1961)]; Zh. Éksp. Teor. Fiz. **46**, 929 (1964) [Sov. Phys. JETP **19**, 634 (1964)].
[9] I. M. Lifshits and A. M. Kosevich, Dokl. Akad. Nauk SSSR **96**, 963 (1954); I. M. Lifshits, and A. M. Kosevich, Zh. Éksp. Teor. Fiz. **29**, 730 (1955) [Sov. Phys. JETP **2**, 636 (1956)].
[10] J. Wosnitza, *Fermi Surfaces of Low-Dimensional Organic Metals*, Springer, Berlin (1996).
[11] I. M. Lifshits and A. V. Pogorelov, Dokl. Akad. Nauk SSSR **96**, 1143 (1954).
[12] A. M. Kosevich and V. V. Andreev, Zh. Éksp. Teor. Fiz. **38**, 882 (1960) [Sov. Phys. JETP **11**, 637 (1960)].
[13] M. Coken and L. Falikov, Phys. Rev. Lett. **5**, 544 (1960).
[14] R. W. Stark and L. M. Falikov, Progress in Low Temperature Physics, v. **5**, North-Holland, Amsterdam (1967), p. 235; M. I. Kaganov and A. A. Slutskin, Phys. Rep. **98**, 189 (1983); Yu. N. Proshin and N. Kh. Useinov, Usp. Fiz. Nauk **165**, 41 (1995).
[15] G. E. Zil'berman, Zh. Éksp. Teor. Fiz. **30**, 1096 (1956) [*sic*]; Zh. Éksp. Teor. Fiz. **32**, 296 (1957) [Sov. Phys. JETP **5**, 208 (1957)].
[16] E. I. Blount, Phys. Rev. **126**, 1636 (1962).
[17] V. M. Gvozdikov, Fiz. Nizk. Temp. **12**, 705 (1986) [Sov. J. Low Temp. Phys. **12**, 399 (1986)].
[18] F. Bloch, Z. Phys. **52**, 555 (1928); C. Zener, Proc. R. Soc. London, Ser. A **145**, 523 (1934).
[19] C. Wannier, Phys. Rev. **117**, 432 (1960); T. Mendes, F. Agullo-Rueda, and J. Hong, Phys. Rev. Lett. **60**, 2426 (1988); P. Voisin, J. Bleuse, C. Bouche, S. Gaillard, C. Albert, and A. Regreny, *ibid.* **61**, 1639 (1988).
[20] A. M. Kosevich, Fiz. Nizk. Temp. **27**, 699 (2001) [Low Temp. Phys. **27**, 513 (2001)].
[21] J. Feldman, K. Leo, J. Shah, D. A. Miller, J. E. Conningham, T. Meier, G. von Plessen, A. Shulze, P. Thomas, and S. Schmitt-Rink, Phys. Rev. B **46**, 7952 (1992); K. Leo, P. Haring Bolivar, F. Brueggemann, R. Schwedler, and K. Koehler, Solid State Commun. **84**, 943 (1992).
[22] C. Waschke, H. Roskos, R. Schwedler, K. Leo, H. Kurz, and K. Koehler, Phys. Rev. Lett. **70**, 3319 (1993).
[23] L. Esaki and R. Tsu, IBM J. Res. Dev. **14**, 61 (1970).
[24] F. G. Bass and A. A. Bulgakov, *Kinetic and Electrodynamic Phenomena in Classical and Quantum Semiconductor Superlattices*, Nova Science Publishers, New York (1998).
[25] S. P. Novikov and A. Yu. Mal'tsev, Usp. Fiz. Nauk **168**, 249 (1998).
[26] M. I. Kaganov and V. G. Peschansky, Phys. Rep. **372**, 445 (2002).
[27] I. M. Lifshits and V. G. Peschanskiĭ, Zh. Eksp. Teor. Fiz. **35**, 1251 (1958) [Sov. Phys. JETP **8**, 875 (1959)].
[28] I. M. Lifshits and V. G. Peschanskiĭ, Zh. Éksp. Teor. Fiz. **38**, 188 (1960) [Sov. Phys. JETP **11**, 137 (1960)].
[29] A. A. Abrikosov, *Introduction to the Theory of Normal Metals* [in Russian], Nauka, Moscow (1972).
[30] A. M. Kosevich and I. D. Wagner, Fiz. Nizk. Temp. **25**, 868 (1999) [Low Temp. Phys. **25**, 650 (1999)].
[31] M. Ya. Azbel' and É. A. Kaner, Zh. Éksp. Teor. Fiz. **32**, 896 (1957) [Sov. Phys. JETP **5**, 730 (1957)]; Phys. Chem. Solids **6**, 113 (1958).
[32] É. A. Kaner, *Selected Works* [in Russian], Naukova Dumka, Kiev (1989).
[33] M. V. Berry, Proc. R. Soc. London, Ser. A **392**, 45 (1984).
[34] L. M. Roth, Phys. Rev. **145**, 434 (1966).
[35] Y. Aharonov and D. Bohm, Phys. Rev. **115**, 485 (1959).
[36] I. O. Kulik, JETP Lett. **11**, 275 (1970).
[37] J. Zak, Phys. Rev. Lett. **62**, 2747 (1989).
[38] W. V. Houston, Phys. Rev. **57**, 184 (1940).
[39] E. M. Lifshitz and L. P. Pitaevskii, *Statistical Physics* Part 2, Pergamon Press, Oxford (1986), Nauka, Moscow (1978).
[40] G. P. Mikitik and V. Shalai, Phys. Rev. Lett. **82**, 2147 (1999).
[41] C. Herring, Phys. Rev. **52**, 365 (1937).
[42] E. I. Blount, Solid State Phys. **13**, 305 (1962).
[43] I. M. Lifshits, Zh. Éksp. Teor. Fiz. **8**, 293 (1948)]; I. M. Lifshitz, Nuovo Cimento, Suppl. **3**, 716 (1956).
[44] I. M. Lifshits and V. I. Peresada, Uchen. Zap. Khar'k. Un-ta, Trudy Fiz. Otd. Fiz.-Mat. Fak. **6**, 37 (1955).
[45] A. M. Kosevich, *Theory of the Crystal Lattice (Physical Mechanics of Crystals)* [in Russian], Kharkov, Vishcha Shkola (1988); Arnold M. Kossevich, *The Crystal Lattice. Phonons, Solitons, Dislocations*, Wiley-VCH, Berlin (1999).
[46] A. G. Every, Phys. Rev. Lett. **79**, 2478 (1997); Phys. Rev. B **58**, 1601 (1998).
[47] J. P. Wolfe, *Imaging Phonons. Acoustic Wave Propagation in Solids*, Cambridge Univ. Press (1998).
[48] A. M. Kosevich, Fiz. Nizk. Temp. **11**, 1106 (1985) [Sov. J. Low Temp. Phys. **11**, 611 (1985)].
[49] J. Heil, M. Primke, K. U. Wurz, and P. Wyder, Phys. Rev. Lett. **74**, 146 (1995); M. Primke, J. Heil, and P. Wyder, Physica B **218**, 26 (1996).
[50] A. M. Kosevich, Yu. A. Kosevich, and E. S. Syrkin, Zh. Éksp. Teor. Fiz. **88**, 1089 (1985) [Sov. Phys. JETP **61**, 639 (1985)]; Yu. A. Kosevich, E. S. Syrkin, and A. M. Kosevich, Prog. Surf. Sci. **55**, 59 (1997).
[51] A. M. Kosevich, *Physical Mechanics of Real Crystals* [in Russian], Naukova Dumka, Kiev (1981).
[52] I. M. Lifshits, Zh. Éksp. Teor. Fiz. **38**, 1569 (1960) [Sov. Phys. JETP **11**, 1130 (1960)].
[53] A. M. Kosevich, Zh. Éksp. Teor. Fiz. **35**, 249 (1958) [Sov. Phys. JETP **8**, 171 (1959)]; *Materials of the Fifth All-Union Conf. on Low Temperature Physics* [in Russian], Akad. Nauk. GrSSR, Tbilisi (1960), p. 153.
[54] I. M. Dmitrenko, B. I. Verkin, and B. G. Lazarev, Zh. Éksp. Teor. Fiz. **33**, 287 (1957) [Sov. Phys. JETP **6**, 223 (1958)]; Zh. Éksp. Teor. Fiz. **35**, 2 (1958) [*sic*].
[55] V. G. Bar'yakhtar and V. I. Makarov, Zh. Éksp. Teor. Fiz. **48**, 1717 (1965) [Sov. Phys. JETP **21**, 1151 (1965)]; Zh. Éksp. Teor. Fiz. **49**, 1934 (1965) [Sov. Phys. JETP **22**, 1320 (1966)].
[56] B. G. Lazarev, L. S. Lazareva, V. I. Makarov, and T. A. Ignat'eva, Zh. Éksp. Teor. Fiz. **48**, 1065 (1965) [Sov. Phys. JETP **21**, 711 (1965)]; N. B. Brandt, N. I. Ginzburg, A. N. Ignat'eva, B. G. Lazarev, and L. S. Lazareva, Zh. Éksp. Teor. Fiz. **49**, 85 (1965) [Sov. Phys. JETP **22**, 61 (1966)]; B. G. Lazarev, L. S. Lazareva, A. N. Ignat'eva, and V. I. Makarov, Doklady AN SSSR **163**, 74 (1965) [Sov. Phys. Dokl. **10**, 620 (1965)].
[57] V. G. Bar'yakhtar, B. G. Lazarev, and V. I. Makarov, Fiz. Met. Metalloved. **24**, 829 (1967).
[58] J. Kortus, I. I. Mazin, K. D. Belashchenko, V. P. Antropov, and L. L. Boyer, Phys. Rev. Lett. **86**, 4656 (2001); J. M. An and W. E. Pickett, Phys. Rev. Lett. **86**, 4366 (2001); Y. Kong, O. V. Dolgov, O. Jepsen, and O. K. Andersen, Phys. Rev. B **64**, R0205011 (2001); T. Yildirim, O. Gulseren, J. W. Lynn, *et al.*, Phys. Rev. Lett. **87**, 037001 (2001).
[59] A. F. Goncharov and V. V. Struzhkin, Physica C **385**, 117 (2003).
[60] J. K. Yanson and Yu. G. Naidyuk, Fiz. Nizk. Temp. **30**, No. 4 (2004) [Low Temp. Phys. **30**, No. 4 (2004)].

Translated by Steve Torstveit